ORTHOGONAL FLUXGATE TYPE MAGNETIC MICROSENSORS WITH WIDE LINEAR OPERATION RANGE

THÈSE N^{O} 4039 (2008)

PRÉSENTÉE LE 1ER AVRIL 2008
À LA FACULTÉ DES SCIENCES ET TECHNIQUES DE L'INGÉNIEUR
LABORATOIRE DE MICROSYSTÈMES 3
PROGRAMME DOCTORAL EN MICROSYSTÈMES ET MICROÉLECTRONIQUE

ÉCOLE POLYTECHNIQUE FÉDÉRALE DE LAUSANNE

POUR L'OBTENTION DU GRADE DE DOCTEUR ÈS SCIENCES

PAR

Özge ZORLU

M.Sc. in Electrical and Electronics Engineering, Middle East Technical University, Ankara, Turquie
et de nationalité turque

acceptée sur proposition du jury:

Prof. Y. Leblebici, président du jury
Dr P. Kejik, directeur de thèse
Dr Ph. Flückiger, rapporteur
Dr F. Gueissaz, rapporteur
Prof. P. Ripka, rapporteur

ÉCOLE POLYTECHNIQUE
FÉDÉRALE DE LAUSANNE

Lausanne, EPFL
2008

TABLE OF CONTENTS

3. ELECTROPLATED FENI LAYERS AS FLUXGATE CORE MATERIAL 47

4. ROD TYPE ORTHOGONAL FLUXGATE: THE MACRO SCALE SENSOR 67

5. ROD TYPE ORTHOGONAL FLUXGATE: THE MICRO SCALE SENSOR 81

ACKNOWLEDGEMENTS

I would like to start by thanking my mom and dad for all their trust, support, and solicitude on me. They have a huge part in every accomplishment I have made, and they will always have a great place in my life.

My very special thanks go to my supervisor, Pavel, who was always there when I needed help, got stuck, or had an idea and looking for someone to discuss. I will never forget how smoothly we overtook many issues that are traditionally painful, and his unbelievable efficiency leading to meetings hardly longer than ten minutes.

I owe a big thank you to all the members of our group for the very nice time we had and for the many fruitful discussions. To start with, Prof. Popovic, our group leader, for letting me be a member of LMIS3, and giving me the chance to work in this environment. Franck and Predrag, for their collaboration during the first phases of this work, and their helpfulness in any subject. Klaus and Mirjana, my office mates, for the nice atmosphere that made me think the office is a place to relax and recover if something is not working in the lab and for many joyful and interesting discussions and chats. I should also credit Mirjana for her enthusiasm in speaking French –which did not work on me anyway– and her diverse food supply to the office. Malika for her sincere help on anything, especially during my first days in Lausanne. Marc, for the French translation of my abstract. Christiano, for sharing the burden of thesis writing during Christmas time. Ilona, our secretary, for her patience and the smile on her face while handling all the administrative work. Giovanni, Pierre-André, Enrico, Charles, Serge, Zhen, Jens, and Yves for their valuable friendship and discussions.

The support, technical experience, and goodwill of the CMI stuff have minimized the hard times of the long clean room hours during this study. I would like to thank especially to P. Fluckiger, G. A. Racine, P. Langlet, G. F. Clerc, C. Hibert, I. Magnenat, and J. Schildknecht for being very helpful anytime I needed either an opinion or a material in the clean room, and also M. Pavius for his patience and effort for the FIB processes.

This work is supported by LEM SA, Geneva through a CTI project. I appreciate the effort and contribution of everyone who is involved in the project, especially W. Teppan, E. Favre, and H. Blanchard. They created a stress-free collaboration environment, and their optimism has always encouraged me during these years.

I should also thank Prof. Tayfun Akın from the Middle East Technical University, Turkey, who introduced MEMS and VLSI to me, which basically shaped my research interests.

I have to reserve a large space here to the Turkish community in Lausanne. Most of them were not here when I arrived, but they started showing up in exactly the right time. I am very grateful to all of them both for the many joyful moments we shared, and for the moments that they converted burden into fun. Lausanne became a better place to live with the unforgettable contribution of them all. To give some highlights, I would like to thank Engin and Mustafa for being my non-skiing photography partners and for many technical photography and "more sophisticated" discussions, further Engin for many "co-head bangs" in Zurich. Zafer and Tolga for being creative in their hobbies, and saving many of our days by constantly introducing new stuff to our lifes. Can and Mithat for their intensive knowledge on what they most think about (they should know what I mean, and I have a reason to put them together), also Can for his taste of music, and Mithat for his gusto. Emre, for sharing many troubles of settling in a new country, and letting us form a solid connection between Lausanne and Geneva. Tolga, for his sincere effort in sharing many of his experiences on Switzerland, also for his hospitality during my days in Luzern. Cumhur, for converting the dead times in the clean room to mini breaks of discussions. Yüksel and Aydın for their great sense of humor. Derin, for his unending helpfulness and friendship. Ayfer, Bilge, Özden, and Dilek for their motivation in playing board games and home cinema sessions. Hüseyin, for his hospitality and help especially during my first months in Lausanne. İsmail, for his companionship during the military service days. Eda, Altuğ, Dinçer, Eren, Deniz, Nilay, Alphan, and Işık, for their valuable friendship.

I would also like to thank Yusuf, Selim, Hüseyin, Deniz, Onur, and Barış for their friendship and support that I have always felt coming from thousands of kilometers away, from different sides of the world.

I believe, the Sleeping Beauty deserves the biggest of hugs for her patience and support, which always gave me the confidence I needed at the very difficult times. Without her, this course would have been much more difficult to walk through.

ABSTRACT

This thesis presents a study on the development of microfabricated fluxgate type magnetic sensors operating within a wide linear operation range. Fluxgate type magnetic sensors are powerful devices due to their high sensitivity, low offset, and high temperature stability. Unfortunately, their linear operation range is limited, since an attempt to increase the linear range also increases the power dissipation of the sensor for the traditionally used parallel fluxgate configuration. In this study, microfabricated fluxgate sensors with wide linear operation range and low power dissipation are developed with the use of the orthogonal fluxgate configuration and a closed magnetization path for the excitation.

In the scope of this work, three different fluxgate microsensor structures suitable for operation within a wide linear range are developed, fabricated, and characterized. The sensor structures are named as: rod type orthogonal macro fluxgate sensor, rod type orthogonal micro fluxgate sensor, and ring type micro fluxgate sensor. All of the structures have a CMOS compatible fabrication process flow. Furthermore, the rod type micro sensor and the ring type micro sensor are fabricated by using only standard thin film deposition and photolithography techniques, enabling batch fabrication of these sensor structures. All of the structures use planar sensing coils and an electroplated FeNi core. Apart from the design and development of the sensor, the FeNi electroplating process is intensively investigated since this process directly affects the performance of the sensors.

The rod type orthogonal macro fluxgate sensor uses a 20 µm diameter gold bonding wire as the excitation rod, and a 10 µm thick FeNi core electroplated over the bonding wire. The AC current passing through the excitation rod creates a periodical excitation field in the radial direction, which is always perpendicular to the external magnetic field to be detected along the core. With this sensor, the idea of increasing the linear operation range without increasing the power dissipation by using a closed magnetization path and the orthogonal structure is verified. By

using a 200 mA-peak sinusoidal excitation current at 100 kHz, passing through the low resistance excitation rod, a linear operation range of ±2.5 mT is reached with a 0.5 mm long core, whereas the linear range is ±250 µT with a 4 mm long core.

The rod type orthogonal micro fluxgate sensor presents a modified version of the macro sensor, which can be fabricated in wafer level with standard deposition and photolithography techniques. For this sensor, the excitation rod is formed with an electroplated layer of copper which is sandwiched between two FeNi layers forming the ferromagnetic core. The cross-sectional dimensions of the excitation rod and the core are 8 µm x 2 µm, and 16 µm x 10 µm, respectively. The sensor operates with 100 mA-peak sinusoidal excitation current at 100 kHz, and the linear operation range for different sensors having 0.5, 1, and 2 mm long cores are 1100, 410, and 160 µT, respectively. The linear operation range is independent of the excitation conditions for current peaks larger than 100 mA, which is required to saturate the core, and operating frequencies lower than 200 kHz, where the skin effect is not dominant. The sensitivity, perming, the equivalent magnetic noise density, and the power dissipation of the 0.5 mm long sensor are 102.8 µV/mT, 7.1 µT, 268 nT/√Hz @ 1 Hz, and 10 mW, respectively for the given excitation conditions. The noise analysis showed that the noise of the sensor increases with decreasing sensor dimensions.

The ring type micro fluxgate sensor has a core composed of cascaded planar 2 µm thick FeNi rings which can be fabricated in a single electroplating step, increasing the control of the magnetic properties of the core. The excitation rod passes through the middle of the FeNi rings as a sewing thread, providing a planar circular excitation loop. The angle between the excitation field and the external magnetic field changes according to the position on the ring, which leads to a partially orthogonal partially parallel fluxgate operation mode. The tests of the sensors showed that the maximum operating frequency is extended to 1 MHz level, which is due to the thinner FeNi layer. A sinusoidal current with 180 mA-peak at 1 MHz is used for the excitation of the sensors. A linear operation range of 2 mT and a sensitivity of 730 µV/mT is reached with a 4-ring structure, with the rings having 22 µm and 38 µm inner and outer radius, respectively.

The comparison of the developed sensors with the previously reported state of the art sensors show that the first microfabricated fluxgate sensors having a wide linear operation range and low power dissipation are realized as an accomplishment of this work. All the sensors are CMOS compatible, and a sensor system can be realized by using the metallization layers of a CMOS process for producing the sensing coils, and fabricating the cores on wafers as a post process.

Keywords: magnetic sensor, orthogonal fluxgate, wide linear range, microfabrication, electroplated FeNi, CMOS compatible, low power.

RÉSUMÉ

Cette thèse présente le développement de capteurs magnétiques de type *fluxgate* microfabriqués présentant une large plage de fonctionnement linéaire. Les capteurs magnétiques de type *fluxgate* sont particulièrement intéressants en raison de leur sensibilité élevée, de leur faible offset et de leur grande stabilité en température. Cependant, dans la configuration parallèle qui est traditionnellement utilisée, leur plage de fonctionnement linéaire est limitée du fait qu'une augmentation de cette plage ne se fait qu'au prix d'une augmentation de la puissance dissipée. Cette étude présente le développement de capteurs *fluxgate* microfabriqués avec une large plage d'opération linéaire et une faible dissipation de puissance, grâce à l'utilisation de la configuration orthogonale et une excitation magnétique en boucle fermée.

Dans le cadre de ce travail, trois structures de capteurs fluxgate microfabriqués à large plage linéaire ont été développés, fabriqués et caractérisés. Les structures des capteurs fabriqués sont dénommées comme suit: *rod type orthogonal macro fluxgate sensor, rod type orthogonal micro fluxgate sensor*, et *ring type micro fluxgate sensor*.

Toutes les structures sont produites suivant un procédé compatible avec la technologie CMOS. En outre, les *rod type micro sensor* et le *ring type micro sensor* sont fabriqués en utilisant des dépositions de couches minces et des techniques de photolithographie standards, permettant une production efficace de ces structures de capteur. Toutes les structures utilisent des bobines planaires de détection et un noyau FeNi déposé par un procédé électrolytique. Outre la conception et le développement de la structure des capteurs, le processus d'électrodéposition du FeNi est étudié en profondeur, car il influe directement sur les performances des capteurs.

Le *rod type orthogonal macro fluxgate sensor* utilise un fil de bonding en or de 20 µm diamètre comme tige d'excitation, et un noyau de FeNi électrodéposé de 10 µm d'épaisseur sur la tige d'excitation. Le courant alternatif passant par la tige

d'excitation crée un champ d'excitation périodique radial, qui est toujours perpendiculaire au champ magnétique extérieur à mesurer, orienté le long du noyau. Avec ce capteur, l'idée d'accroître la plage d'opération linéaire sans augmenter la dissipation de puissance à l'aide d'une boucle d'excitation fermée et d’une structure orthogonale est vérifiée. À l'aide d’un courant d'excitation sinusoïdal de 200 mA-pic à 100 kHz passant par la faible résistance de la tige d'excitation, une plage d’opération linéaire de ± 2.5 mT est atteinte avec un noyau 0.5 mm de long, tandis que la plage de fonctionnement linéaire est de ± 250 µT avec un noyau 4 mm de long.

Le *rod type orthogonal micro fluxgate sensor* est une version modifiée du capteur macroscopique, qui peut être fabriquée dans une technologie planaire, suivant les techniques de dépôt et de photolithographie standards. Pour ce capteur, la tige d'excitation est formée d'une couche de cuivre électrolytique qui est en sandwich entre deux couches de FeNi formant le noyau ferromagnétique. Les dimensions de la section transversale de la tige de l'excitation et du noyau sont 8 µm x 2 µm, et 16 µm x 10 µm respectivement. Le capteur fonctionne avec un courant d'excitation sinusoïdal de 100 mA-pic à 100 kHz, et les plages de fonctionnement linéaire pour les capteurs ayant les noyaux de 0.5, 1 et 2 mm de long, sont de 1100, 410, et 160 µT, respectivement. La plage de fonctionnement linéaire est indépendante du courant d’excitation pic au-delà des 100 mA pic nécessaires pour saturer le noyau aux fréquences inférieures à 200 kHz, où l'effet de peau n'est pas dominant. La sensibilité, le *perming*, la densité de bruit magnétique équivalent, et la dissipation de puissance du capteur de 0,5 mm de long sont 102.8 µV/mT, 7.1 µT, 268 nT/√Hz @ 1 Hz, et 8.1 mW, respectivement pour les conditions d'excitation donnés. L'analyse a montré que le bruit du bruit du capteur augmente avec la diminution des dimensions du capteur.

Le *ring type micro fluxgate sensor* a un noyau composé d’une suite d’anneaux FeNi planaires de 2 µm d'épaisseur. Il peut être fabriqué en une seule étape d’électrodéposition, ce qui permet un meilleur contrôle des propriétés magnétiques du noyau. La tige d'excitation passe par le centre des anneaux FeNi comme un fil à coudre. Elle fournit une excitation circulaire dans le plan des anneaux, qui forment une boucle magnétique fermée. L'angle entre le champ d'excitation et le champ magnétique extérieur change en fonction de la position sur l’anneau, ce qui conduit à un mode de fonctionnement du fluxgate partiellement orthogonal et partiellement parallèle. Les tests de ces capteurs ont montré que la fréquence de fonctionnement maximale est portée à 1 MHz, ce qui est dû à la minceur de la couche de FeNi. Un courant sinusoïdal de 180 mA-pic à 1 MHz est utilisé pour l'excitation des capteurs. Une plage d’opération linéaire de 2 mT et une sensibilité de 730 µV/mT sont

atteintes avec une structure 4-anneaux, avec des anneaux de 22 µm de rayon intérieur et de 38 µm de rayon extérieur.

La comparaison des capteurs mis au point avec les capteurs représentant l'état de l'art montrent que ce travail constitue la première démonstration de capteurs fluxgate microfabriqués présentant une large plage de fonctionnement linéaire associée à une faible dissipation de puissance. Tous les capteurs sont compatibles CMOS. Un système complet peut être réalisé en utilisant les couches de métallisation d'un procédé CMOS pour les bobines de détection et en ajoutant les noyeaux dans une étape de *post-processing*.

Les mots clés: capteur magnétique, fluxgate orthogonal, large plage linéaire, microfabrication, électrodéposition FeNi, compatible CMOS, faible consommation d'énergie.

CHAPTER I

INTRODUCTION

The main motives of the academic and industrial research in the field of microsensors are miniaturization, reducing the fabrication costs, and the power requirements of the devices, while increasing the resolution and the dynamic range of the sensors. Integration of sensor devices with electronics not only speeds up development of systems with the required features, but also leads to compact and portable solutions, rapidly increasing the application areas of these devices.

The goal of this thesis is the development, fabrication, and characterization of a fluxgate type magnetic microsensor structure suitable for operation within a wide linear range. The developed fabrication process should be compatible with the existing CMOS technologies and enable the fabrication of the sensor as a post process on CMOS wafers. The fabrication process should be low cost and the sensor structure should be operable with low power, while maintaining a high resolution. The main challenge of this work is the miniaturization of the sensor dimensions, since the magnetic noise of the ferromagnetic structures rapidly increases as their dimensions are reduced.

In this chapter, the magnetic sensors that are used for measuring high magnetic fields will be presented in Section 1.1. State of the art micro fluxgate sensors will be introduced in Section 1.2. The detailed description of the objectives of the thesis will be given in Section 1.3. Finally, in Section 1.4, the chapter will be summarized and the organization of the thesis will be introduced.

1.1 Magnetic Sensors for High Field Measurements

For the applications requiring the measurement of high magnetic fields such as contactless current measurements or position monitoring, most frequently used sensors are Hall effect sensors. However, with the development in magnetic field sensors, other types of sensors such as anisotropic magnetoresistance, giant magnetoresistance, giant magnetoimpedence, and fluxgate sensors have appeared as alternative devices. In this section, brief review of these sensors will be given, including the basic sensor structure, the nature of the output signal, main advantages and disadvantages, and the application areas of the sensors.

1.1.1 Hall Effect Sensors

Hall effect sensors are the most widely used type of magnetic sensors. The main applications that use Hall effect sensors are angular or linear position, velocity, or rotation sensing and contactless measurement of current. The automotive industry benefits most from these application possibilities as each of today's smart cars accommodate 10 Hall effect sensors in average. Typically, Hall effect sensors work within a magnetic flux density range from several mT to several T, and frequencies from DC to several tens of kHz [1.1].

The Hall effect is discovered by E. Hall [1.2], and is based on the effect of a magnetic field on a moving charged particle. The force **F** on the charged particle is called the Lorentz Force, and is given as:

$$\mathbf{F} = e(\mathbf{E} + (\mathbf{v} \times \mathbf{B})) \tag{1.1}$$

where e is the electrical charge and v is the velocity of the particle, and **E** and **B** are the ambient electric field and magnetic field intensity, respectively. When a current is passed through a simple Hall effect device presented in Figure 1.1, placed in a magnetic field perpendicular to the direction of the current, the movement of carriers are curved to one side, creating an electric field E_H between two sides of the device. This electric field continues increasing up to the value where the Lorentz force on the particles is zero. According to this charge accumulation at the sides, a potential difference occurs between the two sides of the device, called the Hall voltage, V_{Hall}. The Hall voltage is directly proportional to the magnetic field and the current passing thorough the device, and inversely proportional to the thickness of the device:

$$V_H = G \cdot \frac{R_H}{t} \cdot I \cdot B \tag{1.2}$$

where G is called the geometrical factor which is between 0 and 1, and R_H is the Hall coefficient of the material, which is inversely proportional to the carrier concentration.

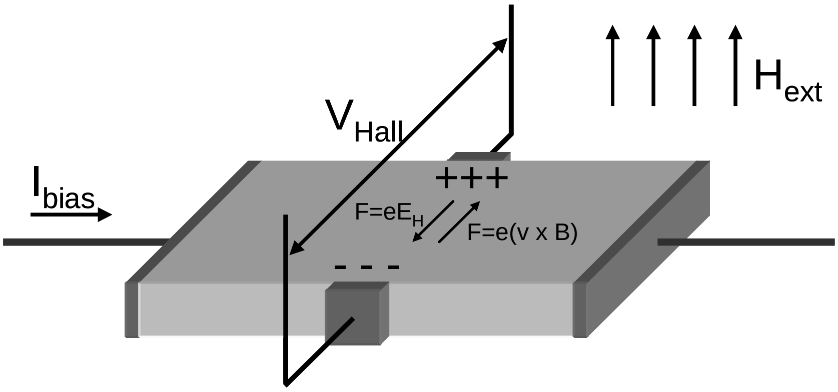

Figure 1.1: The schematic of a Hall effect sensor subjected to a magnetic field and resulting Hall voltage.

The most important advantage of Hall effect sensors apart from their simple structure and good characteristics is their almost perfect compatibility with microfabrication technologies. Hall devices with good characteristics can easily be fabricated by using standard CMOS technologies and the signal conditioning electronics of the sensor can be integrated with the Hall device [1.3].

The main disadvantage of Hall effect sensors is the high offset voltage at the output of the device. The reasons for the offset are the non-symmetric geometry of the device resulting from the misaligned layers during fabrication, the carrier concentration gradients, surface defects, and contact resistance variations. These effects can lead to offset voltages equivalent 10 mT for silicon Hall effect sensors. The value of the offset voltage also depends on temperature and the stress on the device. Furthermore, these dependences degrade the long term stability of the sensor. Another limiting factor for the Hall effect sensors is the 1/f noise, which may introduce a noise equivalent to 1 µT within a 0.1 to 10 Hz operating frequency range.

The current research on Hall effect sensors goes in three main directions. One of them is searching new materials that have better properties as Hall devices such as III-V group semiconductors [1.4]. Looking for new sensor geometries that help in reducing the offset is another branch of the research on Hall effect sensors [1.5]. Development of new signal conditioning techniques in order to reduce the offset, noise, and to compensate the temperature sensitivity of the sensor, and integrating the sensor with all the electronics required is also extensively studied [1.1].

1.1.2 Anisotropic Magnetoresistance Sensors

Anisotropic magnetoresistance (AMR) sensors are mostly used in the read heads of magnetic storage devices, angular and linear position sensing systems, and compass applications due to their simple structure. They typically measure magnetic fields up to 200 µT within a frequency range between DC to several MHz.

The AMR effect is based on the anisotropic resistivity value of a ferromagnetic thin film having magnetic anisotropy. Figure 1.2 shows the basic configuration of an AMR sensor. The rotation θ in the magnetization vector M of the ferromagnetic film when it is subjected to a magnetic field results in change in the resistivity of the material in the order of 2-3 % within the operation range of the device [1.3]. The response of the sensor is unipolar for the rotation of M, so reversing the direction of the applied field does not change the resistivity value of the layer. In order to solve this problem, AMR sensors are designed in a configuration called “barber pole configuration” [1.6], leading the current with an angle of 45 ° along the length of the layer.

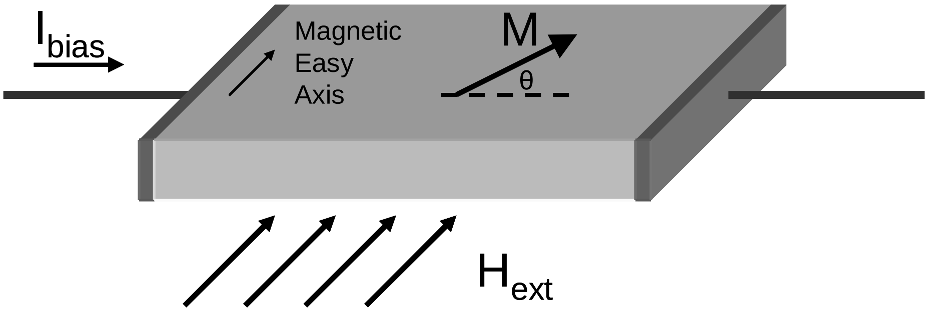

Figure 1.2: Basic configuration of an AMR sensor.

Better AMR behavior is observed for ferromagnetic layers with an easy axis in the direction of the applied field, and a thickness in the order or 20 nm. Because of these requirements, layers are mostly deposited on substrates by evaporation or sputtering, with an ambient field in the order of tens of kA/m during the process. A thermal annealing process is generally necessary for improving the magnetic easy axis properties [1.7]. Due to the thermal annealing process, the AMR sensor cannot be integrated with CMOS electronics; instead the sensor and the electronics are fabricated on different chips and combined afterwards. Another disadvantage of AMR sensors is perming, as they employ ferromagnetic layers as the sensing elements.

The resistance of the sensor increases as the thickness of the layer decreases. If only one sensor element is used, the increase in the resistance increases the offset of the sensor. Because of this, AMR sensors generally operate in the Wheatstone bridge configuration, producing an output voltage proportional to the applied magnetic field [1.8].

1.1.3 Giant Magnetoresistance Sensors

The Giant magnetoresistance (GMR) effect is a relatively newly discovered phenomenon [1.9] based on the principle of spin dependent scattering. When two ferromagnetic thin layers are separated with a conducting non-ferromagnetic layer, and if the thickness of the total structure is smaller than the mean free path of an electron (10-20 nm), scattering of electrons occur between the ferromagnetic layers depending on the respective direction of their magnetization moments. If their magnetizations are in the same direction, the scatterings are minimum and the resistance of the structure is low. The maximum resistance is reached when the moments are in opposite directions. There are a number of GMR sensor configurations, commonly used ones named as: sandwich, multilayer sandwich, and the spin valve configuration. In a typical “spin valve” GMR sensor configuration presented in Figure 1.3, the moment of one of the structures is fixed with the help of an antiferromagnetic layer. The rotation of the moment of the other layer with the applied magnetic field determines the change in the resistance of the sensor. The change in the resistance of the sensor is typically 30 %, which is 10 times more than that of the AMR sensor [1.3].

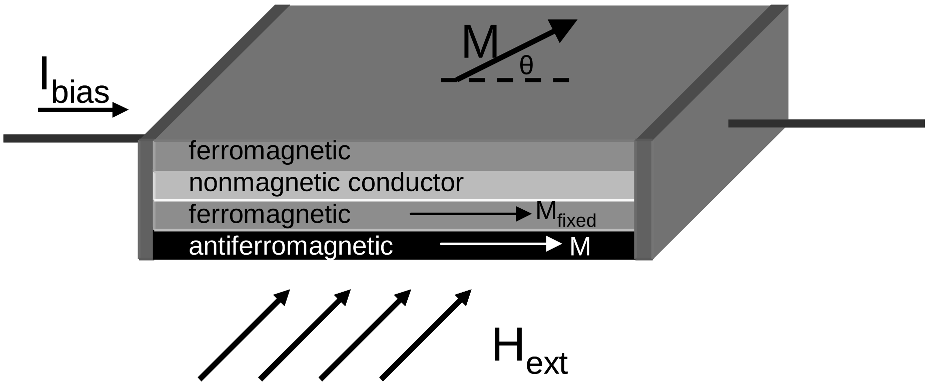

Figure 1.3: A typical “spin valve” GMR sensor configuration.

The materials for GMI sensor enable the realization of sensor with flexible operation range and sensitivity values. The sensing elements can be fabricated in a very small area (~100 µm^2), and the fabrication process is CMOS compatible [1.10].

Furthermore, they can work within a wide bandwidth. These make the GMI sensor very suitable for many applications such as magnetic reading heads, position sensing, and non destructive material evaluation.

The output of the sensor is generally unipolar, however a bipolar output can be achieved by biasing the spin valve structure perpendicularly. The offset of the sensor can be cancelled by using a bridge configuration as in the case of an AMR sensor. The main limitation of a GMR sensor is its perming, which is around 10 µT.

1.1.4 Giant Magnetoimpedance Sensors

Another relatively new type of magnetic sensor is the Giant magnetoimpedance (GMI) sensor. The operation principle is based on the GMI effect, which is the magnetic field dependent change of the impedance value of a soft magnetic structure which is excited with a high frequency current. The permeability and the skin depth of the soft magnetic layer depend on the frequency of excitation as well as the actual magnetic state of the material. According to the applied field and the frequency of excitation, the skin depth and the permeability of the material changes. This affects the resistance and the inductance of the material respectively, leading to a change in the impedance value.

The low fabrication cost and high flexibility of the GMI sensors make them suitable for use in biomedical applications and automation and control in the industry. Most of the GMI sensors employ amorphous wires or soft magnetic thin films as the sensing elements [1.11], [1.12], [1.13]. These types of GMI sensors have a simple structure and can easily be fabricated. However, it is difficult to saturate the middle region of the sensing material at high frequencies due to the skin effect. This leads to magnetic hysteresis error [1.14], decreasing the resolution of the sensor. Annealing reduces the hysteresis error, but it disturbs the CMOS compatibility of the device. The use of sandwiched soft magnetic layers improves the performance of the sensor at the cost of increased fabrication complexity [1.15]. Electroplating of a soft magnetic layer, such as Permalloy, surrounding a copper or gold wire [1.16] is another common configuration. This configuration reduces the saturation and hysteresis problems of single layer soft magnetic films. Unfortunately, it is difficult to integrate these wires with the electronics on the wafer level.

The excitation frequency of GMI sensors vary between several tens of kHz to several MHz, and the GMI ratios between 50 % and 3000 % are reported depending on the properties of the soft magnetic material. The signal is generally read by an impedance analyzer; however, Colpitts oscillator [1.17] can be used to miniaturize the GMI sensor system.

1.1.5 Fluxgate Sensors

Fluxgate type magnetic sensors are used to measure DC or low frequency magnetic fields. The most common application area of fluxgate sensors is navigation, where sensors are employed as compasses or inertial sensors in GPS systems. In automotive industry, they are utilized as proximity sensors for parking aid purposes. Another application area is non-destructive testing where material properties and possible defects on surfaces can be detected with fluxgate sensors. Geomagnetic measurements such as monitoring of local anomalies of the earth's magnetic field, detecting iron constructions like buildings and bridges, and buried constructions like pipelines, tanks, and drums are also realized by using fluxgate sensors.

Figure 1.4 shows the basic configuration of a fluxgate sensor. Generally, the sensor consists of a ferromagnetic bar and sensing and excitation coils wound around it. The operation principle is based on the periodic modulation of the permeability of the ferromagnetic core by creating an AC field with the excitation coil which carries the AC excitation current. The sensing coil senses the periodic change in the permeability of the core, and an induced voltage occurs across its terminals. Without any external magnetic field, this voltage is symmetrical and is composed of only odd harmonics. When there is an external field, the symmetry is disturbed and even harmonics occur on the signal. The magnitude of the 2nd and higher even harmonics of the signal is proportional to the magnitude of the external field. There are two basic fluxgate sensor configurations. In the configuration presented in Figure 1.4, the excitation field and the external field to be measured are parallel to each other and this configuration is known as the parallel fluxgate configuration. Figure 1.5 presents the orthogonal fluxgate configuration where the excitation field is perpendicular to the external magnetic field. The external magnetic field information is at the even harmonic of the signal across the terminals of the sensing coil, similar to the parallel configuration.

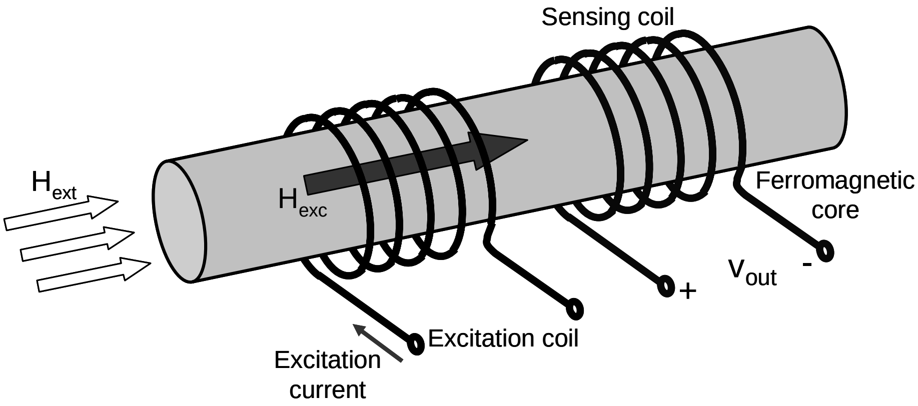

Figure 1.4: Basic configuration of a fluxgate sensor (parallel fluxgate).

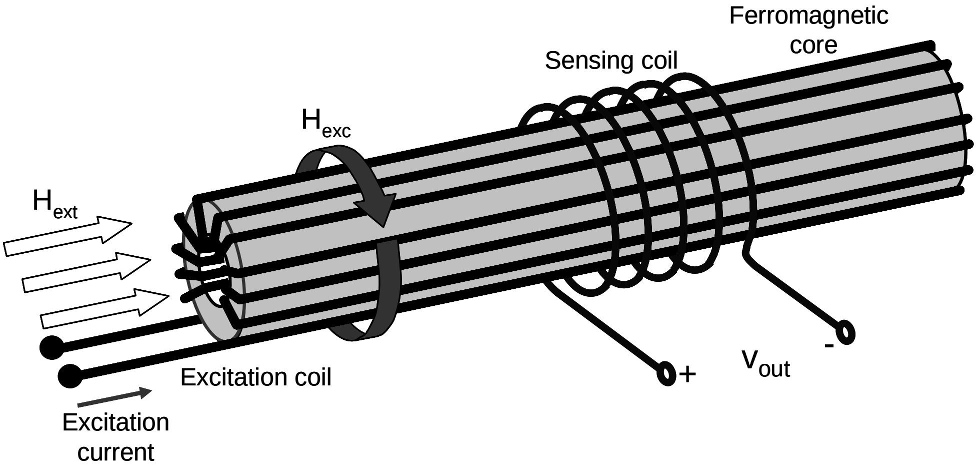

Figure 1.5: The orthogonal fluxgate configuration.

In the parallel configuration, the excitation and detection mechanisms are dependent on each other, so they cannot be designed separately. However, the orthogonal structure has the advantage of having separate excitation and detection mechanisms, enabling the design of both parts independent of each other. In the parallel configuration, a sensor with a higher linear range requires a shorter core with a higher demagnetization factor, which increases the excitation magnetic field for proper operation. However, in the orthogonal structure the decrease in the length of the core does not affect the required excitation field; however, it increases the linear operation range of the device in a similar way.

The main advantage of fluxgate sensors is their low offset and low offset drift. Due to the nature of the useful signal appearing at the even harmonics of the induced voltage, the only offset contribution is the offset coming from the signal conditioning electronics. The temperature coefficient of the offset is also very low, and the sensors can work in a very wide temperature range. Commercial fluxgate sensors commonly have an absolute precision of 10 nT [1.3]. They can work in a wide operation range of several tens of µT to several hundreds of µT with high linearity.

Their relatively high power dissipation and limited operation range are the main disadvantages of fluxgate sensors. Furthermore, most of the fluxgate sensors still use wound coils and large sized ferromagnetic materials. There were several attempts made for miniaturizing the fluxgate sensors, and reducing their power dissipation. Next section will give detailed information on the miniaturized fluxgate sensors.

1.2 Miniaturized Fluxgate Sensors – State of the Art

Many applications such as compasses, navigation systems, magnetic sensor arrays and current sensors require small sized magnetic sensors. Fluxgate sensors are good candidates for these applications due to their advantages mentioned in the previous section. Miniaturization of these sensors is necessary due to a number of reasons. First of all, finding integrated solutions that can replace the wound excitation and sensing coils reduce the fabrication costs of the sensor. Furthermore, it enables the combination of the sensor with its signal conditioning electronics within the same ASIC. Other advantage of miniaturization is the reduced power requirement for the operation of the sensor. However, miniaturization of the fluxgate sensors is a complicated and difficult task, since the magnetic noise of the device dramatically increases with the decrease in the dimensions of the magnetic layers or pieces used in the sensor [1.3].

Several approaches have been made for the miniaturization of the fluxgate devices over the last few decades. There are three mainstreams that are followed. One of them is to use the PCB technology, and the other one is the use of microfabrication technologies for the fabrication of fluxgate devices. Using small sized wires is another approach, which is not as frequently used as the former two. All of these approaches are still used, and devices fabricated by using any of these methods are still being reported.

In the following sections, the state of the art fluxgate sensors will be presented. The main focus will be on the devices which are fabricated by using microfabrication technologies and small sized wires as they are more related to the scope of the work presented in the following chapters. PCB fluxgates will also be mentioned when necessary.

The first attempt to fabricate an integrated fluxgate sensor was made by Seitz, which is reported in 1990 [1.18]. A sputtered Permalloy layer and sensing coils were fabricated on a silicon substrate within a 2 mm x 4mm area, whereas the excitation coil was wound around the silicon chip. A sensitivity of 165 V/T was reported with a triangular excitation at 100 kHz frequency.

In 1994, Kawahito et. al., reported a micromachined fluxgate sensor composed of an electroplated Permalloy rod and solenoidal excitation and sensing coils [1.19]. The Permalloy rod had 2000 µm x 130 µm dimensions. The device had a linear operation range of 200 µT, a sensitivity of 200 V/T, and was operated with 180 mA-peak sinusoidal current. A similar structure was reported by Gottfried-Gottfried, using the metallization lines of the CMOS process in order to fabricate the solenoidal coils, and the Permalloy core was electroplated in between the metal by modifying the CMOS process flow [1.20]. The linear range of the sensor was 50 µT with a sensitivity of 3 V/T, when excited with 2 mA-peak sinusoidal current passing through 520 Ω excitation coil. The total sensor area was 1.5 mm x 1 mm.

Choi et. al. reported the first integrated fluxgate sensor in an NMOS process using two sputtered Permalloy cores on the same plane with a linear operation range of 65 µT [1.21]. The metal layers of the process were used for fabricating the planar excitation and sensing coils. The first fully integrated CMOS fluxgate sensor was reported by Schneider et. al in 1997 [1.22] and Kawahito in 1999 [1.23] with 60 mW power dissipation. The sensor structure was similar to [1.21]; however the cores were fabricated by an electroplated NiFeMo layer. The structure was further improved by Ripka et. al, by adding a symmetrical core layer under the planar coils, which forms an almost closed magnetization path between the upper and lower cores for the excitation [1.24], [1.25]. Electroplated FeNi was used as the core material. The sensor reached a linear operation range of 1 mT, a perming of 5 µT, and a sensitivity of 25 V/T, with a 110 mA-peak sinusoidal current excitation at 1 MHz, passing though excitation coils with 150 Ω total resistance.

Liakopoulos et. al., reported a micromachined fluxgate sensor with a 500 µT linear operation range and 60 nT resolution with 100 mW power dissipation [1.26]. The sensor has a race-track core configuration which is fabricated with electroplated FeNi, and solenoidal excitation and sensing coils were micromachined by electroplated Cu. With this fabrication process, the sensor has 5 x 2.5 x 0.1 mm^3 dimensions. A similar structure with smaller sensor dimensions (2.6 mm x 1.7 mm) was reported by Park et. al, with 8.5 mW power dissipation, and a perming value below 1.7 µT [1.27]. However, the linear operation range was 100 µT, as the sensor was designed for a compass application.

Chiesi et. al. reported a 2D micro fluxgate compass which uses cross-shaped amorphous material (Metgals®), which is patterned and glued on the sensing and excitation coils fabricated by a CMOS process [1.28]. The total power dissipation of the chip was 12.5 mW, and the linear operation range of the sensor was 60 µT. The core fabrication process was improved and another signal conditioning electronics circuit was designed by Drljaca et. al. for low noise applications, and 6 nT/√Hz at 1 Hz noise density was obtained for the same linear operation range, with 35 mW power dissipation [1.29]. Another version of the sensor was characterized with 10 mW power dissipation from a 2.5 V supply, a noise density of 15 nT/√Hz at 1 Hz, and a perming value of 1.4 µT [1.30].

A PCB fluxgate sensor using an electroplated Permalloy ring core with a 5 mm radius, planar excitation coils, and wound sensing coil was reported by Tipek et. al [1.31], [1.32]. This sensor also has a linear operation range of 1 mT, and is opearated with 450 mA-peak current passing through 0.7 Ω excitation coils. The reported perming and the noise of the sensor are 1 µT and 1.2 nT-rms/√Hz, respectively.

All the sensors presented above uses the parallel fluxgate configuration. However, probably the first attempt to miniaturize the fluxgate sensor was done on the orthogonal structure by Gise and Yarborugh [1.33], [1.34]. The sensor was composed of 1/4” and 1/8” wires on which a Permalloy layer was electroplated. Copper coils were wound around the core were used as the sensing coils. After this approach, orthogonal configuration was almost forgotten; however, similar structures were used as GMI sensors [1.35].

After 20 years from the first attempt, Chiesi et. al, reported a microfabricated orthogonal fluxgate sensor [1.36]. The core was patterned in a rectangular shape (600 µm x 100 µm) from an amorphous ferromagnetic ribbon (Vitrovac® 6025Z), and glued on the microfabricated planar sensing coils. The excitation current was provided through the wires which are directly bonded to the core. A linear operation range of 120 µT, and a noise value of 400 nT was reached with a 10 mA-peak sinusoidal excitation current.

In 2000, Kejik et. al. reported a 2D PCB fluxgate sensor working in the orthogonal mode [1.37]. The sensor consists of a pair of excitation and a pair of sensing coils which are placed in a cross shape on the PCB, being orthogonal to each other. Then a ring core was patterned on the coils with photolithography and wet etching. The linear operation rang of the sensor was given as 60 µT, with 160 mA-peak excitation current.

Orthogonal fluxgate sensors formed by electroplating a ferromagnetic layer around a non magnetic conductor wire were re-visited by Ripka et. al, around the same times with the research presented in this thesis. With a 1.8 mm-long electroplated FeNi core, a sensitivity of 11 mV/T and a perming value less than 1 µT was achieved for an excitation of 30 mA-rms [1.38], [1.39]. In [1.40], with an electroplated FeNiCo layer, a linear operation range of 300 µT is reached for 40 mA-rms current.

1.3 Objectives of the Thesis

As it is summarized above, many fluxgate sensors have been developed and fabricated through the past decades. Compact, low power, and CMOS compatible fluxgate sensors have been reported with combined electronics circuits for low field and high resolution applications. However, the fluxgate sensors with wide linear operation range are either fabricated by using PCB technology or micromachined with very large dimensions in the order of 10 mm^2. Furthermore, their power dissipation is around several hundres of mW, placing them far away from the category of low power sensors.

The main goal of this thesis is the design and development of orthogonal fluxgate sensor structures which are suitable for microfabrication, occupying less than 1 mm^2 chip area and having a wide linear operation range, extending up to the mT level. The developed process should be applied as a post-process on CMOS wafers, and the resulting sensor should have low power dissipation around 10 mW. The following paragraphs give a more detailed explanation of the thesis objectives.

Fluxgate type sensors are powerful magnetic sensors due to their low offset, low offset drift with temperature, low noise, high sensitivity, and high linearity. Increasing their linear operation range up to mT ranges enables the use of these devices for measuring higher magnetic fields such as the case of a contactless current sensor. For these applications, traditionally Hall effect devices are employed, which still have high offset, and offset drift problems. Fluxgate sensors can be an alternative to Hall sensors, if the linear operation range is widened.

Most of the fluxgate sensors are built for operation in the parallel fluxgate mode. This makes the excitation and detections mechanisms dependent on each other. A wider linear operation range is obtained by shortening the length of the core due to the demagnetization effect. However, this also increase the field required to saturate the core, leading to an increase in the power dissipation of the sensor. On the other hand, orthogonal configuration has the advantage of having separate excitation and detection mechanisms. Once the excitation mechanism is designed, the linear operation range can be extended by only shortening the length of the core, without affecting the power requirements of the sensor for proper operation. Because of this, using orthogonal configuration is a suitable solution for having a fluxgate sensor with a wide linear operation range.

Integration of the sensor with its signal conditioning electronics is important in order to have a small, compact, and low cost sensor system. In this sense, the fabricated sensor should be small sized and the fabrication process flow should be compatible with contemporary CMOS technologies. The sensitive part of the sensor should be fabricated as a post process on the finished CMOS wafers or chips accommodating the electronics and required coils for the sensors. This can be achieved by the use of thin film technologies for depositing metal layers such as evaporation, sputtering, and electroplating, and patterning them with standard photolithography techniques, which do not require any thermal annealing or harsh polishing steps, which may damage the CMOS electronics.

Reducing the power dissipation of the sensor is always important for CMOS circuits and sensor systems. In the first glance, one may think that miniaturizing the sensor not only increases the compactness of the sensor, but also decreases its power requirements as the dimensions become smaller, and a given magnetic field can be produced with much less current. Unfortunately, this is true only up to a certain degree as the magnetic noise of the ferromagnetic materials drastically increases with miniaturization. Furthermore, the sensitivity of the sensor decreases with reduced dimensions. So, having a small sized fluxgate type magnetic sensor with low power dissipation is a major challenge of this work.

In the scope of this work, three different fluxgate sensors are developed and fabricated which are named as: macro scale orthogonal fluxgate sensor, micro scale orthogonal fluxgate sensor, and ring type fluxgate microsensor. With the macro scale orthogonal fluxgate sensor the idea of increasing the linear operation range without changing the excitation requirements by using a closed excitation magnetization path and the orthogonal structure is verified. Then, the micro scale orthogonal fluxgate sensor is presented as an integrated approach, to which the same idea can be applied. Finally, an alternative structure is presented as the ring type fluxgate micro sensor, which operates in a partially orthogonal partially parallel mode, but still employs a closed magnetization path for excitation. All of the sensors are described in separate chapters in the thesis. A more detailed description of the organization of the thesis is given in the following section.

1.4 Summary and the Plan of the Thesis

In this chapter, common magnetic sensors are introduced with their operation principles, and application areas. The possibility of increasing the linear operation range of a fluxgate sensor without affecting the power requirements of the sensor by using the orthogonal fluxgate configuration is introduced. Then, state of the art for miniaturized fluxgate sensors is summarized. Finally, the objectives of the thesis are explained in detail. The rest of the thesis is organized as follows:

Chapter II explains the operation principles of fluxgate type magnetic sensors, including the demagnetization effect in magnetic materials. An explanation on the operation of orthogonal fluxgate sensors is developed and explained in detail. Also, performance parameters for fluxgate sensors are presented.

Chapter III describes the different types of core materials and deposition methods used in fluxgate sensors. Then, it explains the experiments and test performed in order to optimize the properties of electroplated FeNi layer that are used to form the ferromagnetic core of the sensors.

Chapter IV is on the rod type, macro scale orthogonal fluxgate sensors composed of a gold wire bonding and electroplated FeNi layer over it, developed and fabricated in order to verify the idea of increasing the linear operation range without increasing the power requirements of the sensor.

Chapter V explains the microfabricated orthogonal fluxgate sensor developed in order to achieve the objectives of this thesis. The design procedure is summarized and the developed CMOS compatible process flow is explained in detail. The feasibility of using the orthogonal structure in a wide linear range microsensor application is verified with the presented test results.

Chapter IV presents a ring type semi orthogonal-semi parallel fluxgate microsensor, which can be an alternative to the fully orthogonal device. Again, the design and fabrication procedures are explained and first test results of the fabricated sensors are presented.

Chapter VII gives a summary of the achievements of this work, and compares the developed sensors with the contemporary fluxgate sensors. Several suggestions in order to improve the performance of the sensors, as a continuation of this research are also given.

1.5 References

[1.1] R. S. Popovic, “Hall Effect Devices,” 2nd edition, ISBN 0-7503-0855-9, Institute of Physics Publishing, 2004, Bristol, UK.

[1.2] E. H. Hall, “On a new action of the magnet on electric current,” American Journal of Mathematics, vol. 2, pp. 287-292, 1879.

[1.3] P. Ripka, “Magnetic Sensors and Magnetometers,” ISBN 1-58053-057-5, Artech House, 2001, USA.

[1.4] V. Cambel, G. Karapetrov, V. Novosad, E. Bartolome, D. Gregusova, J. Fedor, R. Kudela, J. Šoltys, “Novel Hall sensors developed for magnetic field imaging systems,” Journal of Magnetism and Magnetic Materials, vol. 316, issue 2, pp. 232-235, September 2007.

[1.5] P. Kejik, S. Reymond, R. S. Popovic, “Circular Hall transducer for angular position sensing,” Transducers '07 & Eurosensors XXI conference, Lyon, France, Digest of technical papers vol. 2, Pages 2593-2596, June 10-14, 2007.

[1.6] C. W. M. P. Sillen, L. Postma, E. A. Draaisma, F. A. Pronk, “Design and technology of sensor-last thin film magnetic heads,” Philips Journal of Research, vol. 51, issue 1, pp. 149-171, 1998.

[1.7] S. Tumanski, “Thin Film Magnetoresistive Sensors,” ISBN 0-7503-0702-1, Institute of Physics Publishing, 2001, Bristol, UK.

[1.8] M. Ilg, B. C. Chang, D. Hepner, A. Thompson, “A microcontroller solution for AMR magnetic sensing in flying munitions systems,” IEEE International Conference on Mechatronics’05, pp. 84-89, 10-12 July 2005.

[1.9] M. N. Baibich, J. M. Broto, A. Fert, F. Nguyen Van Dau, F. Petroff, P. Eitenne, G. Creuzet, A. Friederich, J. Chazelas, “Giant Magnetoresistance of (001)Fe/(001)Cr Magnetic Superlattices,” Physical Review Letters, vol. 61, issue 21, pp. 2472-2475, 1988.

[1.10] W. Granig, C. Kolle, D. Hammerschmidt, B. Schaffer, R. Borgschulze, C. Reidl, J. Zimmer, Juirgen “Integrated Gigant Magnetic Resistance based angle sensor,” Sensors 2006, pp. 542-545, Oct. 2007.

[1.11] K. Mohri T. Kohsawa, K. Kawashima, H. Yoshida, L. V. Panina, “Magneto-inductive effect (MI effect) in amorphous wires,” IEEE Trans. on Magnetics, vol. 28, no. 5, pp. 3150-3152, September 1992.

[1.12] L. V. Panina, K. Mohri, K. Bushida, M. Noda, “Giant magneto-impedance and magneto-inductive effects in amorphous alloys,” J. App. Phys. vol. 76, no. 10, pp. 6198-6203, November 1994.

[1.13] P. Ripka, A. Platil, P. Kaspar, A. Tipek, M. Malatek, L. Kraus, “Permalloy GMI Sensor,” Journal of Magnetism and Magnetic Materials 254-255, pp. 633-635, 2003.

[1.14] D. Garcia, G. V. Kurlyandskaya, M. Vazquez, F. I. Toth, L. K. Varga, “Influence of field annealing on the hysteretic behaviour of the giant magneto-impedance effect of Cu wires covered with $Ni_{80}Fe_{20}$ outer shells” Journal of Magnetism and Magnetic Materials, vol. 203, issues 1-3, pp. 208-210, August 1999.

[1.15] Y. Zhou, J. Yu, X. Zhao, B. Cai, "Giant Magneto-Impedance Effect in the Sandwiched FeSiB/Cu/FeSiB Films," IEEE Transactions on Magnetics, vol. 36 no. 5, pp. 2960-2962, September 2000.

[1.16] R. S. Beach, N. Smith, L. C. Platt, "Magneto-impedance effect in NiFe plated wire," Applied Physics Letters, vol. 68, pp. 2753-2755, May 1996.

[1.17] "Colpitts Oscillator," Wikipedia, 2008. Online 13 Jan. 2008, http://en.wikipedia.org/wiki/Colpitts_oscillator.

[1.18] T. Seitz, "Fluxgate sensor in planar microtechnology," Sensors and Actuators A, vol. 22, issues 1-3, pp. 799-802, June 1989.

[1.19] S. Kawahito, Y. Sasaki, H. Sato, T. Nakamura, Y. Tadokoro, "A fluxgate magnetic sensor with micro-solenoids and electroplated permalloy cores," Sensors and Actuators A, vol. 43, issues 1-3, pp. 128-134, May 1994.

[1.20] R. Gottfried-Gottfried, W. Budde, R. Jahne, H. Kuck, B. Sauer, S. Ulbricht, U. Wende, "A miniaturized magnetic-field sensor system consisting of a planar fluxgate sensor and a CMOS readout circuitry," Sensors and Actuators A, vol. 54, issues 1-3, pp. 443-447, June 1996.

[1.21] S. O. Choi, S. Kawahito, Y. Matsumoto, M. Ishida, Y. Tadokoro, "An integrated micro fluxgate magnetic sensor," Sensors and Actuators A, vol. 55, issues 2-3, pp. 121-126, July 1996.

[1.22] M. Schneider, S. Kawahito, Y. Tadokoro, H. Baltes, "High sensitivity CMOS microfluxgate sensor," International Electron Devices Meeting, Technical Digest pp. 907-910, IEDM-1997.

[1.23] S. Kawahito, C. Maier, M. Schneiher, M. Zimmermann, H. Baltes, "A 2D CMOS microfluxgate sensor system for digital detection of weak magnetic fields," IEEE Journal of Solid State Circuits, vol. 34, issue 12, pp. 1843-1851, 1999.

[1.24] P. Ripka, S. O. Choi, A. Tipek, S. Kawahito, M. Ishida, "Symmetrical core improves micro-fluxgate sensors," Sensors and Actuators A, vol. 92, issues 1-3, pp. 30-36, August 2001.

[1.25] P. Ripka, S. Kawahito, S. O. Choi, A. Tipek, M. Ishida, "Micro-fluxgate sensor with closed core,"Sensors and Actuators A, vol. 91, issues 1-2, pp. 65-69, June 2001.

[1.26] T. M. Liakopoulos, C. H. Ahn, "A micro-fluxgate magnetic sensor using micromachined planar solenoid coils," Sensors and Actuators A, vol. 77, issue 1, pp. 66-72, September 1999.

[1.27] H. S. Park, J. S. Hwang, W. Y. Choi, D. S. Shim, K. W. Na, S. O. Choi, "Development of micro-fluxgate sensors with electroplated magnetic cores for electronic compass," Sensors and Actuators A, vol. 114, issues 2-3, pp. 224-229, September 2004.

[1.28] L. Chiesi, P. Kejik, B. Janossy and R. S. Popovic, "CMOS planar 2D micro-fluxgate sensor," Sensors and Actuators A, vol. 82, issues 1-3, pp. 174-180, May 2000.

[1.29] P. M. Drljaca, P. Kejik, F. Vincent, R. S. Popovic, "Low noise CMOS micro-fluxgate magnetometer," Transducers'03 conference, Boston, USA, Digest of technical papers vol. 1, Pages 304-307, June 8-12, 2003.

[1.30] P. M. Drljaca, P. Kejik, F. Vincent, D. Piguet, R. S. Popovic, “Low-power 2-D fully integrated CMOS fluxgate magnetometer,” IEEE Sensors Journal, vol. 5, issue 5, pp. 909-915, October. 2005.

[1.31] A. Tipek, P. Ripka, Terence O’Donnell and J. Kubik, “PCB technology used in fluxgate sensor construction,” Sensors and Actuators A, vol. 115, issues 2-3, pp. 286-292, September 2004.

[1.32] A. Tipek, T. O'Donnell, P. Ripka, J. Kubik, “Excitation and temperature stability of PCB fluxgate sensor,” IEEE Sensors Journal, vol. 5, issue 6, pp. 1264-1269, December 2005.

[1.33] P. Gise, R. Yarbrough, “An electrodeposited cylindrical magnetometer sensor,” IEEE Transactions on Magnetics, vol. 11, issue 5, pp. 1403-1405, 1975.

[1.34] P. Gise, R. Yarbrough, “An improved cylindrical magnetometer sensor,” IEEE Transactions on Magnetics, vol. 13, issue 5, pp. 1104-1106, 1977.

[1.35] R. S. Beach, N. Smith, C. L. Platt, “Magneto-impedance effect in NiFe plated wire,” Appl. Phys. Letters 68, pp. 2753-2755, May 1996.

[1.36] L. Chiesi, J.A. Flanagan, B. Janossy, R.S. Popovic, “Integrated planar fluxgate sensor with an amorphous core,” Eurosensors XI proceedings, vol. 3, pp. 1607-1610, Warsaw (Poland), 1997.

[1.37] P. Kejik, L. Chiesi, B. Janossy, R. S. Popovic, “A new compact 2D planar fluxgate sensor with amorphous metal core,” Sensors and Actuators A, vol. 81, issues 1-3, pp. 180-183, April 2000.

[1.38] P. Ripka, X. P. Li, J. Fan, “Orthogonal fluxgate effect in electroplated wires,” IEEE Sensors Conference, Irvine CA, USA, Technical Digest pp. 69-72, 31 October – 3 November 2005.

[1.39] J. Fan, X. Li, “Low power orthogonal fluxgate sensor with electroplated $Ni_{80}Fe_{20}$/Cu wire,” Journal of Applied Physics (99), 08B311-1, 2006.

[1.40] P. Ripka, M. Butta, M. Malatek, S. Atalay, F. E. Atalay, “Characterization of magnetic wires for fluxgate cores,” Transducers '07 & Eurosensors XXI conference, Lyon, France, Digest of technical papers vol. 2, Pages 2369-2372, June 10-14, 2007.

CHAPTER II

OPERATION PRINCIPLE OF FLUXGATE TYPE MAGNETIC SENSORS

This chapter explains the operation principles of the fluxgate type magnetic sensors. Section 2.1 starts with the classification of materials according to their magnetic properties, and explains the magnetization curves of ferromagnetic materials. Section 2.2 deals with the demagnetization effect and calculation of the demagnetization factor according to the shapes of magnetic materials. In Section 2.3, the fluxgate operation principle is explained and differences between parallel and orthogonal fluxgate configurations are mentioned. In Section 2.4, performance criteria of fluxgate sensors are presented underlining the preferred core magnetic material properties. Section 2.5 summarizes the chapter.

2.1 Magnetic classification of materials

All materials in the nature show some responses to the applied magnetic fields. Vacuum is the true nonmagnetic environment. However, the responses of some materials to magnetic fields are quite weak, and they can also be regarded as nonmagnetic.

In the presence of a magnetic field H, the corresponding magnetic induction B is given as:

$$B = \mu_0 (H + M) = \mu_0 (H + \chi H) = \mu_0 (1 + \chi) H = \mu_0 \mu_r H \tag{2.1}$$

where μ_0 is the permeability of vacuum and x is the susceptibility of the medium or the material. M is called the magnetization and μ_r is defined as the relative permeability, i.e., the permeability with respect to the vacuum.

2.1.1 Diamagnetic, Paramagnetic, Ferromagnetic Materials

Table 2.1 lists some common materials according to their magnetic properties [2.1]. Materials are classified into several groups according to their magnetic behavior. Diamagnetic materials, paramagnetic materials, and ferromagnetic materials are the three main groups. Diamagnetic materials have susceptibility values slightly less than zero (~ -10^{-5}), which means that the magnetization formed inside the material is in the opposite direction with the applied magnetic field. Diamagnetism is mainly due to the orbital motion of the electrons within an atom. On the other hand, paramagnetic materials produce a small magnetization in the same direction with the applied field, with a positive susceptibility value around 10^{-5} to 10^{-3}. Paramagnetism is explained by the nature of the magnetic dipole moments of the spinning electrons.

Table 2.1: Magnetic classification and relative permeability of some materials.

Material	**Magnetic Classification**	**Relative Permeability $\mu_r = 1 + x$**
Copper	Diamagnetic	0.999991
Water	Diamagnetic	0.999991
Vacuum	Nonmagnetic	1*
Air	Paramagnetic	1.0000004
Aluminum	Paramagnetic	1.00002
Cobalt	Ferromagnetic	250
Nickel	Ferromagnetic	600
Iron	Ferromagnetic	5000
78 Permalloy (78.5Ni)	Ferromagnetic	100000
Mumetal (75Ni, 5Cu, 2Cr)	Ferromagnetic	100000

* By definition

The third main group, ferromagnetic materials, has relative permeability values well greater than 1. This group needs little bit more detailed explanation not only due to their wide use in many magnetic sensor applications but also due to their non linear responses to the magnetic fields. Ferromagnetism is explained in terms of magnetized domains. In this explanation, atoms in a ferromagnetic material are grouped in domains, and the magnetic dipoles are aligned to each other within a domain. This alignment does not necessarily require any non-zero ambient magnetic field. Neighboring domains are separated by domain walls, which are also groups of atoms, but much smaller in number. Domains are composed of about 10^{15} to 10^{16} atoms, whereas domain walls contain about 100 atoms.

Figure 2.1 shows the alignment of domains in a ferromagnetic material with the applied external magnetic field. When there is no magnetic field, the magnetic moment of each domain has different directions. In the presence of an external field, the domain walls starts to move in a way that the domains which have magnetic moments aligned to the external field tend to grow in volume. This process is reversible up to a certain magnetic field value. After this value, all the domains tend to align with the applied magnetic field, and the process becomes irreversible. If the field is reduced to a previous value, the obtained domain structure is different than the original one [2.2]. This phenomenon is often called the memory effect or hysteresis, and magnetic properties of ferromagnetic materials are commonly presented by their hysteresis curves.

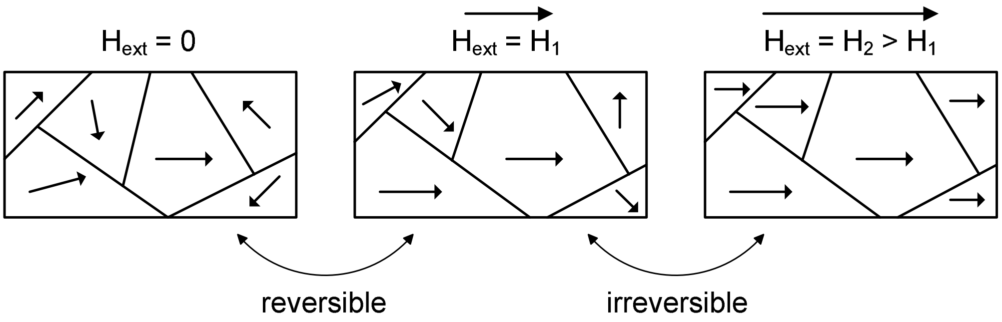

Figure 2.1: Alignment of domains in a ferromagnetic material with the applied external magnetic field.

2.1.2 Magnetization and Hysteresis Curves

Figure 2.2 shows typical magnetization curves of a ferromagnetic material. If a high enough magnetic field is applied, all the domains are aligned with the field and further increase of the field does not change the magnetization of the material. This magnetization value is called the saturation magnetization, M_{sat}. The residual magnetization of the material, which is the obtained magnetization by reducing the field monotonously to zero after M_{sat} is called the remnant magnetization, M_r. After that point, if one starts to increase the field in the opposite direction, the coercive field, H_c, value is reached, which is the field required to have zero magnetization inside the material. M_{sat}, M_r, and H_c are the characteristic points defining an M-H curve. The field value where the magnetization reaches M_{sat} is also an important point on the M-H curve, and marked in Figure 2.2 as H_k. It is important to mention that these points can be reached only by strongly saturating the material, and besides, any point inside the M-H curve is possible to reach by applying the proper magnetic field sequence.

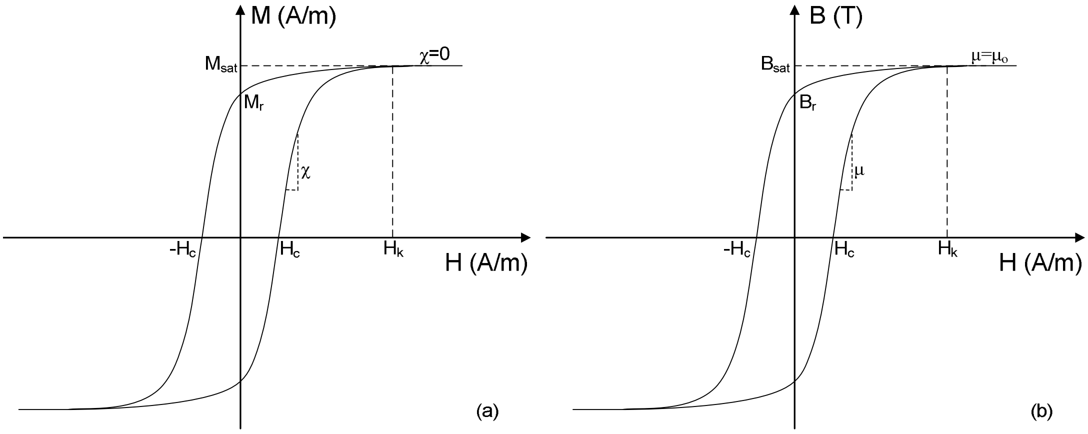

Figure 2.2: Typical magnetization curves: (a) M-H curve, (b) B-H curve.

Another way to represent the hysteresis curve is to use magnetic induction instead of the magnetization of the material as shown in Figure 2.2(b). The difference between these two curves can be recalled from Eq. 2.1: The slope of the M-H curve gives the susceptibility value of the material, whereas the slope of the B-H curve gives its permeability value with respect to the applied field. This results in the fact that the value of the M-H curve stays at M_{sat} after H_k value as x goes to zero, but the B-H curve increases with a slope equal to μ_0. It may be advantageous to use both curves for different representations and explanations.

2.1.3 Soft and Hard Magnetic Materials

Ferromagnetic materials can further be classified in two groups according to the properties of their B-H curves. When a full cycle of the B-H curve is traced, some energy is lost in terms of heat during the domain wall movement process. This is called the hysteresis loss. Hysteresis loss per cycle is calculated as:

$$W = \int H.dB \tag{2.2}$$

which gives the area inside the B-H curve.

Ferromagnetic materials with a tall and narrow B-H curves and smaller loop areas have smaller hysteresis losses, and are called as soft magnetic materials. These materials generally have fewer impurities and domain walls can easily be moved with small amount of energy [2.3].

Materials with wider B-H loops, i.e., with higher remnant magnetization and coercive field values are called hard magnetic materials. Good permanent magnets belong to this group. The coercive field of some hard magnetic materials can be in the order of tens of kA/m, whereas this value may be around 10 to 100 A/m for typical soft magnetic materials. Figure 2.3 shows a comparison of the B-H curves of the soft and hard magnetic materials.

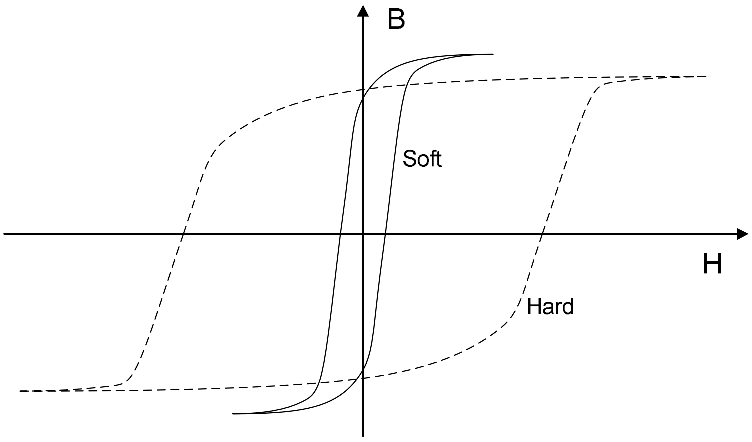

Figure 2.3: Comparison of the B-H curves of the soft and hard magnetic materials.

2.2 The Demagnetization Effect and the Apparent Permeability

General discussion on the magnetic properties of the materials is based on their intrinsic magnetic properties. Intrinsic properties are valid for magnetic materials with infinite dimensions. In practice, magnetic properties are affected by the absolute and respective dimensions of the material, its shape, the magnitude, frequency, and the direction of the magnetic field the material is subjected to, and likewise. The effect of all these to the magnetic properties of the material is called the demagnetization effect. The demagnetization effect can be explained by considering the volume magnetic charges and surface magnetic charges at the edges of the finite sized magnetic samples subjected to an external magnetic field [2.4]. Figure 2.4 shows a ferromagnetic material in an external field where the surface magnetic charges are collected at the edges of the material. When the material is subjected to a magnetic field, a demagnetizing field, opposing the external field, is produced inside the material due to these charges. The magnetic field inside the material can be written as:

$$H_{in} = H_{ext} - H_d = H_{ext} - NM(H_{in}). \tag{2.3}$$

In this equation, H_d represents the demagnetizing field, and it is proportional to the magnetization of the material with the demagnetization factor N, which is a dimensionless quantity between 0 and 1.

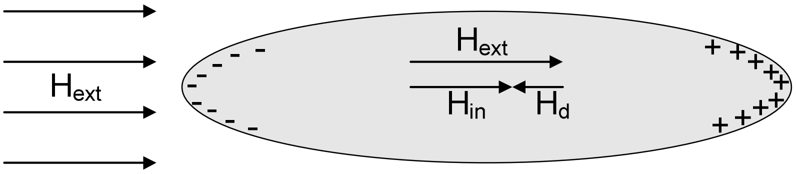

Figure 2.4: A ferromagnetic material with finite size subjected to magnetic field, and the surface magnetic charges at the edges of the material.

The magnetization inside the material can be expressed with a linear approximation as:

$$M(H_{in}) = (\mu_r - 1)H_{in}, \tag{2.4}$$

and the resulting field inside the material can be written as:

$$H_{in} = \frac{H_{ext}}{1 + N(\mu_r - 1)}. \tag{2.5}$$

As it seen from the equation, due to the demagnetization effect the field seen by the ferromagnetic material is reduced. In practice, this can be treated as the decrease of the permeability value of the material. The resulting permeability value is called the apparent permeability and it is given as:

$$\mu_{app} = \frac{\mu_r}{1 + N(\mu_r - 1)}. \tag{2.6}$$

By using the apparent permeability, the behavior of a finite sized sample subjected to a magnetic field can be predicted. In order to calculate the apparent permeability, the demagnetization factor should be known. In general, the demagnetization factor is calculated at each point in a ferromagnetic material for three orthogonal directions and their sum is equal to unity at each point [2.5]:

$$N\big|_{x,y,z} = N(N_x, N_y, N_z) \text{ such that } N_x + N_y + N_z = 1. \tag{2.7}$$

The demagnetization factor is a function of the shape and the dimensions of the material as well as its intrinsic magnetic properties and the field the material is subjected to. Being dependent on so many factors, generally it is not possible to find an analytical calculation for the demagnetization factor. Many approximations are made and numerical methods are used in order to calculate the demagnetization factor of different shapes [2.6]. In the following sections, calculation of the demagnetization factors for different shapes will be discussed.

2.2.1 Demagnetization factor for ellipsoids

Ellipsoids are the only group of shapes for which the demagnetization factor can be analytically calculated [2.5]. Also, it is only a function of the relative dimensions of the sample with respect to each other, and change neither according to the position inside the sample nor with the magnetic properties.

Simplest example to the ellipsoids is a sphere, and since it has a perfectly symmetrical shape, the demagnetization factor for each direction is same and equal to 1/3 as their sum has to be unity.

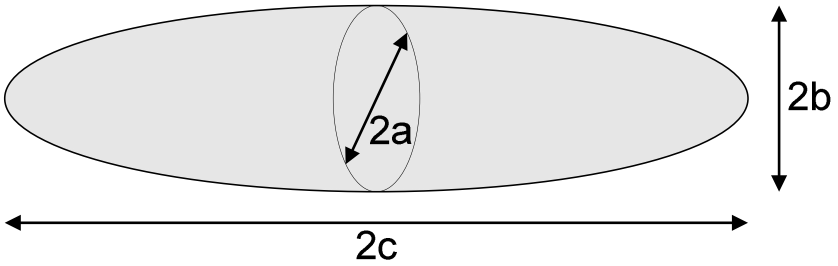

Figure 2.5: Ellipsoid with dimensions c >> a ≥ b.

If the ellipsoid is much longer in one direction that the other two as illustrated in Figure 2.5, the demagnetization factor in this direction can be approximated as [2.5]:

$$N_c = \frac{ab}{c^2}\left[\ln\left(\frac{4c}{a+b}\right)-1\right], \text{ for } c >> a \geq b. \tag{2.8}$$

Figure 2.6 gives the variation of the demagnetization factor of an ellipsoid with the ratio of its dimensions. It shows that the demagnetization factor is reduced as the ellipsoid gets longer in that direction, which means that the apparent permeability value gets closer to the intrinsic permeability value. Figure 2.7 shows the change of the apparent permeability value of an ellipsoid with the demagnetization factor for different intrinsic relative permeability values. From the graph, we can see that the demagnetization factor is more effective for an ellipsoid with higher permeability value.

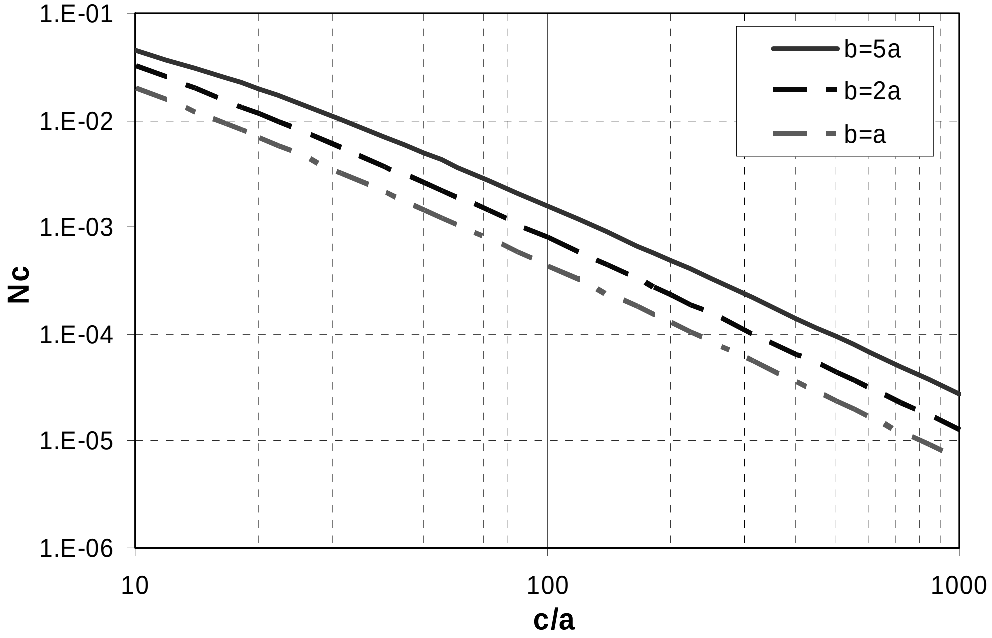

Figure 2.6: The demagnetization factor of an ellipsoid for different dimension ratios.

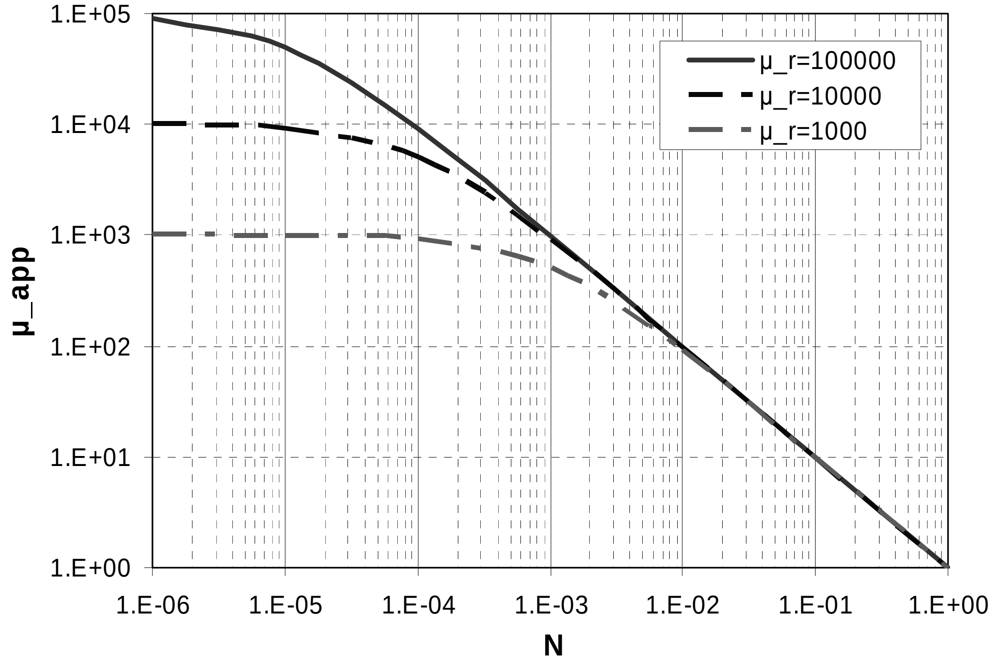

Figure 2.7: The change of the apparent permeability value of an ellipsoid with the demagnetization factor for different intrinsic relative permeability values.

2.2.2 Demagnetization factor for cylinders

Although it is not necessary for the ellipsoids, the aspect ratio between the length of the material in which the demagnetization factor is measured and the area of the midplane of the sample is used for other shapes, as it significantly simplifies the demagnetization factor calculations and comparisons. The aspect ratio, λ, is defined as [2.7]:

$$\lambda \equiv \frac{2c}{\sqrt{A_{a,b}}}. \tag{2.9}$$

For cylinder shapes, the demagnetization factor will be discussed with its dependence to λ. In the case of a cylinder, the demagnetizing factor is a function of the magnetic properties and the position inside the cylinder, as well as of the aspect ratio [2.8]. Due to the position dependence, two definitions of demagnetizing factors are done: the magnetometric demagnetizing factor N_m, and the fluxmetric demagnetizing factor N_f. N_m stands for the average value of the demagnetizing factor through all the volume of the cylinder, whereas N_f stands for the average demagnetizing factor at the midplane. With a susceptibility of zero or infinity, N_m and N_f can be approximated for large λ values (λ>20) as [2.7]:

$$\begin{aligned}
N_f(\chi=0) &= \frac{2}{\pi\lambda^2},\\
N_f(\chi=\infty) &= \frac{4}{\pi\lambda^2}\left(\ln\sqrt{\pi}\lambda-\frac{3}{2}\right),\\
N_m(\chi=0) &= \frac{8}{3\pi^{3/2}\lambda}-\frac{1}{2\pi\lambda^2},\\
N_m(\chi=\infty) &= \frac{6}{\pi\lambda^2}\left(\ln 2\sqrt{\pi}\lambda-\frac{7}{3}\right).
\end{aligned} \tag{2.10}$$

Figure 2.8 gives the variation of N_m and N_f values with λ, calculated with the equations above. The demagnetization factor for an ellipsoid with a circular cross-section is also presented for comparison. Since a cylinder has sharp edges when compared to an ellipsoid, its magnetometric demagnetization factors are always higher than that of an ellipsoid. We can also see that for large susceptibility values, the magnetometric demagnetization factor tends to decrease, and fluxmetric demagnetization factor increases and they both get closer to the demagnetization factor of an ellipsoid. This shows that the distribution of the demagnetization factor is more uniform in a cylinder for higher susceptibility values.

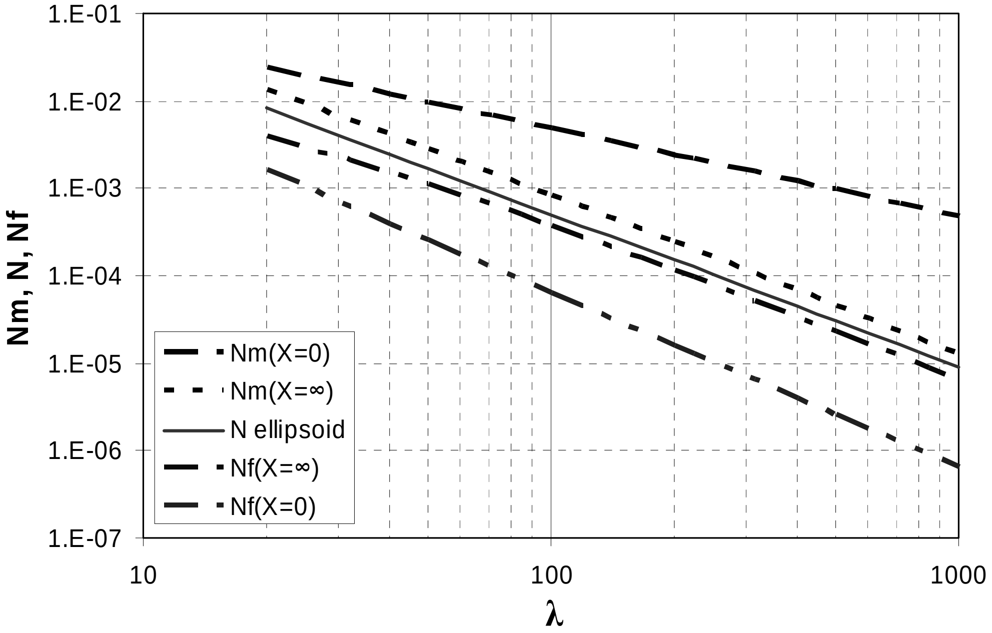

Figure 2.8: The variation of the magnetometric and fluxmetric demagnetization factor values of a cylinder with λ.

2.2.3 Demagnetization factor of rectangular prisms

An analytical model for calculating the fluxmetric and magnetometric demagnetization factor for rectangular prisms for a zero susceptibility value is given in [2.9]. Figure 2.9 shows the variation of the magnetometric and fluxmetric demagnetization factor values with λ according to this analytical model. Again, a comparison with the ellipsoid is presented in the graph. In addition, the values are presented in two different cross-section aspect ratios. It is seen that the values for a square (b=a) and a rectangular (b=4a) cross-section are very close to each other. It is very important to see this result as it shows that it is safe to approximate a rectangular cross-section with a square one as long as they have the same area. The demagnetization factors for rectangular prisms with a square cross-section are calculated for different susceptibility values in [2.10]. Figure 2.10 presents the calculated N_m and N_f values for rectangular prisms with a square cross-section for different susceptibility values and λ.

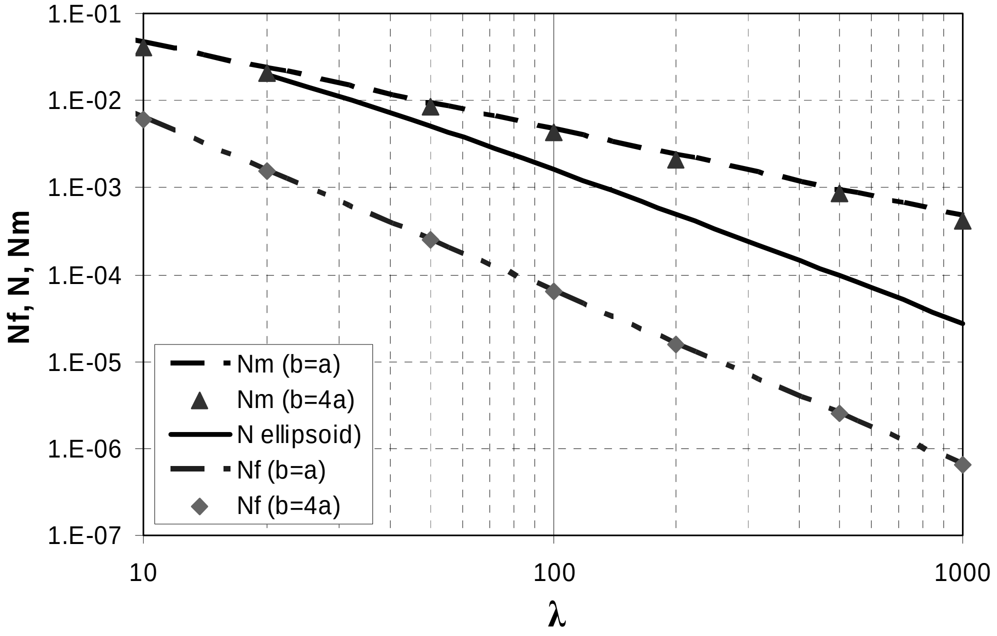

Figure 2.9: The fluxmetric and magnetometric demagnetization factors for rectangular prisms for x=0.

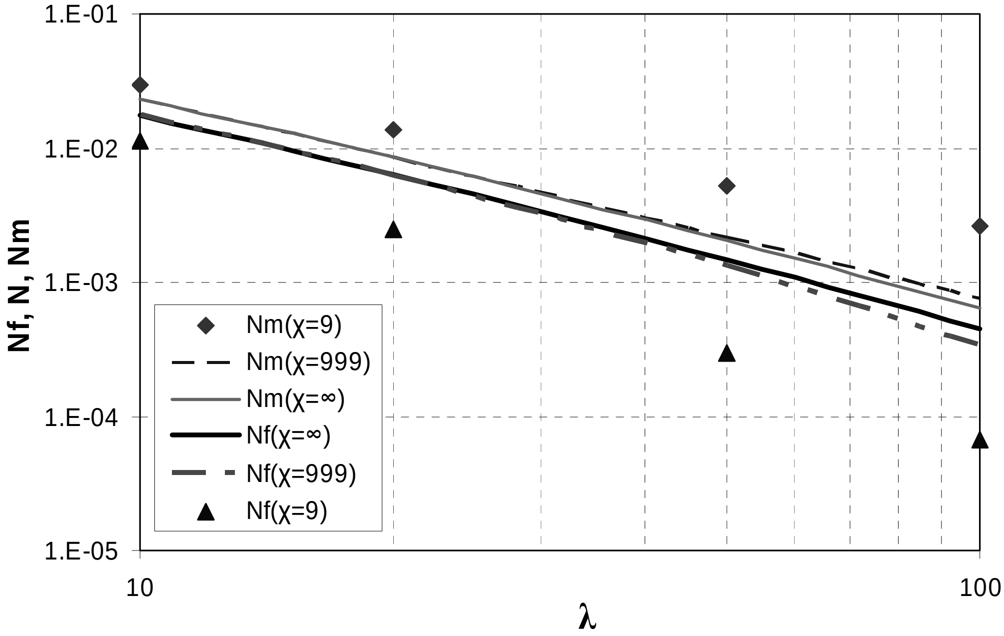

Figure 2.10: The variation of the magnetometric and fluxmetric demagnetization factors for rectangular prisms with a square cross-section.

Comparison of the demagnetization factors for ellipsoids, cylinders, and rectangular prisms presented in Figure 2.8 to Figure 2.10 show that the calculated demagnetization factors differ slightly with the shape for the same λ value. However, the changing tendency is same for all shapes. Furthermore, the demagnetization factors for cylinders and rectangular prisms become very close to each other as λ increases. This shows that these shapes can be approximated for each other while calculating the demagnetization factor for large λ values.

Demagnetization effect plays an important role on the performance parameters of fluxgate type magnetic sensors. The power dissipation, sensitivity, and the linear operation range of the sensor are determined by the effect of the demagnetization factor on the intrinsic magnetic properties of the ferromagnetic material that is used in the sensor. Next section focuses on the operation principle of fluxgate sensors and, in the following section the performance parameters of fluxgate sensors will be discussed by considering the magnetic properties of the core materials.

2.3 Operation Principle of Fluxgate Sensors

Figure 2.11 illustrates the fluxgate operation principle. The operation principle is based on the periodic saturation of a ferromagnetic core material. This is also referred as magnetic chopping. The permeability of the material is modulated according to its B-H curve, between μ_0 and $\mu_0\mu_r$ with a periodic excitation field at a certain frequency. When the material is not saturated it operates in the linear region of its B-H curve, where it has a high permeability which is equal to $\mu_0\mu_r$. Accordingly, the magnetic flux is concentrated inside the core (Figure 2.11(a)). When it is saturated, the permeability of the material drops to μ_0, and magnetic flux passing thorough the material is chopped or “gated” (Figure 2.11(b)) as the name is inspired. This cycle occurs twice in each period, so the external magnetic field information can be seen at the second (and higher even) harmonic component of the power spectrum of the total flux or the change of flux with time (Figure 2.11(c)). This principle is effective in detecting DC or low frequency magnetic fields. Theoretically, according to the Nyquist theorem, the excitation frequency must be at least two times higher than the frequency of the magnetic field to be detected. However, in practice, at least 100 times larger excitation frequency is selected.

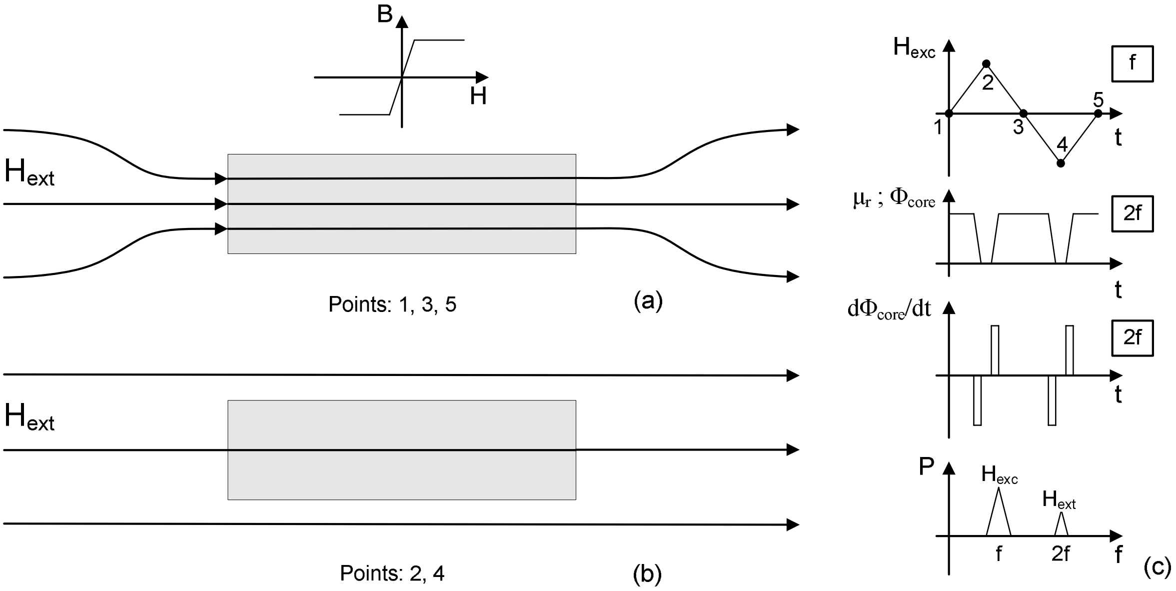

Figure 2.11: The basic fluxgate operation principle.

2.3.1 Parallel and Orthogonal Fluxgate Sensor Configurations

Fluxgate type magnetic sensors are classified according to the direction of the excitation magnetic field and external magnetic field to be measured with respect to each other. Two main configurations are known, called parallel configuration and orthogonal configuration. Figure 2.12 shows basic parallel fluxgate configurations, where the external field and the excitation field are in the same direction. The simplest configuration, known as the single core fluxgate, contains a ferromagnetic core and two coils wound around the core. One of the coils is used as the sensing coil to detect the flux change through the core. The other coil is used to produce the excitation field to saturate the core periodically by passing an AC current through it. For this configuration, the excitation signal has a large 1st harmonic component on the sensing coil. In order to eliminate this component, the Vacquier type is proposed. This configuration has two core elements with separate excitation coils, producing excitation field in opposite directions. Both cores share a single sensing coil, for which the flux generated by the excitation coils is subtracted. For the Vacquier type, saturation of the cores is also easier than the single core version since the 2nd core provides a high permeability return path for the excitation magnetic field. However, the magnetic circuit for the excitation is still not completely closed. A completely closed magnetization path further eases the saturation, as proposed in the ring-core sensor. In this configuration, the excitation coil is wound around a toroidal core. The sensing coil wound above and below the ring core detects the magnetic field parallel to its plane.

The orthogonal fluxgate, for which the excitation field and external field are perpendicular to each other, has two main configurations. Figure 2.13 shows these two configurations known as the Aldredge type. For the first configuration, excitation is provided by passing a current through the ferromagnetic core, producing circular magnetic field in the cross-sectional plane of the core. The second configuration is similar to the ring core parallel type, with a tubular core and the excitation coil wound toroidally around it. Both of these configurations are sensitive to the magnetic field along the length of the ferromagnetic core, and sensing coils wound around the cores are used to detect the signal.

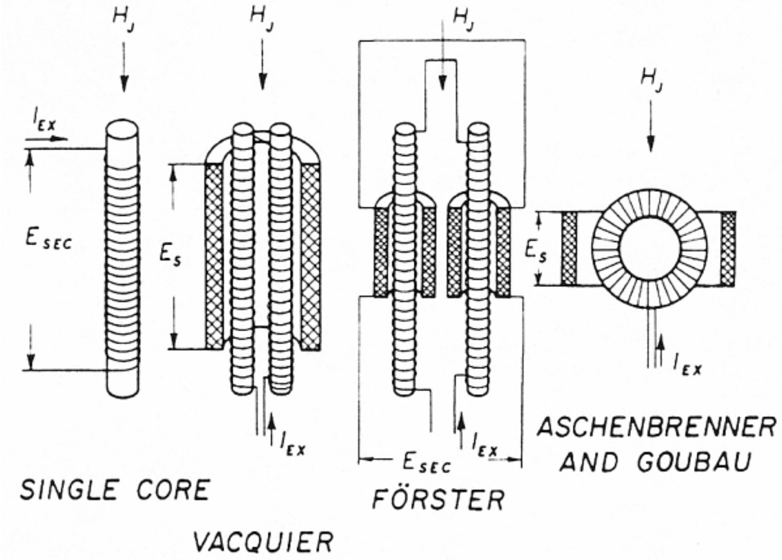

Figure 2.12: Parallel fluxgate configurations [2.3].

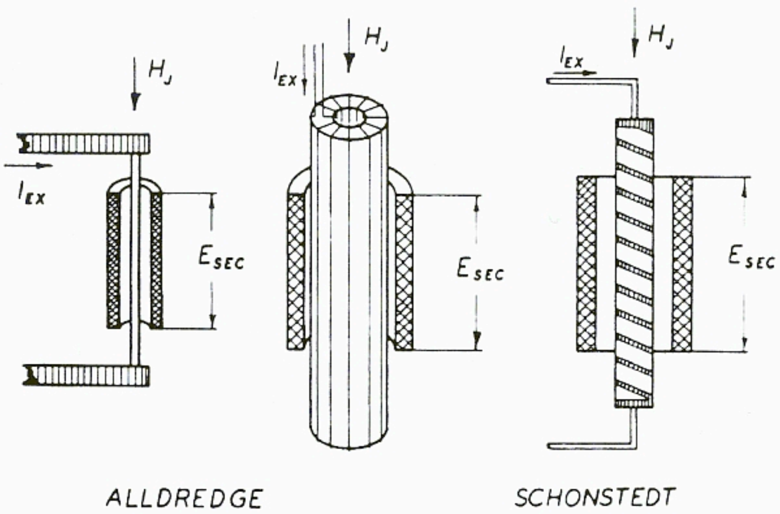

Figure 2.13: Orthogonal (Aldredge) and mixed-mode (Schonstedt) fluxgate configurations [2.3].

A mixed mode sensor is also proposed by Schonstedt (Figure 2.13). This configuration uses a helical ferromagnetic core which is wound with a certain angle to the magnetic field to be measured. The excitation is again provided by the current passing through the helical core, and sensing coil is wound around the core.

2.3.2 Gating Mechanism of Fluxgate Sensors

In this section, the gating mechanism of the fluxgate sensors will be described by examining a ferromagnetic core subjected to a magnetic field H(t), and having a cross-sectional area, A_{core}. The magnetic flux passing through the core cross-section is formulated as:

$$\Phi_{core}(t) = \mu_o \times \mu_r(H(t)) \times H(t) \times A_{core}\,. \tag{2.11}$$

Then, the time derivative of the flux is:

$$\frac{d\Phi_{core}(t)}{dt} = \mu_o A_{core}\left[\mu_r(H(t)) \times \frac{dH(t)}{dt} + \frac{d\mu_r(H(t))}{dt} \times H(t)\right] \tag{2.12}$$

which can be written more explicitly as:

$$\frac{d\Phi_{core}(t)}{dt} = \mu_o A_{core}\left[\mu_r(H(t)) \times \frac{dH(t)}{dt} + \frac{d\mu_r(H(t))}{dH(t)}\frac{dH(t)}{dt} \times H(t)\right]. \tag{2.13}$$

Due to this flux change, an induced voltage $v_{in}(t)$ is formed across the sensing coil having N turns wound around the core:

$$v_{in}(t) = -N\frac{d\Phi_{core}(t)}{dt}\,. \tag{2.14}$$

Equation 2.13 and 2.14 are the basic equations for any kind of fluxgate sensor operation. In order to proceed further, the components of H(t) should be known. Basically it has two components: $H_{exc}(t)$ being the excitation magnetic field; and $H_{ext}(t)$ being the external magnetic field to be sensed. For the parallel configuration, these two components are in the same direction, so H(t) is the scalar sum of them. However, scalar sum is not possible in the orthogonal configuration as they are perpendicular to each other. So, the parallel and orthogonal configurations should be analyzed separately.

2.3.2.1 Parallel Gating Mechanism

For the parallel gating mechanism, the magnetic field around the core can be written as:

$$H(t) = H_{exc}(t) + H_{ext} \tag{2.15}$$

and it is possible to formulate $\mu_r(H(t))$ as:

$$\mu_r(H(t)) = \mu_r(H_{exc}(t) + H_{ext}) = \mu_r(t)\,. \tag{2.16}$$

Normally, the external field may also be a function of time. On the other hand, because of the nature of the chopping technique, it is safe to assume H_{ext} as DC since excitation is selected at a much higher frequency than the external field. Inserting Equation ((2.15)) and Equation ((2.16) into Equation (2.13) we obtain:

$$\frac{d\Phi_{core}(t)}{dt} = \mu_o A_{core}\left[\mu_r(t) \times \frac{dH_{exc}(t)}{dt} + \frac{d\mu_r(t)}{d(t)} \times (H_{exc}(t) + H_{ext})\right]. \tag{2.17}$$

As the external magnetic field information is carried in the 2nd harmonics of the waveform, and it is not desired to disturb this information externally, an odd function is generally employed for the excitation satisfying:

$$H_{exc}\left(t + \frac{T}{2}\right) = -H_{exc}(t) \tag{2.18}$$

where T is the period of the excitation field. Besides, μ_r is an even function of H, so:

$$\mu_r(H) = \mu_r(-H) \Rightarrow \mu_r\left(t + \frac{T}{2}\right) = \mu_r(t). \tag{2.19}$$

Substituting these equations into Eq. 2.17, and examining the case without any external magnetic field leads to the conclusion:

$$\frac{d\Phi_{core}\left(t + \frac{T}{2}\right)}{dt} = -\frac{d\Phi_{core}(t)}{dt} \tag{2.20}$$

showing that $d\Phi/dt$ is also an odd function composed of only odd harmonics under no external magnetic field. However, presence of an external field destroys the odd function form, and even harmonics are also included. These even harmonics are detected by the chopping technique mentioned above.

2.3.2.2 Orthogonal Gating Mechanism

For the orthogonal configuration, the total magnetic field around the core for should be written as the vector sum of excitation and external magnetic fields as they are perpendicular to each other:

$$\mathbf{H}(t) = \mathbf{H}_{\mathbf{exc}}(t) + \mathbf{H}_{\mathbf{ext}} \,. \tag{2.21}$$

As the excitation field is perpendicular to the external field, it does not contribute the flux change through the core. So, the first term in Eq. 2.13 vanishes and it can be re-written as:

$$\frac{d\Phi_{core}(t)}{dt} = \mu_o A_{core}\left[\frac{d\mu_r(\mathbf{H}_{\mathbf{exc}}(t)+\mathbf{H}_{\mathbf{ext}})}{d(\mathbf{H}_{\mathbf{exc}}(t)+\mathbf{H}_{\mathbf{ext}})}\frac{dH_{exc}(t)}{dt}\times H_{ext}\right]. \tag{2.22}$$

It is seen from Eq. 2.22 that, for the orthogonal case, the change of permeability is not a function of a scalar, but a vector quantity. This leads us to the result that the permeability should be treated as a tensor for the rest of the calculations. Then, the relation between the magnetic field H, and the flux density B can be written as a vector relation:

$$\mathbf{B} = \boldsymbol{\mu}_{\mathbf{r}} \times \mathbf{H} \tag{2.23}$$

or more explicitly as:

$$\begin{bmatrix} B_x \\ B_y \\ B_z \end{bmatrix} = \begin{bmatrix} \mu_{11} & \mu_{12} & \mu_{13} \\ \mu_{21} & \mu_{22} & \mu_{23} \\ \mu_{31} & \mu_{32} & \mu_{33} \end{bmatrix} \times \begin{bmatrix} H_x \\ H_y \\ H_z \end{bmatrix} \tag{2.24}$$

which indicates that **B** and **H** may not be in the same direction inside the core. This may be considered by assuming that the magnitude of the resultant flux density is same as the flux density caused by the excitation field, where excitation field is much higher than the external field [2.11]. Figure 2.14 shows the geometrical model based on this assumption. The phenomenon is referred as the rotation of the resultant flux density.

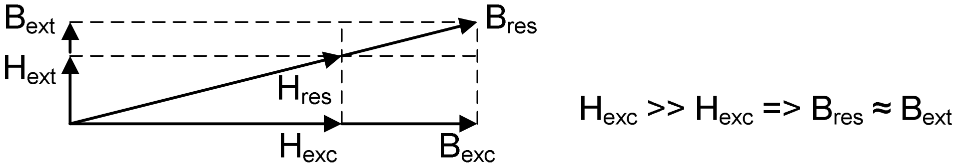

Figure 2.14: The geometrical model showing $B_{res} \approx B_{ext}$.

After this point, it may be more informative to explain the mechanism in a 2D vector plane instead of using only the equations. Figure 2.15 illustrates the operating principle of the orthogonal fluxgate sensor based on the magnetization curve and the magnetization vector plane of the ferromagnetic material [2.12]. The change in the flux density inside the core is given as:

$$\Delta\mathbf{B}=\mu_0 \times \Delta(\mathbf{H}+\mathbf{M}). \tag{2.25}$$

The symbol Δ represents the local variation of the value around a given point on the B-H curve of the core material. The magnetization of the material is a function of the applied magnetic field such that

$$\Delta\mathbf{M}= \mathbf{x} \times \Delta\mathbf{H}, \tag{2.26}$$

x being the susceptibility tensor of the material, whose relation to the relative permeability $\boldsymbol{\mu}_\mathbf{r}$ is:

$$\boldsymbol{\mu}_\mathbf{r}= \mathbf{x}+\mathbf{I} \tag{2.27}$$

where **I** is the identity matrix.

In Figure 2.15(a), a sinusoidal excitation field waveform H_{exc} is shown. The magnetization of the ferromagnetic core reaches the saturation M_{sat} two times for each period of this excitation according to the M-H curve of the ferromagnetic core (Figure 2.15(a)). If no external magnetic field is applied, the vector **M** is in the direction of the excitation field H_{exc}. However, in the presence of an external magnetic field, the **M** vector is composed of two mutually perpendicular components, M_{exc} and M_{ext}, resulting from the excitation magnetic field and external magnetic field, respectively. By increasing the excitation magnetic field H_{exc}, the M_{exc} component of vector **M** starts to increase (y-axis direction in Figure 2.15(b)). However, it can increase up to a value which is equal to M_{sat}, which is the highest possible magnetization inside the ferromagnetic core. This boundary is illustrated with the dashed circle in Figure 2.15(b). The component M_{ext} stays unchanged up to the excitation field values $H_{exc}\approx H_k$. This is represented by the points and arrows 1 and 2 in Figure 2.15(a) and (b). For H_{exc} values higher than H_k, the ferromagnetic core saturates and this forces the M_{ext} component of vector **M** to decrease and to reach the minimum for the peak value of the excitation field H_{exc} (points 3 and 4). When H_{exc} decreases to smaller values, the M_{ext} component starts to increase again, and returns back to its initial value. This cycle creates a periodic change in the flux passing through the core (Φ_{core}). This periodic flux change induces a voltage across the sensing coil which may be wound around the core (Figure 2.15(c) and (d)) according to Equation (2.14). Again, the magnitude of the even harmonics of this induced voltage is proportional to the external magnetic field.

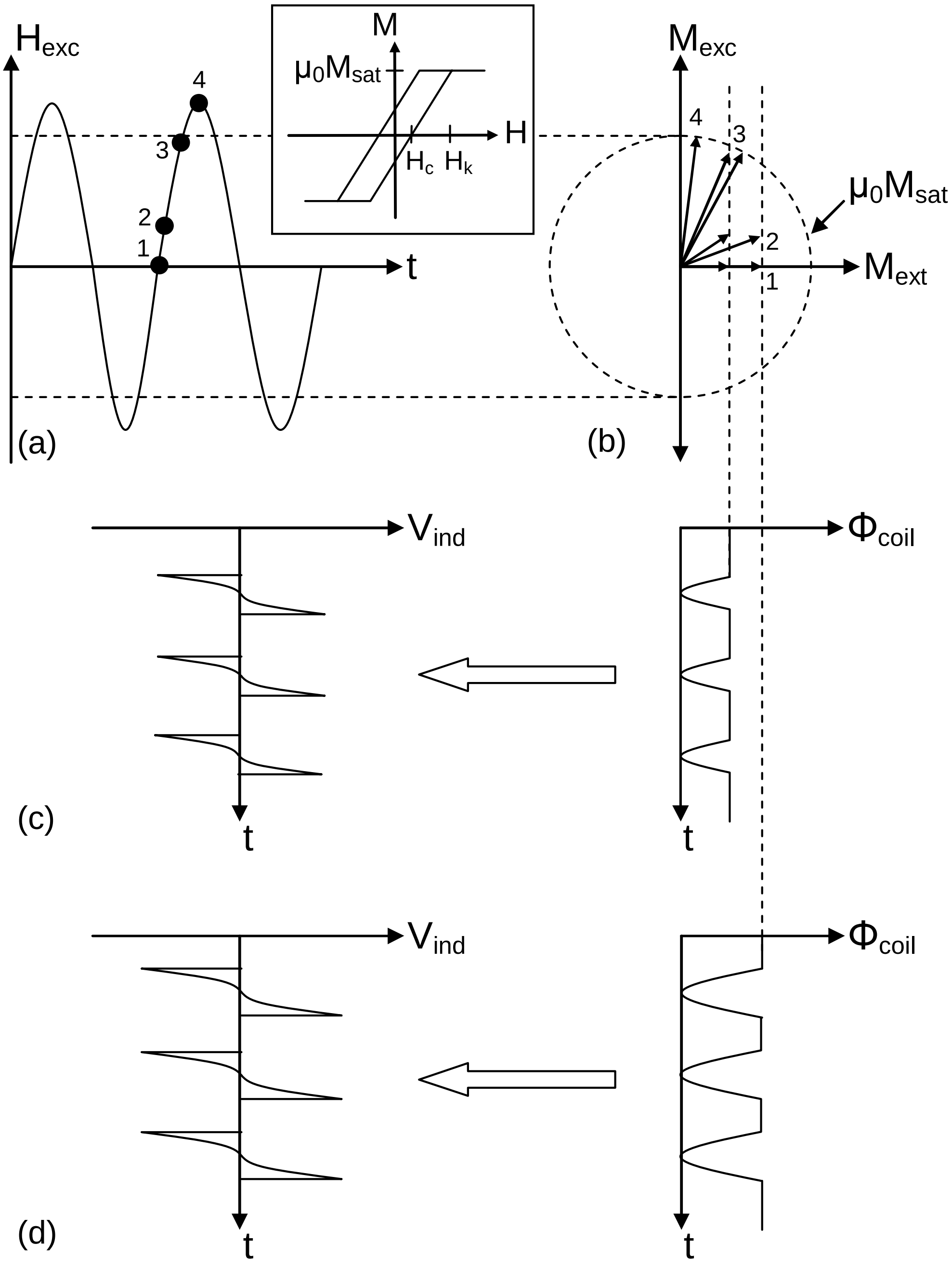

Figure 2.15: (a) The sinusoidal excitation field and the M-H curve of the material. (b) The magnetization vector **M** inside the core with two orthogonal components M_{exc} and M_{ext}. (c, d) The change of flux passing trough the core and the resulting induced voltages for two different external magnetic field values.

2.4 Performance Parameters and Core Material Selection for Fluxgate Sensors

Previous research on fluxgate sensors shows that the ferromagnetic part of the sensor has the main role on the performance of the sensor [2.3]. The selection criteria of the ferromagnetic part are determined by the type, geometry, and the operation aim of the sensor. So, it is difficult to give a list of ideal properties. However, some general requirements may still be useful to consider. In this section, the performance parameters of a fluxgate sensor will be presented over the ferromagnetic properties of the core material as well as other parameters.

Sensitivity: In order to determine the factors that affect the sensitivity of the sensor, it is better to recall the basic fluxgate equation:

$$v_{in}(t) = -N\mu_o A_{core}\left[\mu_r(H(t)) \times \frac{dH(t)}{dt} + \frac{d\mu_r(t)}{dt} \times H(t)\right]. \tag{2.28}$$

As the fluxgate operation principle is based on the periodic modulation of the permeability value of the ferromagnetic material, the most important sensitivity parameter is the $d\mu_r/dt$ term in Eq. 2.13. Higher permeability values, resulting in more abrupt changes, are always preferred for higher sensitivity. However, materials with sharp rectangular B-H curves are known to be much noisier, and this should also be considered [2.3].

Increasing the frequency of the periodic modulation (dH(t)/dt) increases the sensitivity up to a certain value. After that, the eddy current losses or the skin effect start to become dominant, resulting in a decrease in the apparent permeability of the ferromagnetic material. Increase of the peak amplitude of the excitation field also increases the sensitivity of the device in the same way:

$$H(t) = A\sin(\omega t) \quad => \quad \frac{dH(t)}{dt} = A\omega\cos(\omega t). \tag{2.29}$$

Core cross-section is also proportional to the sensitivity of the device, but again skin effect should be taken into consideration as a limiting factor. If a sensing coil is used for signal detection its number of turns, N, is effective on the sensitivity. Increasing the number of turns increases the sensitivity, however, the thermal noise of the sensor also increases as the resistance of the coil increases. Another factor that affects sensitivity is the placement of the coil. Coils wound around the core should be placed around the middle of the core, and planar sensing coils should be placed around the edges of the core.

Linear Operation Range: The linear operation range of the sensor is directly related to the intrinsic magnetic properties of the core and the demagnetization factor in the direction of measurement. Due to the demagnetization factor, the apparent permeability of the material is smaller than its intrinsic permeability. As the saturation magnetic flux density B_{sat} is not affected, the resulting H_k value of the core is higher than the intrinsic one. This results in a wider linear operation range. If the core is very long in the direction of measurement, then it has a very low demagnetization factor, and a smaller linear operation range. As the length of the core is reduced, the demagnetization factor and consequently, the linear range of the core material increase. Figure 2.16 shows the change in the B-H curve of an ellipsoidal core along its length for different geometrical aspect ratios. The intrinsic relative permeability and the saturation magnetic flux density are taken as 10000 and 1 T, respectively for the calculations. It is seen that the linear region of the B-H curve is widened as the core aspect ratio decreases. So, a shorter core has a wider linear operation range than a longer one having the same cross sectional area due to the demagnetization effect.

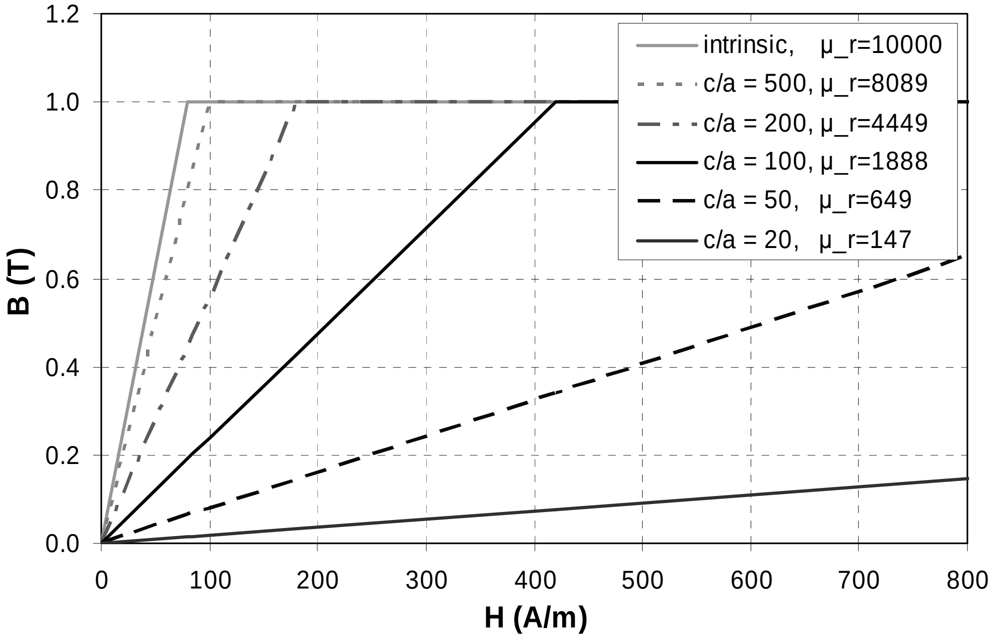

Figure 2.16: The change in the B-H curve of an ellipsoidal core along its length for different geometrical aspect ratios.

In the case of a parallel fluxgate, as the excitation is in the same direction as the external field, same demagnetization factor applies to both of them. As a result, more excitation field is required to saturate the core material having a wider linear range. However, for the orthogonal fluxgate case, the orthogonality of the excitation and external magnetic fields makes the detection mechanism independent of the excitation mechanism. So, one can benefit from the demagnetization effect of the core in the sensing direction to arrange the linear range of the sensor while the demagnetization factor is lower in the excitation direction. As an example, for the Aldredge configuration with a tubular coil, if we change the length of the core, the linear operation range of the core changes due the demagnetization factor whereas the circular excitation mechanism stays unchanged.

Resolution: Two important factors that affect the resolution of the sensor are the thermal noise of the sensing coils and the Barkhausen noise of the ferromagnetic core. The contribution of both of these factors increases as the dimensions of the sensor is reduced.

The thermal noise of the sensing coils increase with the increase of the number of turns and the coil resistance. This is not a significant problem for fluxgate sensors with large sizes. The resistance of a copper soleniodal coil with several hundred turns is in the order of a few tens to hundreds of ohms [2.13]. However, for the microfabricated fluxgates using planar sensing coils, the resistance rapidly increases to the order of kilo-ohms with some tens of turns [2.14].

Barkhausen noise is the discrete change in the magnetization of the ferromagnetic material with continuous change of the ambient field [2.15]. Figure 2.17 illustrates the effect on the magnetization curve of a ferromagnetic material [2.16]. This is explained with the existence of domains and discrete stable states of magnetization in the domains. The magnetization of each domain jumps from one stable state to another stable state as the magnetic field changes. Surface imperfections such as holes, peaks or sharp edges and the impurities or cavities in the ferromagnetic material are sources of noise inducing the Barkhausen effect.

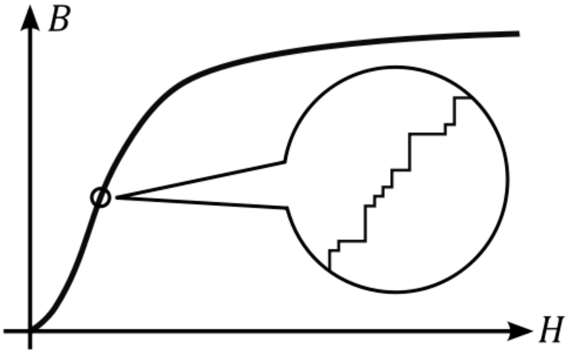

Figure 2.17: The effect of the Barkhausen noise the magnetization curve of a ferromagnetic material (reprint after [2.16]).

Rapid increase in the noise of a ferromagnetic material by scaling down its dimensions is a natural result of this phenomenon. The dimensions of the domains vary between a few micrometers and up to more than one millimeter [2.2]. This results in much smaller number of domains in a small sized core, which increases the discritization.

Perming: Perming effect is one of the most important factors that limit the precision of the sensor [2.17]. It is a "memory effect" of the ferromagnetic materials like hysteresis, and generally defined as the change at the output of the sensor after being subjected to a very high magnetic field. When this field is removed, the output does not return back to its previous value. This is mainly due to the some regions inside the core containing impurities or voids, or the sharp edges of the core, which do not saturate as easily as others. These regions can only be saturated with very high fields, often called as "magnetic shocks" which are more than 10 times the required operation range. When this kind of a field is applied and then removed, these regions do not return back to their original state, causing a different signal at the output of the sensor. The memory of the ferromagnetic material can be "erased" and the core can be returned back to a non-magnetized states by applying a magnetic field sequence in the form of a sinc function in time [2.18], starting with a magnetic field, which is high enough to saturate the core. Perming can lead to changes at the output of a sensor in the order of tens of µT, and this can severely degrade the resolution of the sensor, depending on the operation range.

Bandwidth: Fluxgate type sensors are generally used for the detection of DC or low frequency magnetic fields. Main limitation in the high frequency range is the skin effect or the eddy current losses. The sensor should be excited with a frequency much higher than that of the magnetic field to be measured. At frequencies higher than a certain value, eddy currents become effective inside the core, reducing the magnetization of the core. Decreasing the thickness of the ferromagnetic material helps to reduce the eddy current losses in the cost of reduced sensitivity due to the reduced cross-section area of the core.

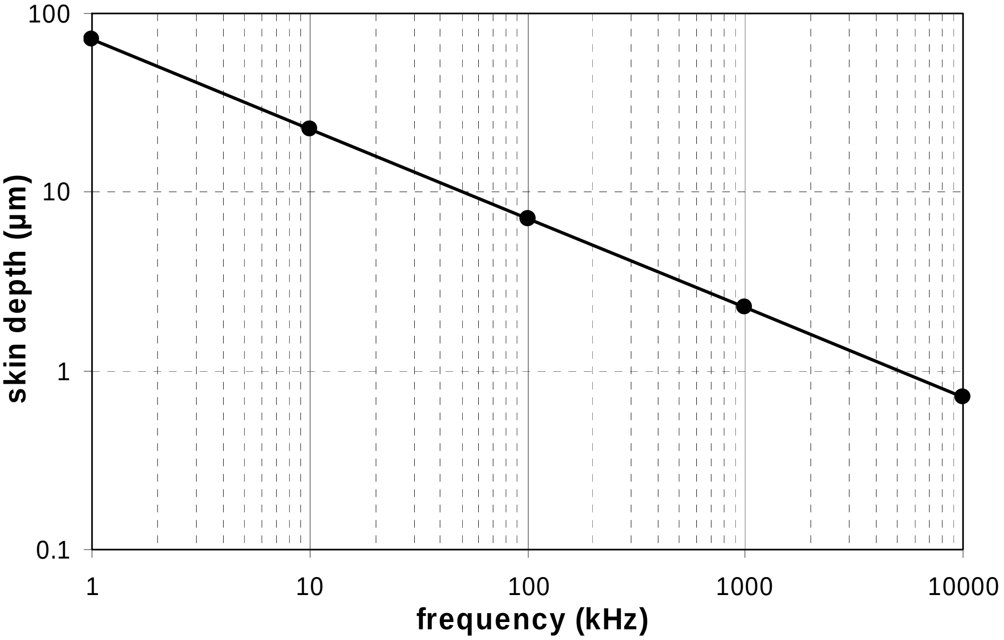

Figure 2.18: The variation of the skin depth with the frequency for a core with ρ=20 µΩcm and μ_r=10000.

If the excitation is provided with a current passing directly through the ferromagnetic material, as in the case of the Aldredge type orthogonal configuration, similar problem occurs at higher frequencies: The current passing through the core starts to concentrate at the outer regions for higher frequencies due to the skin effect. This results in a non-uniform current density across the cross-section. The thickness at which the current density drops to 1/e of its peak value is defined as the skin depth δ, and is given as:

$$\delta = \sqrt{\frac{\rho}{\pi f \mu_o \mu_r}} \qquad (2.30)$$

where ρ is the resistivity of the ferromagnetic layer and f is the operating frequency. Figure 2.18 shows the variation of the skin depth with the frequency for a given core with 20 µΩcm resistivity and 10000 relative permeability. As and example, in order to operate the sensor at 100 kHz excitation, the core should be thinner than 7 µm. With a thicker core, the middle part cannot be controlled as good as required, leading to hysteresis errors. Highly resistive ferromagnetic materials are preferred in order to be able to maximize the operating frequency of the sensor, enabling the detection of fields at higher frequencies.

Power dissipation: In order to minimize the power dissipation of the sensor, ferromagnetic materials with narrow B-H curves are preferred. This leads to the selection of materials with high relative permeability, low B_{sat}, low H_c, and low H_k values in order to minimize the magnetic power losses and the field required to saturate the sensor core.

On the other hand, the field required to saturate the core effects the perming of the sensor. In order to minimize the effect of perming, the magnetic domains should be well controlled. So, the sensor should be excited with a magnetic field which is higher than the saturation magnetic field value (H_k) of the ferromagnetic material used as the sensitive element. Generally, a field several times higher than the H_k value is required for proper operation of the sensor [2.17].

Power dissipation and the linear operation range is always a compromise for the parallel fluxgate configurations as the same demagnetization factor is effective for both of the mechanisms. Ring or race-track shaped cores provide a closed magnetization path for excitation, leading to easier saturation and less power dissipation.

For the orthogonal Aldredge type sensor, saturating the core with small power dissipation is also possible as the current passing through the core creates circular magnetic field. The advantage is the much simpler structure of the sensor. The tubular Aldredge type sensor provides more uniform circular saturation with a more complex structure.

Apart from the sensor configuration, the surface imperfections and the impurities are the factors that are effective in the power dissipation of the sensor. As these parts need more field to be controlled, the power dissipation is increased.

Stability: The stability of magnetic sensors is defined by the change of the offset and sensitivity with time, temperature, and stress of the ferromagnetic material. Fluxgate sensors are known for their low offset and low temperature coefficient of offset, and they are advantageous over other types of magnetic sensors in these terms [2.3].

In the ideal case, the excitation of a fluxgate sensor is done with a signal composed of only odd harmonics, so there is no second harmonic component for zero external field, except the offset coming from the electronics that are used. So, the offset of the sensor system is determined by the offset of the signal conditioning electronics. Hence, the temperature coefficient of the offset is also mainly determined by the signal conditioning electronics. Perming can be considered as another contribution to the offset and to the temperature coefficient of offset of the sensor if it is subjected to magnetic fields much larger than its operation range.

Ferromagnetic materials may be affected from external or internal stress. Using thinner materials reduces the internal stress. Packaging of the sensor is also important to minimize the produced stress. Magnetostriction, the change of shape with the applied magnetic field, is also an important parameter for produced stress especially if the ferromagnetic material is attached to a rigid surface. This may result in field induced stress in the ferromagnetic material, and may disturb the linearity or long term stability. Using a ferromagnetic material with magnetostriction close to zero is the general aim for the fluxgate sensors.

2.5 Conclusion

In this chapter, magnetic classification of the materials is presented, and the properties of soft ferromagnetic materials are summarizes over their magnetization curves. The demagnetization effect is investigated and several methods are presented for the calculation of the demagnetization factor for different core shapes. The fluxgate operation principle and fluxgate sensor configurations are studied for both parallel and orthogonal fluxgate sensors. Finally, performance parameters of fluxgate sensors are discussed generally referencing the magnetic properties of the core materials.

Next chapter will deal with the core material selection for microfabricated fluxgate sensors and electroplated FeNi layers will be discussed in detail.

2.6 References

[2.1] J. D. Kraus, “Electromagnetics,” ISBN 0-07-066380-7, McGraw-Hill Inc, 1984, Japan.

[2.2] D. K. Cheng, “Fundementals of Engineering Electromagnetics,” ISBN 0-201-56611-7, Addison Wesley Publishing Co., 1993, USA.

[2.3] P. Ripka, “Magnetic Sensors and Magnetometers,” ISBN 1-58053-057-5, Artech House, 2001, USA.

[2.4] R. C. O’Handley, “Modern Magnetic Materials, Principles and Applications,” ISBN 0-471-15566-7, John Wiley and Sons, 2000, USA.

[2.5] J. A. Osborn, “Demagnetizing Factors for the General Ellipsoid,” Physical Review, Vol. 67, No. 11-12, June 1-15, pp. 351-357, 1945.

[2.6] M. Kobayashi, “Surface magnetic charge distributions and demagnetizing factors of circular cylinders,” IEEE Transactions on Magnetics, vol. 28, no. 3, pp. 1810-1814, May 1992.

[2.7] D. X. Chen, E. Pardo, A. Sanchez, “Demagnetizing factors of rectangular prisms and ellipsoids,” IEEE Transactions on Magnetics, vol. 38, no. 4, pp. 1742-1752, July 2002.

[2.8] D. X. Chen, J. A. Brug, R. B. Goldfarb, “Demagnetizing Factors for Cylinders,” IEEE Transactions on Magnetics, vol. 27, no. 4, pp. 3601-3619, July 1991.

[2.9] A. Aharoni, “Demagnetizing factors for rectangular ferromagnetic prisms,” Journal of Applied Physics, vol. 83, no. 6, pp. 3432-3434, March 1998.

[2.10] E. Pardo, D. X. Chen, A. Sanchez, “Demagnetizing factors for square bars,” IEEE Transactions on Magnetics, vol. 40, No. 3, pp. 1491-1498, May 2004.

[2.11] F. Primdahl, “The fluxgate mechanism: Part I: The gating curves of parallel and orthogonal fluxgates,” IEEE Transactions on Magnetics, vol. mag. 6, no. 2, pp. 376-383, June 1970.

[2.12] O. Zorlu, P. Kejik, R. S. Popovic, "An orthogonal fluxgate-type magnetic microsensor with electroplated Permalloy core ", Sensors and Actuators A: Physical, vol. 135, issue 1, pp. 43-49, March 2007.

[2.13] P. Ripka, “New directions in fluxgate sensors,” Journal of Magnetism and Magnetic Maerials, vol. 215-216, pp. 735-739, 2000.

[2.14] P. M. Drljaca, “Integrated Fluxgate Compass for Portable Applications,” ISBN 3-89649-958-0, Hartung-Gorre, 2004, Konstanz, Germany.

[2.15] H: Barkhausen, “Zwei mit hilfe der neuen verstäker entdectkte erscheinungen,” Physik. Zeitschr., vol.20, pp.401-407, 1919.

[2.16] “Barkhausen Effect,” Wikipedia, 2007. Online 2 Nov. 2007, http://en.wikipedia.org/wiki/Barkhausen_effect.

[2.17] P. Ripka, “Advances in fluxgate sensors,” Sensors and Actuators A: Physical, vol. 106, pp. 8-14, 2003.

[2.18] Weisstein, Eric W. "Sinc Function." From MathWorld--A Wolfram Web Resource, http://mathworld.wolfram.com/SincFunction.html, Online 3 Jan 2008.

CHAPTER III

ELECTROPLATED FeNi LAYERS AS FLUXGATE CORE MATERIAL

In this section, the work on the fluxgate core material selection is presented. Section 3.1 summarizes the previously reported different types of core materials. Section 3.2 presents the process of electroplating, electroplating solutions, different electroplated ferromagnetic layers, and particularly, affects of process parameters on the electroplated FeNi layers. In Section 3.3, the tests conducted in this work, on the process parameters of FeNi electroplating are presented and results are discussed. Section 3.4 summarizes the obtained results.

3.1 Core Materials of Fluxgate Sensors

In the previous chapter, the performance parameters of fluxgate sensors are presented by mainly referencing the magnetic properties of the core materials. Generally, the cores of the fluxgate sensors are made of materials with high permeability, low coercivity, low magnetostriction, and high electrical resistivity.

Up to now, many different materials are used as the core elements for fluxgate sensors. Thin tapes of Permalloy are regarded as the traditional core material [3.1]. Two examples of Permalloy films are the 81.6 Ni 6 Mo developed by Naval Ordnance Laboratory [3.2] and USSR production 81 NMA Permalloy [3.3]. Electroplated layers of ferrites [3.4] or FeNi based alloys [3.5] are also used as the core material. After 1980's amorphous magnetic materials, which are also called as magnetic glasses, became popular due to their superior magnetic properties [3.6], [3.7]. The list of core materials is extensive enough to cover ferrofluids [3.8] and high temperature superconductors [3.9].

Among all the materials mentioned above, magnetic glasses and electroplated ferromagnetic layers came into prominence with the trend of miniaturizing the sensors, and producing them together with the signal conditioning electronics. Several fluxgate sensors and compasses are prototyped as ICs or on PCBs by using the magnetic glasses as the core material [3.10], [3.11], [3.12]. For IC applications, the core is placed onto the IC chip, which is carrying the signal conditioning electronics. This is generally done by gluing the magnetic glass foil on the whole silicon wafer surface, and then patterning it in the shape of a core with photolithography and chemical etching. Generally, low stress glues and processes are used for these steps. Still, in order to recover the intrinsic properties of the magnetic glass, a complicated process including mechanical polishing, wet chemical thinning, and thermal annealing may be required [3.13].

The other promising method of integration is realizing the core materials by using electroplating, which is already taking its place in the advanced IC fabrication technologies and being used in order to fabricate thick metal lines [3.14]. After the first attempt to miniaturize a fluxgate sensor by Seitz [3.15] by using an electroplated FeNi layer, many research has been conducted in the same direction. Sensors developed either on PCB substrates [3.16], or on silicon wafers are reported [3.17], [3.18], [3.19], all using electroplated FeNi as the core material. The use of other electroplated layers of FeNiMo [3.20] and FeNiCo [3.21] are also reported. However, these materials could not be as popular as FeNi, even if their magnetic properties are intensively studied. This is most probably due to their rather complicated electroplating mechanism.

The possibility of easier integration to IC fabrication technologies and rather simple fabrication procedure of electroplating are the two main motives in our selection of this method over using magnetic glasses for the sensor core fabrication. In the following section, the electroplating process and the parameters affecting the ferromagnetic material properties will be briefly discussed.

3.2 Electroplating of Ferromagnetic Materials

Electroplating is the process of depositing metallic layers on a substrate through a solution by applying a potential difference. Usually there is an anode (positively charged electrode), which is the source of the material to be deposited; a cathode (the negatively charged electrode) which is the substrate to be coated; and the electrochemical solution (electrolyte) which is the medium through which ions are exchanged between the anode and the cathode. Electroplating is an oxidation-reduction reaction, where one material gives up electrons (gets oxidized) and the other material gains electrons (gets reduced). The anode is the electrode at which oxidation occurs, and the cathode is the electrode at which reduction occurs. Figure 3.1 presents a typical electroplating setup. In this setup, Nickel (Ni) is electrodeposited from a NiCl and KCl solution. A Nickel anode and a Copper (Cu) cathode is used. In a condition such that the anode is at sufficiently positive and the cathode is at sufficiently negative electrical potential with respect to the electrolyte, the following reactions occur:

Cathode reaction: $Ni^{2+} + 2e^- \rightarrow Ni$
Anode reaction: $2Cl^- \rightarrow Cl_2 + 2e^-$
Total: $NiCl_2 \rightarrow Ni + Cl_2$

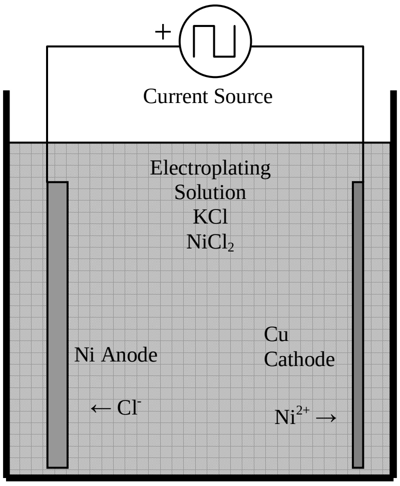

Figure 3.1: A typical electroplating setup.

According to these reactions, Ni is deposited on the Cu substrate and Cl_2 is formed at the anode in gas form. The rate of the deposition is related to the number of electrons passing through the electrolyte per unit time, i.e., the electrical current passing through the circuit. The properties of the electroplated layer are mainly determined by the composition of the electrolyte, applied current density, and the electroplating temperature.

When electroplating of more than one element is done in the same electrolyte, the issues become a little bit more complicated. For these electroplating setups, the interactions between the electroplated atoms are also effective. The ratio of the electroplated atoms is not necessarily equal to the ratio of the ions in the electrolyte. Furthermore, the applied current density (or the potential) may change the ratio of the electroplated atoms. This is called anomalous codeposition. The codeposition of Iron, Cobalt, and Nickel is referred as an electroplating of the anomalous type since the less noble metal is deposited preferentially and its percentage in the deposit is obviously higher than that of it in the electrolyte [3.22]. Due to this complex nature of electroplating, the main focus of this part of the work is given to the electroplating of binary alloys, and in particular to Permalloy or FeNi, which is very widely used in the fabrication of fluxgate sensors. The other electroplated binary alloys like NiCo [3.23] and CoFe [3.24] are reported with harder magnetic properties with respect to FeNi. This makes FeNi the most popular binary alloy for fluxgate sensor fabrication. However, it is worth noting that a number of ternary alloys such as FeNiCo [3.24], NiFeMo, NiFeCr [3.25], and CoFeCr [3.26] are reported in the literature, some of which may also be used in magnetic sensor fabrication.

The factors affecting the magnetic properties of ferromagnetic thin films are their composition, grain size, and the internal stress. For electroplated FeNi alloys, lower H_c values are obtained around 20 % Fe - 80 % Ni composition, with smaller grain size (<30 nm). Alloys composed of smaller grains have lower internal stress results and this result in lower H_k values and lower magnetostriction. Alloy composition, grain size, and internal stress are determined by the composition of the electrolyte, electroplating temperature, applied current density, addition of organic additives, and applied magnetic field during electroplating.

The electrodeposition of binary or ternary alloys is studied various times by using different electrolytes [3.22], [3.27]. Most widely used solutions are mainly composed of sulfate or sometimes chloride salts of the materials to be electroplated.

The ion concentration of the electrolyte affects the electroplating speed, the composition and the stress of the resulting layer. Higher concentration of ions increase the electroplating speed, however, the internal stress is also increased [3.28]. This results in higher H_k values of the layer. Increasing the temperature of the electrolyte is widely preferred as it helps in reducing the internal stress of the layer [3.29], [3.30]. It should also be noted that the stress of the layer tends to increase with its thickness [3.22]. Keeping the same ion concentration around the electroplating surface during the electroplating process is important for obtaining a layer with a uniform alloy composition. This can be provided by maintaining a circulation of the electrolyte (stirring), continuously refreshing the electrolyte around the cathode.

The applied current density not only affects the electroplating speed but also the composition and the grain size of the resulting layer. The electroplating speed increases whereas the iron composition decreases with the increased current density [3.31], [3.32]. It is also reported that the grain size is decreased and internal stresses are increased with the current density, indicating an optimum operating point [3.33]. Instead of DC electroplating current, pulsed or pulse-reversed electroplating techniques may be utilized which may further reduce the grain size of about 15 % [3.29], [3.34]. Addition of organic additives such as saccharin to the electroplating solution also reduces the grain size and results in more uniform and shiny electroplated surfaces [3.22], [3.35]. Another factor that decreases the grain size is the smoothness of the seed layer for electroplating. Generally, layers electroplated on evaporated or sputtered seed layers result in smaller grain sizes when compared to layers electroplated on rough surfaces like copper wires [3.36].

It is also important to note that the ratio of the grain size to the overall dimensions of the layer is as important as the absolute value of the grain size. Thicker layers having smaller H_c values when compared to the thinner ones electroplated with same conditions are reported [3.31]. Similar phenomenon is valid if electroplated nanowires are compared to the electroplated thin films [3.37].

The application of a magnetic field up to a certain value also reduces the grain size. If a magnetic field is applied parallel to the electroplating surface, it creates a magnetic easy axis in its direction, along which one can obtain softer magnetic properties [3.38], [3.39]. In that sense, anisotropic layers may be produced.

In the light of the reported data in the literature, it is decided to select a commonly used sulfate based FeNi electroplating solution [3.31], [3.30], [3.39]. In order to find the optimum electroplating conditions, several experiments are conducted. The effect of stirring, the temperature of the electrolyte, applied current density, and applied magnetic field are investigated through the measured magnetization curves of the electroplated layers. Next section will focus on these experiments and evaluation of the obtained results, including the description of the electroplating and measurement methodology and electroplating setup.

3.3 Properties of Electroplated FeNi Layers

In this section, the effect of the electroplating conditions on the magnetic properties of FeNi layers will be presented. Table 3.1 presents the composition of the FeNi electroplating solution used during this work. The use of this electrolyte composition gives smaller grain sizes, a more uniform electroplated surface, and magnetic properties more suitable for utilization in a fluxgate type sensor. During this study, the electrolyte is renewed three times since its composition changes as it is used. These will be referred as Bath I, Bath II, and Bath III for the rest of the text. Bath I and Bath II are identical, whereas Bath III contains a different H_3BO_3 provided by another supplier. The experiments presented here are studied by using Bath I and Bath II. The level of the electroplating solution is controlled before each electroplating step and de-ionized (DI) water is added to the solution if some evaporation is observed. The substrates that are used for electroplating are brass, glass (or Pyrex®), or silicon substrates. Evaporated Chromium-Copper (Cr/Cu) is used as seed layer on glass and silicon substrates. The shape of the electroplated layers is either rectangular or square. Rectangular samples have smaller demagnetization factor along their long edge, so these samples are used in order to observe the intrinsic magnetic properties. On the other hand, circular samples have larger, but uniform demagnetization factor over the electroplating plane. Because of this the magnetic anisotropy of the electroplated layer can be measured on the same sample without being affected by the contribution of different demagnetization factors. Furthermore, the effect of the possible electroplating non uniformities such as composition or thickness differences over the electroplating surface are eliminated by using a single sample for measurements.

Table 3.1: The electrolyte composition.

Chemicals	**Concentration**	
	(mol/l)	(g/l)
$NiSO_4.6H_2O$	0.7	184
$FeSO_4.7H_2O$	0.03	8.34
$NiCl_2.6H_2O$	0.02	4.75
H_3BO_3	0.4	24.73
Saccharine	0.016	2.93
DI water volume	3.2 l	
pH	2.3 @ room temperature (RT)	

3.3.1 The Electroplating Setup

Figure 3.2 shows the picture of the electroplating setup. The electroplating setup is mainly composed of an activator solution, rinsing DI water, and the electroplating solution. The substrates are immersed into an activator solution for 15 to 60 seconds before electroplating in order to remove the oxidized layer on the substrates. The activator solution consists of 0.2 l H_2SO_4, 0.2 l Dekacid concentrate activator, and 3.6 l DI water. After the activation process, the sample is rinsed with DI water for 1 to 2 minutes. Then, it is directly immersed into the electroplating solution. The pump provides the circulation, and heater is used to control the temperature of the electroplating solution. The magnetic field is controlled with the Helmholtz-like coils placed around the container of the electroplating solution. The current is applied through a PDD 3502A Dual 35 V–2 A power supply or an HP 33120A function generator connected to a power amplifier.

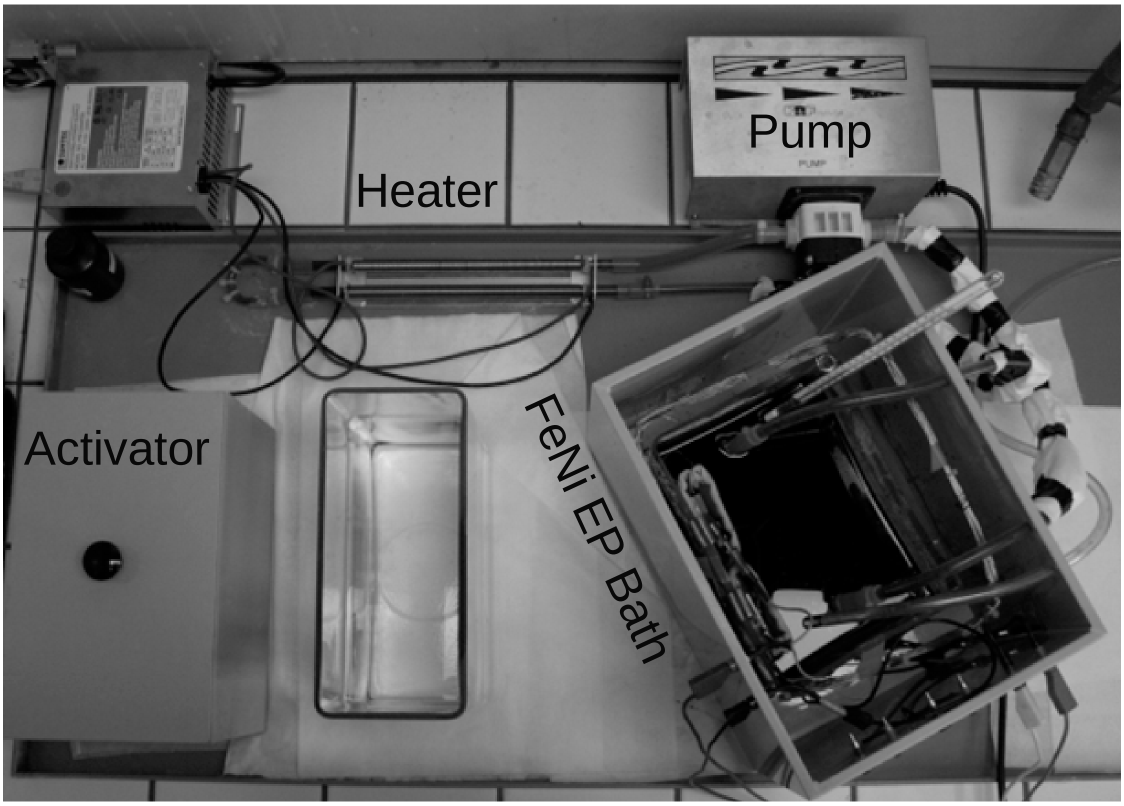

Figure 3.2: The electroplating setup.

3.3.2 The magnetization curve measurement setups

Two different setups are used to measure the magnetization curve of the electroplated layers. One of the test setups measures the DC magnetization curve and the other one measures the AC magnetization curve.

Figure 3.3(a) shows the setup that is used for the DC magnetization curve measurements. The Helmholtz coils provide the external magnetic field, and the voltage across the pick-up coil gives the magnetization information. The current passing through the Helmholtz coils and thus the magnetic field around the sample is varied with small steps and the induced voltage across the pick-up coils is measured by a fluxmeter. The output of the fluxmeter is the integral of the induced voltage, and it gives the magnetization curve information. The PC control of the system is done with LabView. The output waveform with respect to the applied magnetic field is given in Figure 3.3(b).

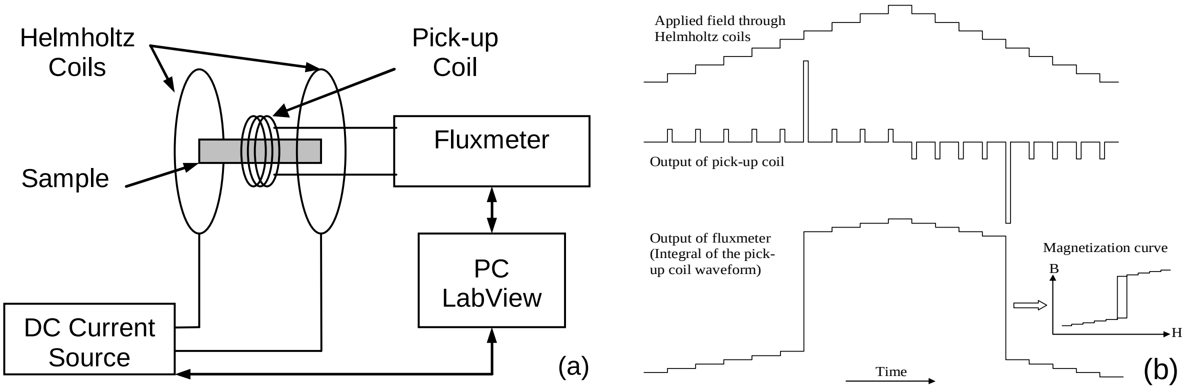

Figure 3.3: (a) The setup for the measurement of DC magnetization curves. (b) The applied field and obtained waveforms.

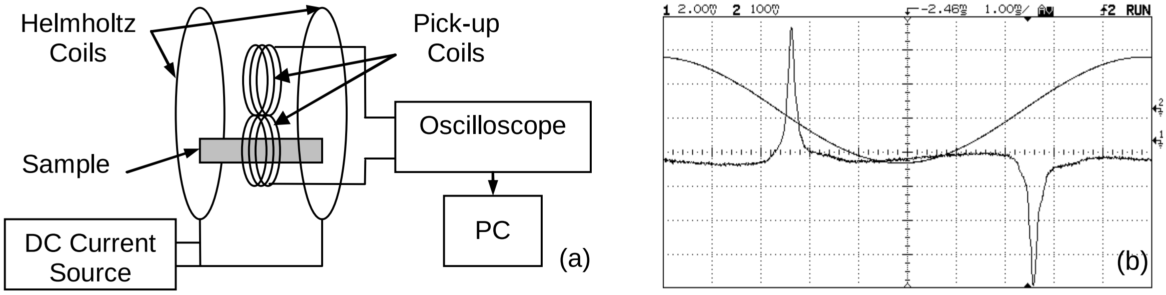

Figure 3.4: (a) The setup for the measurement of AC magnetization curves. (b) The waveform captures from the oscilloscope.

For the AC measurements, a similar setup is used. Figure 3.4(a) shows the setup for measuring the AC magnetization curves. An anti serially connected two-coil configuration provides the cancellation of the flux change resulting from the air inside the coils. The output of the coils is connected to an oscilloscope which is able to record the displayed waveform values and has a PC interface. Then, this waveform is numerically integrated in order to obtain the magnetization curve. The frequency of the applied field is set to 100 Hz. Figure 3.4(b) shows the screen capture from the oscilloscope with applied field and induced voltage waveforms.

3.3.3 The Effect of Stirring

The effect of stirring is tested with Bath I. The solution temperature is set to 40 °C. Electroplated is done with DC current of 14.5 mA/cm^2 density for 5 minutes. Three rectangular brass plates with 7 cm x 1 cm area are electroplated. One of the samples is electroplated with stirring provided with the pump; the other one is electroplated without any stirring, and the last sample is electroplated while stirring the solution manually. Figure 3.5 shows the normalized AC magnetization curves measured at 100 Hz frequency. It is seen that the magnetic properties improve drastically with stirring. This is probably due to anomalous co-deposition Iron-Nickel alloys and Nickel deposition being diffusion controlled [3.22]. Refreshing the electrolyte around the cathode by continuous stirring helps in forming the expected composition with better magnetic properties.

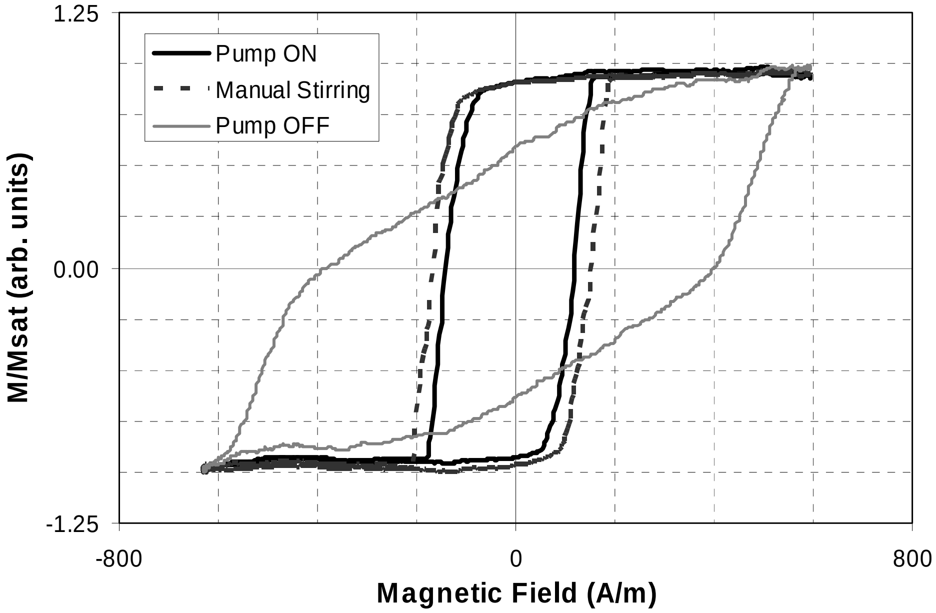

Figure 3.5: Normalized AC magnetization curves for different stirring conditions.

3.3.4 Temperature of the Electrolyte

Brass samples with circular openings having a 30 mm diameter are electroplated with 14.5 mA/cm^2 current density in Bath I. The duration of each electroplating is 5 minutes and the magnetic field around the cathode is cancelled during the process. Five samples are electroplated at 20 °C, 35 °C, 40 °C, 50 °C, and 65 °C. Figure 3.6 shows the normalized DC magnetization curves of the samples. A higher coercive field H_c is observed for the samples electroplated at 20 °C and 65 °C. It is seen that the shape of the magnetization curve gets better with the increased temperature up to 50 °C. At low temperature the stress induced effects are visualized in the magnetization curves as multiple slopes in the linear region. The curves become smoother for higher temperatures. The best magnetization curve with an H_c of 75 A/m is obtained with a temperature of 50 °C. However, the evaporation of the solution gets much faster at this temperature, and the control of the bath composition becomes very difficult. Considering this practical problem, it is concluded that 40 °C is the optimum electroplating temperature as it also results in a very similar H_c value of 80 A/m.

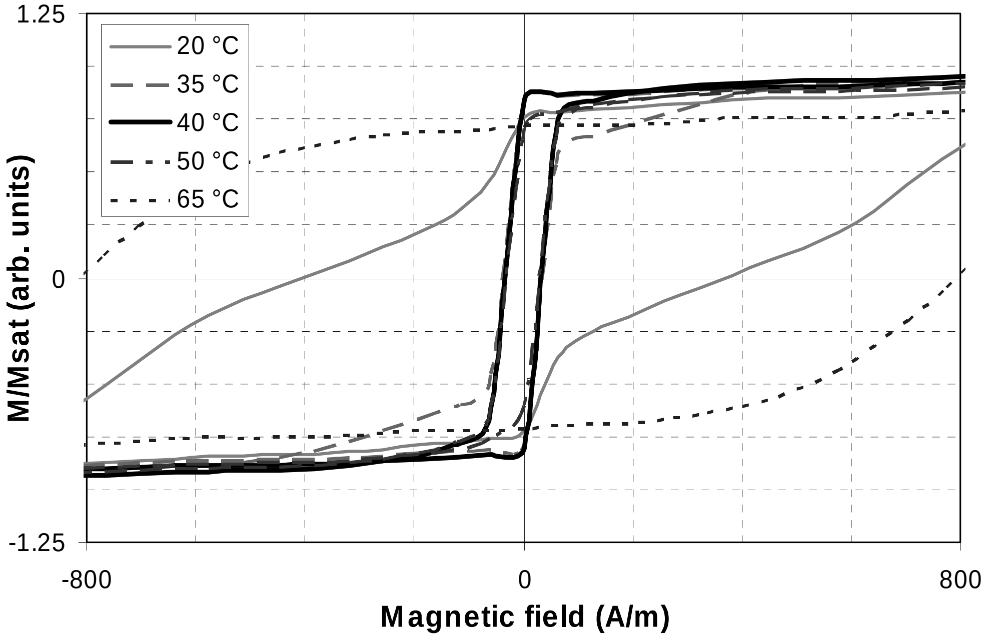

Figure 3.6: Normalized DC magnetization curves for different electrolyte temperatures.

3.3.5 The Effect of Current Density

The differences in the magnetization curves resulting from the change in the current density of the electroplating is investigated with Bath II. The solution temperature is kept at 40 °C, and electroplating process time is 5 minutes for all samples. Brass samples with 7 cm x 1 cm area are used as substrates. Current densities between 7.5 mA/cm^2 and 30 mA/cm^2 are tested with 2.5 mA/cm^2 steps. Figure 3.7 shows the variation of H_c value with the current density. The minimum H_c of 40 A/m is reached at 22.5 mA/cm^2 current density. Figure 3.7 also shows the relation between the applied electroplating current density and total difference in the measured magnetic flux ($\Delta\Phi$) which is calculated from the difference of two values at two applied field extremes of the magnetization curve. The total flux difference is directly proportional to the saturation magnetization flux density and the cross sectional area of the measured sample. If we assume that the deposition rate increases linearly with the current density [3.31], the variation of the saturation magnetization can be estimated from the graph. From this, we can conclude that the M_{sat} value stays almost same for the tested current density range. This information can be used to compare the relative permeability values obtained by using different electroplating current density values.

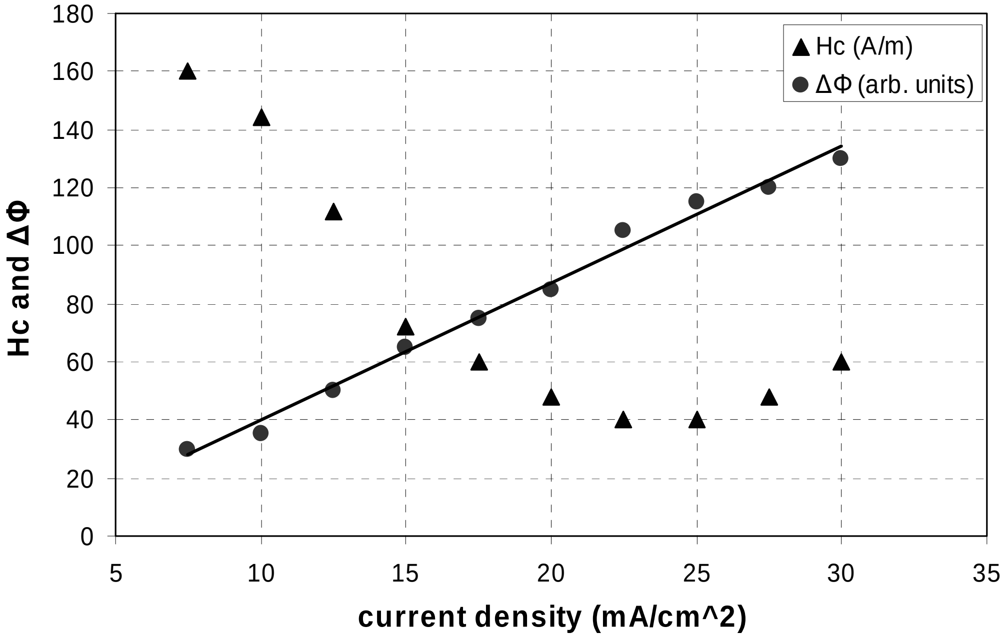

Figure 3.7: The variation of H_c and $\Delta\Phi$ with the current density.

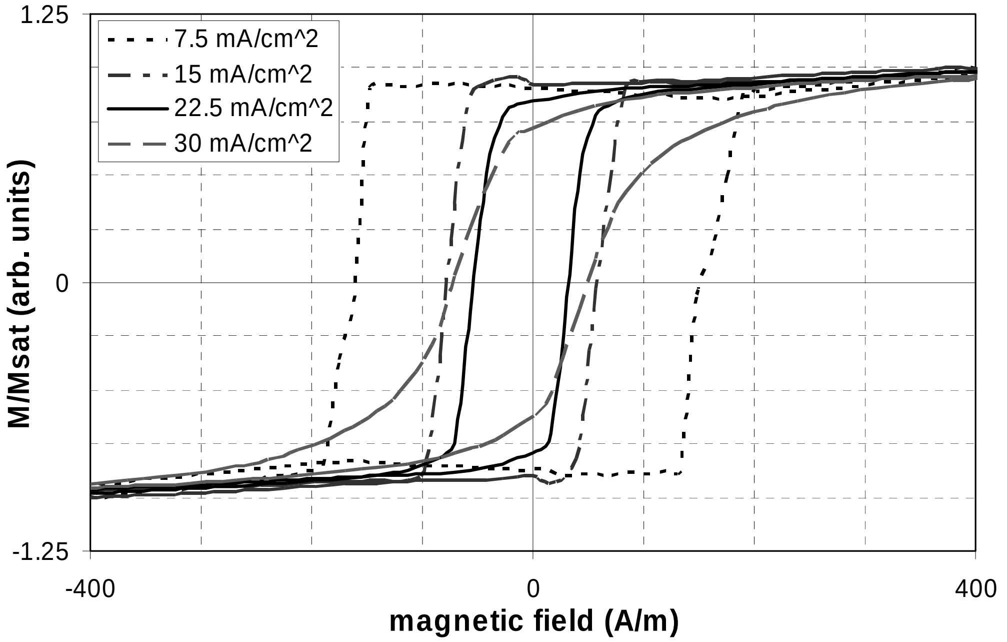

Figure 3.8: The measured magnetization curves obtained from samples with 7.5, 15, 22.5, 30 mA/cm^2 current density values.

Figure 3.8 shows some of the measured magnetization curves obtained from samples with different current density values. Assuming very similar M_{sat} values, the magnetization curves show that the highest relative permeability values are reached for current density values between 15 mA/cm^2 and 22.5 mA/cm^2 as they have similar sharp slopes at the linear region of the magnetization curve. The H_k value is slightly smaller and around 90 A/m in the case of 15 mA/cm^2 current density.

3.3.6 Effect of Applied Magnetic Field

In order to measure the effect of the applied magnetic field, circular and rectangular test structures are prepared and patterned on silicon wafers having Cr/Cu seed layers. Figure 3.9 shows one of the electroplated test wafers. With the rectangular structures, magnetization curves parallel and perpendicular to the applied magnetic field can be measured. Since these structures have low demagnetization factor, measured curves are closer to the intrinsic magnetization curves. However, wafer level non-uniformities of the electroplating process is also effective on the results with these structures. Using a circular layer gives the possibility to compare the effect of the applied field on the same sample, and it eliminates the effect of having different magnetic properties due to the non uniform electroplating over the sample. By knowing that the M_{sat} value and the cross section of the sample is not changing, a better comparison of different directions can be made. Furthermore, it is possible to measure the magnetization curves at any desired angle. The only disadvantage is the larger demagnetization factor of the circle, which results in a smaller apparent permeability value.

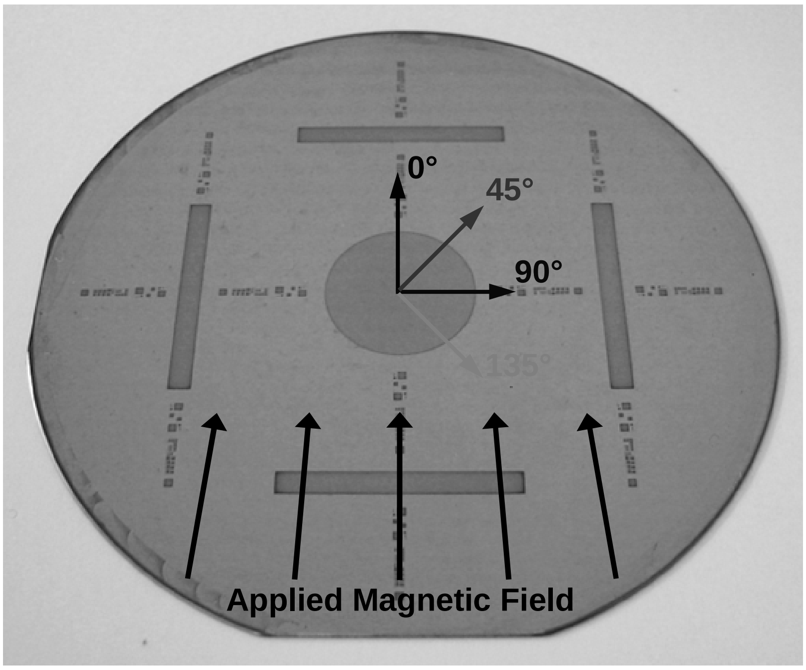

Figure 3.9: The electroplated test wafer, applied magnetic field and measurement directions.

Bath II is used for electroplating of the test samples. The positioning of the container of the electroplating solution is seen in Figure 3.2. With this placement, the magnetic field parallel to the electroplating surface (90° direction in Figure 3.9) is zero. A perpendicular and vertical field of around 40 µT and 80 µT respectively exists around the cathode, which is the combination of the earth magnetic field and the effect of neighboring magnetic pieces. The vertical component of the magnetic field is modified by using the Helmholtz like coils placed around the electroplating solution. Three samples are electroplated with current density of 14.5 mA/cm^2 for 10 minutes. Wafer I is electroplated at room temperature with zero vertical field. The other two are electroplated at 40 °C, Wafer II with zero and Wafer III with 400 µT vertical field.

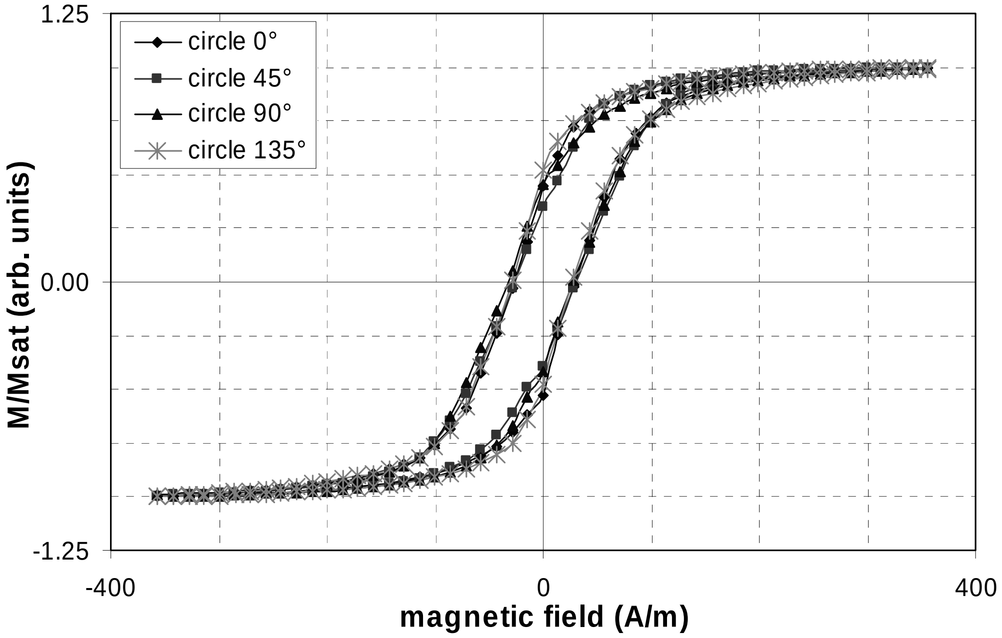

Figure 3.10: The magnetization curves of circular sample of Wafer I at different measurement angles. (Electroplating at RT with cancelled vertical magnetic field)

Figure 3.10 shows the magnetization curves measured with the circular samples of Wafer I at different angles. It is seen that cancelling the magnetic field around the electroplating region results in isotropic magnetic properties. The measurement results for Wafer II are given in Figure 3.11. It is seen that raising the electrolyte temperature does not disturb the isotropy, but results in a better magnetization curve in terms of relative permeability and H_k value. Measurements of the rectangular samples presented as an inset in Figure 3.11 demonstrate the effect of smaller demagnetization factor resulting in steeper magnetization curves having smaller H_k values. Comparing the magnetization curves obtained from circular and rectangular samples, it is seen that both shapes have similar Hc values around 40 A/m, whereas the rectangular samples have smaller H_k values around 90 A/m and circular ones have H_k values of around 150 A/m.

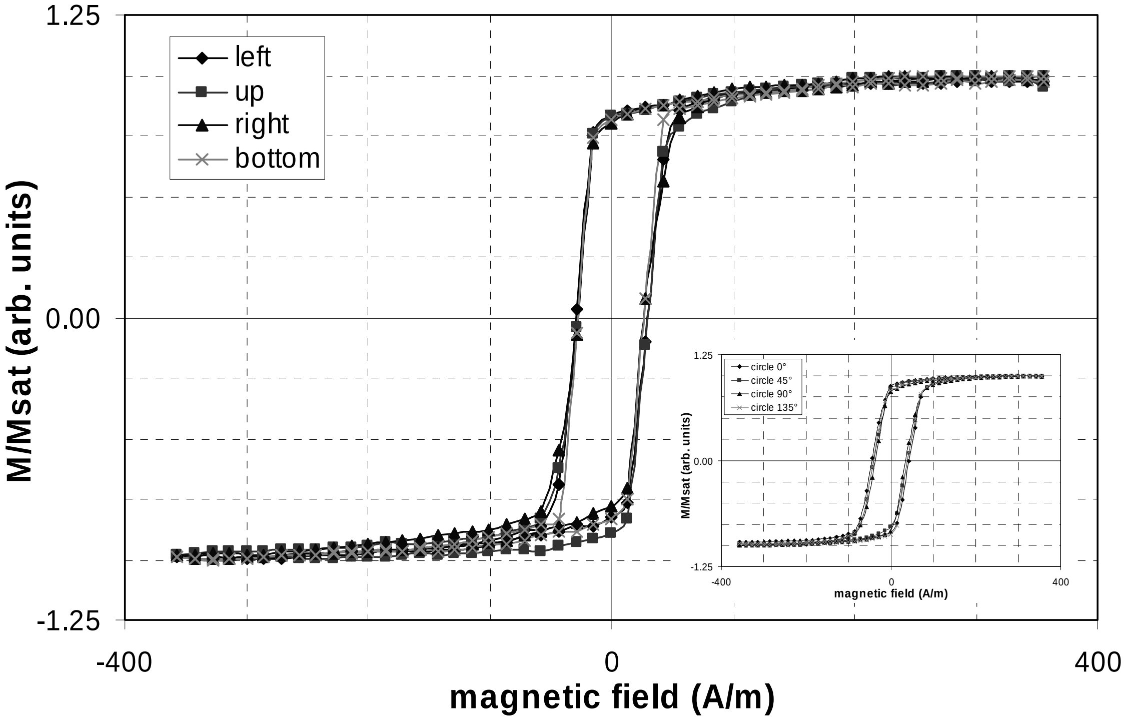

Figure 3.11: The magnetization curves of circular and rectangular (inset) samples of Wafer II. (Electroplating at 40 °C with cancelled vertical magnetic field)

Figure 3.12 presents the effect of applied magnetic field in the vertical direction. The electroplated samples are anisotropic: The easy and hard axes are clearly seen from the magnetization curves being parallel (0°) and perpendicular (90°) to the applied magnetic field direction, showing an agreement with the previously reported data [3.39]. The H_c value of the sample is drastically reduced when compared to the zero field cases of Wafer I and Wafer II. However, the H_k value is dependent on the measurement angle, and its value for the hard axis is more than twice the value for the easy axis. Figure 3.13 shows the measurement results of the rectangular samples of Wafer III. The magnetic anisotropy is also visible for these samples. Furthermore, slightly different curves of the samples having the same orientation but placed away from each other show that either the magnetic field distribution or the electrodeposition is not entirely uniform over the surface of the wafer. The effect of magnetic field distribution is likely to be more dominant since this difference is not observed for the rectangular samples of Wafer II, for which the vertical field is cancelled.

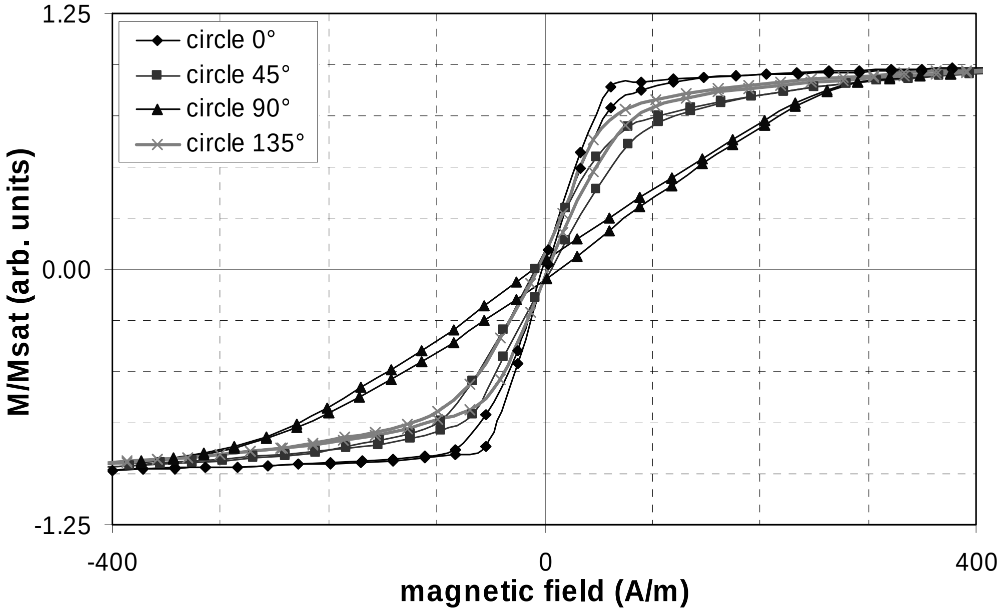

Figure 3.12: The magnetization curves of circular sample of Wafer III. (Electroplating at 40 °C with 400 µT vertical magnetic field)

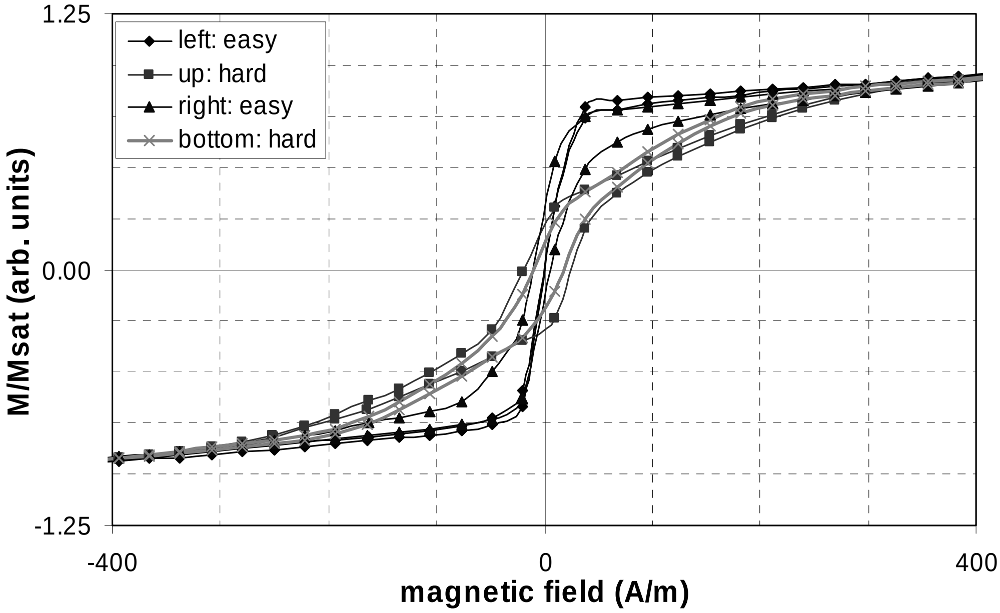

Figure 3.13: The magnetization curves of rectangular samples of Wafer III. (Electroplating at 40 °C with 400 µT vertical magnetic field)

The decision on whether applying a magnetic field during electroplating depends on the application that the layer will be used. If the magnetic properties in one direction are important for the application, then electroplating with a magnetic field in this direction during the electroplating process is advantageous. The case of a parallel fluxgate sensor application fits to this situation. However, if the application requires isotropic properties, it is better to cancel the magnetic field around the electroplating region. An orthogonal fluxgate application is an example for that, where we need soft magnetic properties in all directions.

3.4 Conclusion

In this chapter, the work on the fluxgate core material selection is presented. Different core materials and fabrication techniques are discussed, and electroplating is selected due to its compatibility with IC fabrication technologies. Electroplated FeNi layers are preferred among many different ferromagnetic layers since the resulting layers have soft magnetic properties, and their electroplating process is relatively simple when compared to the ternary alloys. The electroplating conditions affecting the magnetic properties of the layers are discussed and tested. Magnetization curves of layers electroplated with different conditions are measured.

It is seen that stirring during the electroplating process is necessary for good soft magnetic properties. The optimum electrolyte temperature is 40 °C, and the electroplating current density between 15 and 22.5 mA/cm^2 gives better magnetization curves. It is possible to obtain layers with H_c and H_k values of 40 and 90 A/m, respectively. Assuming a typical saturation magnetization density value of 0.85 T for electroplated FeNi layers, an intrinsic relative permeability around 40000 can be reached.

Soft magnetic properties can be enhanced in one direction if a magnetic field is applied during the electroplating process. On the contrary, it is possible to obtain an isotropic magnetic layer by canceling the magnetic field around the electroplating surface. The decision on the applied magnetic field depends on the application: A magnetic field bias can be useful for parallel fluxgates; however, canceling the magnetic field is more suitable for orthogonal fluxgate sensor fabrication, as it results in uniform magnetic properties in all directions.

Three different fluxgate sensor configurations are fabricated using electroplated FeNi layers as the ferromagnetic core material in the frame of this work will be presented. These sensors are named as rod-type orthogonal macro fluxgate sensor; rod-type orthogonal micro fluxgate sensor; and ring type fluxgate micro sensor. These sensors will be presented in the flowing three chapters.

3.5 References

[3.1] P. Ripka, “Magnetic Sensors and Magnetometers,” ISBN 1-58053-057-5, Artech House, 2001, USA.

[3.2] D. Gordon, R. Lundsten, R. Chiarodo, H. Helms, “A fluxgate sensor of high stability for low field magnetometry,” IEEE Transactions on Magnetics, vol. 4, issue. 3, pp. 397-401, September 1968.

[3.3] P. Ripka, “Review of fluxgate sensors,” Sensors and Actuators A: Physical, vol. 33, pp. 129-141, 1992.

[3.4] F. Primdahl, “The fluxgate magnetometer,” Journal of Physics E: Scientific Instrumentation, vol. 12, pp. 241-253, 1979.

[3.5] P. E. Gise, R. B. Yarbrough, “An improved cylindrical magnetometer sensor,” IEEE Transactions on Magnetics, vol. 12, issue 5, pp. 1104-1106, September 1977.

[3.6] K. Mohri, “Review of recent advances in the field of amorphous metal sensors and transducers,” IEEE Transactions on Magnetics, vol-mag. 20, no. 5, pp. 397-401, September 1984.

[3.7] A. Engelter, “A fluxgate magnetometer with a metallic glass core,” IEEE Transactions on Magnetics, vol-mag. 22, no. 4, pp. 299-300, July 1986.

[3.8] O. Baltag, D. Costandache, “Sensor with ferrofluid for magnetic measurements,” IEEE Transactions on Instrumentation and Measurement, vol. 46, issue 2, pp. 629 – 631, April 1997.

[3.9] M. Gersherson, “High temperature superconductive flux gate magnetometer” IEEE Transactions on Magnetics, vol. 27, pp. 3055-3057, 1991.

[3.10] L. Chiesi, P. Kejik, B. Janossy, R. S. Popovic “CMOS planar 2D micro-fluxgate sensor,” Sensors and Actuators A: Physical, vol. 82, issue. 1-3, pp. 174-180, May 2000.

[3.11] P. M. Drljaca, P. Kejik, F. Vincent, D. Piguet, F. Gueissaz, R. S. Popovic “Single core fully integrated CMOS micro-fluxgate magnetometer,” Sensors and Actuators A: Physical, vol. 110, issues. 1-3, pp. 236-241, February 2004.

[3.12] B. Ando, S. Baglio, R. Bulsara, V. Sacco, “Residence times difference fluxgate magnetometers,” IEEE Sensors Journal, vol. 5, no. 5, pp. 895-904, October 2005.

[3.13] P. M. Drljaca, F. Vincent, P. Kejík, R. S. Popovic, “Advanced process of the magnetic core integration for the micro fluxgate magnetometer,” Sensors and Actuators A: Physical, vol. 129, issues. 1-2, pp. 58-61, May 2006.

[3.14] S. Krongelb, L. T. Romankiw, J. A. Tornello, “Electrochemical process for advanced package fabrication,” IBM Journal of Research and Development: Electrochemical Microfabrication, vol. 42, no 5, pp. 575-586, 1998.

[3.15] T. Seitz, “Fluxgate sensor in planar microtechnology,” Sensors and Actuators A: Physical, vol. 22, issues. 1-3, pp. 799-802, June 1989.

[3.16] T. O’Donnel, A. Tipek, A. Connell, P. McCloskey, S. C. O’Mathuna, “Planar fluxgate current sensor integared in printed circuit board,” Sensors and Actuators A: Physical, vol. 129, issues. 1-2, pp. 20-24, May 2006.

[3.17] S. Kawahito, H. Satoh, M. Sutoh, Y. Tadokoro, “Micro-fluxgate magnetic sensing elements using closely-coupled excitation and pickup coils,” TRANSDUCERS 1995, International Solid-State Sensors, Actuators and Microsystems Conference, Stockholm, Sweden, pp. 233 – 236, 25-29 June 1995.

[3.18] T. M. Liakopoulos, C. H. Ahn, “A micro-fluxgate magnetic sensor using micromachined planar solenoid coils,” Sensors and Actuators A: Physical, vol. 77, issue. 1, , pp. 66-72, September 1999.

[3.19] H. S. Park, J. S. Hwang, W. Y. Choi, D. S. Shim, K. W. Na, S. O. Choi, “Development of micro-fluxgate sensors with electroplated magnetic cores for electronic compass,” Sensors and Actuators A: Physical, vol. 114, issues. 2-3, pp. 224-229, September 2004.

[3.20] S. Kawahito, C. Maier, M. Schneiher, M. Zimmermann, H. Baltes, “A 2D CMOS microfluxgate sensor system for digital detection of weak magnetic fields,” IEEE Journal of Solid-State Circuits, vol. 34, issue 12, pp. 1843 – 1851, December 1999.

[3.21] P. Ripka, M. Butta M. Malatek, S. Atalay, F. E. Atalay, “Characterisation of Magnetic Wires for Fluxgate Cores,” TRANSDUCERS 2007, International Solid-State Sensors, Actuators and Microsystems Conference, Lyon, France, pp. 2369 – 2372, 10-14 June 2007.

[3.22] S. N. Srimathi, S. M. Mayanna, B. S. Sheshadri, B S, “Electrodeposition of Binary Magnetic Alloys,” Surface Technology, vol. 16, no. 4, pp. 277-322, August 1982.

[3.23] N. Fenineche, A.M. Chaze, C. Coddet, “Effect of pH and current density on the magnetic properties of electrodeposited Co-Ni-P alloys,” Surface and Coatings Technology, vol. 88, issues 1-3, pp. 264-268, January 1997.

[3.24] X. Liu, P. Evans, G. Zangari, “Electrodeposited Co-Fe and Co-Fe-Ni alloy films for magnetic recording write heads” IEEE Transactions on Magnetics, vol. 36, no. 5, pp. 3479-3481, September 2000.

[3.25] K. Hoshino, M. Sano, S. Narumi, M. Fuyama, “Magnetic properties and thermal stability of electroplated NiFeCr and NiFeMo films with high resistivity,” IEEE Transactions on Magnetics, vol. 35, issue 5, pp. 3433 – 3435, September 1999.

[3.26] F. Lallemand, D. Comte, L. Ricq, P. Renaux, J. Pagetti, C. Dieppedale, P. Gaud, “Effects of organic additives on electroplated soft magnetic CoFeCr films,” Applied Surface Science, vol. 225, issues 1-4, pp. 59-71, March 2004.

[3.27] S. C. Srivastava, “Electrodeposition of ternary alloys: Developments in 1972-1978,” Surface Technology, vol. 10, issue. 4, pp. 237-257, April 1980.

[3.28] Y. Zhang, G. Ding, H. Wang, S. Fu, B. Cai, “Low-Stress Permalloy for Magnetic MEMS Switches,” IEEE Transactions on Magnetics, vol. 42, no. 1, pp. 51-55, January 2006.

[3.29] M. Föhse, T. Kohlmeier, H. H. Gatzen, “Thinfilm technologies to fabricate a linear microactuator,” Sensors and Actuators A: Physical, vol. 91, issues 1-2, pp. 145-149, June 2001.

[3.30] J. Y. Park, M. G. Allen, “Integrated electroplated micromachined magnetic devices using low temperature fabrication processes,” IEEE Transactions on Electronics Packaging Manufacturing, vol. 23, no. 1, pp. 48-55, January 2000.

[3.31] J. M. Quemper, S. Nicolas, J. P. Gilles, J. P. Grandchamp, A. Bosseboeuf, T. Bourouina, E. Dufour-Gergam, “Permalloy electroplating through photoresist molds,” Sensors and Actuators A: Physical, vol. 74, issues. 1-3, pp. 1-4, April 1999.

[3.32] D. Flynn, A. Toon, L. Allen, R. Dhariwal, M. P. Y. Desmulliez, “Characterization of core materials for microscale magnetic components operating in the megahertz frequency range,” IEEE Transactions on Magnetics, vol. 43, no. 7, pp. 3171-3180, July 2007.

[3.33] H.L. Seet, X.P. Li, Z.J. Zhao, L.C. Wong, H.M. Zheng, K.S. Lee, “Current density effect on magnetic properties of nanocrystalline electroplated $Ni_{80}Fe_{20}$/Cu composite wires,” Journal of Magnetism and Magnetic Materials, vol. 302, issue. 1, pp.113–117, July 2006.

[3.34] H.L. Seet, X.P. Li, K.S. Lee, H.Y. Chia, “Nanocrystalline grain size control for $Ni_{80}Fe_{20}$/Cu micro-composite wires by different electrodeposition methods,” Journal of Materials Processing Technology, vol. 192-193, pp. 225-228, October 2007.

[3.35] S. Sam, G. Fortas, A. Guittoum, N. Gabouze, S. Djebbar, “Electrodeposition of NiFe films on Si(1 0 0) substrate,” Surface Science, vol. 601, issue. 18, 15 pp. 4270-4273, September 2007.

[3.36] X. P. Li, J.B.Yi, H. L. Seet, J.H.Yin, S. Thongmee, J. Ding, “Effect of Sputtered Seed Layer on Electrodeposited NiFe/Cu Composite Wires,” IEEE Transactions on Magnetics, vol. 43, no. 6, pp. 2983-2985, June 2007.

[3.37] H. R. Khan, K. Petrikowski, “Anisotropic structural and magnetic properties of arrays of Fe26Ni74 nanowires electrodeposited in the pores of anodic alumina,” Journal of Magnetism and Magnetic Materials, vol. 215-216, pp. 526-528, June 2000.

[3.38] J. B. Yi, X. P. Li, J. Ding, J.H.Yin, S. Thongmee, H. L. Seet, “Microstructure evolution of $Ni_{80}Fe_{20}$–Cu deposited by electroplating under an applied field,” IEEE Transactions on Magnetics, vol. 43, no. 6, pp. 2980-2982, June 2007.

[3.39] W. P. Taylor, M. Schneider, H. Baltes, M. G. Allen, “Electroplated soft magnetic materials for microsensors and microactuators,” TRANSDUCERS '97 International Conference on Solid State Sensors and Actuators, Chicago, USA, pp. 1445-1448, 16-19 June 1997.

CHAPTER IV

ROD TYPE ORTHOGONAL FLUXGATE: THE MACRO SCALE SENSOR

In this chapter, the first approach for the miniaturization of the orthogonal fluxgate structure is presented. The operation principle and the idea of effective use of the demagnetization factor in order to change the linear operation range of the sensor is validated [4.1]. Section 4.1 shows the conventional Aldredge type orthogonal structure from which the new structure is inspired and how it is modified. Section 4.2 is on the fabrication of the sensor. Section 4.3 presents the basic test results of the fabricated sensor. Section 4.4 discusses the effect of demagnetization factor on the sensor linear operation range and other performance parameters. Section 4.5 summarizes and concludes the chapter.

4.1 Orthogonal Fluxgate Sensor Structure

Figure 4.1 shows a conventional orthogonal fluxgate sensor structure. This structure utilizes a toroidal cylinder shaped ferromagnetic material as the core element. The excitation coil is wound inside and outside the ferromagnetic core. With this configuration, an AC current passing through the excitation coil provides a circular excitation field, H_{exc}, which periodically saturates the ferromagnetic core. The resulting periodic flux change is detected by a sensing coil which is wound around the core. The 2nd harmonic of the induced voltage changes according to the external DC or low frequency magnetic field, H_{ext}.

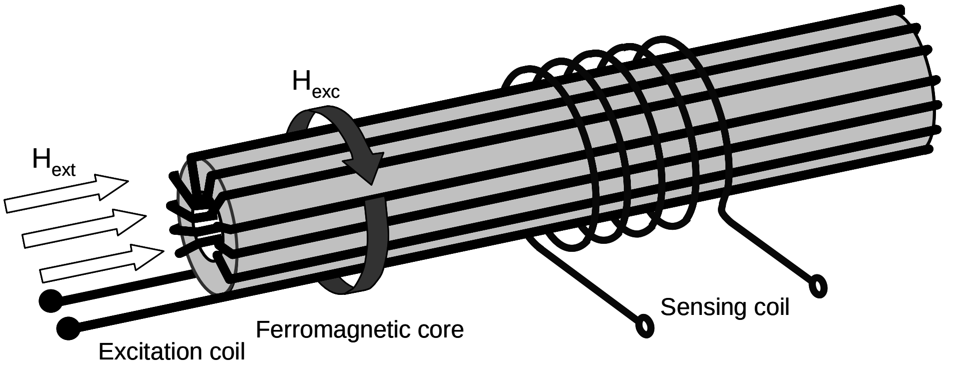

Figure 4.1: A conventional orthogonal fluxgate structure.

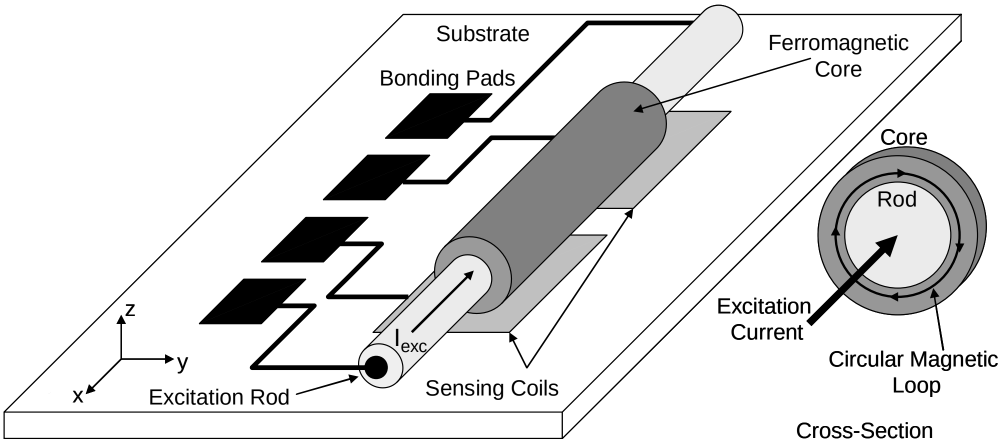

Figure 4.2: The sensor structure.

Although the configuration in Figure 4.1 is used for conventional large scale orthogonal fluxgate sensors, it is not possible to directly scale down the structure to have a small sized sensor. This is especially due to the toroidally wound excitation coil and the sensing coil. However, it is possible to have a similar structure, which is more suitable for scaling down.

Figure 4.2 shows the modified structure of the orthogonal fluxgate sensor. The excitation coil is replaced by an excitation rod, creating a similar circular excitation field. The use of planar sensing coils instead of a solenoid structure further simplifies the fabrication procedure.

The simulation result showing the circular magnetic field on two YZ cross-sections at different places of the ferromagnetic core which is created by the current passing through the excitation rod is presented in Figure 4.3. It is seen that the inner side of the core is very close to saturation, whereas the outer side is still not saturated. By increasing the current, fully saturated core is obtained.

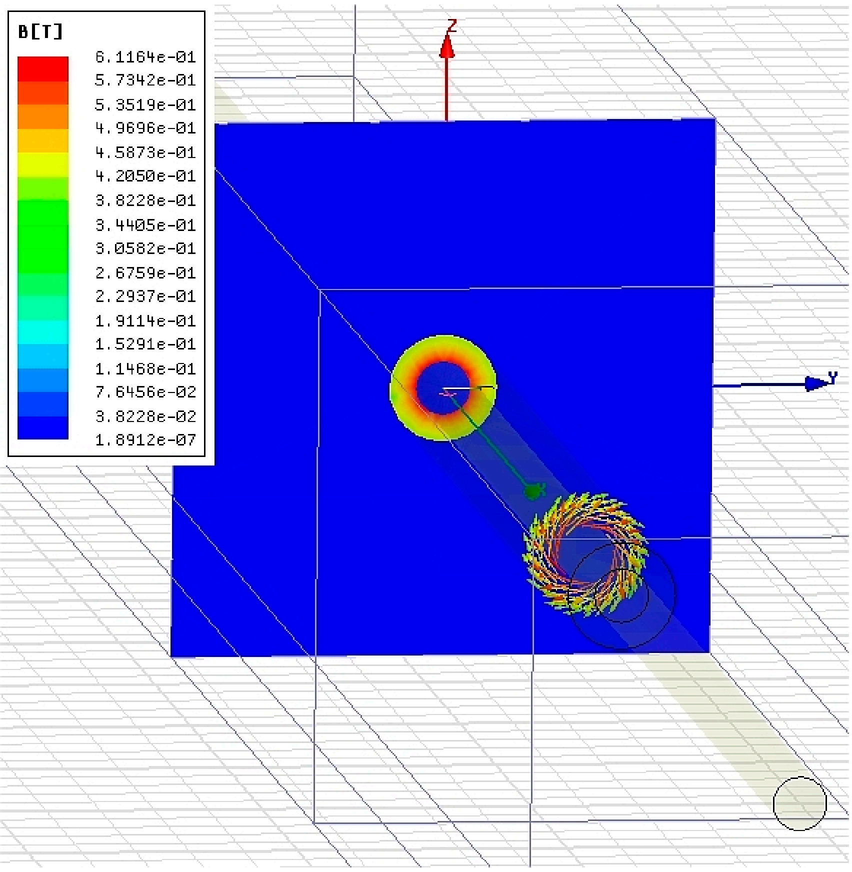

Figure 4.3: Magnetic field created by the current passing through the excitation rod.

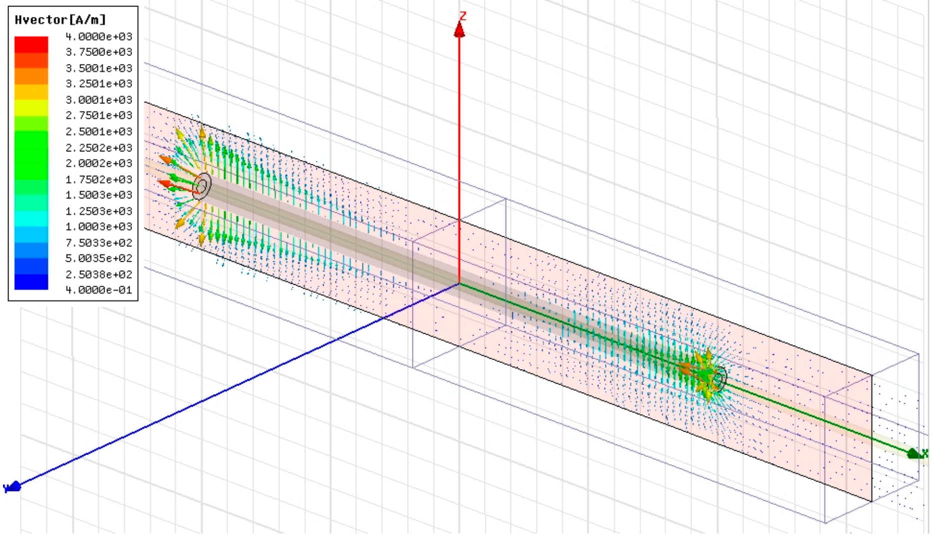

Figure 4.4: Magnetic flux around the ferromagnetic core with an applied magnetic field in X-direction.

Figure 4.4 shows the distribution of the magnetic field lines around the core when an external field in X-direction is applied to the system. Due to the high permeability of the core, the magnetic flux is concentrated inside the core. However, when the permeability of the core is reduced, i.e, when it is saturated, the magnetic flux is not concentrated in the core any more. This flux change is conventionally detected by the solenoidal coil. But, the replacement of the solenoidal sensing coil with the planar sensing coils placed under the edges of the ferromagnetic core is also possible as it seen in Figure 4.4.

4.2 Fabrication

The sensor consists of planar sensing coils, a gold bonding wire serving as the excitation rod, and a FeNi layer electroplated over the bonding wire. Figure 4.5 shows the fabrication steps of the sensor prototype. The fabrication starts with forming the sensing coils on a Pyrex substrate by sputtering, photolithography, and patterning (a). Then, a gold wire which is passing over two sensing coils and having 20 µm diameter is bonded to the substrate (b). After this step, the two edges of the gold wire are covered with an epoxy (c). The epoxy is used as a mask to determine the length and placement of the electroplated FeNi layer on the gold wire. A standard FeNi bath is used for the electroplating process [4.2] (d). A 10 µm thick and 4 mm long toroidal FeNi layer is electroplated over the gold wire. Electroplating is done at room temperature using DC current with 14.5 mA/cm^2 current density. Figure 4.6 shows microscope photos of the fabricated sensor prototype.

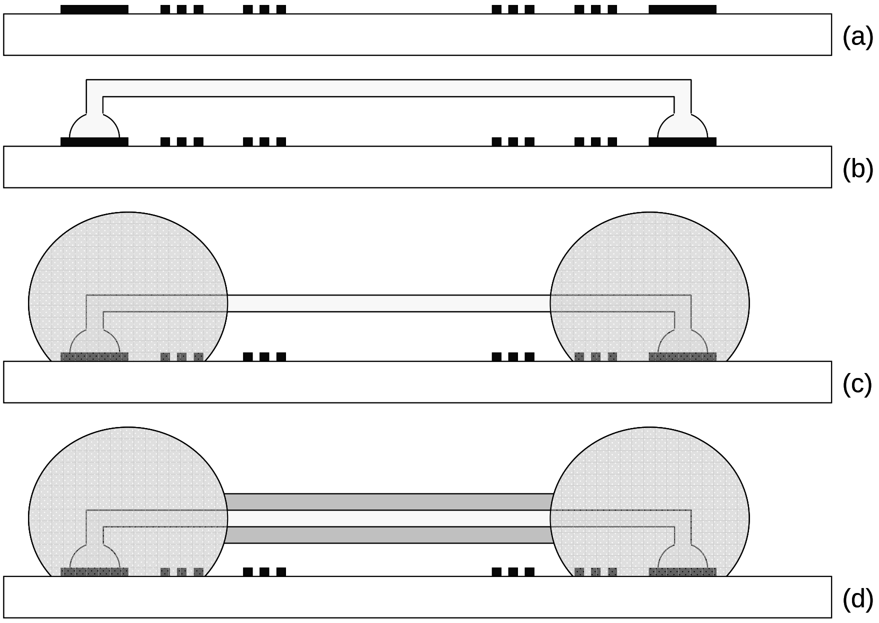

Figure 4.5: Fabrication steps of the macro sensor.

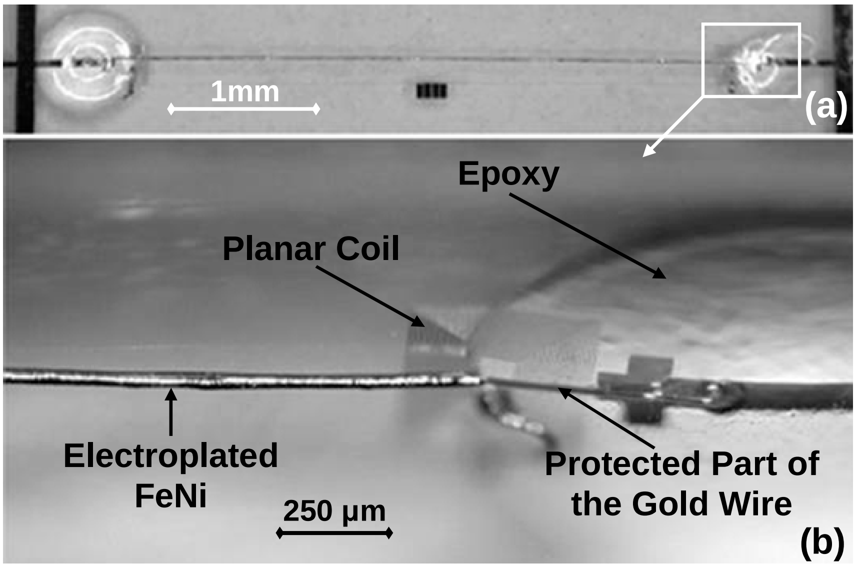

Figure 4.6: (a) The fabricated sensor. (b) Closer view to one edge. The planar coil, the electroplated and protected parts of the gold wire, and the epoxy is seen.

4.3 Sensor Characterization

Figure 4.7 shows the test setup used for characterizing the sensor. The tests of the sensor are done by passing a sinusoidal current through the excitation rod. The frequency of the current is kept constant at 100 kHz, whereas its amplitude is varied. External magnetic field to be measured is produced by a pair of Helmholtz coil. The excitation current leads to an induced voltage across the sensing coils whose 2nd harmonic is proportional to external magnetic field. The 2nd harmonic of the induced voltage is measured with a lock-in amplifier and the linear operation range, sensitivity, and the perming of the sensor are analyzed.

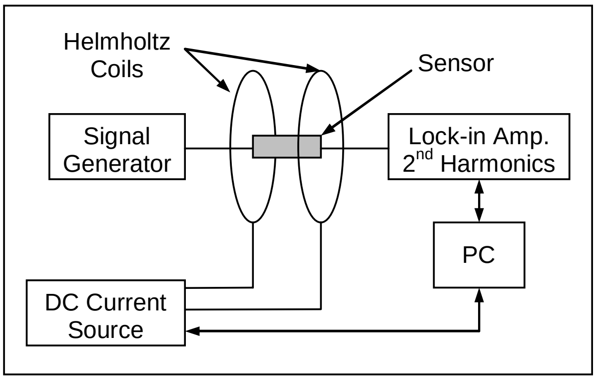

Figure 4.7: The test setup.

Figure 4.8 shows the test results of the sensor with different excitation current peak values within ±2 mT external magnetic field range. The linear operation range is defined as the region in which the waveform fits to a linear function with 1 % nonlinearity. It can be seen from Figure 4.8 that the linear operation range is independent of the excitation current.

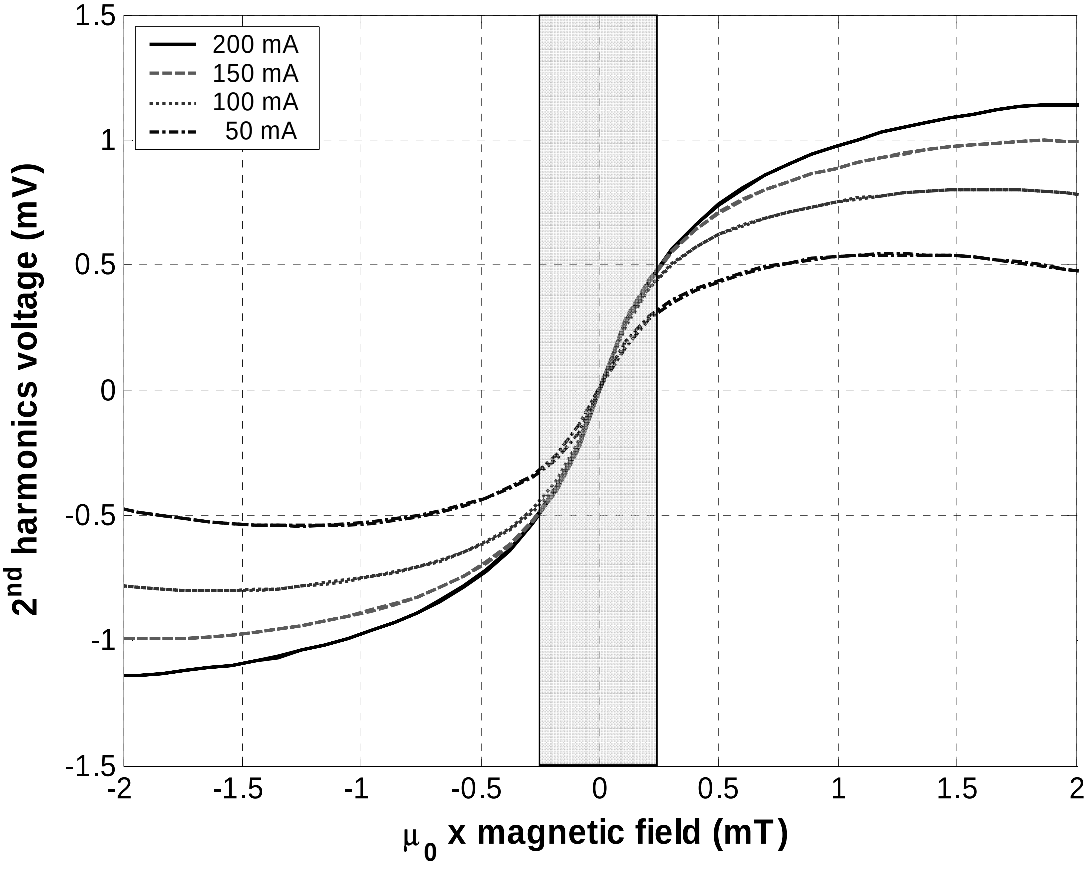

Figure 4.8: The sensor response within ±2 mT range for different levels of the sinusoidal excitation current at 100 kHz. The linear operation range (shaded region) is independent of the excitation current.

The slopes of the linear lines give the sensitivity of the sensor over this linear operation range. Figure 4.9 shows the variation of the sensitivity with the excitation current. The sensitivity of the sensor increases with the excitation current and tends to saturate after 100 mA-peak excitation current.

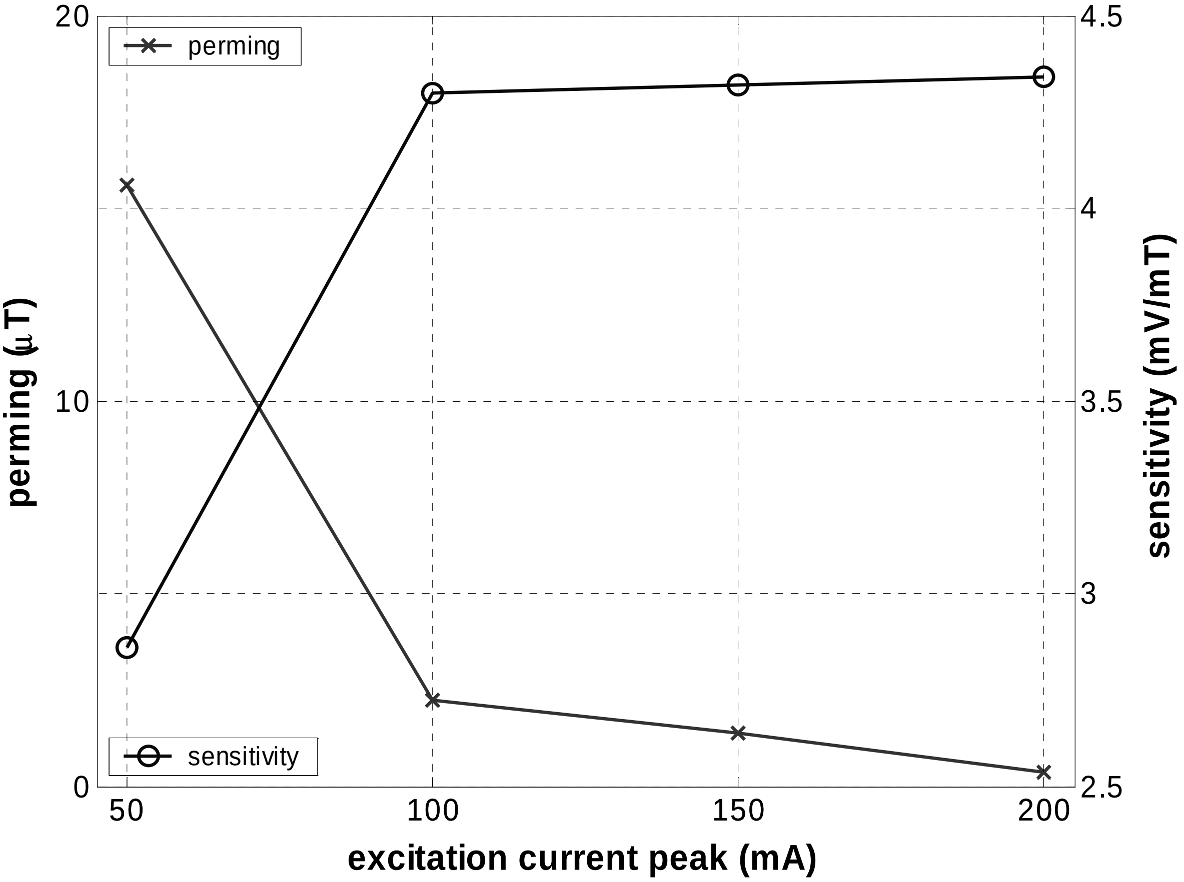

Figure 4.9: The variation of the sensitivity and the perming of the sensor with the magnitude of the excitation current.

Figure 4.9 shows also the variation of the perming value of the sensor with the excitation current. In order to measure the effect of perming, an external field of about 50 mT is applied to the sensor, and then the field is reduced to ambient. Then the stabilized value seen on the lock-in amplifier is recorded. The same procedure is repeated with a field in the opposite direction. The difference between the two measured values gives the perming voltage. This voltage is then converted into the equivalent input magnetic field by dividing the value by the sensitivity at the ambient field value. It is seen from Figure 4.9 that the perming decreases with the excitation current due to the better saturation of the core.

The measurements show that, with 200 mA-peak excitation current at the frequency of 100 kHz, the sensor shows a linear response in the range of ±250 μT with a perming below 400 nT and a sensitivity of 4.3 mV/mT.

4.4 Effect of Demagnetization

The effect of demagnetization on the sensitivity, linear operation range, and perming were also investigated. It is decided to perform the measurements on the same sample with only one sensing coil by reducing the core length by ½ after performing all tests. Figure 4.10 summarises the followed procedure: In order to achieve different core lengths, half of the ferromagnetic core is protected by photoresist and the other half is etched by an H_2SO_4 based solution. The tests are then performed on the new structure having smaller core length. With this method, structures with 2 mm, 1 mm, and 0.5 mm lengths are obtained and tested. For these tests, the induced voltage is recorded by using one sensing coil under the core.

The advantage of this method over fabricating sensors with different lengths is that the sensor response is only dependent on the change in the length of the ferromagnetic core, but not on the variations on the electroplating thickness and the core distance from substrate. These two would not be well controlled if the tests were performed with different samples.

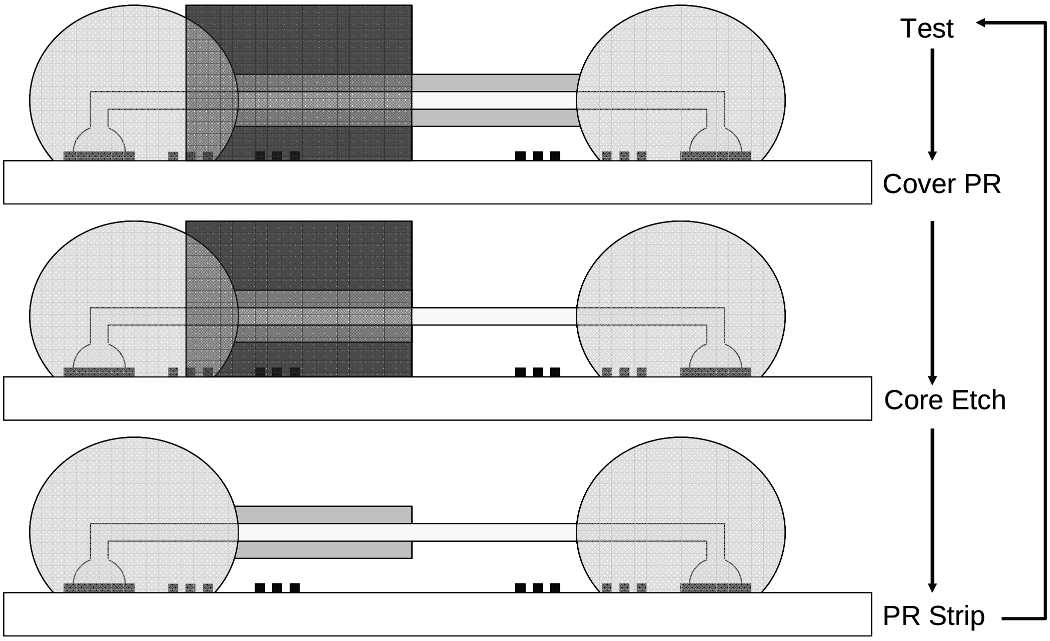

Figure 4.10: The followed procedure for testing the effect of demagnetization.

4.4.1 Linear Operation Range

Figure 4.11 gives the responses of the sensors having different core lengths with a 200 mA-peak excitation current. It should be noted that for better comparison, the voltage values for the 4mm-long sensor are divided by 2. The measurements verify the increase in the linear operation range and the decrease in the sensitivity of the sensor with decreasing core length. These are both due to the increasing demagnetization factor of the sensor core as its length decreases. The linear operation range of the sensor is increased by a factor of 10, to 2.5 mT by decreasing the core length form 4 mm to 0.5 mm.

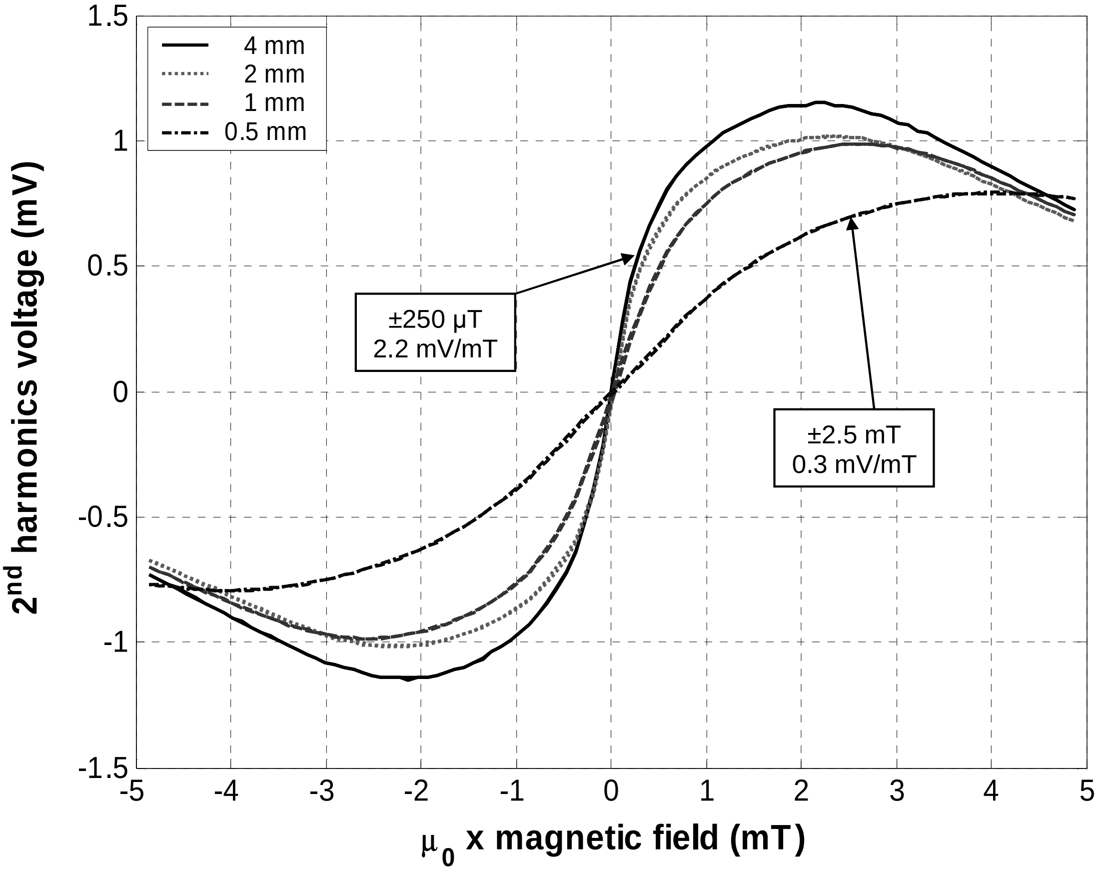

Figure 4.11: The response of the sensors with different core lengths at 200 mA-peak current. The change in the linear operation range and the sensitivity with length is seen.

Figure 4.12 provides another view of the change of the linear operation range with the sensor length. As well as the data for four different lengths, the variation of the inverse of the apparent permeability, μ_{app}, which is calculated for a μ_i of 1000 with, by assuming that the core has an ellipsoidal shape [4.3], is presented. The linear operation range follows the $1/\mu_{app}$ curve as expected. Furthermore, Figure 4.12 shows that the linear operation range stays almost unchanged for the same sensor length for different excitation values, which is previously depicted in Figure 4.8.

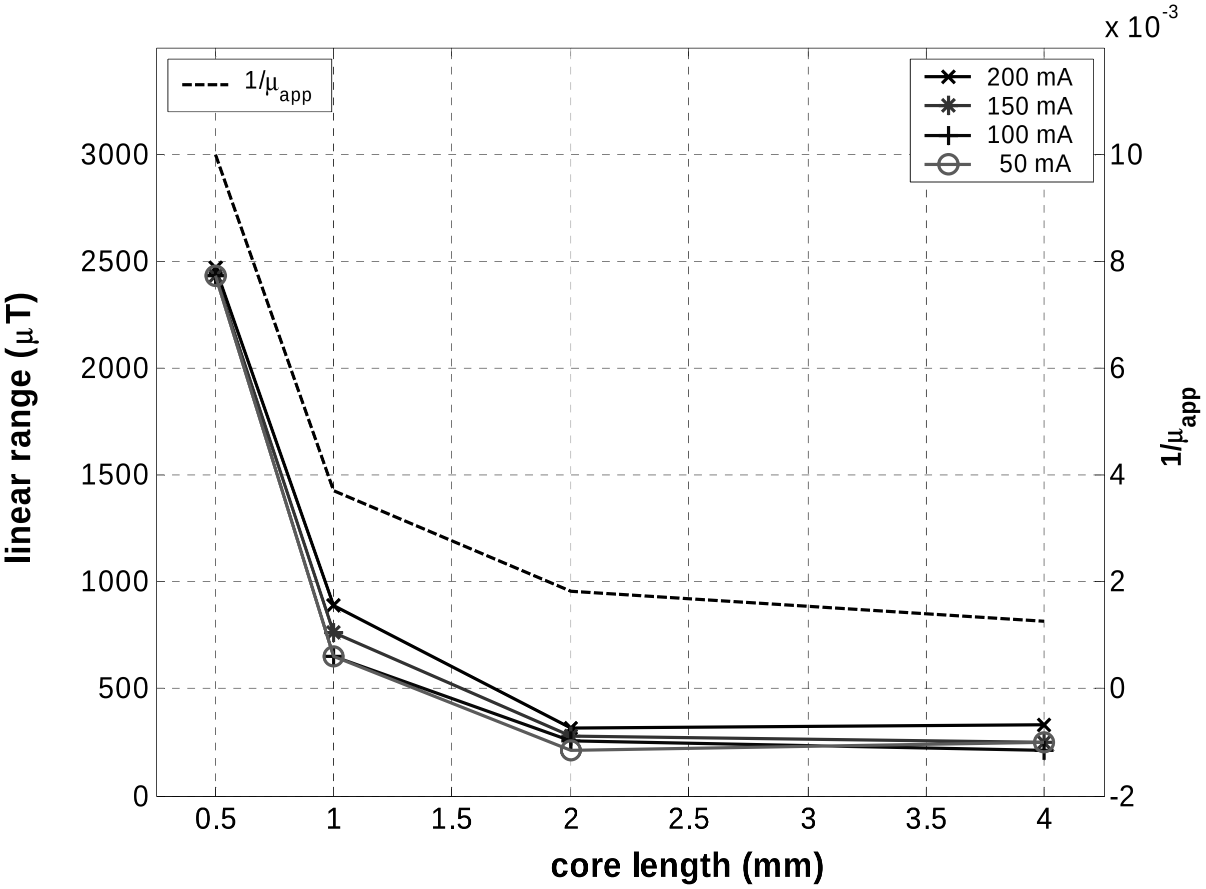

Figure 4.12: The change of the linear operation range with the sensor length for different excitation current values and the comparison with the $1/\mu_{app}$ values.

4.4.2 Sensitivity

Figure 4.13 shows the variation of the sensitivity with the core length, and its comparison with the variation of the apparent permeability μ_{app}. The sensitivity tends to saturate for longer core lengths due to the fact that the demagnetization factor for longer cores is close to zero and does not have such a big effect when compared to the smaller lengths. This is also in good agreement with the very small change in the linear operation range between 2 mm and 4 mm cores which is seen in Figure 4.12.

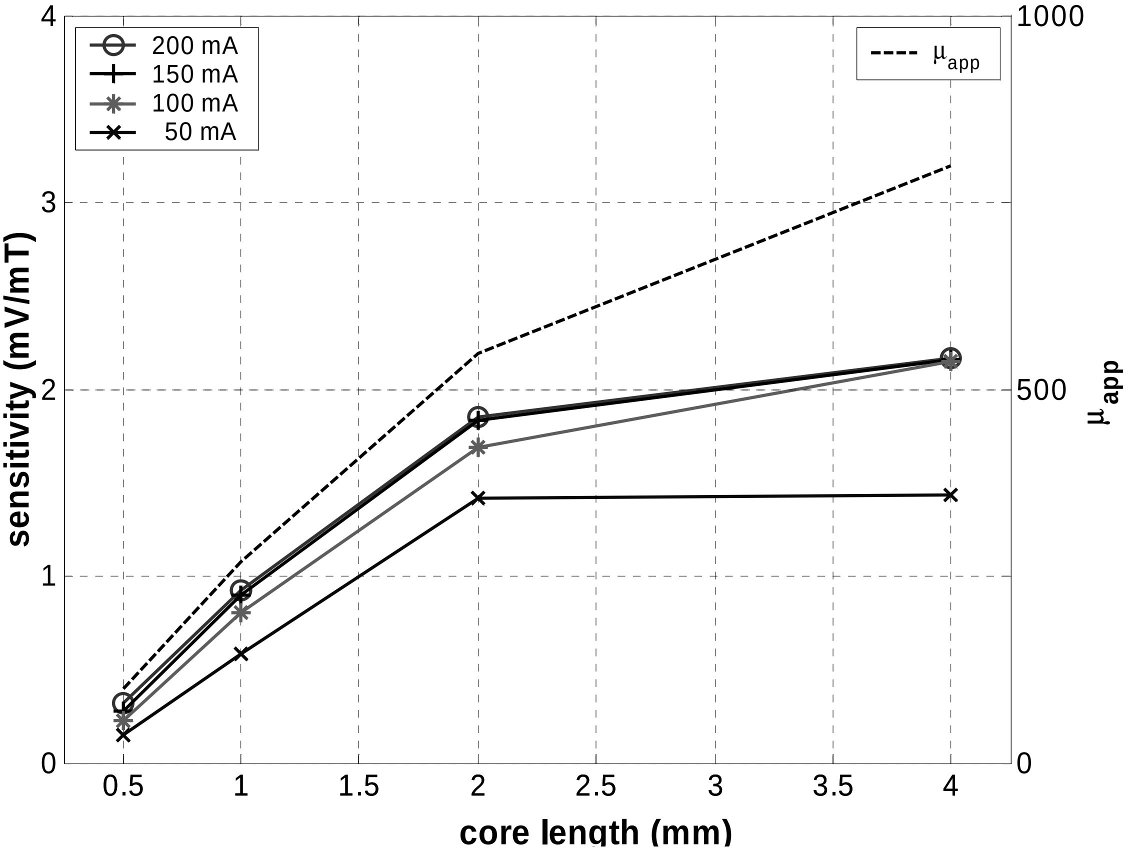

Figure 4.13: The variation of the sensitivity with the core length, and its comparison with the variation of the apparent permeability, μ_{app}.

4.4.3 Perming

Figure 4.14 shows the variation of perming with the excitation current for a given core length. For higher excitation currents, the sensor is saturated more strongly in the orthogonal direction. This results in the better alignment of the magnetic domains inside the core which gives rise to a smaller perming value. On the other hand, the magnetic properties in the radial direction are independent of the core length, which gives the same remanent magnetization for different core lengths with the same excitation current. However, the sensitivity of the sensor is smaller, and this gives rise to a larger perming value.

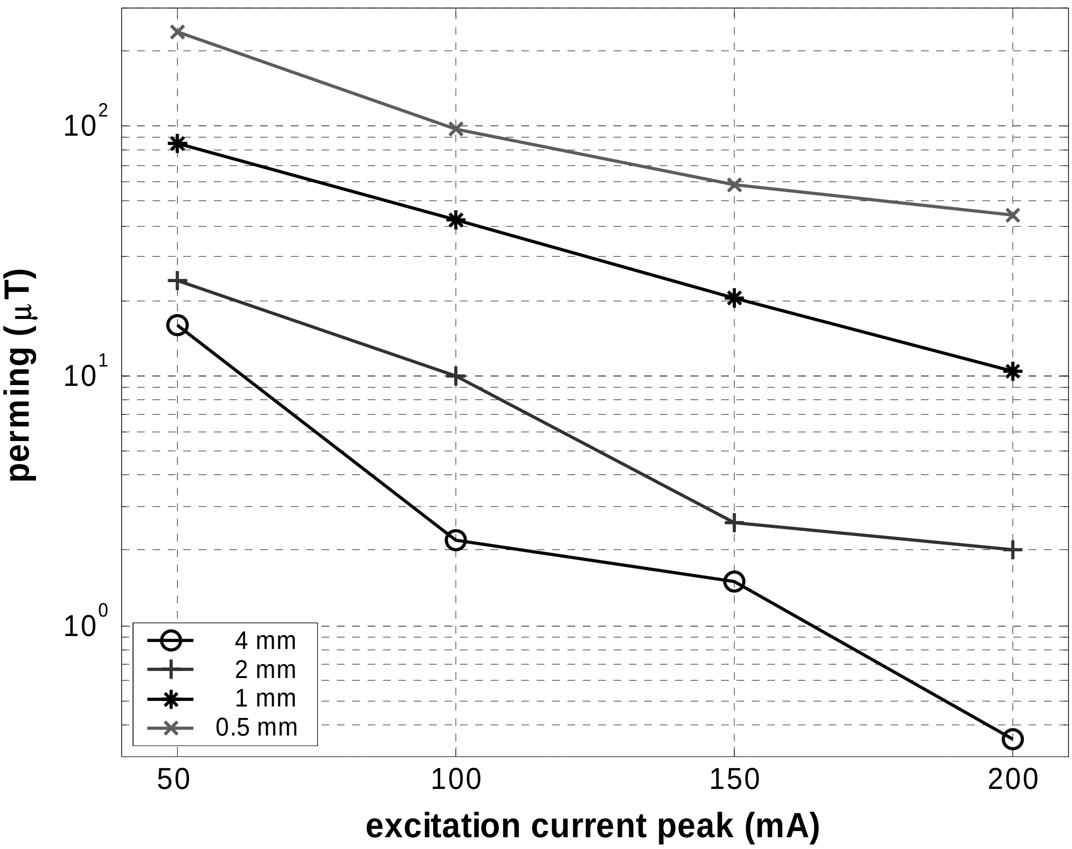

Figure 4.14: The variation of perming with the excitation current for a given core length.

4.5 Conclusion

In this chapter, the first approach for miniaturizing the orthogonal fluxgate sensor is presented, and the feasibility of the idea is verified by the fabricated sensor prototype. The fabricated sensor consists of planar sensing coils, a gold bonding wire serving as the excitation rod, and an electroplated FeNi core layer around the excitation rod. The sensor with a 4 mm long core has a linear operation range of ±250 μT, a sensitivity of 4.3 mV/mT, a and perming below 400 nT for 200 mA-peak sinusoidal excitation current at 100 kHz. The effect of demagnetization on the linear operation range, sensitivity, and perming of sensor is also demonstrated by shortening the length of the ferromagnetic core with chemical etching. When the core length is reduced to 0.5 mm, the linear operation range widens to ±2.5 mT, while the sensitivity decreases to 0.3 mV/mT for a single sensing coil.

On the other hand, the presented sensor is not completely suitable for fabrication with standard microfabrication technologies due to the wire bonded excitation rod.

Another fabrication method should be developed which enables the integration of the sensor into standard CMOS processes. Next chapter explains the scaled down version of the sensor, with a modified core, which can fabricated by standard photolithography and thin film deposition technologies.

4.6 References

[4.1] O. Zorlu, P. Kejik, F. Vincent, R. S. Popovic, “A novel planar magnetic sensor based on orthogonal fluxgate principle”, IEEE PRIME’05 Conference. Lausanne, Switzerland, July 2005.

[4.2] J.M. Quemper, et. al, “Permalloy electroplating through photoresist molds,” Sensors & Actuators A74, pp. 1-4, 1999.

[4.3] J. A. Osborn, “Demagnetizing Factors for the General Ellipsoid,” Physical Review, Vol. 67, No. 11-12, June 1-15, pp. 351-357, 1945.

CHAPTER V

ROD TYPE ORTHOGONAL FLUXGATE: THE MICRO SCALE SENSOR

In this chapter, the orthogonal fluxgate microsensor is presented. Section 5.1 explains the structure of the sensor. Section 5.2 is on the design issues concerning the core and the sensing coils of the sensor. Section 5.3 presents the fabrication process flow developed for the sensors, and gives some intermediate results obtained during the fabrication process. Section 5.4 presents the detailed characterization and the test results of the fabricated sensors. Section 5.5 summarizes the chapter.

5.1 The Orthogonal Micro Fluxgate Structure

In Chapter IV, the method used to miniaturize the sensor was introduced. This method enables the fabrication of small sized sensors; however, it is still not completely suitable for using the standard microfabrication techniques and wafer level production. This is due to the wire-bonded excitation rod, which has to be fabricated one by one. The core structure of the sensors should be further modified so that it can be fabricated with standard photolithography and metallization techniques. Figure 5.1 shows the proposed core structure of the micro scale sensor with the sensing coils, suitable for wafer level fabrication. If the structure is compared with the one presented in Figure 4.2 in Chapter IV, it is seen that the cylindrical core structure placed above the sensing coils are replaced with a prism core structure standing on the substrate.

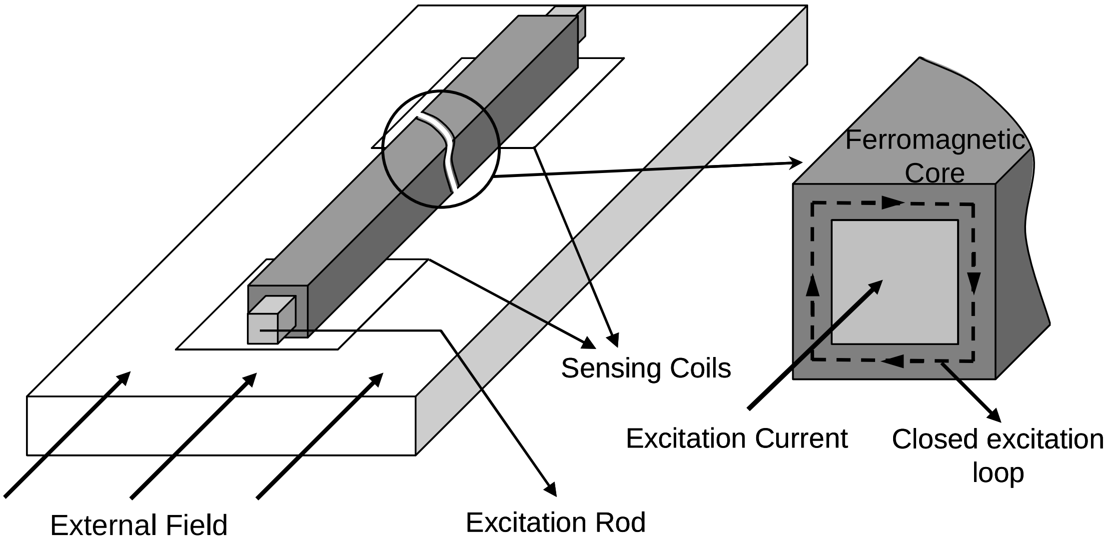

Figure 5.1: The structure of the micro scale sensor including the core and the sensing coils.

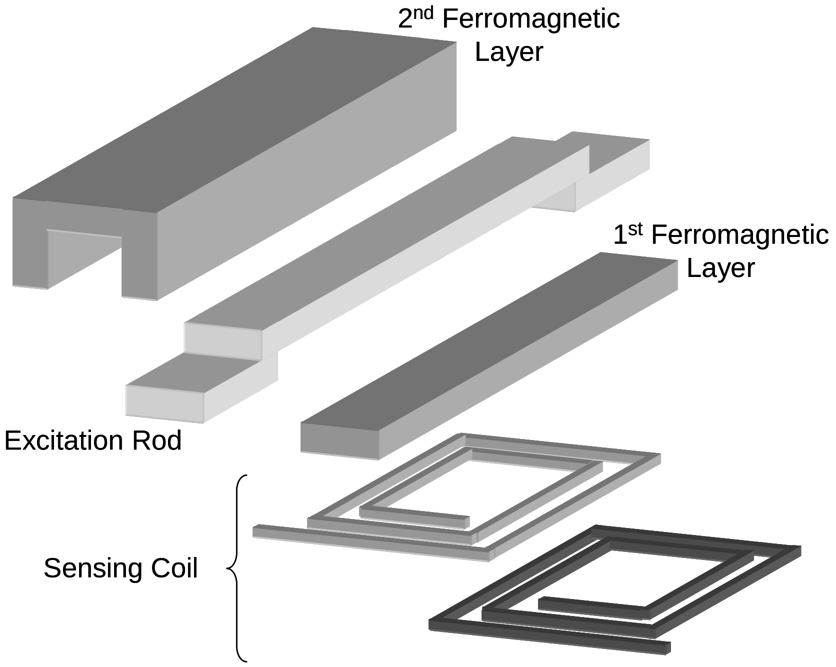

Figure 5.2: The conceptual fabrication process flow for the proposed structure.

Figure 5.2 shows the conceptual fabrication process flow with which this structure can be fabricated. In this process the sensing coils are realized with two metal layers. Above the sensing coils, the core is fabricated in three steps. In the first step, the bottom part of the ferromagnetic layer is electroplated. Then, the excitation rod is fabricated by electroplating a non-magnetic conductor layer over the first layer. The upper part of the ferromagnetic layer is electroplated around the first two layers. In this way, the excitation rod is sandwiched between two ferromagnetic layers, and the closed magnetization path for excitation is realized inside the ferromagnetic core.

5.2 Design of the Sensor

In this section, the strategy followed during the design of the sensors will be introduced. Figure 5.3 shows the cross-section and top view sketch of the sensor structure including the core and one of the sensing coils with the labeled geometrical design parameters. Table 5.1 lists these labels with their explanations. The relation between these parameters and the performance criterions of the sensor such as sensitivity, power dissipation, linear operation range, fabrication simplicity etc., are analyzed. Both analytical methods and finite element analysis (FEM) tools (Ansoft Maxwell 3D v.2.9-2.11) are used during the design process. The most suitable geometry for the core and the sensing coils is found according to the simulations. However, sensors with many different dimensions are designed and fabricated in order to be more immune to possible variations in the process parameters during the fabrication phase.

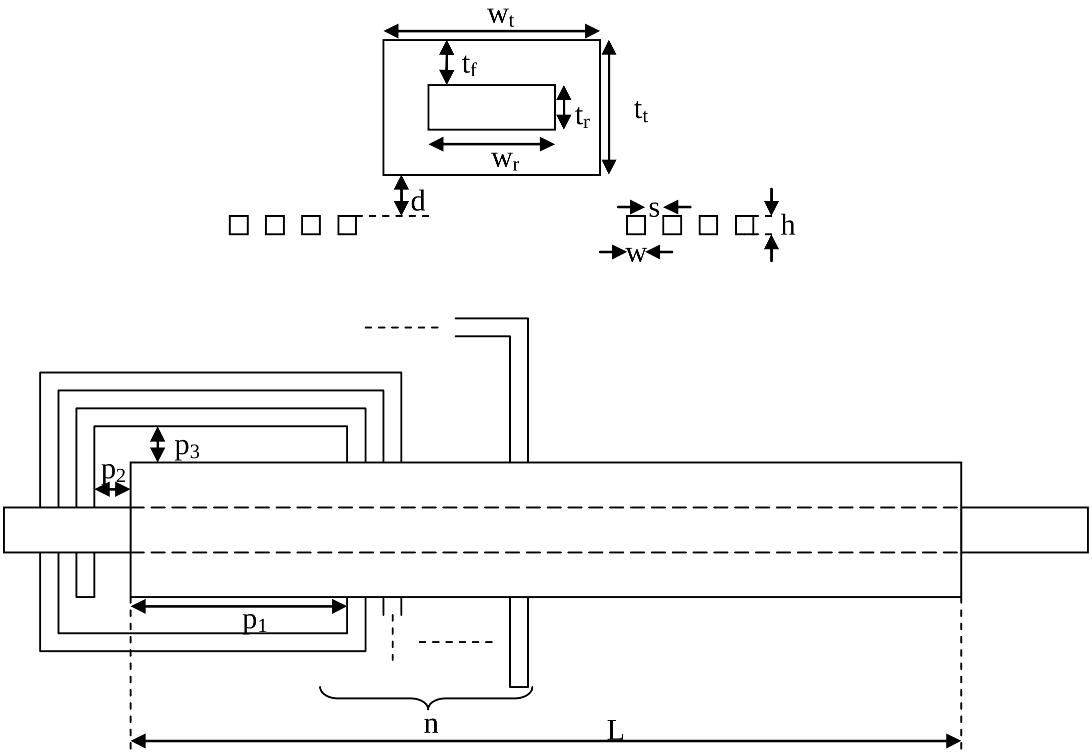

Figure 5.3: The cross-section and top view sketch of the sensor including the core and one of the sensing coils with labeled geometrical design parameters.

Table 5.1: Design parameter labels and their explanations.

Label	Explanation
w_t	Total width of the core
t_t	Total thickness of the core
t_f	Thickness of the ferromagnetic layer
w_r	Width of the excitation rod
t_r	Thickness of the excitation rod
L	Length of the ferromagnetic part of the core
d	Distance between the core and the sensing coil
w	Width of the sensing coil turns
s	Spacing between the sensing coil turns
h	Height of the sensing coil turns
n	The total number of turns of the sensing coil
p_1	Position of the fist sensing coil turn w.r.t. the core edge, under the core
p_2	Extension of the fist sensing coil turn after the core edge
p_3	Extension of the fist sensing coil turn from the sides of the core

5.2.1 The Design of the Sensor Core

As it is previously presented in Section 2.2, the apparent magnetic properties of the ferromagnetic materials are affected by the dimensions of the core according to its demagnetization effect, as well as its intrinsic magnetic properties. For an orthogonal fluxgate sensor, with given magnetic properties of the core material, and given sensing elements, the excitation field required to saturate the core depends on the cross-sectional geometry of the core. Besides, the linear operation range is dependant on the aspect ratio, λ of the core, and the sensitivity is affected again by λ as well as the scale of the ferromagnetic material. In this sense, if the core cross-section is fixed according to the excitation requirements, the linear operation range and the sensitivity of the sensor is determined by the length of the core.

5.2.1.1 FEM Modeling and Methodology

Figure 5.4 shows a typical setup used during the 3D FEM simulations. The core is placed in the Cartesian coordinate system with its long edge along the x-axis. The boundaries of the solution space are defined with a prism (called background) whose dimensions are 2 to 10 times larger than the core dimensions in each direction. Background material is selected as vacuum, and the externally applied magnetic field in x-direction is assigned to the faces of the background. The solution in Figure 5.4 shows the distribution of the z-component of the B vector over the xy-plane at a certain distance, d, from the bottom of the core. For the analysis, the magnetic flux passing through plane is calculated. This is done by numerically integrating the magnetic field intensity vector over an xy-plane. This can be formulated as:

$$\Phi_{xy}\Big|_{z=c} = \int \vec{B} \bullet dA = \iint_{xy} B_z dxdy \Big|_{z=c} = \int_{x=0}^{xi} \int_{y=0}^{yj} B_z dydx = \sum_{x=0}^{i} \sum_{y=0}^{j} B_z (i, j) \times \Delta x \Delta y \, . \tag{5.1}$$

The output of the actual sensor is proportional to this magnetic flux, so by using Equation 5.1 it is possible to compare the sensitivity and linear operation range of different structures. Here, it is important to note that the integration should be done over the half of the plane with respect to the y-axis, since the integral over the whole plane gives zero according to the anti-symmetric distribution of the B vector.

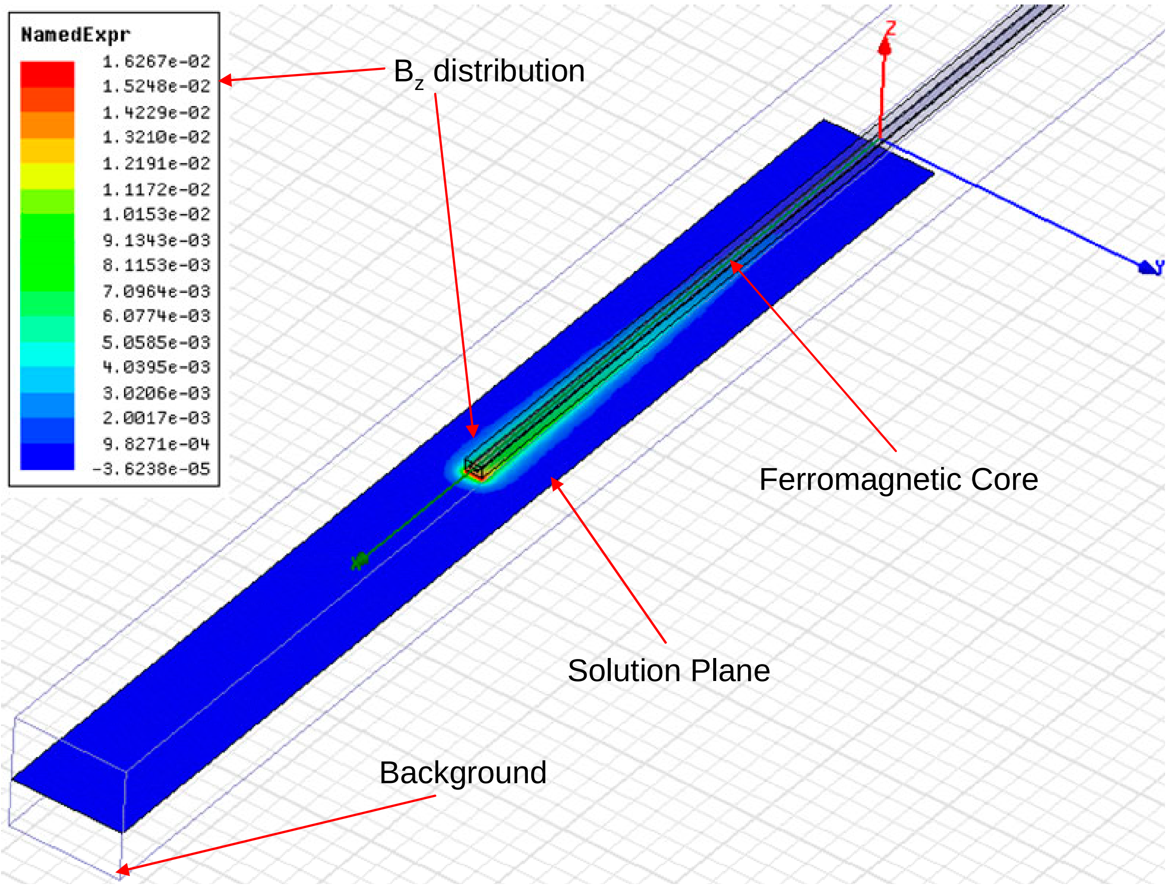

Figure 5.4: Typical setup used for FEM simulations.

5.2.1.2 Assigning the Materials

The core is assigned as a non-linear magnetic material with constant relative permeability of 1000 and 10000 up to its saturation magnetization value, B_{sat}. The B_{sat} value is selected as 0.85 T, which is a typical value for the electroplated FeNi layers. Unfortunately, it is not possible to model the hysteresis in Maxwell 3D, so the coercive field value H_c, cannot be introduced. This does not create any problem for the sensitivity and linear range calculations. However, for the simulations related to the excitation, the important value is the H_k value of the material rather than its permeability, so the magnetic model has to be changed according to this consideration. The resistivity of the core is selected as 20 μΩcm, again a typical value for electroplated FeNi layers. Whenever it is used, the excitation rod is assigned as Copper from the material database of Maxwell 3D, with a resistivity and relative permeability of 1.8 μΩcm and 0.999991, respectively.

5.2.1.3 Square or Rectangular Cross-Section

Most of the research on the demagnetizing factors on prisms covers the case of a prism with a square cross-section. In this sense, a core with a square cross-section may be the first choice. However, from the microfabrication point of view, wider and thinner structures are easier to fabricate. Furthermore, these structures are more repeatable and more robust.

Figure 5.5 shows the distribution of y and z components of the B vector on the xz- and xy-planes, respectively, for a core having 16 x 8 x 500 (μm^3) dimensions and an apparent permeability of 1000 under 400 A/m applied field. Both planes are equally away from the core, and the distributions of the vertical component of the B vector to the corresponding planes are quite similar. The flux resulting from B_z and B_y are 22.3×10^{-12} and 20.9×10^{-12} Wb, respectively, showing that slightly more flux is concentrated under the wider side. So, it is more advantageous to have a wide and thin structure than a narrow and thick one also from the magnetic performance side.

The effect of having a square or rectangular prism is demonstrated by simulating three structures having the same aspect ratio value (λ) of 100. The dimensions of these structures are 10 x 10 x 1000, 12.5 x 8 x 1000, and 20 x 5 x 1000 (μm^3) and the relative permeability is selected as 10000. Figure 5.6 shows the magnetic flux under the core for these three structures versus the applied external field. The distance between the calculation plane and the core is 2 μm. It is seen from the simulation results that the rectangular cross section gives slightly higher sensitivity, whereas the linear range is almost same for all cores. This is also in agreement with the results presented in Chapter II (Figure 2.9 and Figure 2.10). As a conclusion, a rectangular cross-section can be preferred for easier fabrication, without affecting the linear operation range of the sensor.

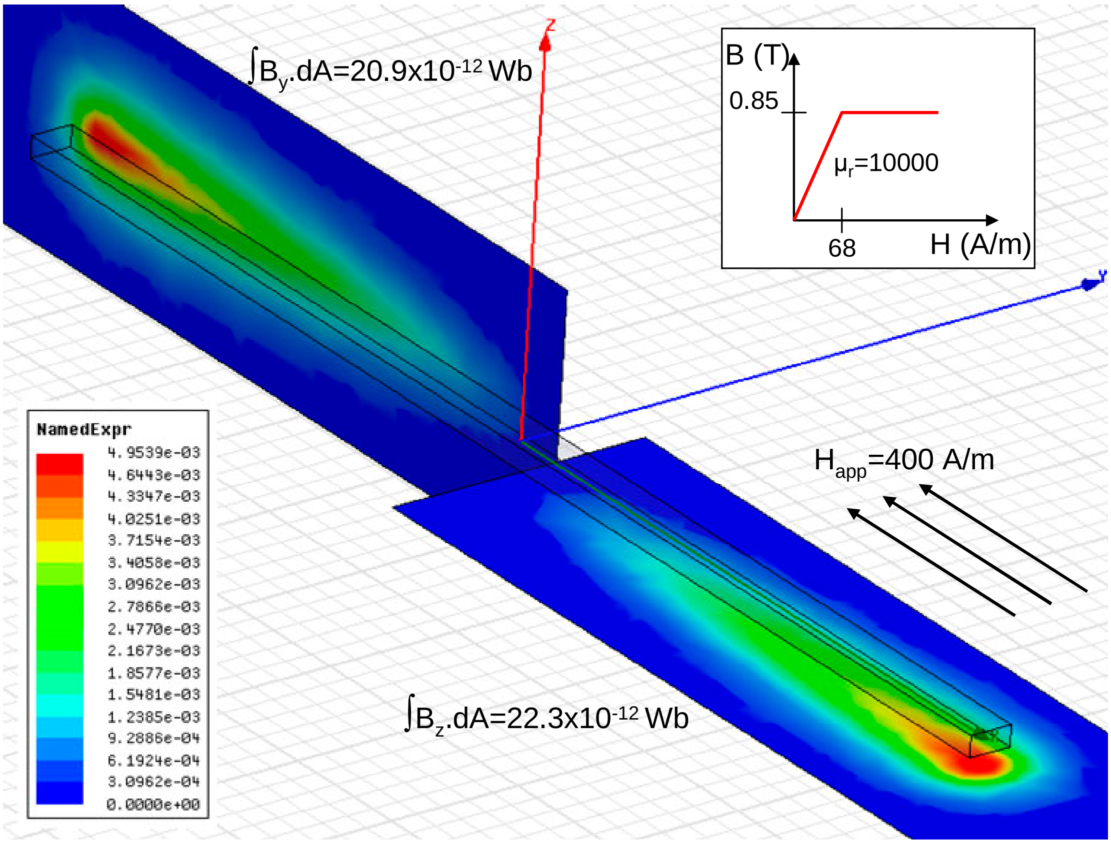

Figure 5.5: The distribution of y and z components of B on the xz and xy planes.

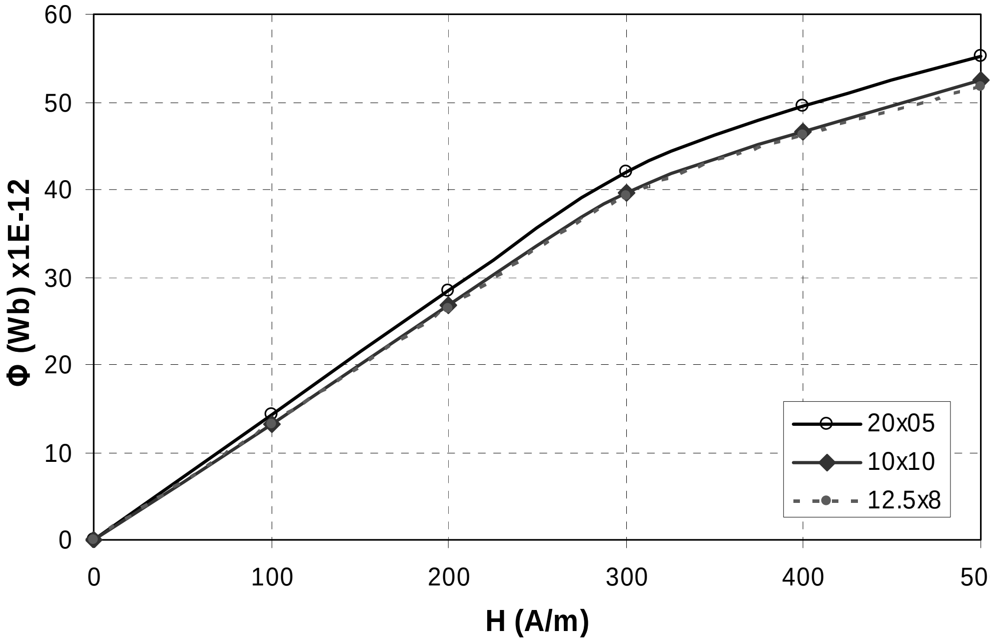

Figure 5.6: The magnetic flux under the core versus the applied external field for cores with 10 μm x 10 μm, 12.5 μm x 8 μm and 20 μm x 5 μm cross-sections.

5.2.1.4 Thickness of the Ferromagnetic Layer

The thickness of the ferromagnetic material affects the required excitation field for the core material and the maximum operation frequency. The linear operation range and sensitivity are also affected for a given length, due to the change in the aspect ratio of the core.

For a given operating frequency, the thickness of the ferromagnetic layer of the core should not exceed the skin depth. For a ferromagnetic material with relative permeability and resistivity of 10000 and 20 µΩcm, respectively, the skin depth is 7 µm at 100 kHz operating frequency (Equation 2.30). So, the thickness of the layer should be less than 7 µm.

Figure 5.7 shows the variation of the flux concentrated under the core with the applied magnetic field for different thicknesses of the ferromagnetic layer. All the simulated cores are 1 mm long, and have a relative permeability of 10000. There is a gap of 2 µm x 8 µm at their cross-section, along the length of the core, representing the excitation rod. The flux is calculated on a plane which is 2 µm below the core. The linear operating range increases with the core thickness due to the increasing demagnetization effect.

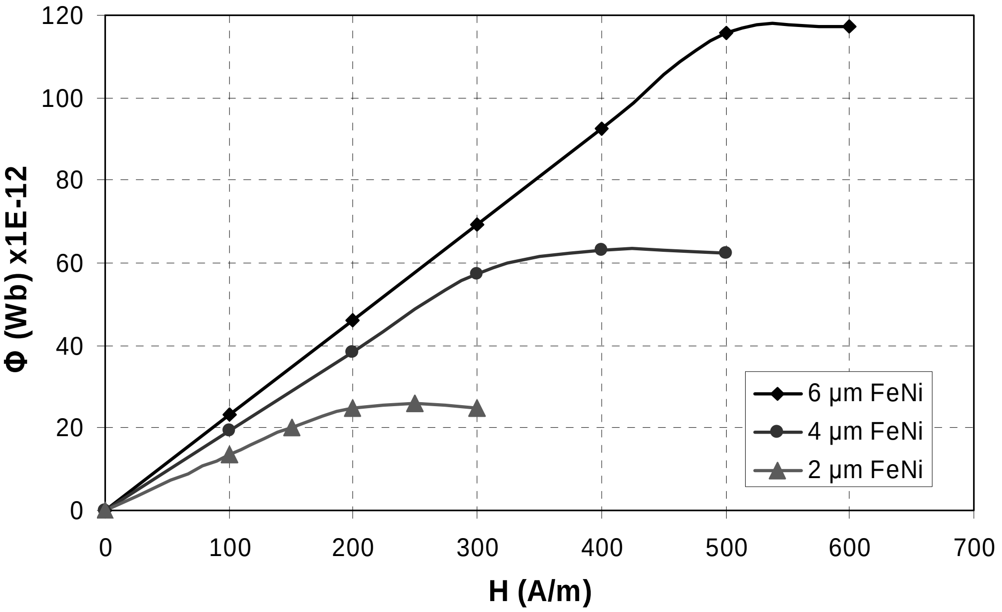

Figure 5.7: The flux collected under the core versus the applied magnetic field for 2, 4, and 6 µm thick the ferromagnetic layer.

The sensitivity of the device decreases accordingly with the decreasing demagnetization factor; however the contrary situation observed in Figure 5.7. This is due to keeping the measurement plane at the same distance to the core for all simulations. For a thicker device, the plane becomes virtually closer to the core, leading to a higher sensitivity value, as observed in Figure 5.7.

From the excitation point pf view, as the core cross-section gets thicker, more current passing through the excitation rod will be required to produce the magnetic field required to saturate the ferromagnetic material. This is due to the increase in the distance between the core center and edge:

$$H = \frac{I}{2\pi r}. \tag{5.2}$$

As an example, according to Equation 5.2, the current required to produce 200 A/m magnetic field 10 µm away from the core center is 12.5 mA, and the required current linearly increases with the thickness of the core.

The effect of the core thickness on the required excitation current is simulated with Maxwell for various core and excitation rod dimensions. It is important to note that, for saturation, the H_k value of the magnetization curve of the material is more effective than its relative permeability. So, these simulations are performed with a magnetization curve having an H_k value of 200 A/m, which corresponds to a relative permeability of 3382. Figure 5.8 shows the distribution of the magnitude of the magnetic flux density, B, over different cross-sections of the sensor ferromagnetic core. The current applied though the 8 µm x 2 µm excitation rod is 10 mA, and the length of the core is 500 µm for each simulation. The thickness of the ferromagnetic material is varied between 2, 4, and 6 µm, resulting in 12 x 6, 16 x 10, and 20 x14 µm^2 core cross-sections, respectively. There are three cut planes for each core placed in the middle of the core (x=0 µm), one edge of the core (x=250 µm), and between the middle and the edge of the core (x=125 µm). The increased area of non-saturated regions for thicker cores is easily realized by examining the plots. Figure 5.9 gives the variation of the arithmetical average of the B value over the core cross-section for different dimensions, which shows the same relations in numeric form. Another information that can be extracted from Figure 5.9 is the similar B_{avg} values obtained over different cut planes of the cores. This shows that the cores are uniformly saturated along their length. Obviously, the saturation can be increased by increasing the excitation current. Figure 5.10 shows the variation the B_{avg} value over the middle cut plane of different cores with different excitation current values. For thinner structures, the B_{sat} value of 0.85 T is reached at 50 mA. However, thicker cores still need more current for saturation.

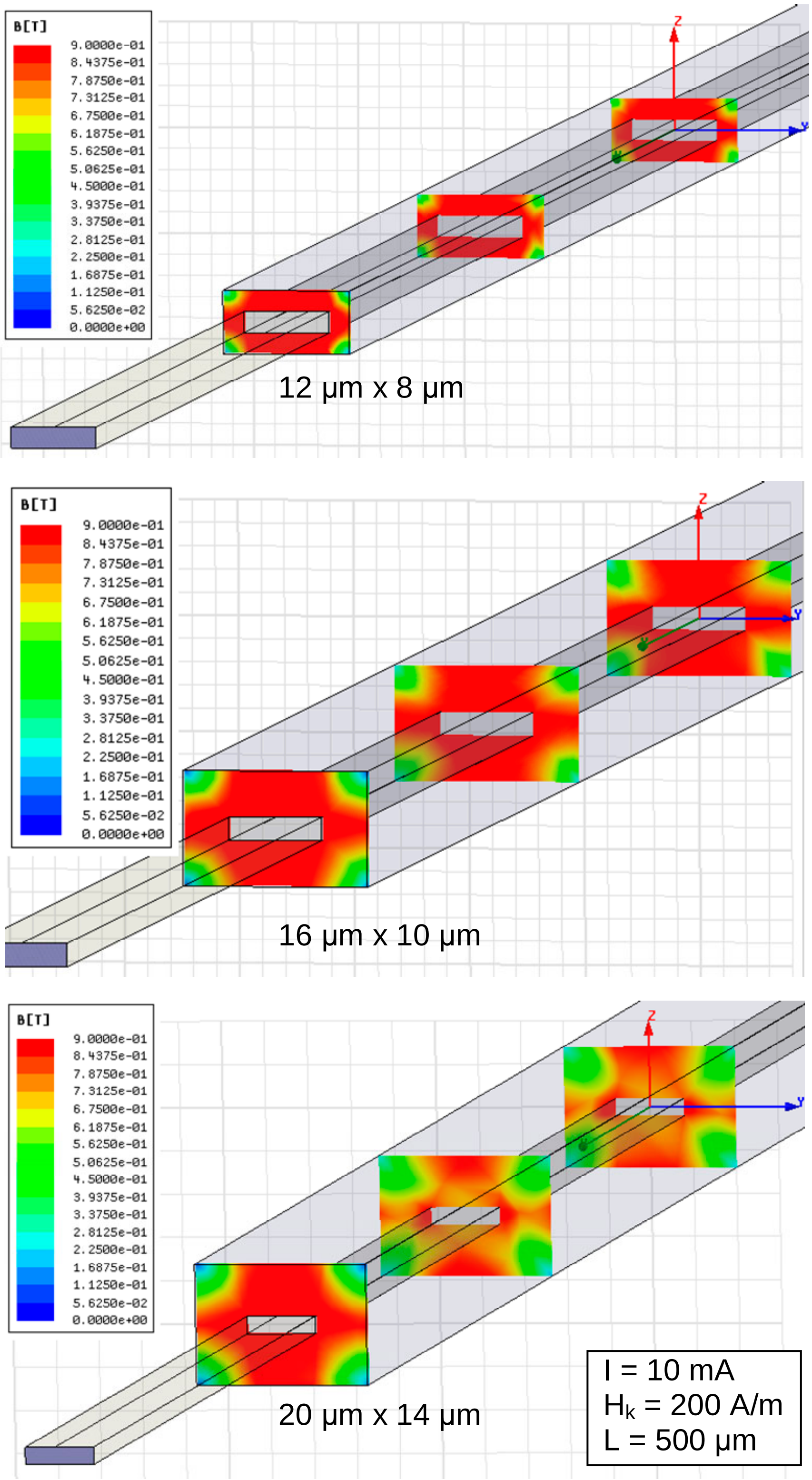

Figure 5.8: The distribution of the magnitude of the magnetic flux density, over different cross-sections of the sensor ferromagnetic core, with 10 mA excitation current.

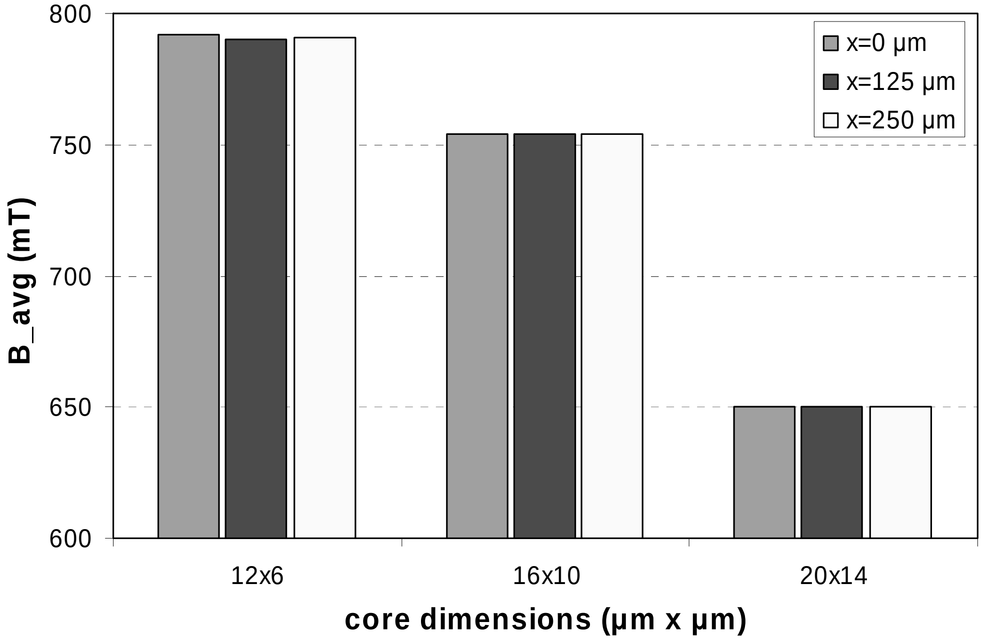

Figure 5.9: The variation of the arithmetical average of the B value over several cut planes for different core dimensions.

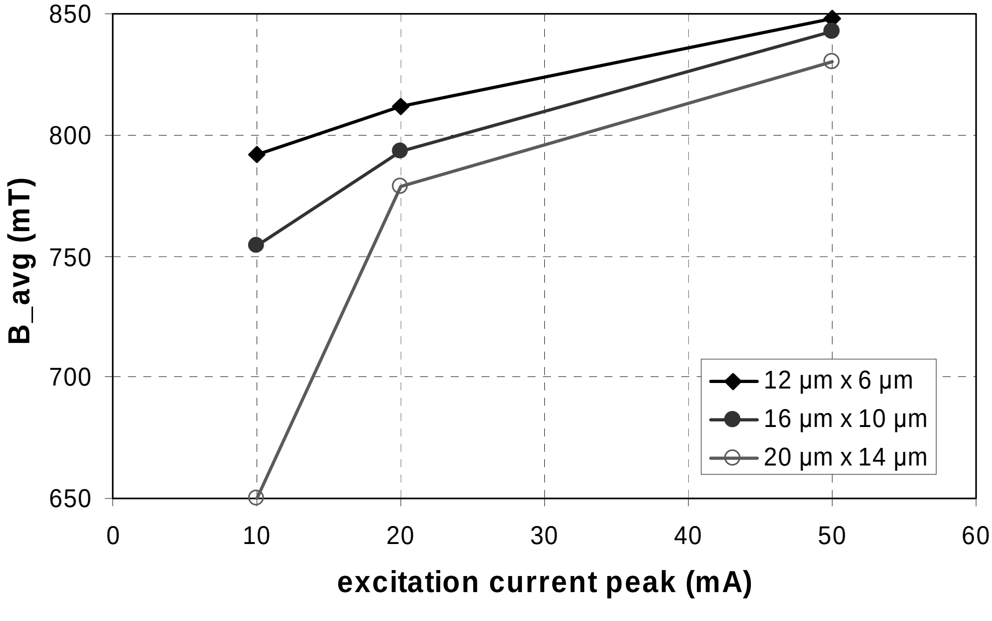

Figure 5.10: The variation the average B value over the middle cut planes of different cores with different excitation current values.

5.2.1.5 The Length of the Ferromagnetic Structure

Once the geometry of the cross-section is determined, the length of the core can be varied according to the required linear operation range and the sensitivity of the sensor. Shorter cores have wider linear operation range and smaller sensitivity due to the demagnetization effect. Figure 5.11 and Figure 5.12 show the change of the flux with the applied magnetic field for cores having different lengths. The intrinsic relative permeability values of the ferromagnetic cores are 1000 and 10000, respectively for the figures. The cores have the same cross-section: 16 µm x 10 µm total area with an 8 µm x 2 µm gap in the middle for the excitation rod. According to the simulations, a linear range of 1400 A/m can be reached with a 0.5 mm long core having an intrinsic relative permeability of 1000, whereas the linear range is around 1200 A/m, if the relative permeability is 10000. The apparent relative permeability is around 500 for both of the structures. Reducing the core length still increases the linear operation range. However the relative permeability and the sensitivity of the cores start to decrease very rapidly for shorter cores ($\mu_r \approx 100$ for 250 µm length). On the other hand, a linear range of 150 A/m with very high sensitivity can be obtained with a 2 mm long core having a relative permeability of 10000.

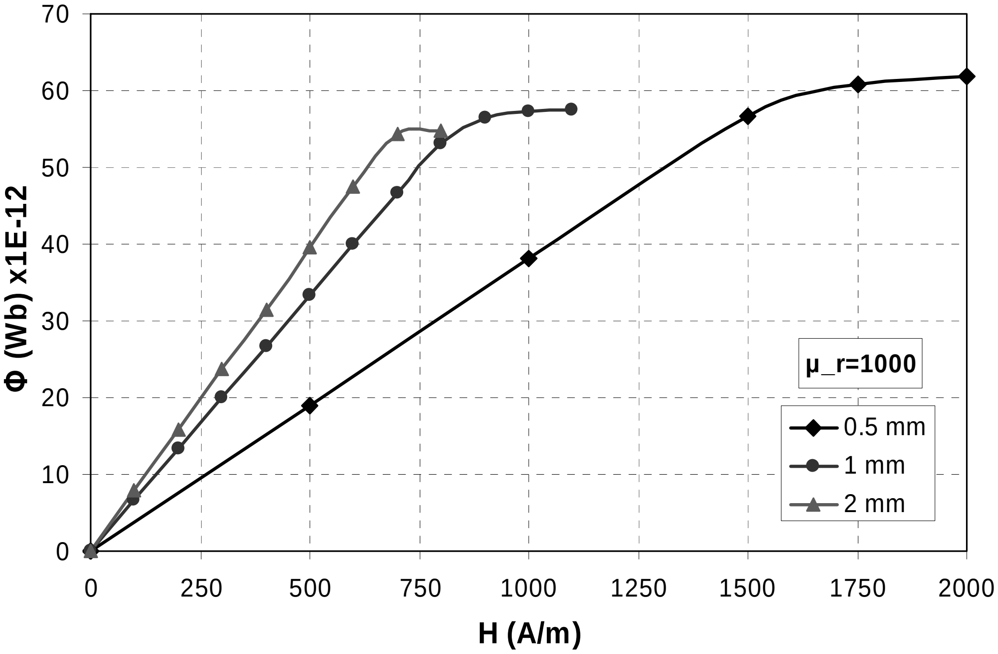

Figure 5.11: The change of the flux with the applied magnetic field for cores having different lengths with an intrinsic relative permeability of 1000.

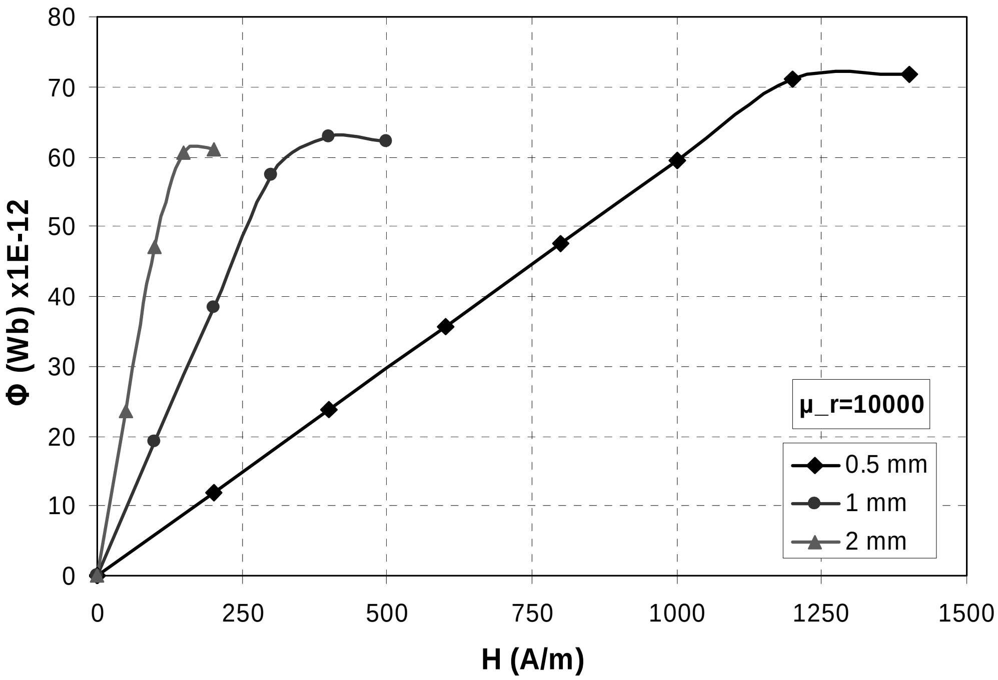

Figure 5.12: The change of the flux with the applied magnetic field for cores having different lengths with an intrinsic relative permeability of 10000.

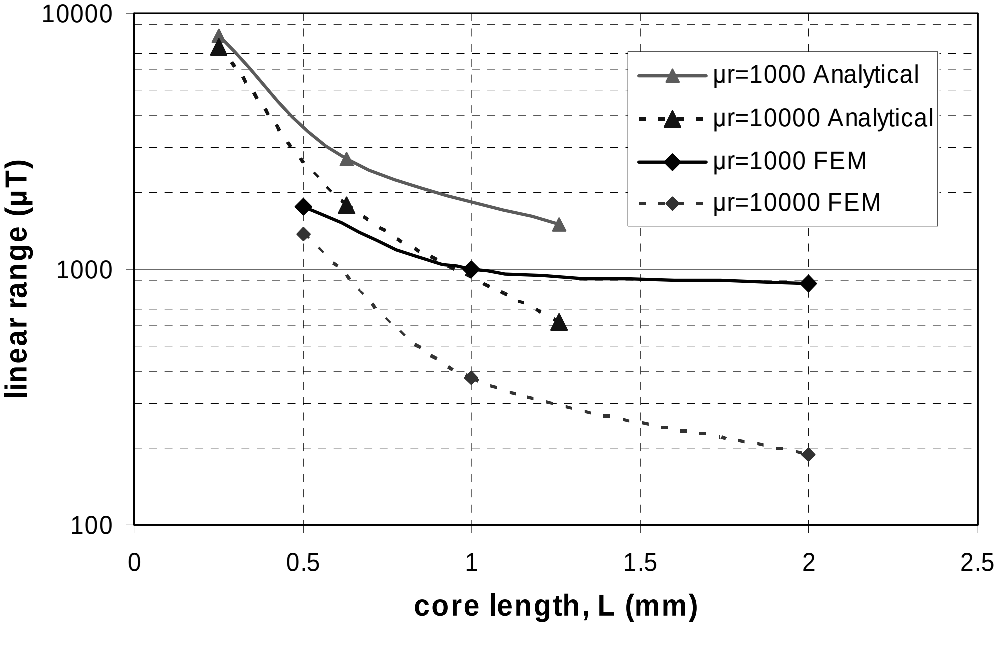

Figure 5.13: The simulation and calculation results for the change of the linear operation range with the core length.

Figure 5.13 gives a summary of linear range versus core length calculations, including the values obtained by using the demagnetization factors calculated for square prisms. The λ-based values for square prisms are converted to core length by taking an equal cross-sectional area with the rectangular cores. Also, the magnetic field values in A/m are converted to the equivalent magnetic flux density in vacuum in µT ($B=\mu_0 H$). For the rest of the text the magnetic field will be expressed in its equivalent flux density in vacuum. It is seen from Figure 5.13 that there is a significant difference between the results obtained from analytical model and FEM simulations. This is expectable since the analytical model is developed for prisms; however the simulated structure contains a gap in the middle for the excitation rod.

5.2.2 The Design of the Sensing Coils

The sensing coils should be placed under the core edges so that they provide the maximum sensitivity with a minimum noise. The design parameters which are given in Figure 5.3 and Table 5.1 are the coil pitch (s+w), the number of turns of the coil (n), and the distance of the coil plane from the core (d). The placement of the first turn of the coil (p_1, p_2, and p_3) is also important for maximizing the signal-to-noise ratio (SNR) of the coils.

5.2.2.1 Coil Pitch and Thickness

It is decided to fabricate the coils with minimum realizable pitch that could be fabricated. This provides fitting more coil turns into the same dedicated area and picking the maximum flux out of this region. The coil pitch is fixed as 4 µm: 2 µm line and 2 µm spacing. The thickness of the coils is 0.5 µm, resulting in an aspect ratio that can be safely realized with standard techniques and leads to a low resistance value. Two level metal coils are used as the sensing coils of the sensor in order to increase the sensitivity.

5.2.2.2 Placement of the First Turn and the Total Number of Turns

It is possible to estimate the placement of the first turn of the coil by examining the distribution of the perpendicular component of the magnetic flux density, B, over a given plane under the core. It is seen that the flux is concentrated just under the trajectory of the short edge of the core (+x, +y, and –y directions in the simulations). In addition, the field is rapidly reduced at points little bit away from the trajectory of the core. These intuitively show that the first turn should be placed in such a way that it just encircles the trajectory of the core. On the other hand, the decrease in the magnetic field is much slower while moving under the core (–x direction). The placement of the first turn can be studied for this direction.

Figure 5.14 shows the variation of the resistance of each single turn and the total coil with respect to the number of turns for the first coil turn placed 40 µm and 200 µm inside the core edge. The coil pitch is 4 µm (2 µm line, 2 µm spacing) and the line thickness and resistivity are 0.5 µm and 2.65 µΩcm, respectively. The resistance of the coils for each position exceeds 1 kΩ after 30 and 40 turns.

Figure 5.15 shows the flux picked by each single coil turn for several first coil turn positions for a 1 mm long core. The flux for each turn is calculated in a similar manner as in Equation 5.1, within the area covered by the corresponding coil turn. As expected, the coil which is placed farther away from the edge picks more flux.

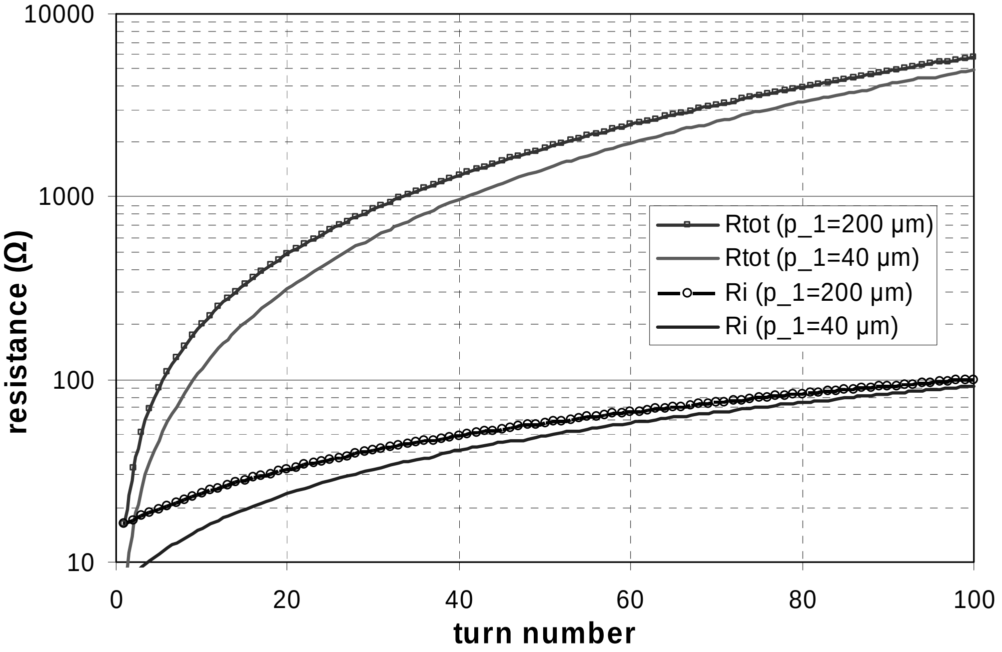

Figure 5.14: The variation of the resistance of each single turn and the total coil with respect to the number of turns for the first coil turn placed 40 µm and 200 µm inside the core edge.

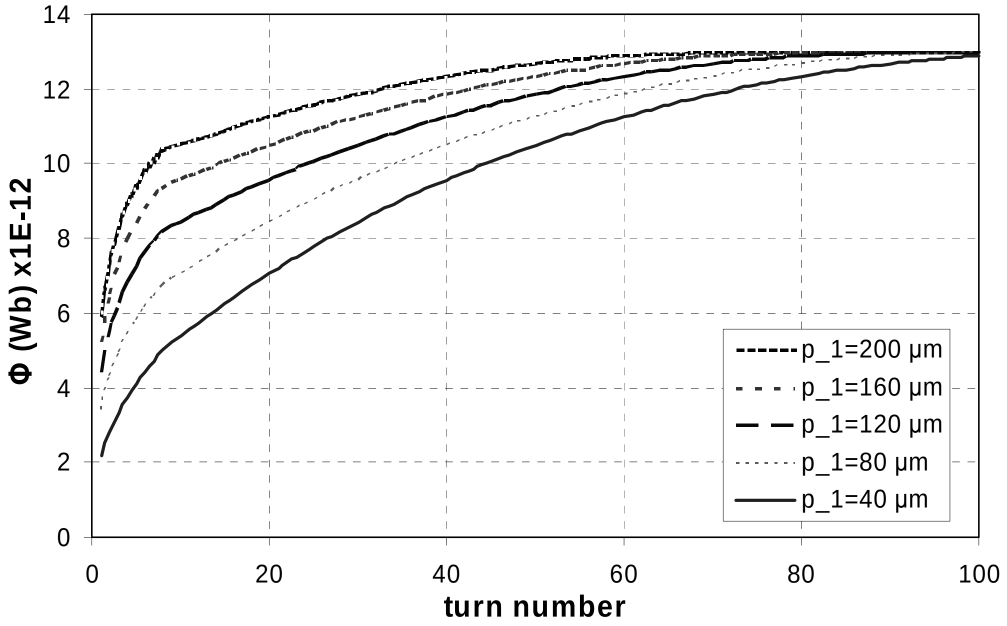

Figure 5.15: The flux picked by each single coil turn for several first coil placement positions for a 1 mm long core.

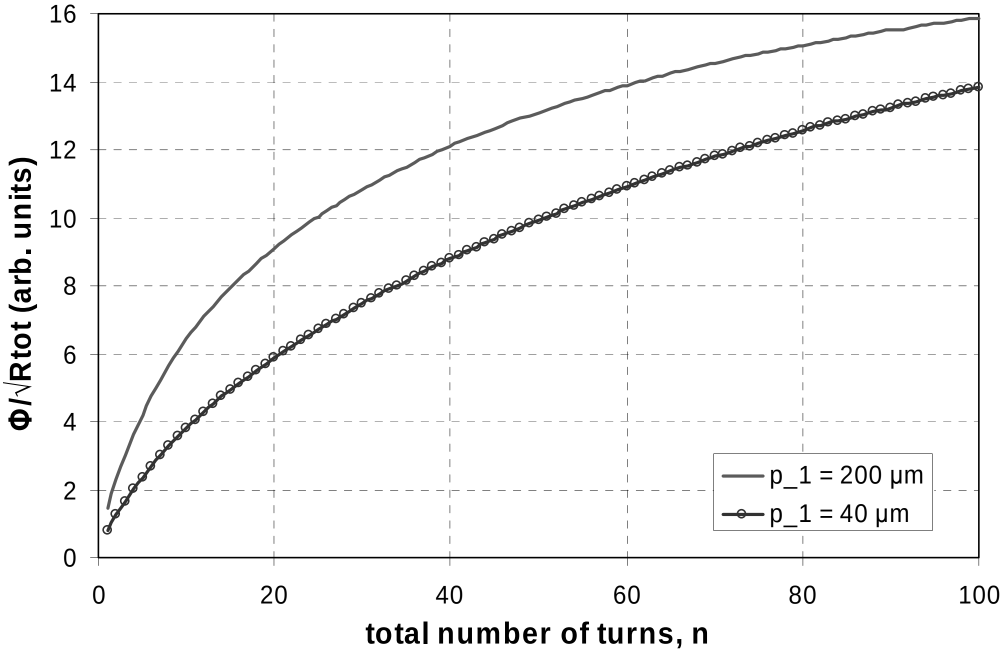

Figure 5.16: The calculated SNR value for two different first turn placement.

Figure 5.16 shows the calculated SNR value for two different first coil turn placements. It is seen that the coil placed farther away from the core edge has a better SNR, so this positioning should be selected for the first turn. Generally, there should be an optimum point for the SNR value. On the contrary, for the given core and coil dimensions, the SNR value monotonically increases by increasing the number of turns, indicating that the number of turns should be extended as the last turn passes under the middle of the ferromagnetic core. However, this is not a proper decision from the fabrication point of view, as the possibility of having an open circuit in the core increases as the metal lines become longer, decreasing the yield. We have selected using 30 turns for each level of coils, resulting in a resistance value around 2 kΩ. The coils are placed under the two edges of the core improving the SNR of the sensor by a factor of √2.

For the cores having lengths different than 1 mm, the simulations are not repeated. It is decided to keep the ratio between the core length and the first turn placement. So, for 0.5 mm and 2 mm long cores, the first turn is placed 100 µm and 400 µm inside the core edge, respectively. The number of turns is also kept as 30.

5.2.2.3 Distance between the coils and the core

The distance between the core and the sensing coils (d) is last design parameter that is presented in this section. Figure 5.17 shows the total flux under a 1 mm long core for coil planes at different distances away from the core. The intrinsic relative permeability of the core is 10000, and the applied external magnetic field is 100 A/m. It is seen that as the plane gets closer to the core, the total flux is increased. So, the coils should be placed as close to the core as possible. Furthermore, the distance between the two levels of the coils should be minimized in order to increase the sensitivity of the sensor. Both of these distances are limited by the fabrication processes. The planarization of the surface and avoiding short circuits are important factors requiring thicker isolation layers between the metal layers.

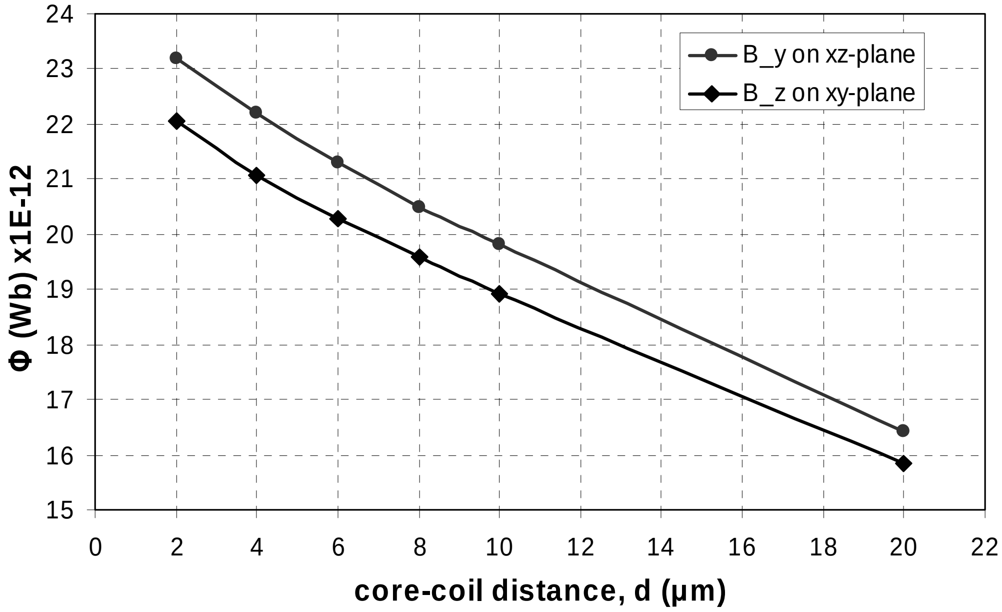

Figure 5.17: The total flux under a 1 mm long core for coil planes at different distances away from the core.

5.3 Fabrication

Figure 5.18 shows process flow developed for the fabrication of the sensors [5.1]. The detailed process flow is given in Appendix I. Silicon wafers with 4 inch diameter are used as substrates for the fabrication of the sensors. There is a 0.5 μm-thick SiO_2 layer on the wafers, which provides electrical isolation between the substrate and the sensor parts (Figure 5.18(a)). The fabrication starts with forming two-level sensing coils separated by an isolation layer on the substrate (Figure 5.18(b)). The sensing coils are made of 0.5 μm-thick AlSi(1%), and 1 μm-thick SiO_2 is used as the isolation layer. These layers are deposited by sputtering and patterned by dry etching.

A passivation layer is formed on the coils by spinning a 1.4 μm-thick SU8 layer over the coils. The SU-8 layer is patterned, leaving the pad areas open, and then hard baked in order to form a structural layer (Figure 5.18(c)). This layer also provides a planar surface for the rest of the process. Figure 5.2 shows the surface profiler scans of one of the sensors: (a) after the patterning of the SiO_2 layer and (b) after spinning the SU-8 layer. In Figure 5.2(a) a height difference of 0.5 μm is seen at the middle region of the coil. This height difference is doubled with the deposition and patterning of the second AlSi layer. Figure 5.2(b) shows that this difference is reduced to less than 0.3 μm with the coating of the SU-8 layer.

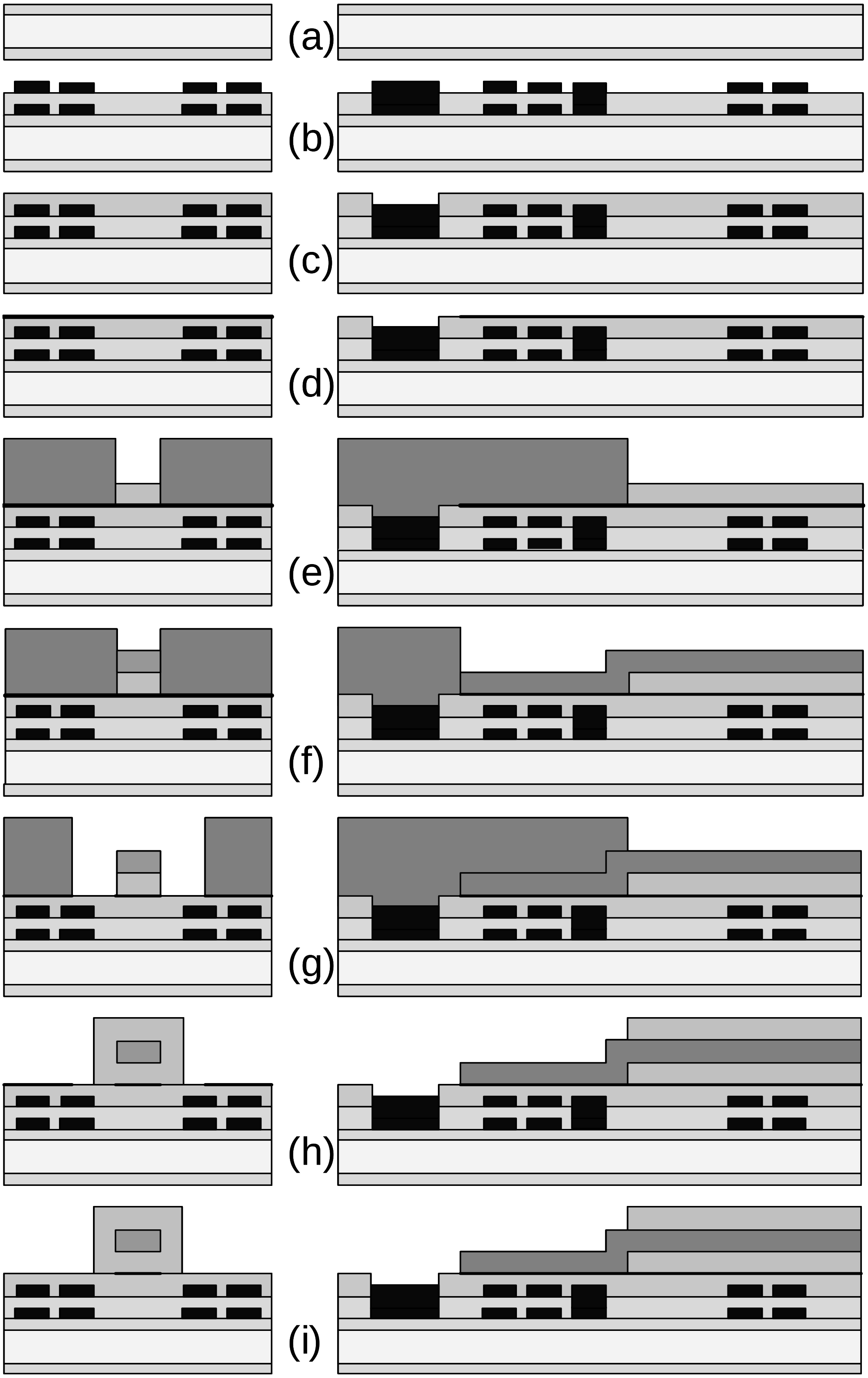

Figure 5.18: The cross-sectional view of the fabrication process flow.

Next step is the evaporation of a 20 nm/200 nm Cr/Cu seed layer on the SU8 layer. This layer is used as the seed layer for the following electroplating steps. The Cr/Cu layer is patterned by wet etching in order to electrically isolate the AlSi layers from the electroplating solution (Figure 5.18(d)).

After patterning the seed layer, an AZ9260 photoresist mold is provided for electroplating the bottom part of the ferromagnetic core. The 1st FeNi layer is electroplated into the openings of the photoresist mold (Figure 5.18(e)). The electroplating is performed at 40 °C with 22.5 mA/cm^2 current density. The earth magnetic field around the cathode is cancelled during the electroplating to minimize the magnetic anisotropy of the FeNi layer. Then, the copper excitation rod is electroplated (Figure 5.18(f)). After these two electroplating steps, the seed layer around the electroplated layers is etched with a photoresist mask (Figure 5.18(g)). This photoresist mask also serves as an isolating mold for the second FeNi electroplating (Figure 5.18(h)). This step forms a homogeneously closed ferromagnetic layer around the copper excitation rod. The process ends by stripping the photoresist mold.

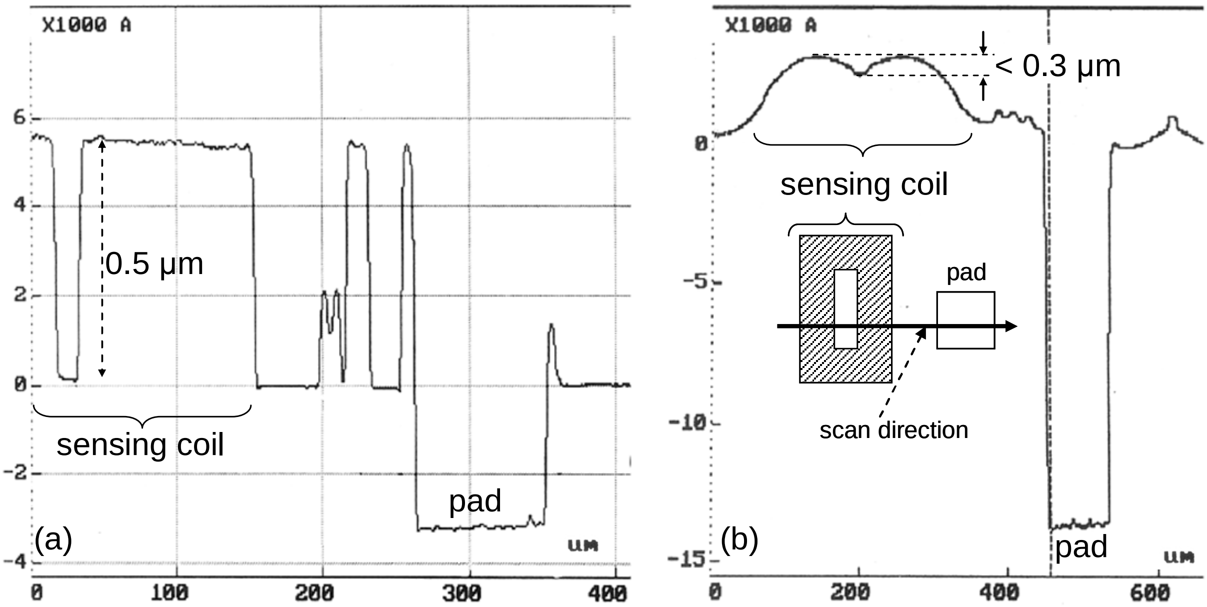

Figure 5.19: The surface profiler scans of one of the sensors: (a) after the patterning the SiO_2 layer, and (b) after spinning the SU-8 layer.

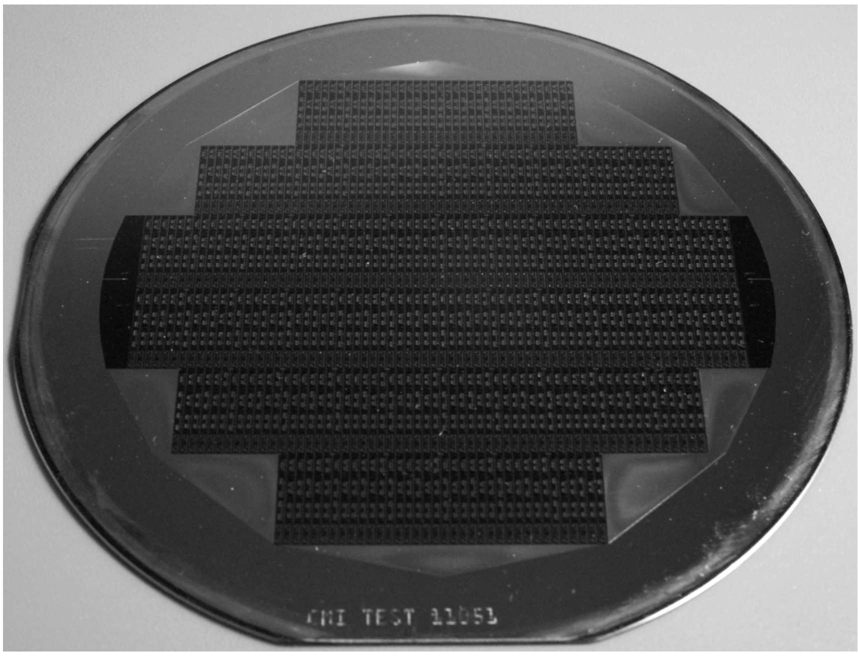

Figure 5.20: Photograph of the fabricated wafer.

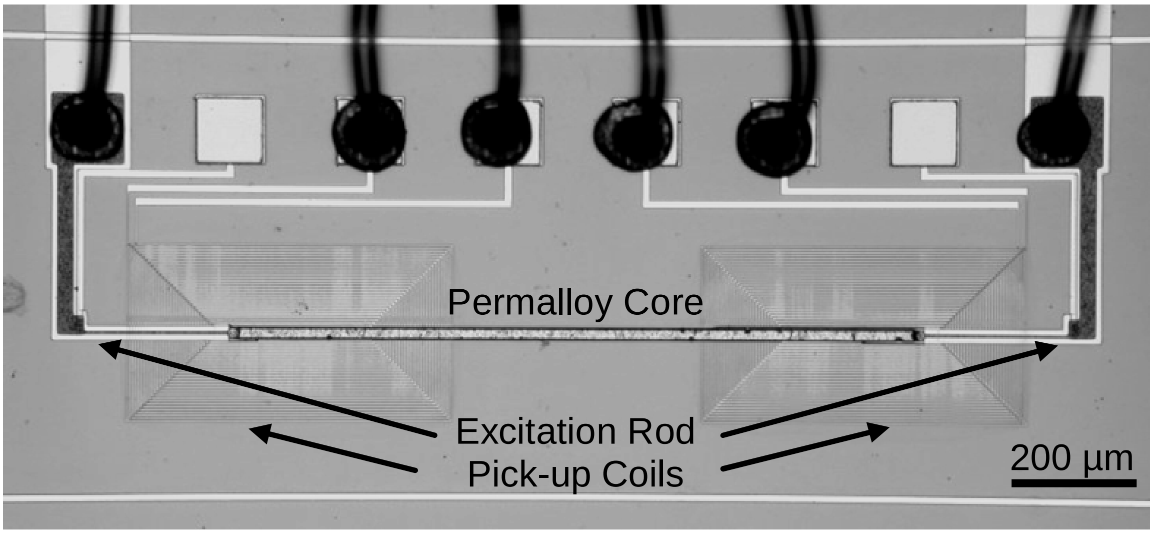

Figure 5.21: Microscope picture of one of the fabricated sensors having a 1 mm-long core.

Figure 5.20 shows the photograph of one of the fabricated wafers. There are around 1300 cells on each wafer including sensors and test structures, with 3 mm x 1 mm dimensions. Figure 5.21 shows the microscope picture of one of the fabricated sensors having a 1 mm-long core. Figure 5.22 shows the SEM view of one edge of the core. The cross-sectional dimensions of the specific structure and the copper layer are 16 µm x 10 µm and 8 µm x 2 µm, respectively.

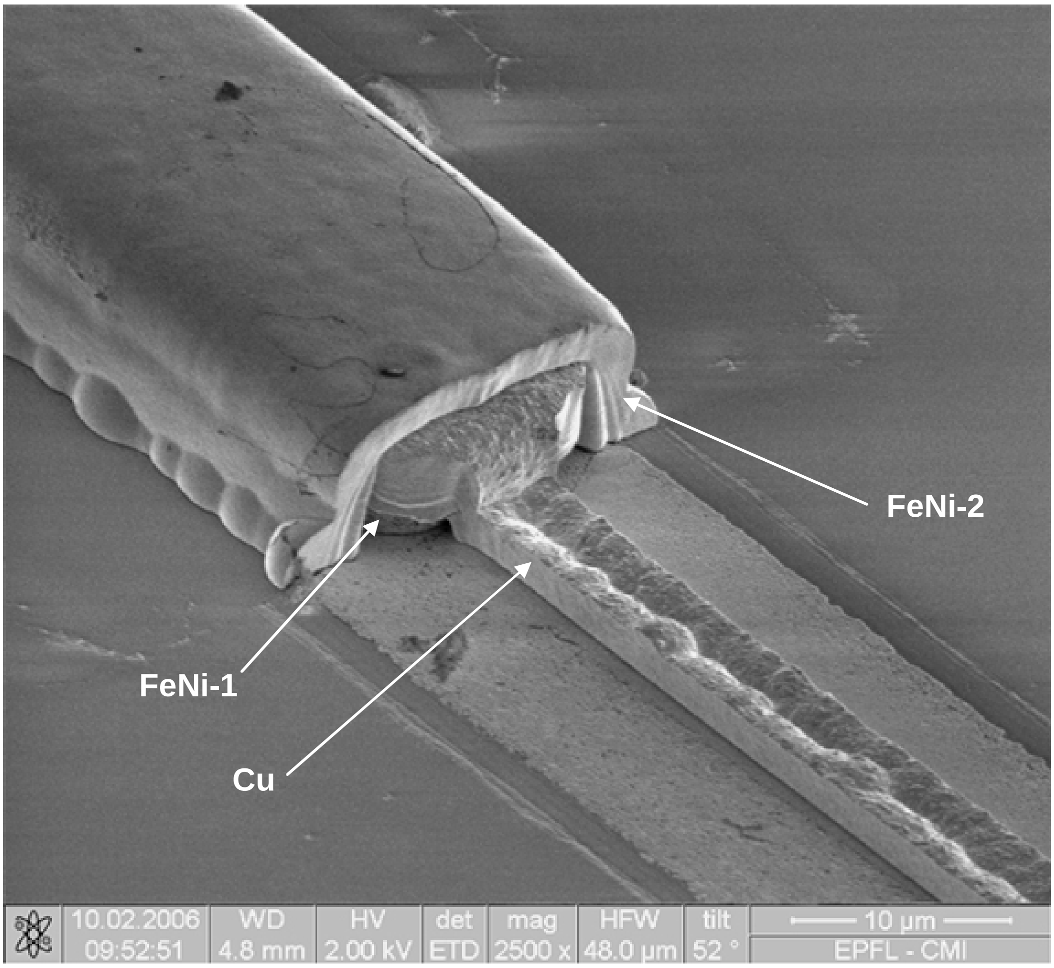

Figure 5.22: SEM image of the edge of the sensor core.

Table 5.2: The variation of the thickness of the electroplated layers over the wafer.

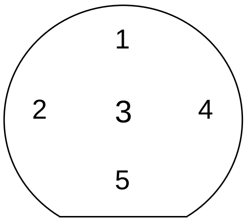

Region	FeNi-1 (µm)	Cu (µm)
1	1.4	0.8
2	4.4	1.8
3	4.2	2.0
4	4.3	2.0
5	1.3	1.4

Table 5.2 presents the thickness values of the electroplated layers. The measurements are taken with a surface profiler, at the points marked on the wafer at the left side of the table. The same structure is measured at each region. A variation of the thickness over the wafer is seen for all electroplating steps. Less material is deposited at the edges of the top and bottom parts of the wafer, where there is less circulation of the electrolyte. The electroplating is at the desired thickness and also more uniform at the middle part of the wafer.

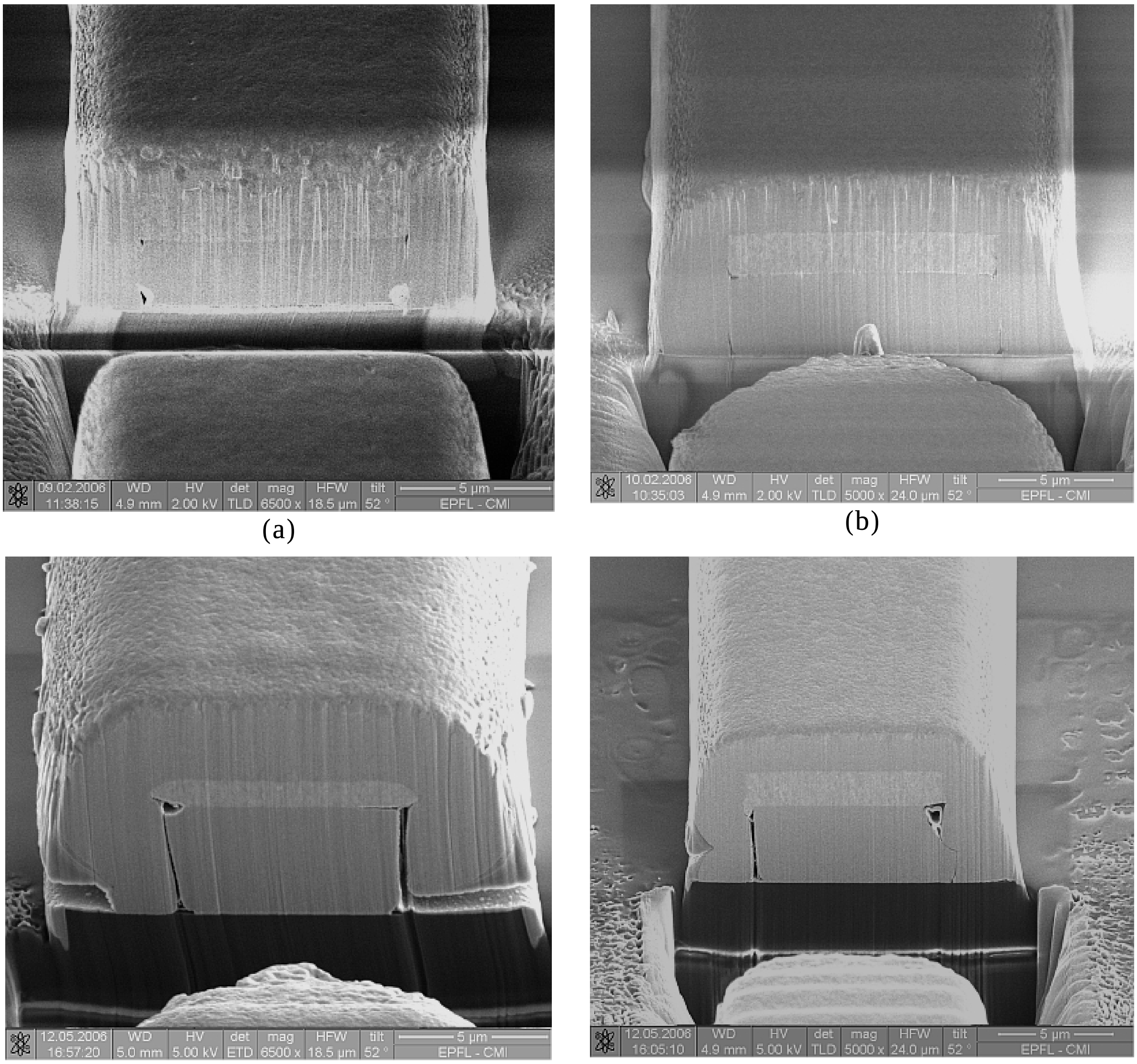

(a) (b)

(c) (d)

Figure 5.23: The SEM images taken after FIB milling, showing the core cross-sections. (a and b) uniformly covered, (c and d) containing defects.

Focused Ion Beam (FIB) milling is performed in order to see whether a uniformly closed FeNi core is formed around the copper excitation rod. Figure 5.23 shows the SEM images taken after FIB milling, showing the cross-section of the cores. It is seen that for some of the cores (a and b), FeNi electroplating uniformly covers the copper rod, and the closed magnetization path is formed. However, for some of the structures (c and d), there are some uncovered regions. Unfortunately, it is not possible to say whether these openings are due to the electroplating process or formed during the FIB milling. Most probably, the circular gaps are formed during electroplating, with the H_2 molecules that are formed at the cathode and trapped on the surface due to inadequate stirring. These gaps can be treated as surface defects that disturb the domain structure of the layer. On the other hand, the gaps in the shape of a line may be formed during milling. The reason for these linear gaps may be the poor sticking two electroplated layers to each other.

5.4 Sensor test results

In this section, the test results of the fabricated sensors will be presented. These tests include the characterization of the sensing coils and the electroplated FeNi layer, as well as the detailed analysis of the response of different sensors.

5.4.1 The Sensing Coils

The resistance values of the sensing coils are measured as their fabrication is completed in order to verify their operation. Figure 5.24 shows the distribution of the resistance value of one of the sensing coils used for a 1 mm long core over the wafer. It is seen that in the outer regions of the wafer, the resistance value is larger than these in the middle region. This is due to the variation of the metal etching process over the wafer. The outer regions are etched faster than the inner ones, resulting in more undercut in these regions, and accordingly, narrower metal lines.

The targeted value of 2 kΩ is almost reached in the middle regions of the wafer. Still, the values are little higher than expected. The main reason for this is the photoresist mask formed over the metal lines before etching, which is slightly narrower than the width on the mask. Furthermore, some non working coils also exist over the wafer. These are marked as OVL (overload) even if they have a finite resistance, but over 100 kΩ. Since no resistance between 5 kΩ and 100 kΩ is measured, it can be said that these high values are due to local surface defects affecting the photolithography. The highly resistive contact opening at these regions may also be another reason for the non-working coils.

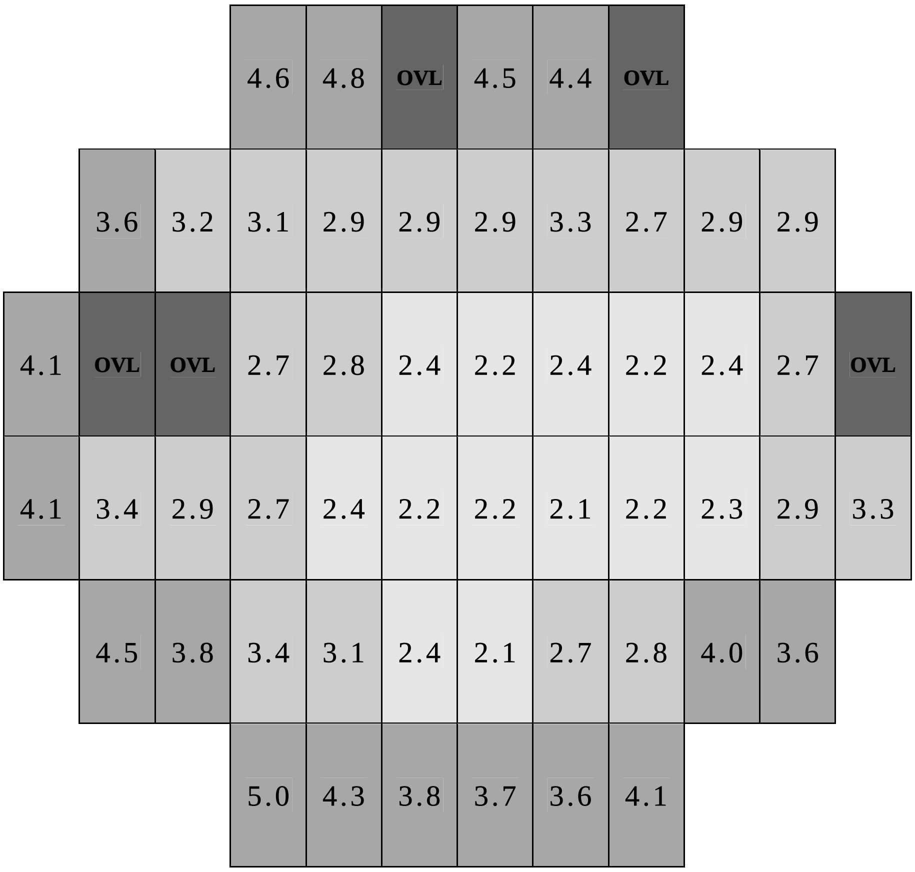

			4.6	4.8	OVL	4.5	4.4	OVL			
	3.6	3.2	3.1	2.9	2.9	2.9	3.3	2.7	2.9	2.9	
4.1	OVL	OVL	2.7	2.8	2.4	2.2	2.4	2.2	2.4	2.7	OVL
4.1	3.4	2.9	2.7	2.4	2.2	2.2	2.1	2.2	2.3	2.9	3.3
	4.5	3.8	3.4	3.1	2.4	2.1	2.7	2.8	4.0	3.6	
			5.0	4.3	3.8	3.7	3.6	4.1			

Figure 5.24: The distribution of the resistance value (in kΩ) of one of the sensing coils used for a 1 mm long core over the wafer. (OVL=overload)

5.4.2 Electroplated Permalloy layer properties

The magnetic properties of the electroplated layer are determined by measuring its magnetization (B-H) curve. Figure 5.25 shows the measured B-H curve of a 7 cm x 1 cm FeNi layer which is electroplated just after the 2nd FeNi layer of the process wafers. The M-H curve is measured by using the induction method, as described in Chapter III. The measured H_c and H_k values are 70 A/m and 750 A/m, respectively. The saturation magnetic induction value, B_{sat}, of the electroplated layer is measured by ferromagnetic resonance technique [5.2], and found to be 0.85 T. Figure 5.26 shows the variation of the relative permeability of the layer, calculated from its B-H curve. Maximum relative permeability of 10000 is reached at 20 A/m magnetic field.

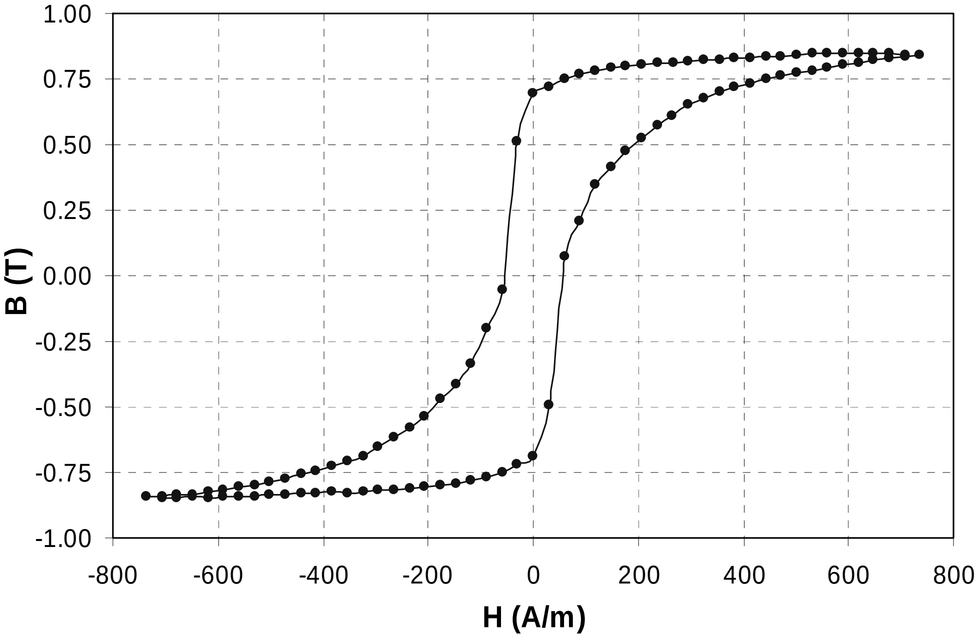

Figure 5.25: The measured magnetization curve of the electroplated FeNi layer.

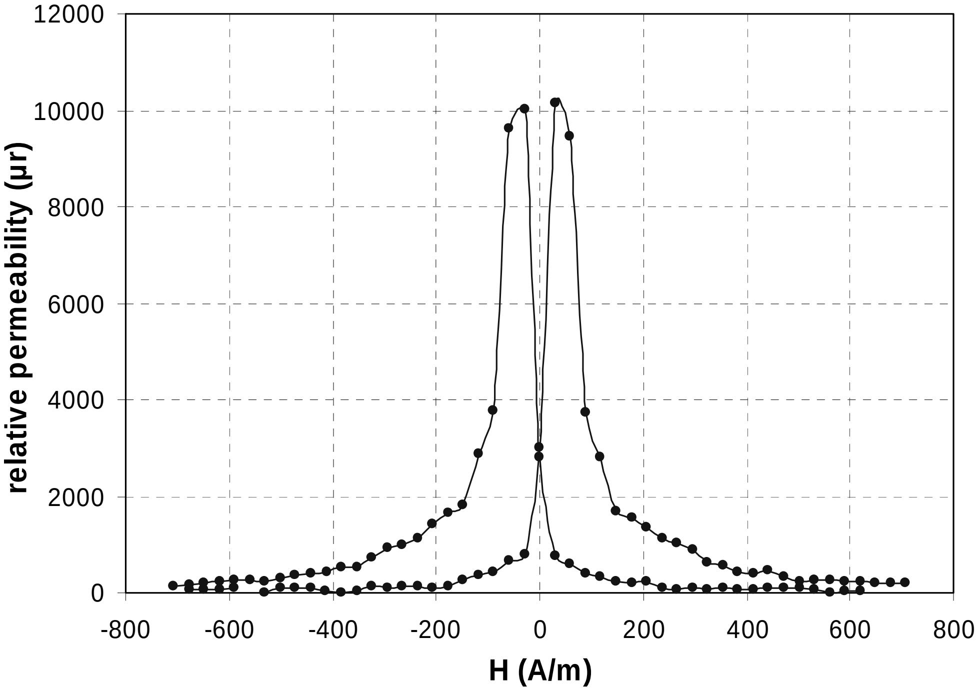

Figure 5.26: The variation of the relative permeability of the layer.

The discrepancy between the measurements results presented in Chapter III and this one is probably due to the degraded electroplating bath during several experiments between the first and second electroplating step. At this point, it is important to note the difference between the H_k value used during the simulations and the actual value. The 3.5 times higher value of H_k results in 3.5 times higher excitation current value (12 mA to 42 mA) required for proper operation.

5.4.3 Mounting of the sensor chips

In order to test the sensor chips separately, the wafer is diced, and sensor chips are glued to substrates by using an epoxy. Ceramic substrates with gold connection lines are used as they do not contain any magnetic pieces or layers. Figure 5.27 shows one of the sensor chips glued on the substrate with a silver epoxy. After gluing, the wire bondings are done (visible in Figure 5.21), and the sensor and the wires are protected with a plastic cap.

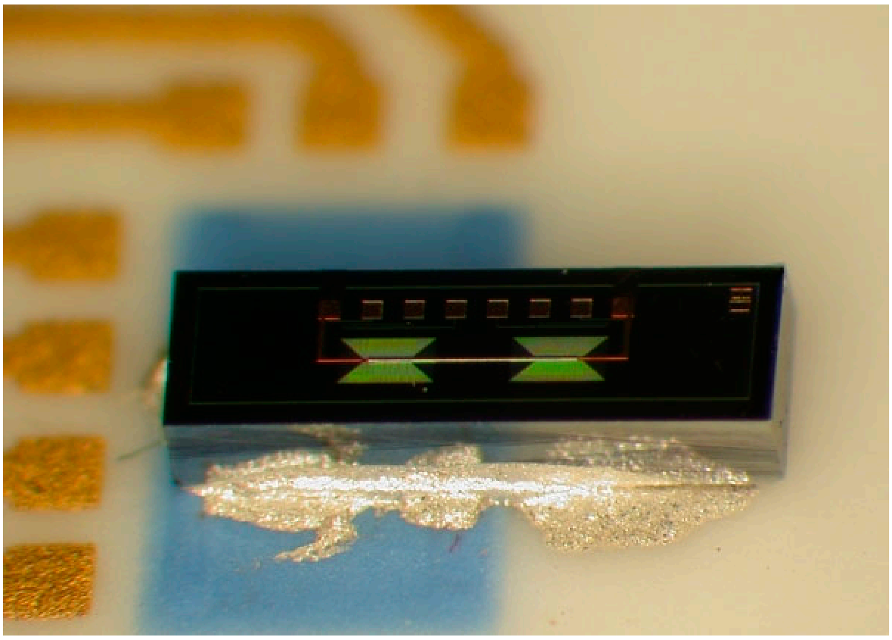

Figure 5.27: The sensor chip attached to the ceramic substrate with silver epoxy.

5.4.4 The sensor performance

The signal conditioning of the sensor is done by external electronics. Figure 5.28 shows the schematic view of the test setup. The same setup described in Chapter IV is used during the experiments: A sinusoidal excitation current produced by a signal generator is fed to the excitation rod. The Helmholtz coils produce the external magnetic field to be measured. The 2nd harmonic component of the induced voltage across the pick-up coils is measured with a lock-in amplifier synchronized with the signal generator.

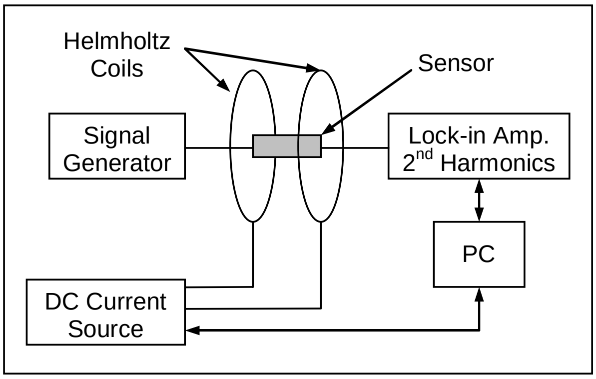

Figure 5.28: The sensor test setup.

5.4.4.1 Sensitivity and Linear Operation Range

Figure 5.29 shows the response of the sensor with 0.5 mm long core for 100 mA-peak sinusoidal current excitation at 100 kHz frequency within ±4 mT external magnetic flux density range. The sensitivity of the sensor is 102.8 µV/mT in a ±1100 µT linear operating range. The linear operating range is calculated as the range for which the output response fits to a linear function with an r-squared value of 99%, and the sensitivity of the sensor is the slope of this linear function.

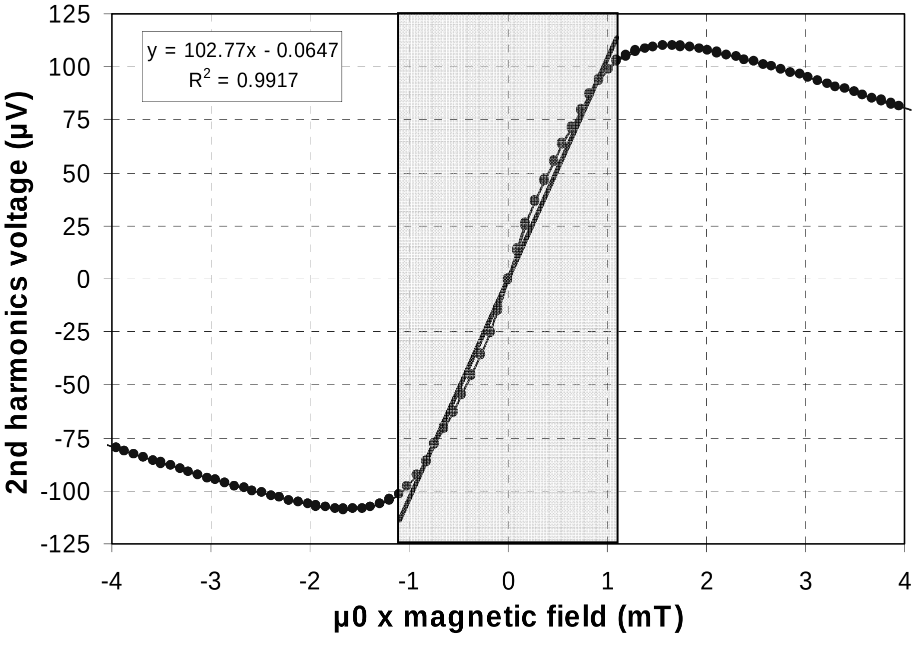

Figure 5.29: The test results of the sensor with different excitation currents within ±4 mT external magnetic field density range. The sensitivity of the sensor is 102.8 µV/mT and the linear range is ±1100 µT.

The sensor is tested with several excitation current magnitude and frequency values in order to find the optimum operating conditions. The change in the linear operating range, sensitivity, perming and the total noise of the sensor is investigated as the performance criterions. It should be noted that for the results presented below, the current peak value is swept as a parameter at an excitation frequency of 100 kHz, and the excitation frequency is swept at a current peak value of 100 mA.

Figure 5.30 demonstrates the change in the linear range of the sensor with the excitation current amplitude and the frequency. At excitation current peak amplitudes less than 100 mA, the linear operation range changes with the excitation current, showing that the sensor is not saturated for these excitation values. For the saturation of the core, current peak values higher than 100 mA are required. With these currents, the linear operation range becomes independent of the excitation current value. This property of the closed magnetization path for excitation and the orthogonal configuration can be better understood if it is compared to the open loop excitation in a typical single core parallel fluxgate configuration, which will be discussed in Section 5.4.4.6.

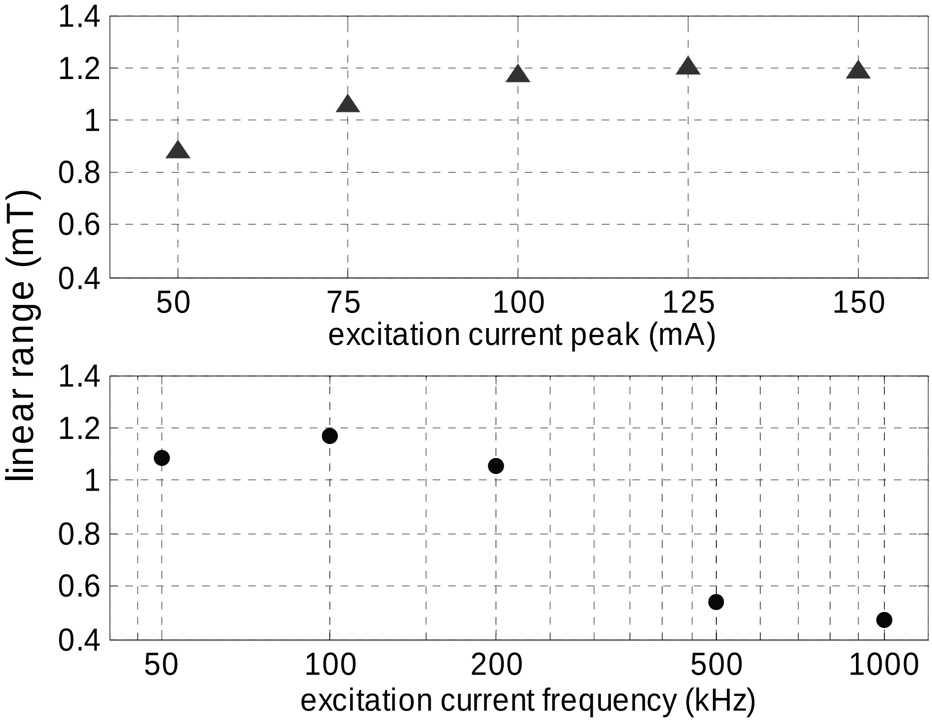

Figure 5.30: Effect of excitation current peak value and frequency on the linear operating range of the sensor.

The operation frequency of the sensor is determined by the magnetic and electrical properties and the thickness of the FeNi layer. The thickness of the ferromagnetic layer was selected for operation at 100 kHz. The measurements show that the linear operation range of the sensor is not affected from the frequency of the excitation signal up to 200 kHz. The variation in the linear range is 10 %. However, for excitation frequencies higher than 200 kHz, the sensor response becomes less linear, leading to a decrease in the linear operation range of the sensor. This is due to the increasing eddy currents and the skin effect with the operation frequency, which decrease the control of the magnetic domains and the saturation of the sensor.

Figure 5.31 shows the change in the sensitivity of the sensor corresponding to the linear range presented in Figure 5.30, with the excitation current amplitude and the excitation frequency. The sensitivity of the sensor increases proportionally with the peak value of the excitation current. However, the increase with the excitation frequency is more logarithmic. This can also be explained by considering the degrading magnetic properties of the electroplated ferromagnetic layer at higher frequencies.

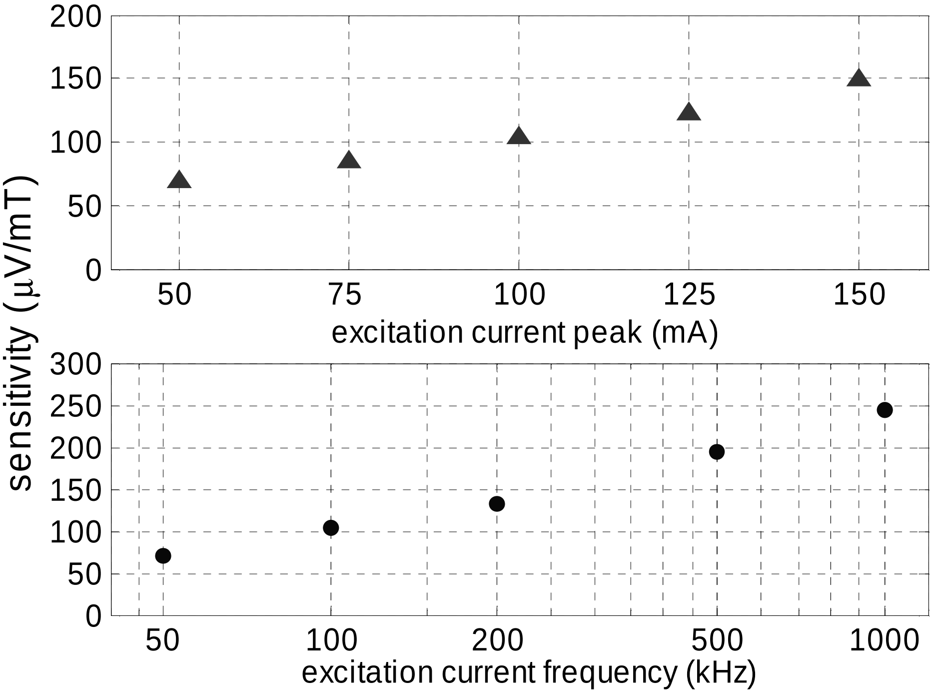

Figure 5.31: Effect of excitation current peak value and frequency on the sensitivity of the sensor.

5.4.4.2 The Perming of the Sensor

The perming of the sensor is measured by applying an external field several times higher than the linear operation range of the sensor. The field is applied and then reduced to ambient. Then the output of the sensor is recorded. The same procedure is repeated with a field in the opposite direction. The difference between the two measured values gives the perming voltage. This voltage is then converted into the equivalent input magnetic field by dividing the value by the sensitivity at the ambient field value. Figure 5.32 presents the perming values of the sensor for different excitation conditions. The perming value decreases as the excitation current peak value increases up to 100 mA-peak. For higher currents, the perming is almost stabilized, indicating that the saturation of the sensor is reached at this excitation value. It is important to mention that with a 50 mA-peak excitation current, a field which is equal to the measured H_k value of the FeNi layer is created over the surface of the core. However, a low perming value can be reached only after doubling the current because of the difference between the DC and AC magnetization curves of the FeNi layer.

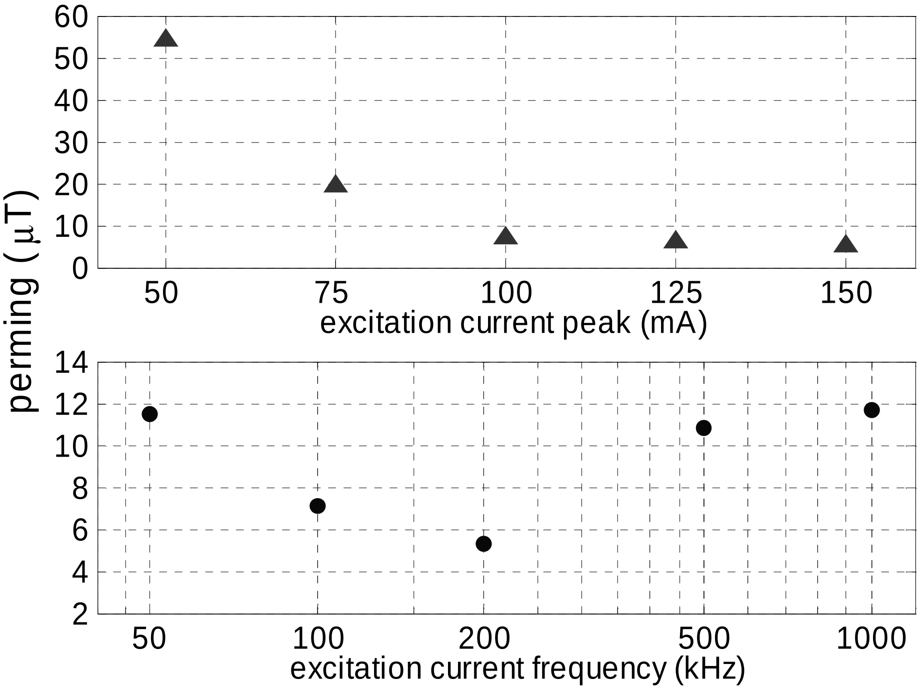

Figure 5.32: The perming value of the sensor for different excitation conditions.

The perming of the sensor decreases with increasing excitation frequency up to 200 kHz. The skin effect is not dominant and the magnetization curves of the FeNi layer are same for these frequencies. This results in a similar remanent magnetization in the radial direction of the sensor core, which creates a similar perming voltage at the output of the sensor. Then a smaller perming value is obtained for the excitation condition with higher sensitivity. The inverse proportionality between the sensitivity and the perming of the sensor can be seen if Figure 5.31 and Figure 5.32 are compared. After 200 kHz, skin effect becomes dominant, and all magnetic domains cannot be controlled completely, which increases the perming of the sensor.

5.4.4.3 The Noise of the Sensor

In order to determine the senor resolution, the noise as well as the sensitivity of the sensor has to be measured. Both frequency domain and time domain measurements are performed as noise measurements. No magnetic shielding is used during the measurements; instead, the measurements are done under a certain magnetic field which is within the linear operation range of the sensor. Figure 5.33 shows the equivalent magnetic noise values of the sensor measured at 1 Hz and in a 0.3 to 10 Hz frequency range. The noise decreases by increasing the excitation peak value as the ferromagnetic layer saturates better for higher excitation current values. On the other hand, there exists a minimum noise value around 100 to 200 kHz when the excitation frequency is considered. This can also be referred to the change in the AC magnetic properties of the electroplated ferromagnetic layer.

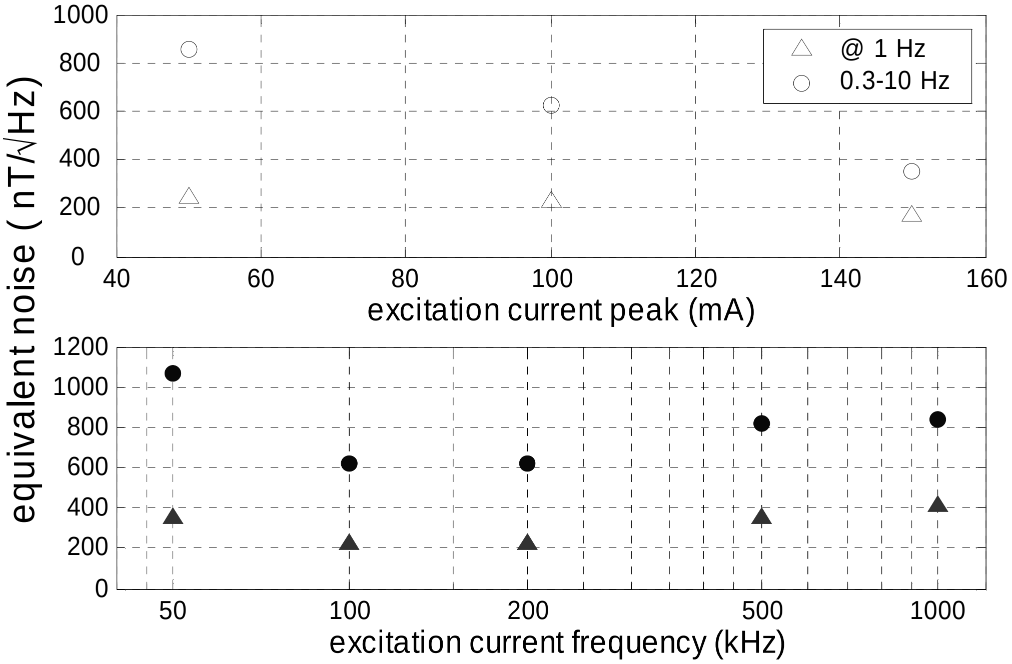

Figure 5.33: Effect of excitation current peak value and frequency on the magnetic noise of the sensor.

Figure 5.34 presents the equivalent magnetic noise spectrum of the sensor for 100 mA-peak excitation at 100 kHz frequency. The spectrum is measured under 230 µT external magnetic field with a lock-in amplifier whose output is connected to the spectrum analyzer. The time constant of the lock-in amplifier is kept at the minimum value of 100 µs so that the averaging of the lock-in amplifier itself does not filter the higher frequency components of the noise spectrum. The measured equivalent magnetic noise density is 268 nT/√Hz at 1 Hz and the RMS noise is 622 nT within 0.3 to 10 Hz bandwidth. Figure 5.35 shows the time-domain noise information of the sensor for two different external magnetic field values. For this measurement, the time constant of the lock-in amplifier is set to 100 ms, which corresponds to 10 Hz bandwidth, and the output is sampled every 500 ms, and recorded through a multimeter. The standard deviation of the output noise calculated through this measurement is 44 nV which corresponds a equivalent magnetic noise around 400 nT. The difference between the values calculated from frequency domain and time domain measurements is probably due to the averaging of the multimeter, which results in a lower value for the time domain measurements.

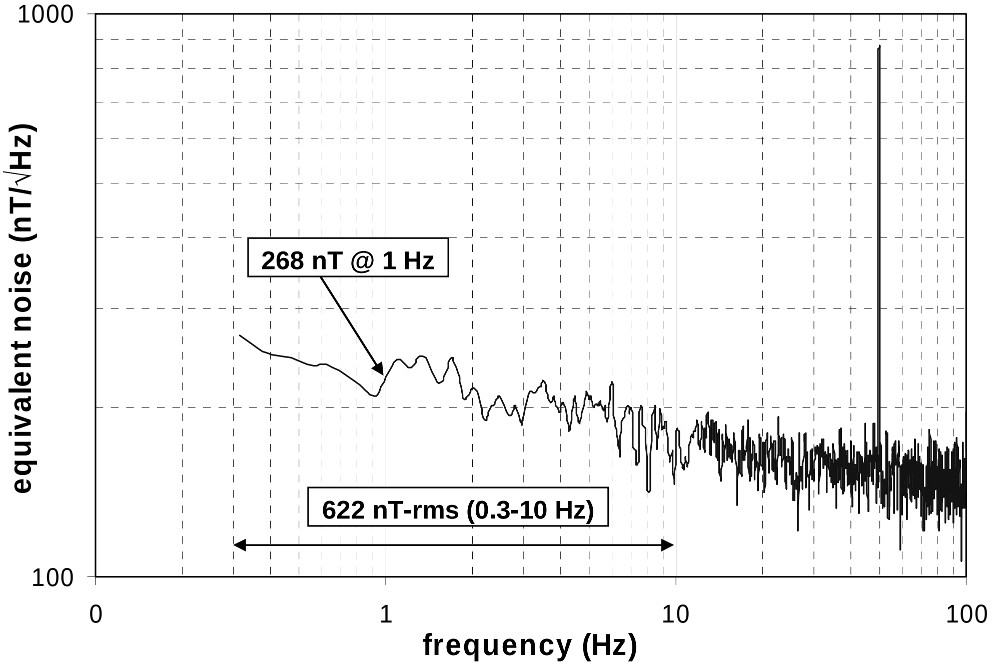

Figure 5.34: The magnetic noise spectrum of the sensor up to 100 Hz for 100mA-peak excitation at 100 kHz frequency.

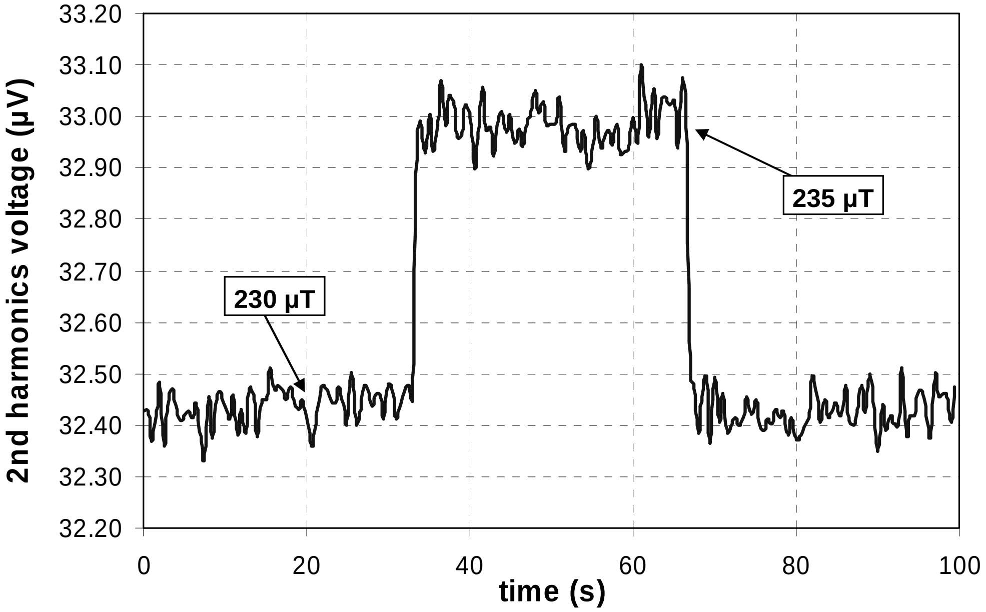

Figure 5.35: Time domain response of the sensor for 10 Hz bandwidth with two different external field values.

5.4.4.4 The Power Dissipation

The resistance of the core is also important for the power dissipation of the sensor. Four-wire resistance measurements are performed on the devices. The typical resistance of a 1 mm-long device having 16 µm x 10 µm cross-section is found to be 2 Ω. This results in an average power consumption of 10 mW for 100 mA-peak sinusoidal excitation current. The voltage drop across the core is 200 mV-peak, which makes the sensor also compatible with low-voltage advanced CMOS technologies.

5.4.4.5 Variation of the Core Length

The sensors having different lengths and similar cross-section areas are tested and the linear operation range, sensitivity, and the noise of the sensors are compared [5.3]. The sensor samples that are placed close to each other over the wafer are selected in order to minimize the possible differences between the magnetic properties of the FeNi cores. Figure 5.36 shows the response of three sensors having 0.5, 1, and 2 mm core lengths. The excitation current is 100 mA-peak with 100 kHz frequency for all of the sensors. The presented results verify the increase in the linear operation range with the decreasing core length due to the increase in the demagnetization factor along the length of the core. The measured linear ranges for the sensors with 0.5 mm, 1 mm, and 2 mm long cores are ±1100 µT,

± 410 µT, and ±160 µT. The obtained values are also in good agreement with the FEM simulation results with a core having an intrinsic relative permeability of 10000, which are presented in Figure 5.13.

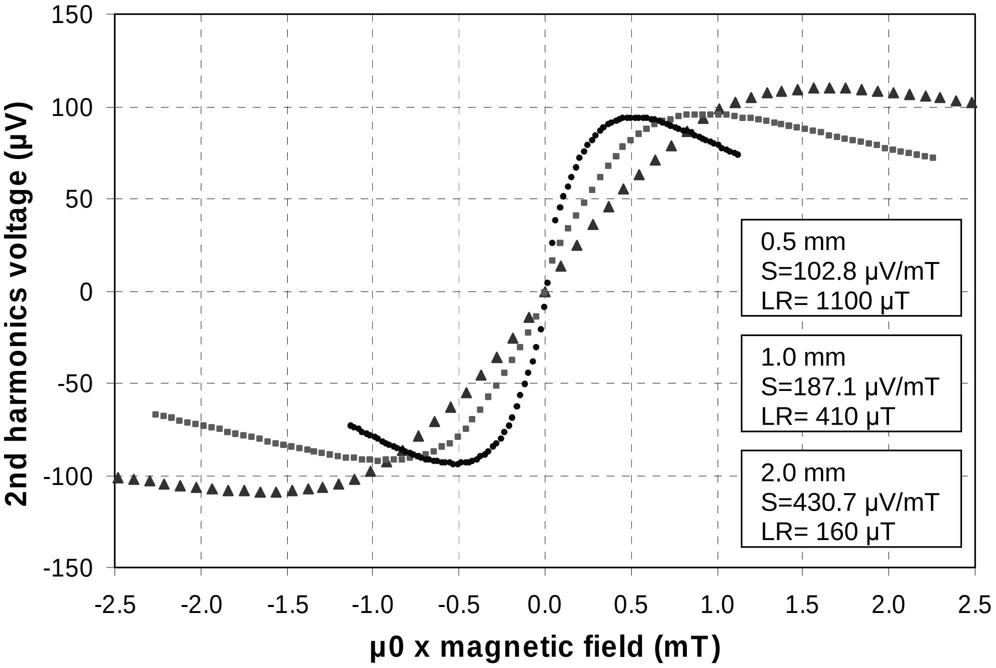

Figure 5.36: Response of the sensors having cores with different lengths in orthogonal mode using 100 mA-peak sinusoidal excitation at 100 kHz. Shorter core has wider linear range.

The wider linear operation range can be obtained by reducing the length of the core, which, on the other side, decreases the sensitivity of the sensor. This is an expected result since the demagnetization factor affects the linear operation range and the sensitivity in opposite ways. As a result of the decrease in the sensitivity, the equivalent magnetic noise of the sensor increases. Figure 5.37 shows the equivalent magnetic noise density of the sensors measured at 1 Hz and the noise measured between 0.3 and 10 Hz frequency band for an excitation of 100 mA-peak at 100 kHz frequency. It is seen that the noise decreases as the core length and the sensitivity of the sensor increases.

Another factor increasing the noise may be the increase in the Barkhausen (magnetic) noise of the FeNi layer with the decrease in the dimensions of the core. In order to investigate this, the noise components should be separated. There are two contributions to the total noise of the sensors: the Barkhausen noise of the core and the thermal noise of the sensing coils. For 0.5, 1, and 2 mm long cores, the measured total coil resistances are 3.3, 5.5, and 7.3 kΩ, respectively, resulting in

23, 30, and 34 nV of thermal noise in a 10 Hz bandwidth. The magnetic equivalent of this noise N_{TH}, is calculated by dividing the value by the sensitivity of the sensor. Then, the resulting value is subtracted from the total noise N_{tot}, giving the contribution of the magnetic noise:

$$N_{Mag} = \sqrt{N_{tot}^2 - N_{TH}^2} \ . \tag{5.3}$$

Figure 5.38 shows the summary of the performed analysis. It is seen that the main noise contribution coming from the Barkhausen noise. Furthermore, the decrease in the Barkhausen noise is more than the increase in the sensitivity of the sensor with the increased core length. For example, the Barkhausen noise of the sensors with 0.5 and 2 mm long cores are 580 and 99 nT, respectively for 0.3 to 10 Hz frequency band. It is seen that the noise is decreased by a factor of 6, however the increase in the sensitivity is 4 times. This difference points the increase in the Barkhausen noise of the cores as the dimensions of the ferromagnetic layers scale down, which is one of the biggest challenges in the miniaturization of fluxgate sensors.

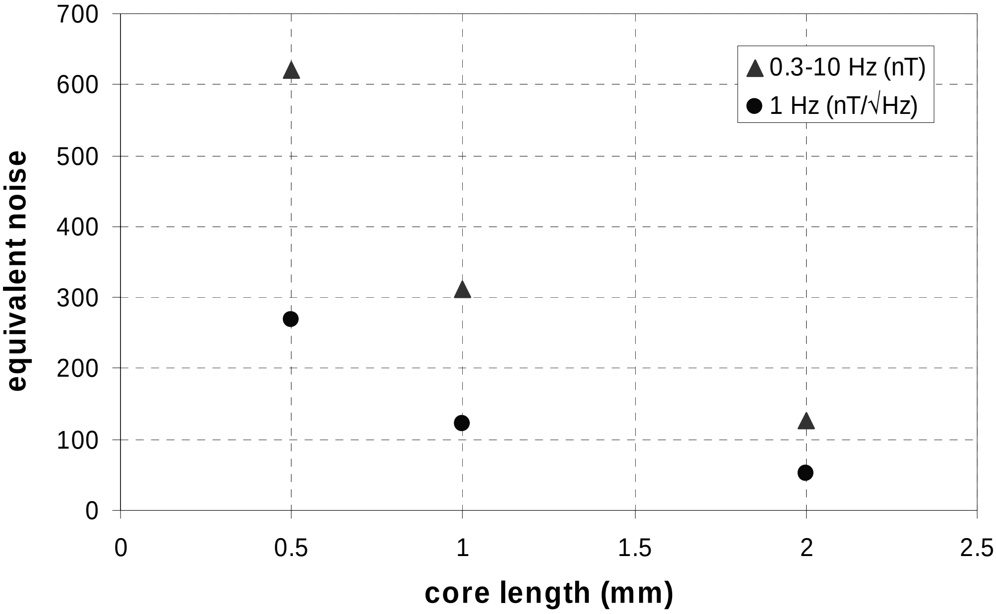

Figure 5.37: The equivalent noise of the sensors having different core lengths.

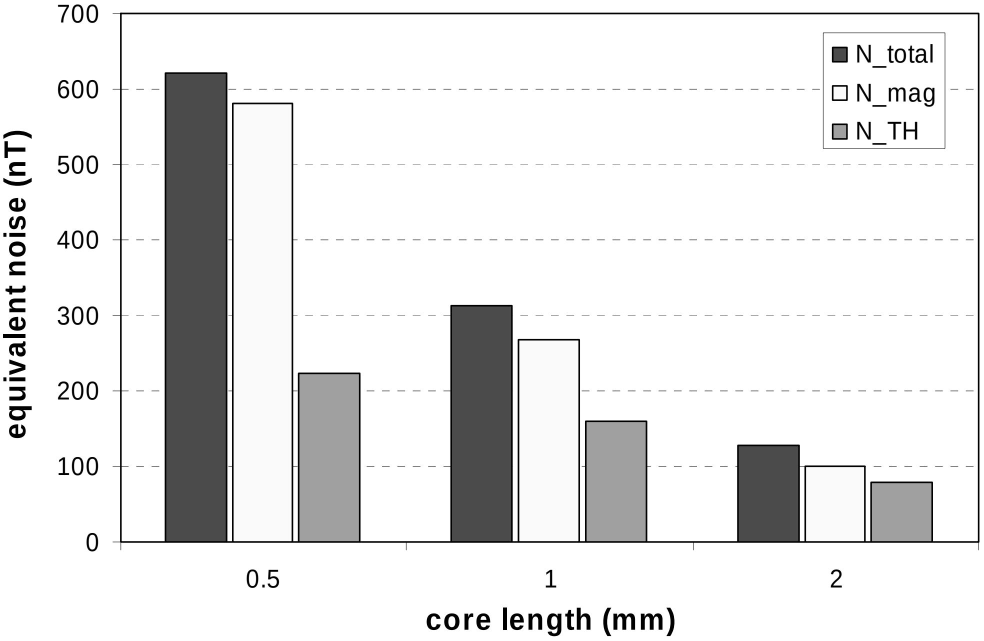

5.38: The variation of the total (N_{tot}), thermal (N_{TH}), and magnetic (N_{mag}) noise of the sensors with core length within a 10 Hz bandwidth.

5.4.4.6 Comparison of Parallel and Orthogonal Operation Modes

The sensor structure is also suitable for parallel mode operation, which enables the comparison of the two fluxgate principles. For the parallel operation, an excitation field at 10 kHz is externally supplied which is parallel to the measuring direction. Figure 5.39 and Figure 5.40 show the responses of the sensor with 0.5 mm-long core in orthogonal and parallel operating modes, respectively, where the sensor is excited at the optimal conditions for both modes. It should be noted that the excitation values are given in mA and A/m for orthogonal and parallel excitation modes, respectively. For the orthogonal mode, the linear operating range changes negligibly with the excitation, and is around ±1100 µT. This proves that the excitation and detection mechanisms are independent of each other due to the closed structure of the excitation mechanism. For the parallel mode, however, linear range strongly depends on excitation and increases to a value of only ±35 µT, and the response starts to get disturbed if the excitation field is further increased. Wider linear operation ranges can still be obtained by shortening the core for both modes. This accompanies with an increase in the excitation field level for the parallel mode, which increases the power consumption of the sensor, whereas the excitation of the orthogonal mode stays at the same level.

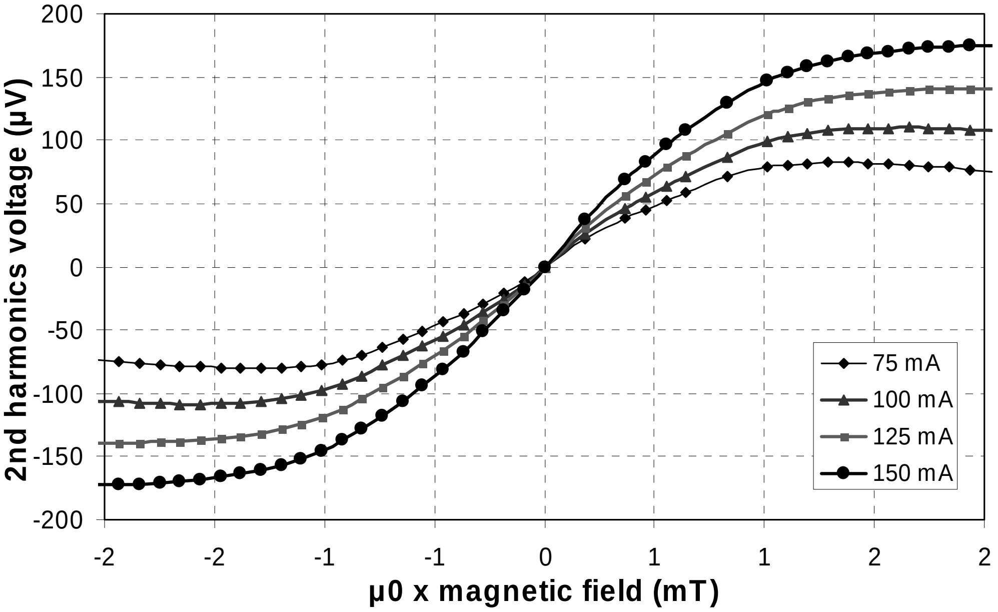

Figure 5.39: Orthogonal mode response of the sensor having 0.5mm-long core with sinusoidal excitation at 100 kHz.

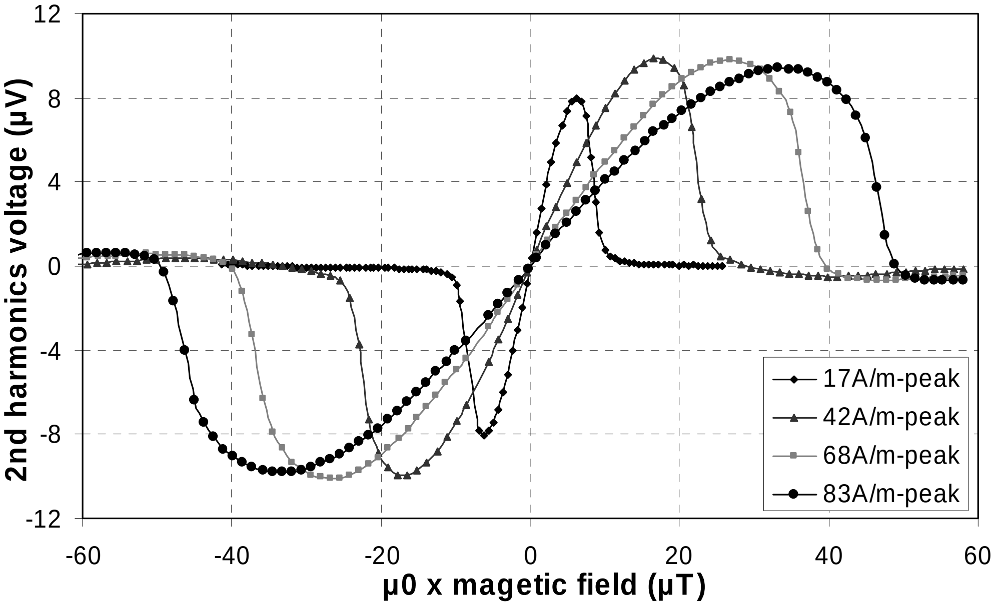

Figure 5.40: Parallel mode response of the sensor having 0.5mm-long core with sinusoidal excitation at 10 kHz.

5.4.4.7 The GMI effect in rod type orthogonal fluxgate structure

In this section, we present our work on the giant-magneto-impedance effect in rod-type orthogonal fluxgate structure [5.4]. Most of the GMI sensors use similar structures to the rod type orthogonal fluxgate structure, but most of them are in bigger sizes.

Figure 5.41 illustrates the test setup. The sensor is tested by applying a DC magnetic field through Helmholtz coils and by measuring the resistance and inductance values of the device with an RLC meter. Serial resistor – serial inductor (R_s – L_s) network model is used for the measurements. A 15 mA_{RMS} excitation current with various frequencies is supplied to the device from the RLC meter. Figure 5.42 presents the measured R_s and L_s values for different frequencies at zero magnetic field. The resistance value of the device remains unchanged for low frequency excitation. If the excitation is in MHz range, then the skin effect becomes significant, and the resistance value increases for higher frequencies. For the inductance value, we observe a decrease with increasing excitation frequency. This is due to the increased magnetic losses of the electroplated core at higher excitation frequencies.

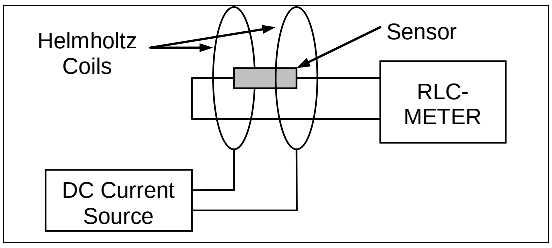

Figure 5.41: The sensor test setup for GMI measurements.

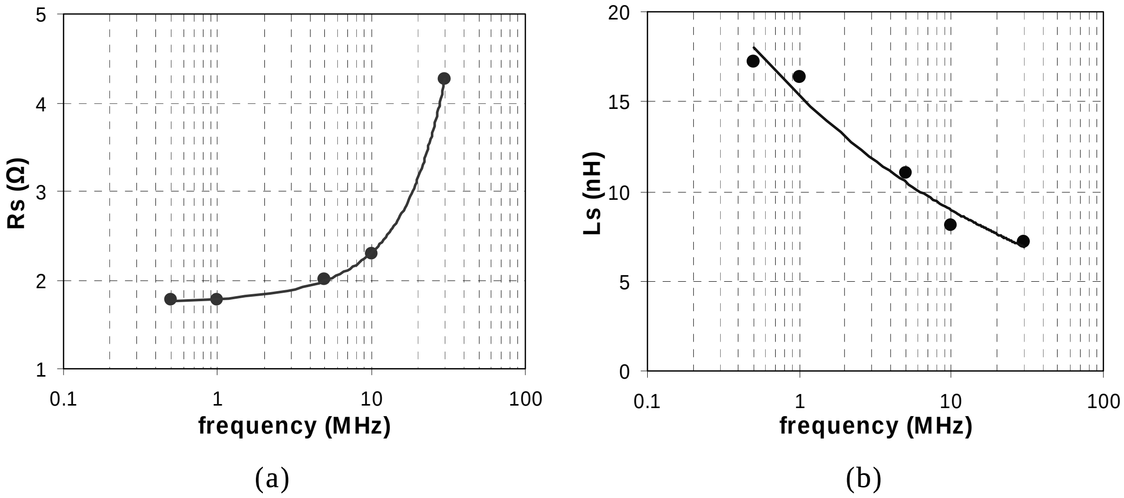

(a) (b)

Figure 5.42: Measured series resistance (R_s) and inductance (L_s) values for different frequencies at zero magnetic field.

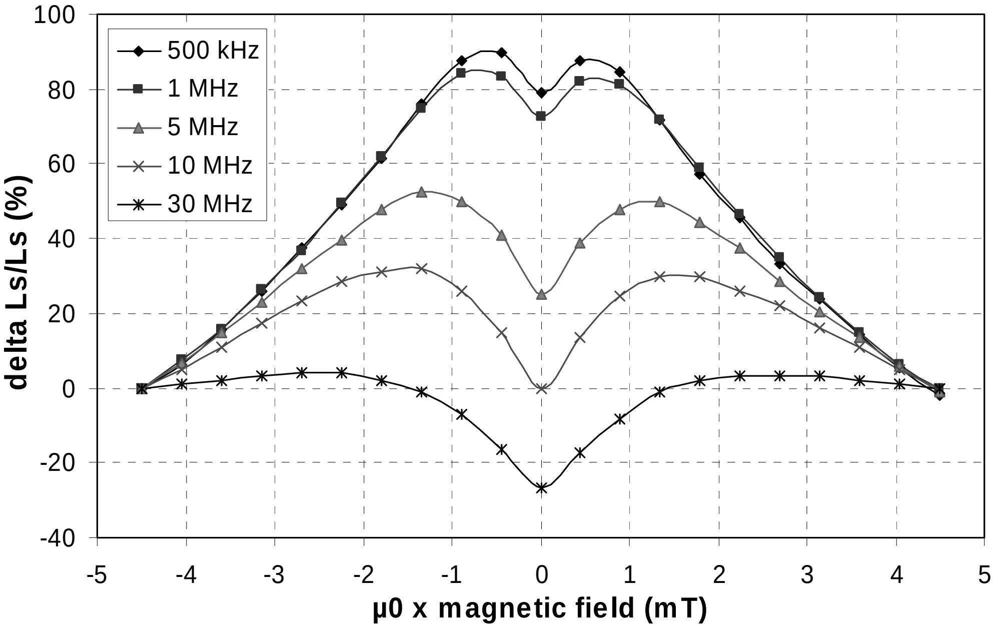

Figure 5.43: The %-change in the inductance value.

Figure 5.43 shows the percentage change in the inductance value of the device with the applied magnetic field H, for different excitation frequencies, which is calculated as [5.5]:

$$\frac{\Delta L}{L}(B)\% = \frac{L(B) - L(B_{\max})}{L(B_{\max})} \times 100 \tag{5.4}$$

where $B=\mu_0 \times H$. Maximum inductance change of 90% is obtained at 500 kHz, and the change is less for higher frequencies. This can be explained by the decrease in the relative permeability (μ_r) value of the electroplated layer for higher excitation frequencies.

5.5 Summary and Conclusion

In this Chapter, a new orthogonal fluxgate sensor structure that can be fabricated by using standard microfabrication techniques is proposed. It consists of two-level planar sensing coils and a core placed on the coils. The core consists of a copper excitation rod and a FeNi layer which surrounds the rod and is electroplated in steps.

The geometrical parameters affecting the operation of the structure are determined and their effects are investigated. It is seen that thicker ferromagnetic layers increase the sensitivity and the linear operation range of the sensor. However, the maximum operating frequency decreases due to the skin effect, and the excitation field required for complete saturation increases. Using a rectangular cross-section is advantageous over the square cross-section in both fabrication and sensitivity points of view. After fixing the cross-sectional geometry, the linear operation range of the sensor is determined by the length of the core length.

The sensing coils should be placed as close as possible to the core, and their pitch should be the minimum that can be fabricated. The wider area occupied by each turn and the increasing number of turns improve the SNR of the sensor in the expense of decreased fabrication yield resulting from the increased line length.

According to the simulations and calculations, 8 µm x 2 µm copper excitation rod surrounded by a 4 µm thick FeNi layer, resulting in 16 µm x 10 µm total core area is decided to be used as the core cross-section. The length of the core is varied between 0.5 mm and 2 mm in order to obtain different operation ranges. Several structures with different dimensions is also designed in order to compensate for possible process variations.

A fabrication process flow is developed for the production of the sensors. The sensing coils are fabricated on a silicon substrate by using sputtered AlSi and SiO_2 layers. The isolation between the core and the coils are provided with a thin SU-8 layer. The core is fabricated by successively electroplating FeNi, Cu, and FeNi layers on a Cr/Cu seed layer.

The measurements show that the sensing coils are fabricated with high yield. Furthermore, the SU-8 layer between the coils and the core provides enough planarization for the following electroplating steps. The electroplated FeNi layer has an intrinsic relative permeability of 10000 at 20 A/m external field, and H_c and B_{sat} values are 70 A/m and 0.85 T, respectively. However, the H_k value is measured as 750 A/m which is more than the expected value, which is caused most probably by the degraded electroplating bath between two FeNi electroplating steps. This would cause more excitation field required for proper operation and decrease the sensitivity of the sensors. The closed ferromagnetic core is formed for the sensors; however, some of the sensor cores contain gaps or cracks inside the electroplating borders, which disturb the magnetic behavior of the layers.

The sensors are tested with various excitation conditions. For the complete saturation of the sensor core, 100 mA-peak current is necessary, and the maximum operating frequency before the skin effect becomes dominant is 200 kHz. The optimum conditions are found at 100 mA-peak sinusoidal excitation of 100 kHz frequency. The sensor having a 0.5 mm long core tested with these excitation conditions has a linear operation range of ±1100 µT, a sensitivity of 102.7 µV/mT, a perming value of 7.1 µT, and an equivalent noise of 268 nT/√Hz at 1 Hz and an RMS noise of 622 nT within 0.3 to 10 Hz bandwidth. The sensitivity, perming and noise figures of the sensor can be improved by increasing the excitation current peak value. The idea of increasing the linear operation range of the sensor by decreasing the core length, while keeping the excitation conditions is verified by the tests of the sensors having different lengths. Linear operation ranges of ±1100 µT, ± 410 µT, and ±160 µT are measured for sensors having 0.5 mm, 1 mm, and 2 mm long cores. The results are in good agreement with the simulations. The linear operation range increases in the expense of reduced sensitivity and increased noise of the sensor. The noise increases more than the decrease in the sensitivity indicating the increase in the Barkhausen noise resulting from scaling down the sensor. The typical resistance of the sensor cores is 2 Ω, which results in an avearge power consumption of 10 mW for 100 mA-peak sinusoidal excitation.

The sensor structure is also tested in parallel fluxgate mode and as a GMI sensor, and different operation principles are compared for the same sensor.

The goal of having a wide linear operation range is achieved with the fabricated structure. However, electroplating is not an easily repeatable process, and successive electroplating steps results in high dependence of the sensor performance on the process variations. Furthermore, gaps formed between two electroplated layers disturb the operation of the sensors. Especially, 2-layer FeNi electroplating is the most critical process of the whole fabrication procedure. The process dependence of the sensor performance can be reduced with a process forming the ferromagnetic core with a single electroplating step. An attempt to realize such a fluxgate sensor structure will be explained in the following chapter.

5.6 References

[5.1] O. Zorlu, P. Kejik, R. S. Popovic, “An orthogonal fluxgate-type magnetic microsensor with electroplated Permalloy core,” Sensors and Actuators A: Phsyical, vol. 135, issue 1, pp. 43-49, March 2007.

[5.2] S. Chikazumi, “Physics of Ferromagnetism,” Oxford University Press, 1997.

[5.3] O. Zorlu, P. Kejik, R. S. Popovic, "Fluxgate-type magnetic microsensors for wide linear measuring range ", Sensors and Applications Symposium (SAS07), San Diego CA,USA, 6-8th February 2007.

[5.4] O. Zorlu, P. Kejik, R. S. Popovic, "Investigation of Giant-Magneto-Impedance (GMI) effect and magnetic hysteresis in microfabricated Permalloy/Coper device," Transducers '07 & Eurosensors XXI conference, Lyon, France, Digest of technical papers vol. 2, Pages 2577-2580, June 10-14th 2007.

[5.5] P. Ripka, “Magnetic Sensors & Magnetometers,” ISBN 1-58053-057-5, Artech House Publishers, January 2001.

CHAPTER VI

RING TYPE FLUXGATE MICROSENSOR

In this chapter, the ring type fluxgate microsensor developed as the 3rd phase of this work is presented. Section 5.1 explains the structure of the sensor. Section 5.2 is on the design issues concerning the core, excitation rod, and the sensing coils of the sensor. Section 5.3 presents the fabrication process flow developed for the sensors, and gives some intermediate results obtained during the fabrication process. Section 5.4 presents the test results of the fabricated sensors. Finally, Section 5.5 summarizes the chapter.

6.1 The Ring Type Fluxgate Structure

The structure of the ring type fluxgate sensor is based on the rod type structures presented in Chapter IV and Chapter V. The macro-scale structure presented in Chapter IV cannot be fabricated by using standard planar fabrication processes. The disadvantage of the structure presented in Chapter V is the 2-step FeNi electroplating that is used to form a closed magnetization path for the excitation field. The gaps and cracks that may possibly occur between these two layers disturb the magnetically closed cross-sectional structure. Also, two-step electroplating decreases the control on the process parameters of the ferromagnetic layer. So it is worth thinking a way to fabricate the ferromagnetic layer in a single step, while keeping the closed magnetization path for excitation.

Figure 6.1 shows the evolution of the ring type structure starting from the rod type sensor. In terms of excitation, the rod structure can be thought as a cascade of thin ring shaped ferromagnetic layers and short excitation rods (Figure 6.1(b)).

Flipping all these structures such that they are aligned on a plane enables fabricating the ferromagnetic layer in one step while keeping the closed magnetization path. A single ring structure can also be used as a fluxgate sensor as in the case of a parallel ring-type fluxgate [6.1], [6.2]. However, that structure has a very high demagnetization factor in the sensing direction, which results in a very low sensitivity. Because of this, several rings overlapping each other should be placed on the plane (Figure 6.1(c)). This provides a lower demagnetization factor along the length of the cascade of the rings than that of a single ring. This makes the new form sensitive to the external magnetic field in the same direction as the previous structure. The excitation rod should be connected in such a way that the two neighboring rods carry current in different directions, enhancing the saturation of the ferromagnetic region between them. In this region the excitation field and the external field are perpendicular to each other. However, the angle between them depends on the position on the ring, and they become parallel to each other at the two sides of the ring. Because of this, the ring type structure is excited in a partially parallel partially orthogonal mode, but the output signal is mainly due to the parallel operation mode. On the other hand, the change of flux can be detected in the same way as presented for other structures, with sensing coils placed under the edges of the ferromagnetic core.

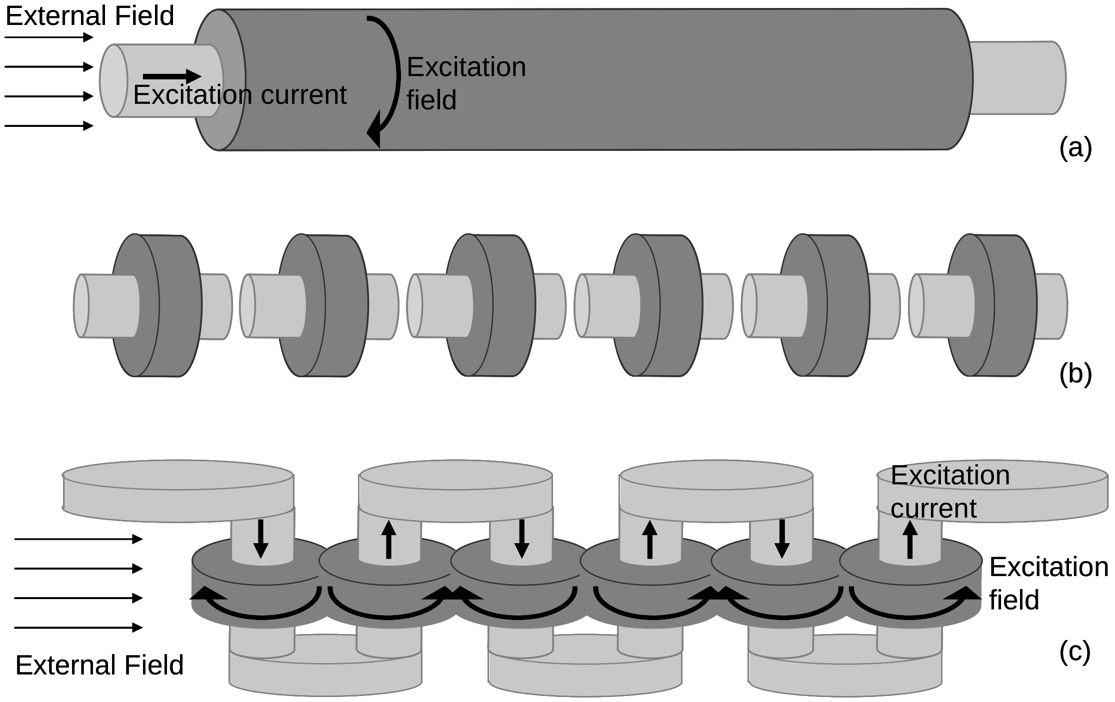

Figure 6.1: The evolution of the ring type structure starting from the rod type structure.

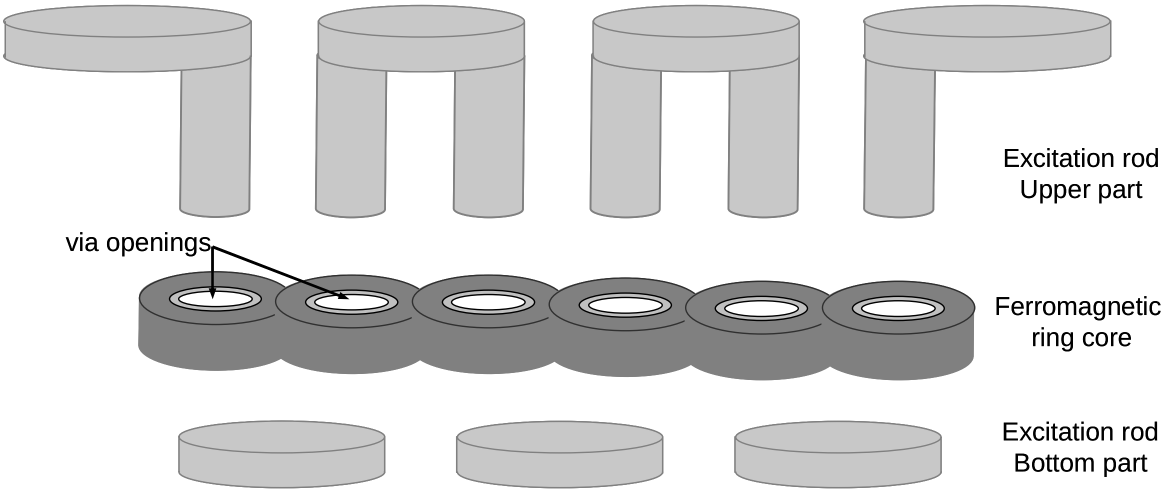

Figure 6.2: The conceptual fabrication process flow of the ring type fluxgate sensor.

Figure 6.2 shows the conceptual fabrication process flow of the ring type fluxgate sensor. The sensing coils are not illustrated in the figure as they can be fabricated in the same way as presented in Chapter V. Above the sensing coils, the sensor core is fabricated in three metallization steps. The isolation of the ferromagnetic part from the excitation rod is provided with an insulating layer. In the first step, the bottom part of the excitation rod is fabricated. Then, the ferromagnetic core is electroplated over the bottom part of the excitation rod. In the last step, the via openings are formed in the insulating layer, through the middle of the ferromagnetic rings, and the upper part of the excitation rod is fabricated.

6.2 Design of the Sensor

In this section, the method followed during the design of the sensors will be introduced. Finite element modeling method is employed during the design of the structure by using Maxwell 3D (ver. 3.10-3.11) as the FEM tool. The core of the sensor is designed based on the single ring element structure. Figure 6.3 shows the top view and side view of a single ring with labeled dimensions. The radius of the excitation rod is labeled as r_1; d_2 is the distance between the excitation rod and the ferromagnetic ring; d_3 is the width of the ferromagnetic ring. The thicknesses of the three isolation layers (t_1, t_3, and t_5), the bottom and upper parts of the excitation rod (t_2, and t_6), and the ferromagnetic layer (t_5) are also shown in the figure. The number of rings forming the structure, n, is another parameter that is not presented in Figure 6.3. The parameters are optimized according to the simulations; however sensors with many different dimensions are designed and fabricated as it is done for the rod-type fluxgate sensor.

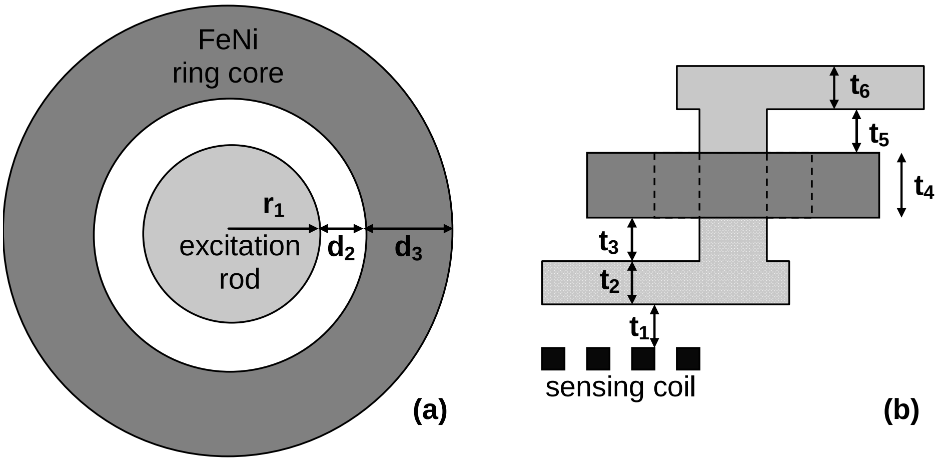

Figure 6.3: Top view (a) and the side view (b) of the single ring structure with labeled dimensions.

6.2.1 The ring radius

The total current required to saturate the core is determined by the total radius of the ring structure ($r_1+d_2+d_3$). In order to decrease the required current, the radius of the excitation rod (r_1) and the distance between the rod and the core (d_2) should be minimized. So, these parameters are determined by the fabrication technology limits. On the other hand, the width of the ferromagnetic ring (d_3) has to be optimized as wider layers increase the linear operation range of the sensor as well as the excitation current required to saturate the core. Figure 6.4 shows the simulation results for different ring structures with r_1 and d_2 are fixed to 3 µm and 4 µm, respectively, while d_3 is varied between 3, 6, 10, and 15 µm. The core thickness (t_4) is set to 2 µm. The simulated ferromagnetic material has B_{sat} and H_k values of 0.85 T and 200 A/m, respectively, and the current passing through the excitation rod is 20 mA. The plotted value is the magnitude of the magnetic flux density on the cutplane at the middle of the ferromagnetic core. As the radius of the structure increases, the outer edges of the core require more current for saturation. It is possible to saturate a structure having a 6 µm wide ferromagnetic core with a current slightly higher than 20 mA.

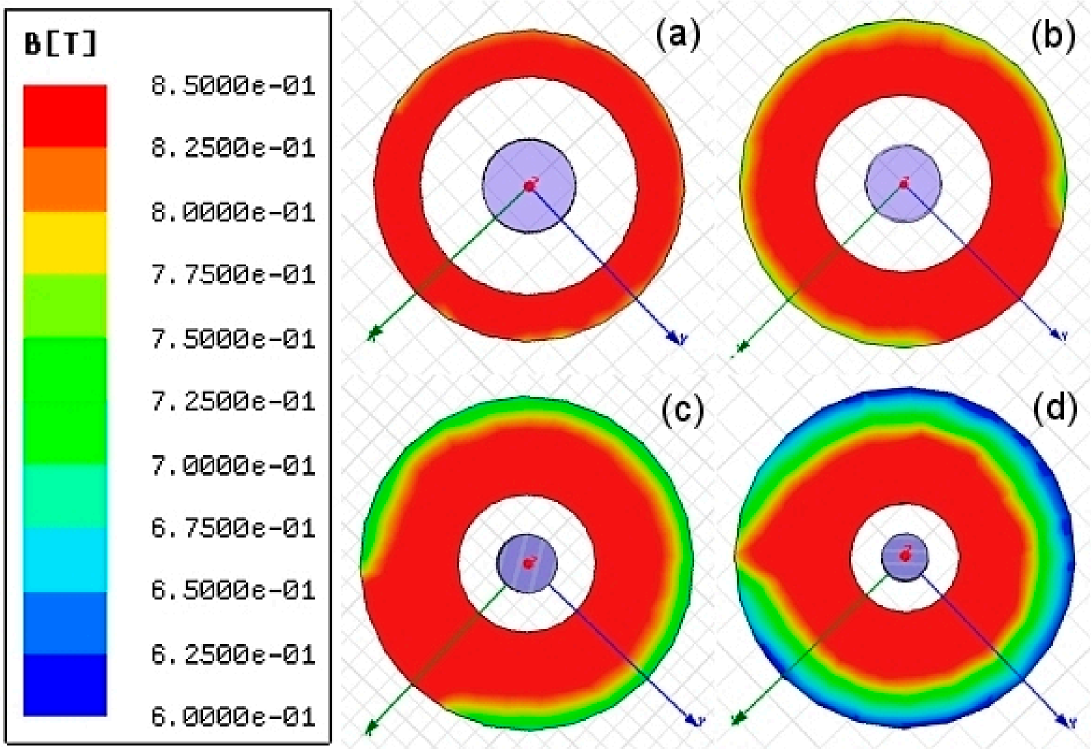

Figure 6.4: The distribution of the magnetic flux density inside the ferromagnetic core for different structures with core widths: (a) 3 µm, (b) 6 µm, (c) 10 µm, and (d) 15 µm. The r_1 and d_2 values are fixed to 3 µm and 4 µm, respectively.

6.2.2 The core thickness

Increasing the core thickness increases the linear operation range, however, limits the maximum operation frequency of the sensor. Figure 6.5 shows the results obtained by simulating two cores composed of 12 rings (r_1= 3 µm, d_2= 4 µm, d_3= 6 µm) with 2 µm and 4 µm thicknesses. The ferromagnetic material has an intrinsic relative permeability of 10000. The flux is calculated by integrating the B_z value on a plane which is 6 µm under the core as given in Equation 5.1. Increasing the core thickness increases the linear operation range, and this increase is almost proportional. A slight increase in the sensitivity is also observed in the simulation results. On the other hand, increasing the thickness of the ferromagnetic layer increases the thickness of the via openings, and this makes the fabrication process more difficult and less reliable. Therefore, thinner layers are preferred for the ferromagnetic core, as it will be discussed in Section 6.3.

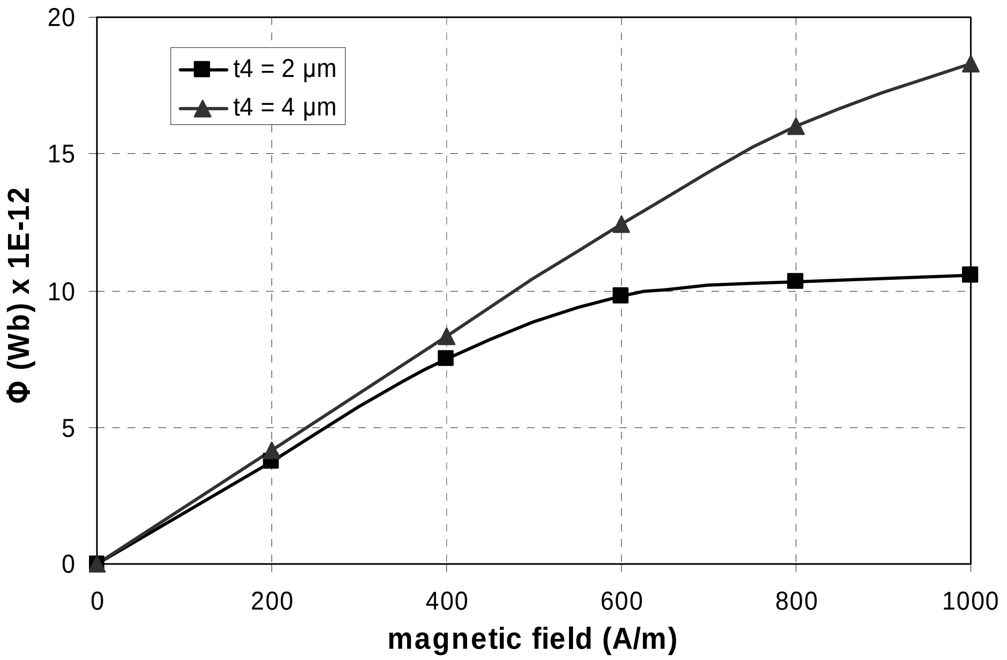

Figure 6.5: Simulation results of two cores composed of 12 rings with 2 µm and 4 µm thicknesses.

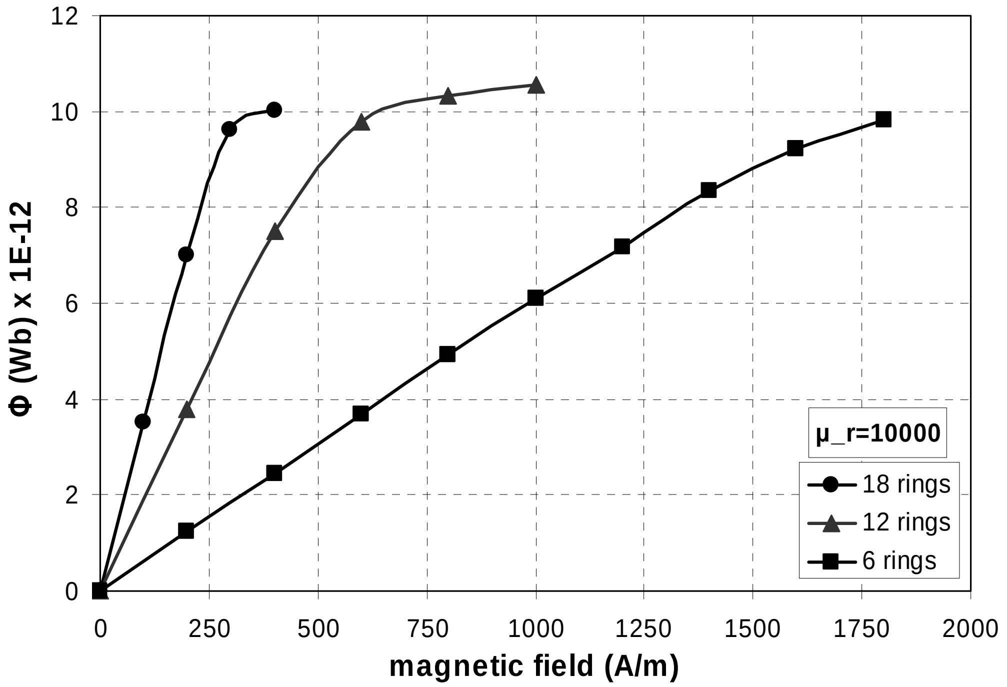

Figure 6.6: The effect of the number of rings on the linear operation range and sensitivity.

6.2.3 The number of rings

The number of rings to be used determines the sensitivity and the linear operation range of the resulting structure. Figure 6.6 shows the effect of the increased number of rings on the linear operation range and sensitivity. The increase in the linear operation range with smaller number of rings due to the increasing demagnetization effect is verified with the simulation results. A linear range of around 1600 A/m can be obtained by using 6 rings. However, the sensitivity is very low for this case, and this may reduce the resolution of the sensor. The sensitivity increases with higher number of rings. A reasonably wide linear range and high sensitivity can be obtained by using 12 rings to form the core.

6.2.4 The thickness of the isolation layers

The thickness of the first two isolation layers (t_1 and t_3) should be minimized in order to have a minimum distance between the core and the sensing coils. This increases the sensitivity of the sensor as previously presented in Chapter V in Figure 5.17. So, these thickness values are limited with the fabrication technology: The isolation layer should be thick enough to isolate the layer over and under it, and should provide a planar surface for the rest of the process. The required minimum thickness depends on the material and the technology of deposition. For example for SU-8 and polyimide layers deposited by spin coating, a safe thickness value may be determined by increasing the maximum thickness change of the underlying layer by 50 to 100%. The 1st isolation layer which will cover a 0.5 µm metal layer may be around 1 µm-thick. Similarly, the 2nd isolation layer covering a 2 µm-thick metal layer may be around 3 µm-thick.

The thickness of the 3rd isolation layer (t_5) is one of the parameters determining the via depth. It is more difficult to open a deeper via while keeping the opening area fixed. On the other hand, a planar surface for the last metal layer is necessary in order to improve the adhesion between the layers. This can be obtained by having a thicker layer. So, doubling the thickness of the underlying FeNi core, resulting in 4 µm-thick layer, is a reasonable choice for the 3rd isolation layer.

6.2.5 The thickness of the excitation rod

Both lower and upper parts of the excitation rod should be thick enough to carry the current required for saturation of the ferromagnetic core. Furthermore, the upper part of the excitation rod should be thick enough to cover the step that forms the via whose thickness is the sum of t_3, t_4, and t_5. Furthermore t_3 is determined according to the thickness of the lower part of the excitation rod (t_2). Due to these, it is decided to use different thicknesses, 2 µm and 2.5 µm, for the lower and upper parts of the excitation rod, respectively.

6.2.6 Placement of the sensing coils

Two-level AlSi sensing coils with 2 µm line width and 2 µm spacing are used for detecting the output signal of the sensor. Analysis for the rod-type sensor presented in Section 5.2.2 shows that increasing the number of turns of the sensing coil increases both the sensitivity and the SNR of the sensor. In addition to that, wider turns also result in higher SNR values. According to these conclusions, the number of turns of the sensing coils is limited by the reliability of the fabrication technology.

The same arguments are also valid for the ring-type sensors, however, the total length of the ring type sensors is typically between 100 µm and 250 µm, which is much shorter than the rod-type sensor. The length of the sensor core already limits the number of turns. Because of this, the sensing coils are designed in such a way that the shortest structures have as many turns as possible: The first turn is very narrow and placed under the edge of the sensor core, turns are continued up to the center of the core. With this configuration, 6, 12, and 18-ring devices have 12, 25, and 39 turns respectively for each level of sensing coils centered under each edge of the sensor core.

6.3 Fabrication

Figure 6.7 shows process flow developed for the fabrication of the ring-type fluxgate sensors. The detailed process flow is given in Appendix II. Silicon wafers with 4 inch diameter are used as substrates for the fabrication of the sensors. There is a 0.5 µm-thick SiO_2 layer on the wafers, which provides electrical isolation between the substrate and the sensor parts (Figure 6.7(a)). The fabrication starts with forming two-level sensing coils separated by an isolation layer on the substrate (Figure 6.7(b)). The sensing coils are made of 0.5 µm-thick AlSi(1%), and 0.8 µm-thick SiO_2 is used as the isolation layer. These layers are deposited by sputtering and patterned by dry etching.

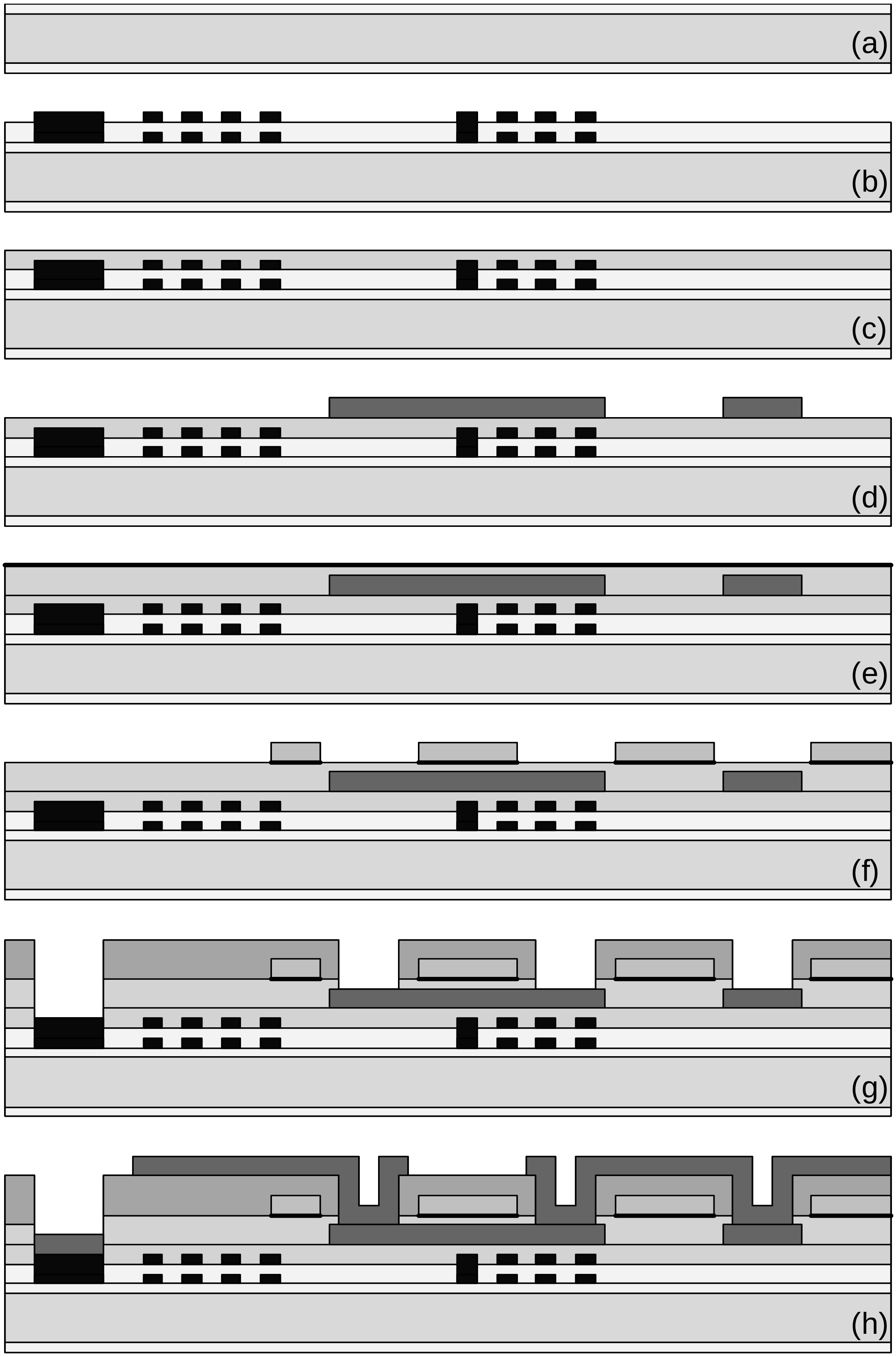

Figure 6.7: The cross-sectional view of the fabrication process flow of the ring-type sensor.

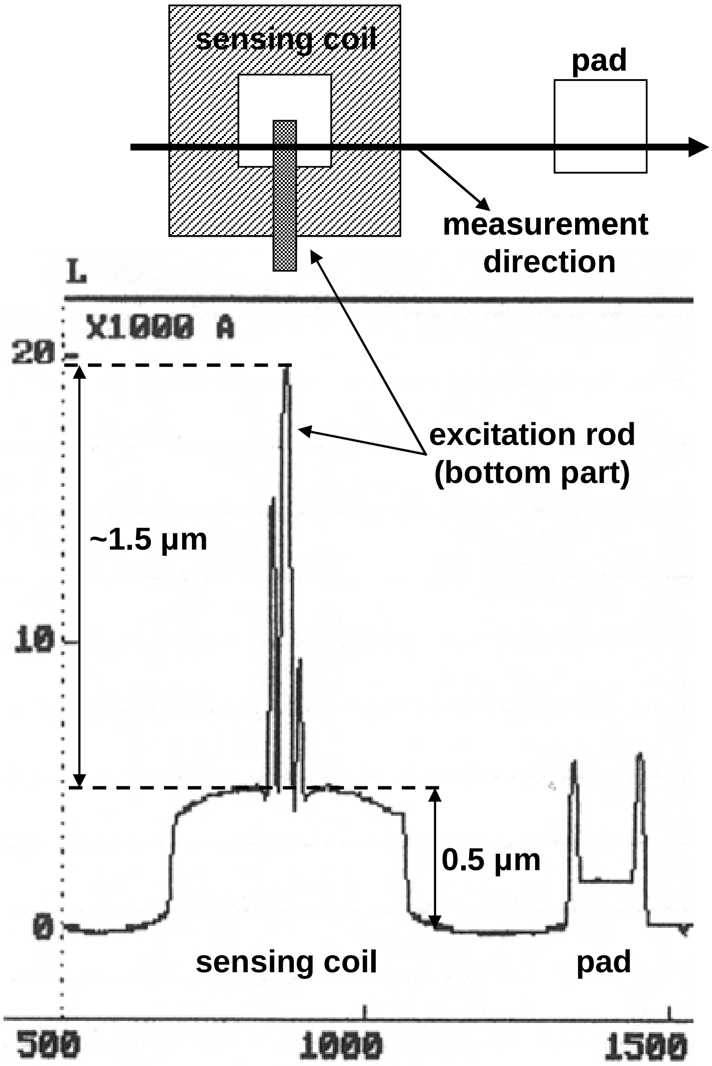

Figure 6.8: The surface profiler scan of one of the sensors after the 2nd polyimide coating.

A passivation layer is formed on the coils by spinning a 1.5 µm-thick polyimide [6.3] layer over the coils (Figure 6.7(c)). Polyimide is selected over previously used SU-8 since it can be anisotropically patterned by dry etching, resulting in higher aspect ratio of the openings with the available fabrication technology. Actually, SU-8 provides a more planar surface than polyimide does, for the same coating thickness and surface topography. Because of this, a thicker layer should be coated if polyimide is used instead of SU-8 as the isolation layer. A low viscosity polyimide (PI-2610) is used for this process.

After this step, the 3rd AlSi layer is deposited and patterned over the polyimide layer (Figure 6.7(d)). This layer serves as the bottom part of the excitation rod. The thickness of the metal layer is selected as 2 µm, since low resistance is required for the excitation rod. The 2nd polyimide layer, which is 2.5 µm-thick is covered over the 3rd metal layer. Figure 6.8 shows the surface profiler scan of one of the sensors after coating the 2nd polyimide coating. A decrease from 0.8 µm to 0.5 µm over the sensing coils, and 2 µm to 1.5 µm over the bottom part of the excitation rod is observed. Comparing these result with the ones presented in Chapter V for SU-8 process verifies that SU-8 provides a more planar surface whereas polyimide results in a more conformal coating.

Next step is the evaporation of a 20 nm/200 nm Cr/Cu seed layer on the surface (Figure 6.7(e)). This layer is used as the seed layer for the FeNi electroplating step. An AZ9260 photoresist mold is provided for electroplating the ferromagnetic ring core structures. Then, the FeNi layer is electroplated into the openings of the photoresist mold. The electroplating is performed at 40 °C with 14.5 mA/cm^2 current density. The earth magnetic field around the cathode is kept constant for this process in order to induce a slight magnetic anisotropy and an easy axis along the length of the sensor cores. After the electroplating the photoresist is removed and the seed layer is stripped over the wafer by wet etching, without using any protective mask (Figure 6.7(f)).

The 3rd and the last polyimide layer is coated over the FeNi layer. The thickness of this layer is 3.5 µm, covering the FeNi layer. The used polyimide is a more viscous one, called PI 2611. The polyimide is patterned after this step by dry etching with an AZ9260 photoresist mask. This step etches all the polyimide layers down to the AlSi layer underneath the etching region, and provides the via openings for the excitation rod and the pad openings for the sensing coils (Figure 6.7(g)). The thickness and accordingly the etching time difference for different regions is not critical thanks to the high etching ratio of the process between AlSi and polyimide.

The last step of the process is the deposition and patterning of the 4th AlSi layer. This layer forms the upper part of the excitation rod including the via fillings. A slightly higher thickness of 2.5 µm is selected in order to ensure enough step coverage at the via regions for electrical contact. Figure 6.9 shows the SEM views of the via regions having 12 µm (a and b) and 3 µm radius (c). The step coverage of the metal layer is good enough to provide electrical contact even for the smallest structures.

Figure 6.10 shows the photograph of one of the fabricated wafers. There are 1400 cells on each wafer including sensors and test structures, with 2 mm x 1.5 mm dimensions. Figure 6.11 shows the microscope picture of one of the fabricated sensors having a 12-ring core.

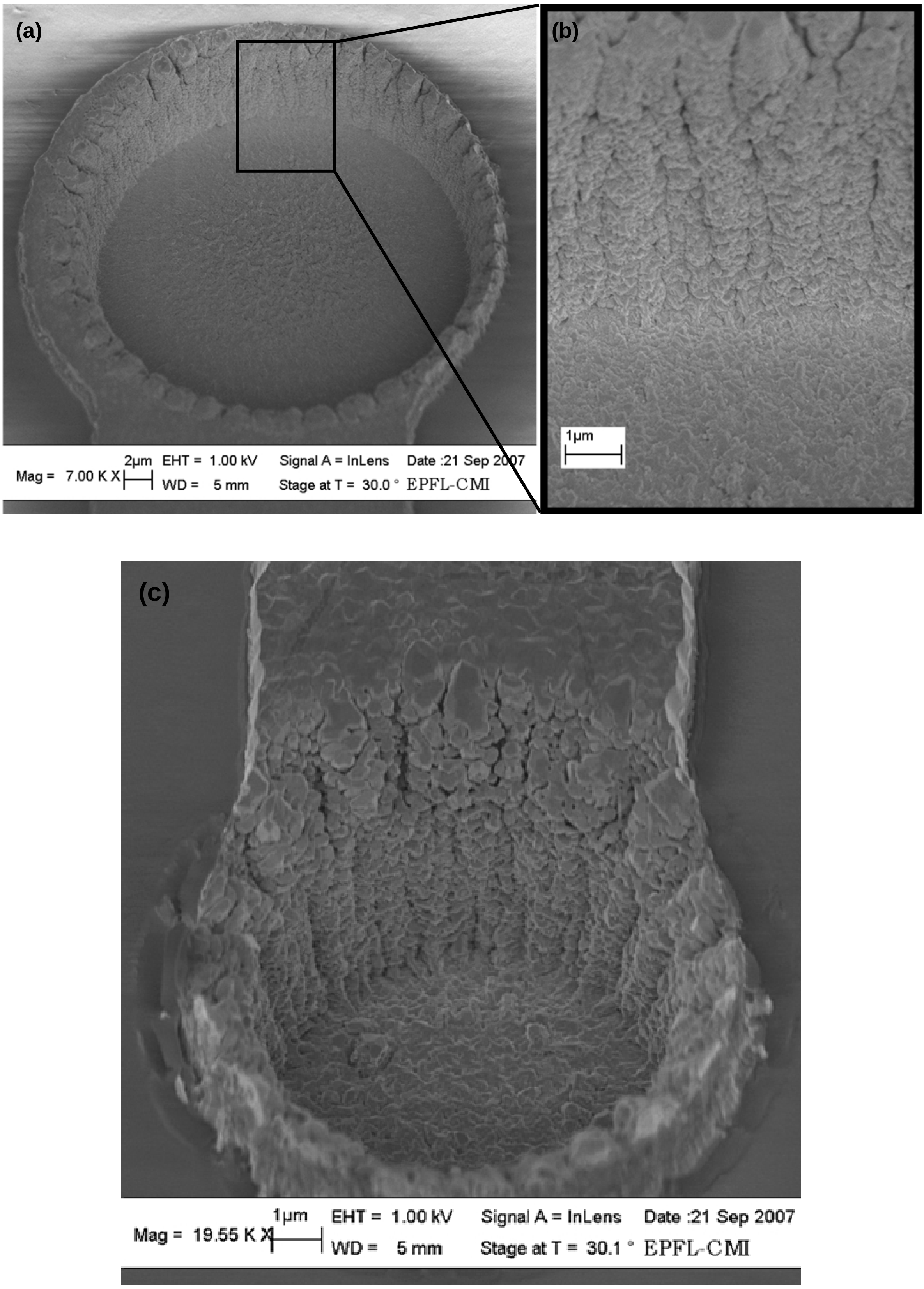

Figure 6.9: The SEM views of the via regions having 12 µm (a and b) and 3 µm radius (c), showing the step coverage of the 4th metal layer.

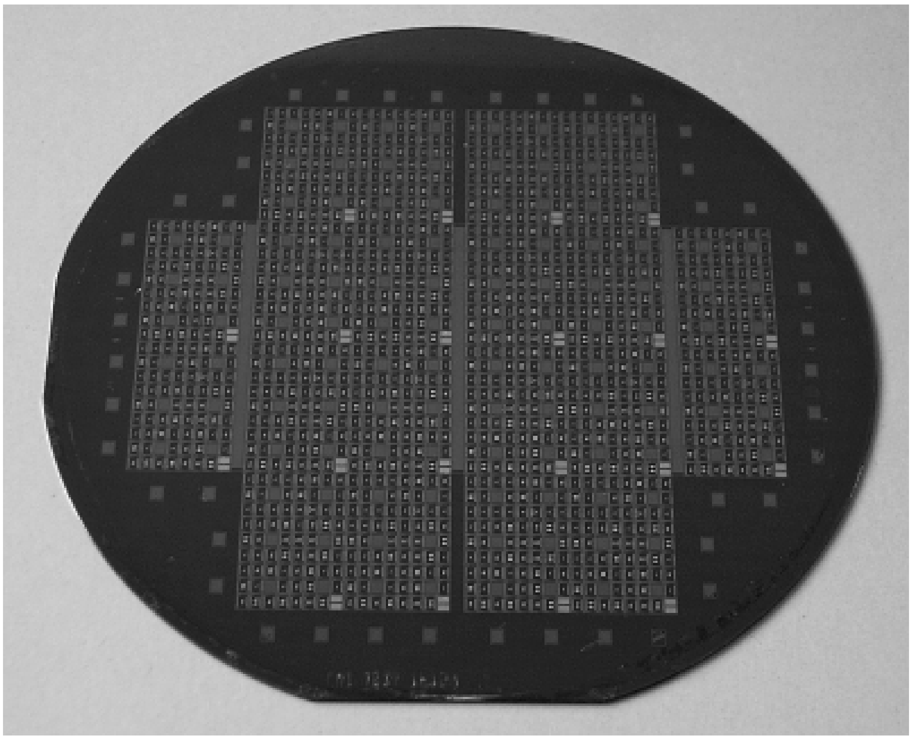

Figure 6.10: Photograph of the fabricated wafer.

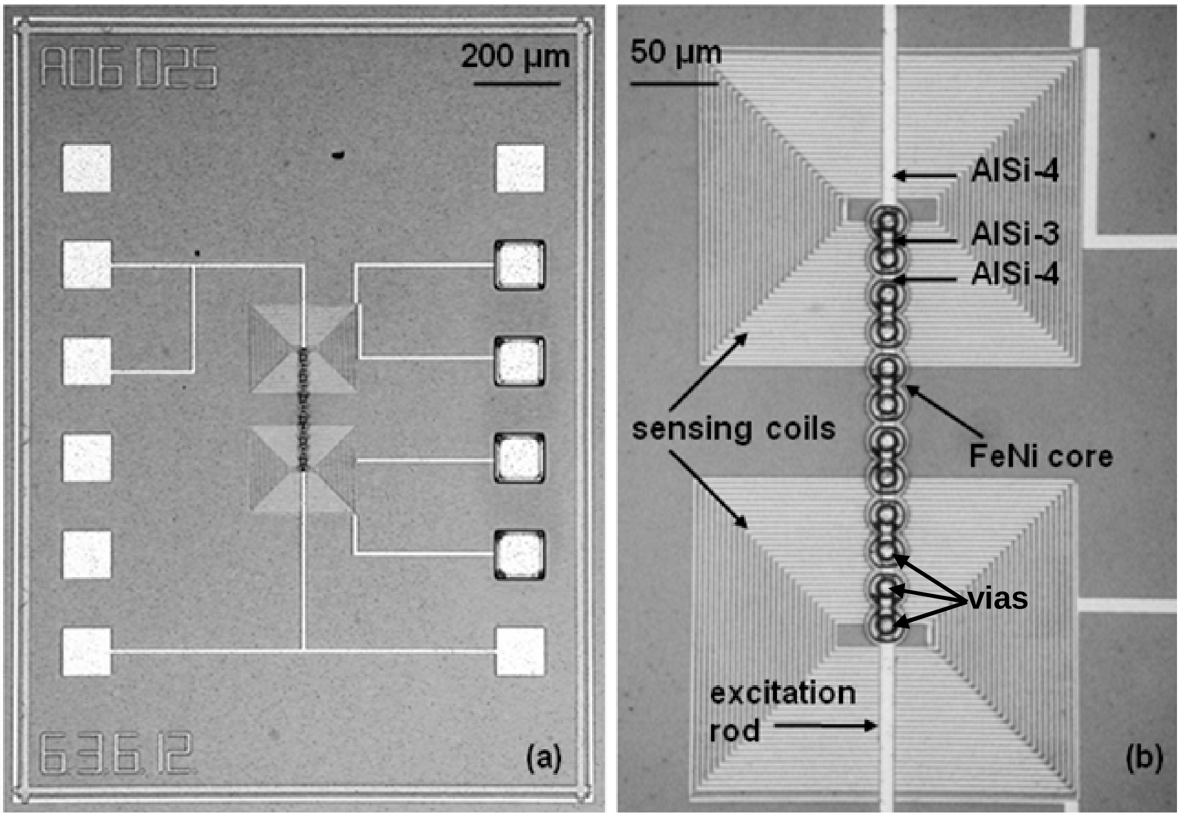

Figure 6.11: Microscope picture of one of the fabricated sensors having a 12-ring core.

6.4 Sensor Test Results

In this section, the test results of the fabricated sensors will be presented. These tests include characterization of the ferromagnetic layer and the analysis of the fabricated sensor responses.

6.4.1 Electroplated Ferromagnetic Layer Properties

The electroplating of the FeNi layer is done by using Bath III. The magnetic properties of the resulting layer are determined by measuring its magnetization (M-H) curve. Figure 6.12 shows the measured M-H curve of a 1.25 mm x 35 mm FeNi layer which is placed over the wafer as a test structure, and electroplated at the same time with the structures. The M-H curve is measured by using the induction method, as described in Chapter III. The measured H_c and H_k values are 60 A/m and 130 A/m, respectively. The relative permeability of the material is around 30000 with an assumed B_{sat} value of 0.85 T. The obtained results are in agreement with the ones obtained in Chapter III, due to the use of a fresh electroplating bath.

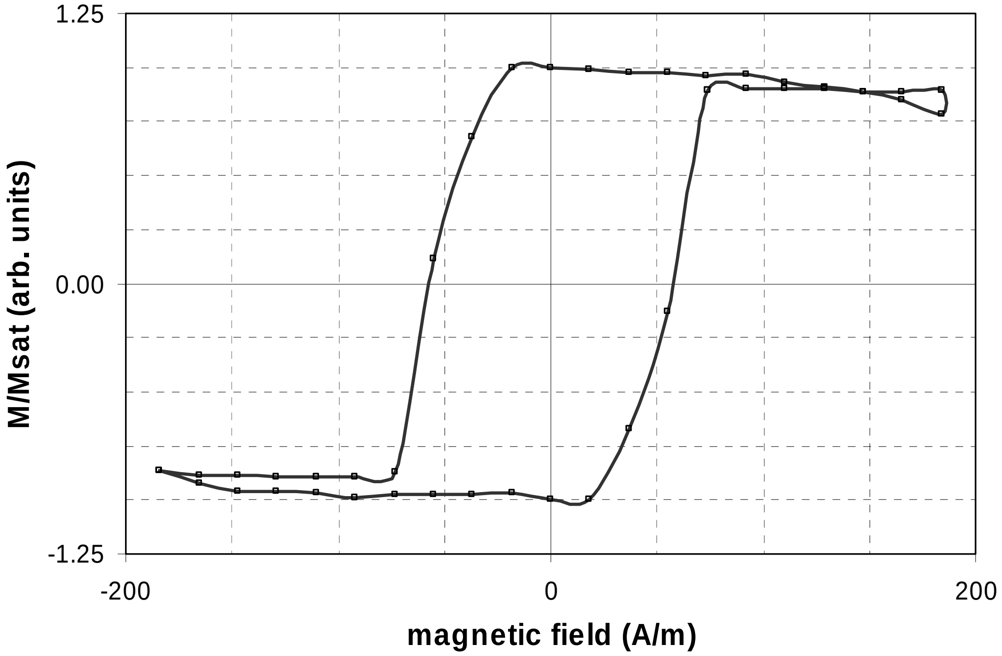

Figure 6.12: M-H curve of the electroplated layer.

Figure 6.13 presents the thickness values of the electroplated FeNi layers. The measurements are taken with a surface profiler, at the regions where the data is written. The thickness of the same structure is measured at each region. When this measurement is compared to the similar measurements presented in Chapter V, much smaller variation is observed for this case. This is due to the uniformly distributed electroplating area over the wafer. For both of the designs, there are dummy electroplating regions placed on the wafer with much larger area with respect to the core electroplating area. These regions are used to control the current density against the possible area changes of the electroplating region that may be caused by over- or under-exposure of the molding photoresist. Figure 6.14 shows the dummy electroplating regions on the wafer level layouts of the rod-type (a) and the ring-type (b) fluxgate sensors. The dummy electroplating regions are collected at the edges of the wafer in triangular shapes for the rod-type sensor layout. The electroplated core areas which are very close to these dummy structures tend to be thinner as the current prefers a conduction path through the dummy electroplating regions which occupy a larger area. In the middle regions of the wafer, the core electroplating becomes thicker, since these structures are away from the dummy regions. However, for the ring-type sensor, the dummy electroplating regions are placed uniformly over the wafer, leading to a more uniform current and resulting FeNi layer thickness distribution over the wafer.

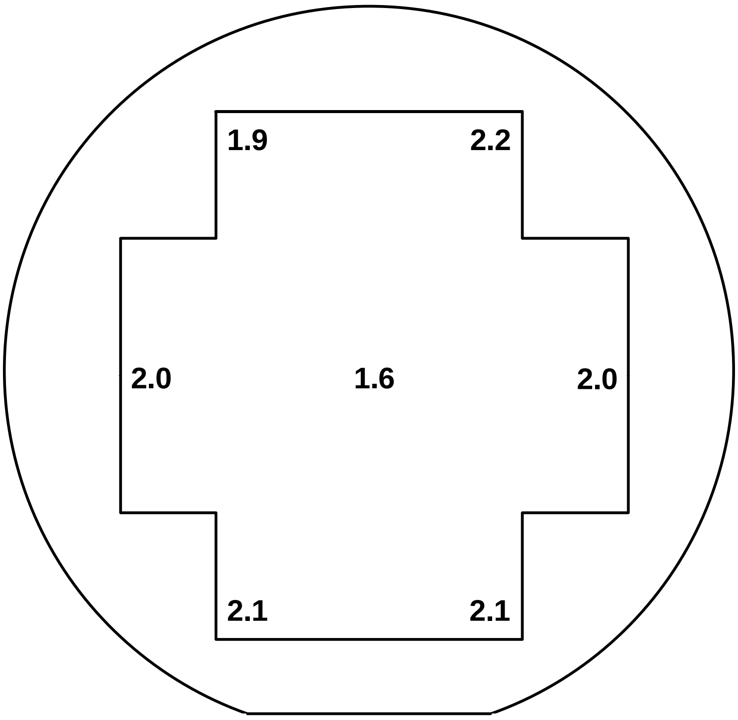

Figure 6.13: The thickness measurement of the electroplated FeNi layers.

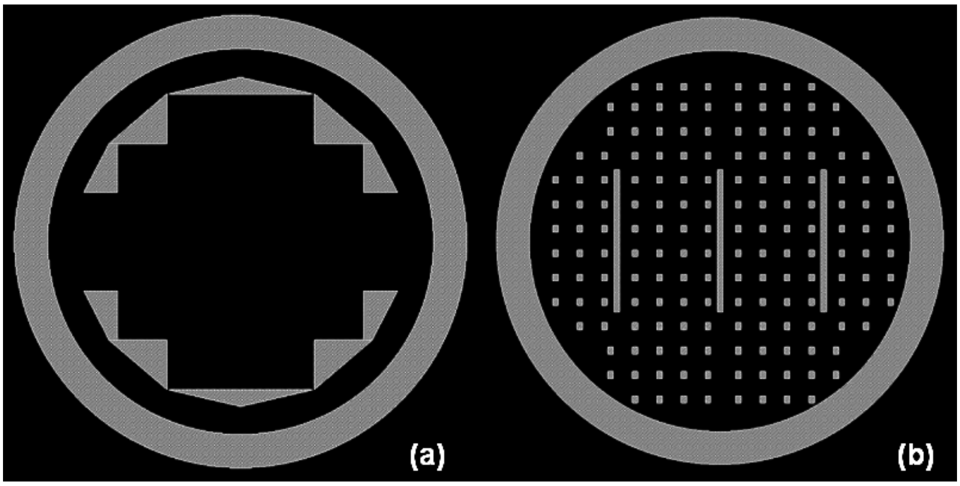

Figure 6.14: The dummy electroplating regions on the wafer level layouts of the rod-tpye (a) and the ring-type (b) fluxgate sensors.

6.4.2 The sensor performance

The signal conditioning of the sensor is done by external electronics. The same setup described in Chapter IV and Chapter V is used during the experiments. However, for the ring-type fluxgate sensor, various operating frequency values are tested.

Figure 6.15 shows the response of a sensor for two different excitation current peak values at 100 kHz frequency. The sensor has 18 rings and the r_1, d_2, and d_3 dimensions of the rings are 3 µm, 4 µm, and 6 µm, respectively. The thickness of the FeNi layer (t_4) is 2 µm. The sensor has a 300 µT linear operation range with 248 µV/mT sensitivity for 170 mA-peak excitation. The obtained linear operation range is in good agreement with the simulation results presented in Figure 6.6.

The response of the sensor with 85 mA-peak current has a wide hysteresis loop, showing that the sensor cannot be completely saturated with this current value. According to the measured DC M-H curve of the electroplated FeNi layer and the simulations, even a 50 mA-peak excitation current should be enough for deep saturation of the sensor core with the corresponding dimensions. One reason of the disagreement with the simulation and test results may be the increased H_k value of the AC hysteresis curve of the FeNi layer. Another reason may be a short circuit between the core and the excitation rod, which changes the flow direction of the applied current. Unfortunately, there were no test structures on the wafer that can be used to test this condition.

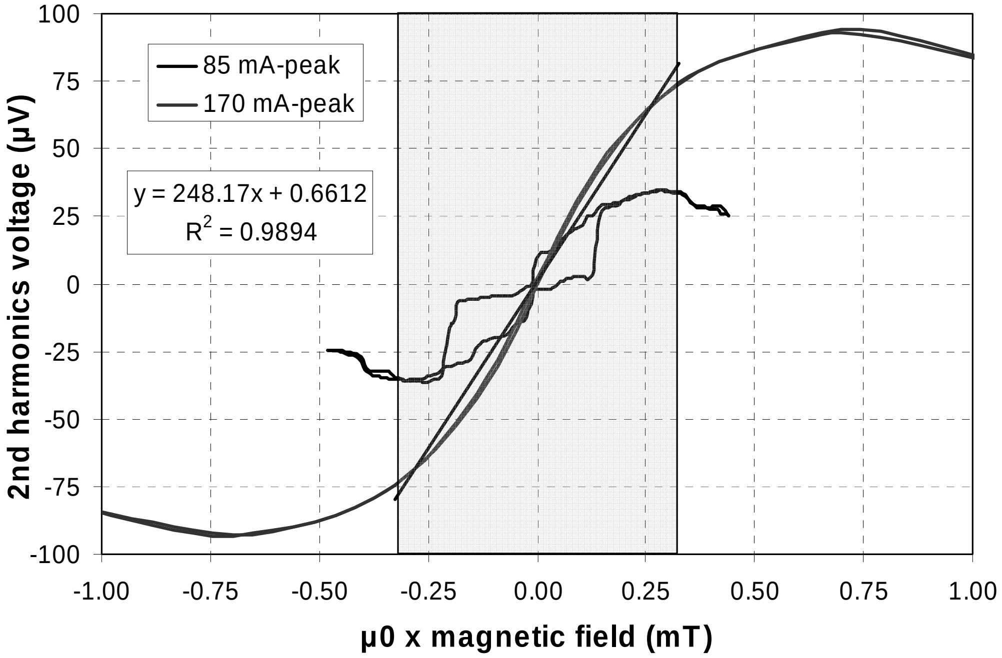

Figure 6.15: The response of a sensor for two different excitation current peak values at 100 kHz frequency. The linear operation range is 300 µT with 248 µV/mT sensitivity.

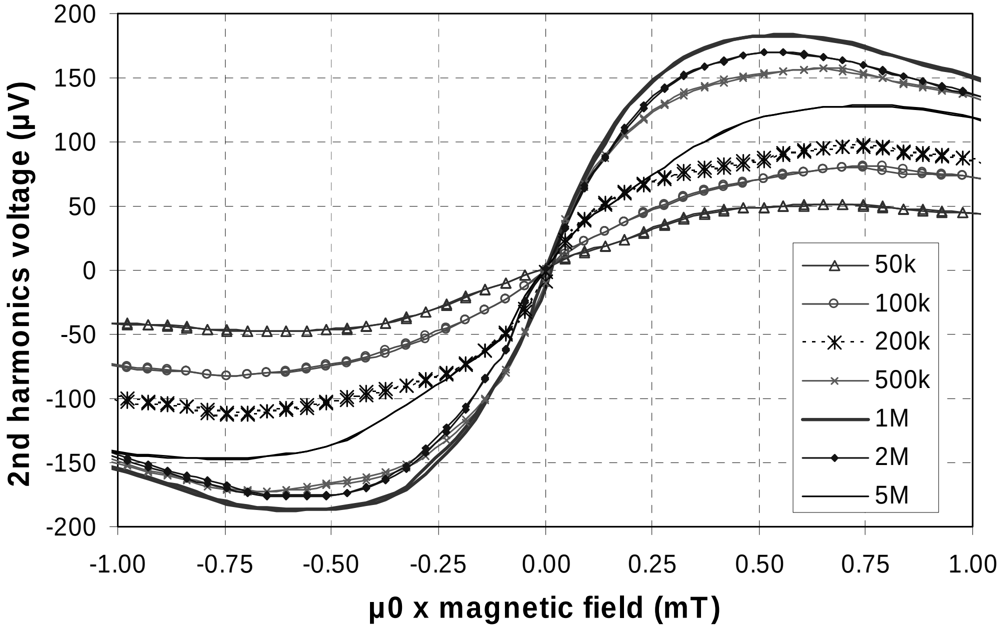

Figure 6.16: The response of the sensor for different excitation current frequency values, with highest sensitivity at 1 MHz excitation frequency.

Figure 6.16 shows the response of the sensor for different excitation current frequency values. The sensitivity of the current increases with the frequency up to 1 MHz. For higher frequencies, a decrease in the sensitivity is observed due to the decreasing relative permeability of the electroplated FeNi layer. The increase in the operation frequency with respect to the rod type micro fluxgate sensor is due to the thinner FeNi layer and the fresh electroplating solution. The linear operation range stays almost unchanged for different excitation frequencies. A linear range of 300 µT can be reached with 620 µV/mT sensitivity at 1 MHz excitation frequency.

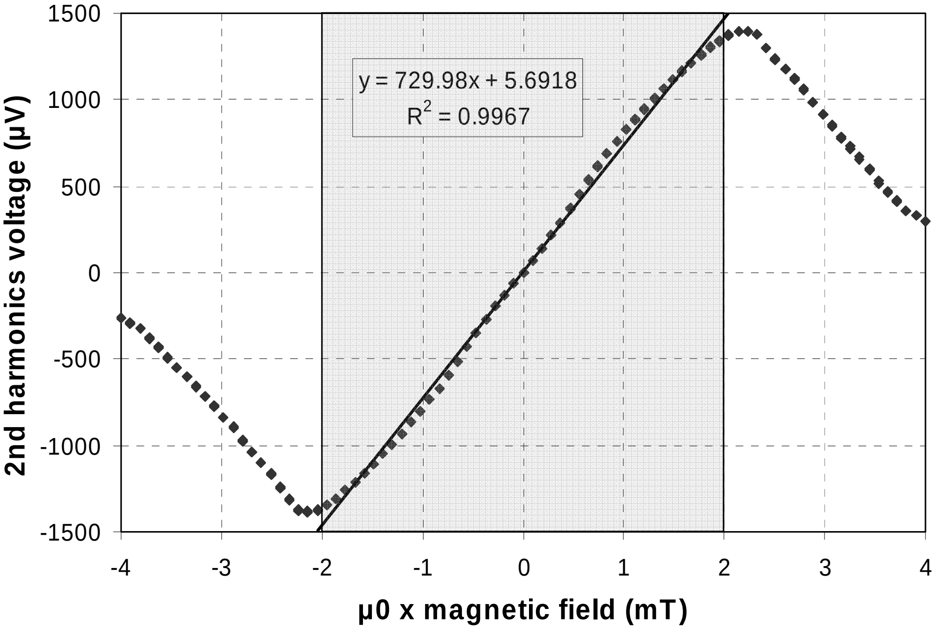

Figure 6.17: The response of the sensor excited at 1 MHz with 180 mA-peak current.

The maximum linear operation range and sensitivity is obtained with a structure composed of 4 rings and has r_1, d_2, and d_3 dimensions of 12 µm, 10 µm, and 16 µm, respectively. The thickness of the FeNi core is 2 µm. Figure 6.17 shows the response of the sensor excited at 1 MHz with 180 mA-peak current. The linear operation range of this sensor is 2 mT, with a sensitivity of 730 µV/mT. The increase in the linear operation range with respect to the sensor with 18 rings is due to the much higher demagnetization factor of the structure. The sensitivity of the sensor is slightly higher than the previous sensor, and this is due to the increased amount of magnetic material existing in the larger ring structure. Furthermore, the excitation current value that is used is an expectable value for the ferromagnetic rings with 38 µm outer radius. This may show that there is no short circuit between the core and the excitation rod for this structure, and the current flows only through the excitation rod in the designed direction.

6.5 Summary and Conclusion

In this chapter, a ring type fluxgate sensor that can be fabricated by using standard microfabrication techniques is proposed. The structure is developed based on the rod-type orthogonal fluxgate. However, the resulting sensor has a partially parallel-partially orthogonal configuration. The new structure enables the fabrication of the ferromagnetic core of the sensor in a single electroplating step while keeping the closed magnetic excitation path.

The sensor consists of 2-level AlSi pickup coils, an AlSi excitation rod which is fabricated in two steps, and a FeNi ferromagnetic core. The ferromagnetic core is composed of cascaded ring structures. The AlSi layers are fabricated by sputtering and dry etching, whereas the FeNi core is electroplated. The isolation layers between metal layers is formed by using polyimide, which can be patterned by dry etching in order to form the via openings.

The geometrical parameters affecting the operation of the structure are determined and their affects are investigated. It is seen that thicker ferromagnetic layers increase the sensitivity and the linear operation range of the sensor. However, thicker layers increase the thickness of the via opening and makes the fabrication process more difficult. Increasing the outer radius of the ferromagnetic ring increases the sensitivity and the linear operation range, as well as the excitation current required to saturate the sensor.

The designed ring cores have 2 µm thickness and inner and outer radius dimensions of 7 µm, and 13 µm, respectively. The number of rings forming the sensor core is varied between 6 and 18. Several structures with different dimensions is also designed in order to compensate for possible process variations. Furthermore, the dummy electroplating regions are distributed more uniformly over the wafer, resulting in a more uniform electroplated FeNi layer thickness distribution.

The measurements show that the polyimide layers provide more conformal surface than SU-8, but still can be used as the isolation layer for the process. The possible short circuits between the excitation rod and the ferromagnetic core may be because of this non-planar surface, which increases the undercut during the dry etching of the polyimide layer.

The electroplated FeNi layer has H_c and H_k values of 60 A/m and 130 A/m, respectively. The relative permeability of the material is around 30000 with an assumed B_{sat} value of 0.85 T. The uniformity of the electroplating is also increased with the uniform placement of the dummy electroplating areas.

The 18-ring core sensor has a liner operation range of 300 µT and a sensitivity of 248 µV/mT with a 170 mA-peak sinusoidal excitation at 100 kHz operating frequency. The output of the sensor contains a hysteresis loop for smaller excitation current values. This may be due to the short circuit between the core and the excitation rod. Unfortunately, the structures wth 6 and 12 cores could not be tested due to the same problem.

The tests with higher excitation frequency values showed that the maximum sensitivity is obtained at 1 MHz for the 18-ring core sensor. Furthermore, the linear operation range is not affected significantly from the changes in the excitation frequency.

The maximum linear operation range is obtained with another structure composed of 4 rings having inner and outer radius dimensions of 22 µm, and 38 µm, respectively. The measured linear range is 2 mT with 180 mA-peak excitation current at 1 MHz frequency.

The goal of having a wide linear operation range is achieved with the fabricated structure. However, polyimide coating and dry etching processes should be revised in order to increase the yield of the sensors. Using thicker polyimide layers in order to obtain a more planar surface and possibly increasing the dimensions of the ferromagnetic ring structures may increase the reliability of the fabrication process.

6.6 References

[6.1] L. Perez, C. Aroca, P. Sanchez, E. Lopez, M. C. Sanchez, “Planar fluxgate sensor with an electrodeposited amorphous core,” Sensors and Actuators A: Phsyical, vol. 109, issue 3, pp. 208-211, January 2004.

[6.2] P. Ripka, “Advances in fluxgate sensors,” Sensors and Actuators A: Phsyical, vol. 106, issue 1-3, pp. 8.14, September 2003.

[6.3] "Product Application Areas," HD Microsystems, 2007, Online, 23 Dec. 2007, http://www.hdmicrosystems.com/prod/app.html.

CHAPTER VII

CONCLUSIONS AND OUTLOOK

In this chapter, the achievements of this thesis are summarized. Then, the performance figures of the realized sensors are compared with the previously reported state of the art fluxgate sensors. The chapter is finalized by listing several suggestions for the further improvement of the fabrication processes and the sensor performances.

In the scope of this work, fluxgate sensor structures suitable for operation within a wide linear range are developed, fabricated, and characterized. The fabricated sensor structures are named as: rod type orthogonal macro fluxgate sensor, rod type orthogonal micro fluxgate sensor, and ring type micro fluxgate sensor. All of the structures have a CMOS compatible fabrication process flow. Furthermore, the rod type micro sensor and the ring type sensor are fabricated by using only standard thin film deposition and photolithography techniques, enabling batch fabrication of these sensor structures. All of the structures use planar sensing coils and an electroplated FeNi core.

The objectives of operation within a wide linear range, low power dissipation, and small sensor size are achieved with the microfabricated fluxgate sensors. With the rod type orthogonal macro fluxgate sensor the idea of increasing the linear operation range without changing the excitation requirements by using a closed magnetization path for excitation and the orthogonal fluxgate operation is verified. This structure contains a gold bonding wire serving as the excitation rod, and a FeNi layer electroplated over this wire. Inclusion of the bonding wire to the fabrication process prevents the sensor from having a wafer level batch fabrication process. In the second phase of this work, the sensor structure is modified and miniaturized in such a way that it can be fabricated in wafer level, forming the rod type orthogonal micro fluxgate sensor as an integrated solution, to which the same idea can be applied. The core of this structure consists of an electroplated copper excitation rod which is sandwiched between two electroplated FeNi layers. The test results of this sensor show that the main goals of this work are achieved. On the other hand, it is also seen that 2-level FeNi electroplating decreases the control on the magnetic properties of the core. This could be improved by having a single FeNi electroplating step. As a result of this foresight, an alternative structure is presented as the third phase of the work, named as the ring type fluxgate sensor, which has a partially orthogonal, partially parallel configuration. In this structure, closed magnetization path is preserved by a cascade of a number of planar FeNi rings, which can be fabricated in a single electroplating step. On the contrary, the excitation rod is fabricated in two steps, crossing the rings such as a sewing thread. The wide linear operation range is also maintained with this structure; however the fabrication process still needs some more optimization in order to increase the repeatability of the sensors.

The objective of having a wide linear operation range is achieved by using the demagnetization factor: by reducing the length of the cores of the sensors having similar cross-sectional geometries for the rod type sensors, and by decreasing the number of rings for the ring type sensor. This approach increases the power dissipation of the sensor for the commonly used parallel configuration. Because of this, very long and thin ferromagnetic structures, having small demagnetization factor are preferred for these devices. This results in a high sensitivity device which can be operated with relatively low power. On the other hand, the long and thin layer limits the linear operation range of the sensor down to several tens of µT. However, in the orthogonal configuration, the excitation and detection mechanisms are separate, so decreasing the length of the core does not increase the power requirements of the sensor. For the rod type macro sensor, one sample is used for demonstrating the effect of reducing the core length: the length of the core is halved by chemical etching after completing the measurement with the given core length. A linear operation range of ±2.5 mT is reached with a 0.5 mm long core, whereas the linear operation range is ±250 µT with a 4 mm long core. The rod type micro sensor verified the same behavior: for core lengths of 2, 1, and 0.5 mm, the linear range is measured to be 160, 410, and 1100 µT, which are in good agreement with the simulated results. Furthermore, a linear operation range of 2 mT is obtained with the ring type micro sensor.

Another objective of this work is to realize sensors operating with low power. This is achieved with several methods and approaches. The main approach is the use of a closed magnetization path for the excitation of the sensors. Since the magnetic circuit has a closed path for the excitation magnetic field, the demagnetization factor is practically zero for this kind of geometry. This provides the minimum H_k value possible in this direction. The small cross-sectional dimensions of the sensors is another factor decreasing the power dissipation. As the radial dimensions of the core are smaller, the current required to produce the excitation magnetic field is reduced. As an example, for the rod type micro sensor, the distance between the center and the edge of the core and the core edge is around 10 µm, and the sensor can be operated with 100 mA-peak sinusoidal current. This current peak is enough to create 1600 A/m (twice the H_k value of the FeNi layer) magnetic field at the corners of the core. The low resistance core and the excitation rod carrying the excitation current is the third factor leading to low power dissipation. The traditional parallel micro fluxgate sensors are excited with a similar current passing through planar excitation coils with resistance values in the order of 100 Ω, with a resulting power dissipation of around 100 mW. On the other hand, the 100 mA-peak sinusoidal current passing over a 2 Ω excitation rod leads to an average power dissipation of only 10 mW for the rod type orthogonal fluxgate sensor.

Miniaturization of a fluxgate sensor is a challenge. The Barkhausen (magnetic) noise of the ferromagnetic materials increases as their dimensions are reduced. Unfortunately there is no existing model related to the fluxgate sensors for predicting this increase in ferromagnetic materials. However, some conclusions can be derived from the characterization results of the sensors. The noises of the sensors having different core lengths are measured and the contributions of magnetic and thermal noise are separated. According to the noise measurements presented for the rod type orthogonal micro fluxgate sensor, the Barkhausen noise of the ferromagnetic core is the dominant noise contribution over the thermal noise of the sensing coils. For 100 mA-peak sinusoidal current excitation at 100 kHz, the total noise of a sensor having a 0.5 mm long core is 628 nT for a 0.3 to 10 Hz bandwidth. The contributions of the equivalent thermal noise of the sensing coils and the Barkhausen noise are 220 nT and 580 nT, respectively. Further analysis showed that the sensor with a 0.5 mm core has 6 times higher magnetic noise than the 2 mm long one, although it has only 4 times lower sensitivity. This difference points the increase in the Barkhausen noise of the cores as the dimensions of the ferromagnetic layers are reduced.

CMOS compatibility of the sensors is ensured by using standard micro fabrication technologies such as sputtering, evaporation, electroplating, and photolithography. Furthermore, no thermal annealing steps are applied after ferromagnetic layer deposition, which may damage the CMOS circuitry. For an integration attempt, metal layers of a CMOS process can be used for realizing the sensing coils. In addition, the passivation layer of the process can also replace the SU-8 or polyimide isolation layers of the developed process flows during this work. Then, the post process to be done is only the fabrication of the sensor core over the CMOS wafer.

The electroplating of the FeNi layer is the most critical step of the fabrication process as it determines the magnetic properties of the ferromagnetic core. An electroplating solution proving soft magnetic thin FeNi layers is selected through a literature research. The bath operating conditions are optimized through several tests investigating the effects of applied current density, the temperature of the solution, stirring of the solution during the process, and applied magnetic field around the electroplating area. The best magnetic properties are achieved with electroplating at 40 °C with stirring for a current density between 14.5 and 22.5 mA/cm^2, agreeing with the previously reported data. It is observed that the cancellation of the magnetic field around the electroplating area is more suitable for an orthogonal fluxgate sensor application. An applied magnetic field bias, on the other hand, may enhance the performance of a parallel fluxgate sensor by creating a magnetic easy axis along the core. According to these, for the rod type orthogonal fluxgate micro sensor, the magnetic field is cancelled during the electroplating process, whereas a magnetic field of around 40 µT along the core is kept for the ring type micro fluxgate sensor.

Table 7.1: Comparison of the previously reported fluxgate micro sensors with the sensors developed in this work.

Ref.	**Technology**	**Core**	**Operation Mode**	**LR (µT)**	**S (V/T)**	**B_p (µT)**	**I_{exc} (mA$_{peak}$)**	**P (mW)**	**A (mm^2)**
[7.1]	Microfabricated	FeNi	Parallel	1000	22.5	5	110	~800	> 2.2x0.5
[7.2]	Microfabricated	FeNi	Parallel	500	360	-	300	100	5x2.5
[7.3]	PCB + Wound coil	FeNi	Parallel	1000	1800	1	450	~60	> 80
[7.4]	Rod + Wound coil	FeNiCo	Orthogonal	300	~44	-	40	-	-
1	Rod + Planar coils	FeNi	Orthogonal	2500	0.320	45	200	-	-
2	Microfabricated	FeNi	Orthogonal	1100	0.103	7.1	100	10	0.77x0.25
3	Microfabricated	FeNi	Parallel/ Orthogonal	2000	0.730	-	180	~55	0.51x0.50

LR: Linear operation range
S: Sensitivity
B_p: Perming
I_{exc}: Excitation current
P: Average power dissipation on the core
A: Total area of the core and the sensing coils

1: Rod type orthogonal fluxgate sensor – Macro scale
2: Rod type orthogonal fluxgate sensor – Micro scale
3: Ring type orthogonal micro sensor

Table 7.1 presents the comparison of the state of the art miniaturized fluxgate sensors with the sensors developed during this work. For the comparison, previously reported fluxgate sensors having a linear operation range larger than 300 µT and sensors of this work having the widest linear range are selected. This comparison shows that the sensors developed and fabricated during this work are the first microfabricated fluxgate sensors having a wide linear operation range and low power dissipation.

7.1 Future Work and Outlook

The characterization of the sensors shows that the main goals of this work are reached with the developed sensors. However, there are some points that could be improved:

The magnetic properties of the FeNi layers of the rod type orthogonal fluxgate micro sensor were worse than expected (lower μ_r, higher H_k). This was mainly attributed to the changing composition of the electroplating solution with time. Fabricating the sensors with a fresh electroplating solution may increase the performance of the sensors. With a lower H_k value, proportionally lower power dissipation can be expected. Therefore, better maintenance of the electroplating solution should be provided in order to control the magnetic properties of the electroplated layers, and accordingly, to increase the repeatability of the fabricated sensors.

Fabricating the sensor cores by using electroplated ternary alloys such as FeNiCo, having better soft magnetic properties can be tried as alternative processes. Of course, the electroplating solution becomes more complex, and the control of the bath becomes more difficult if ternary alloys are used. Using sputtered ferromagnetic layers instead of electroplated ones for the core fabrication is another possible alternative that can be tried.

Some problems occurred during the fabrication of the ring type micro fluxgate sensor. The major problem is the short circuits between the excitation rod and the FeNi core. The main reason for this is the non uniform thickness of the polyimide isolation layer, and its etching undercut value being much higher than expected. The polyimide patterning process should be well characterized, and the design should be modified according to this, if necessary. The surface planarization of the polyimide is also not as good as that of SU-8, which is used for the rod type micro sensor. One for having more planar surfaces is using a thicker layer of polyimide. However, this increases the distances between the metal layers, and eventually the distance between the core and the sensing coils, decreasing the sensitivity of the sensor. Another solution is to use SU-8 instead of polyimide. However, this requires the development of a pattering process for SU-8 after hard bake, which is not yet available in the clean room facilities.

The characterization of the sensors is always done by using a sinusoidal excitation current. The excitation can be provided in terms of different waveforms, depending on the requirements of the application for which the sensor is used. As an example, the duty cycle of the excitation current can be reduced for lower power dissipation, sacrificing from the sensitivity of the sensor.

The CMOS compatible processes of the sensors enable the integration of the sensors with signal conditioning electronics. The signal conditioning electronics of the sensor can be designed and fabricated with a CMOS process, and the sensor core can be fabricated on the CMOS wafer in order to realize a complete sensor system. For this approach, a suitable way to connect the excitation rod to the signal conditioning electronics should be developed. With this integration, a better noise performance can be expected from the sensors.

7.2 References

[7.1] P. Ripka, S. O. Choi, A. Tipek, S. Kawahito, M. Ishida, “Symmetrical core improves micro-fluxgate sensors,” Sensors and Actuators A, vol. 92, issues 1-3, pp. 30-36, August 2001.

[7.2] T. M. Liakopoulos, C. H. Ahn, “A micro-fluxgate magnetic sensor using micromachined planar solenoid coils,” Sensors and Actuators A, vol. 77, issue 1, pp. 66-72, September 1999.

[7.3] A. Tipek, P. Ripka, Terence O’Donnell and J. Kubik, “PCB technology used in fluxgate sensor construction,” Sensors and Actuators A, vol. 115, issues 2-3, pp. 286-292, September 2004.

[7.4] P. Ripka, M. Butta, M. Malatek, S. Atalay, F. E. Atalay, “Characterization of magnetic wires for fluxgate cores,” Transducers '07 & Eurosensors XXI conference, Lyon, France, Digest of technical papers vol. 2, Pages 2369-2372, June 10-14, 2007.

APPENDIX A–I

FABRICATION PROCESS FLOW FOR THE ROD TYPE ORTHOGONAL FLUXGATE MICRO SENSOR

Step No	Description	Equipment	Time	Speed (rpm)	Temp. (°C)	Source/ Composition/ Gases/ Solvents	Power	Mask	Target	Remarks
1.00	**WAFER CLEANING**									
1.01	Piranha cleaning	Z2,WB_Piranha	5 min + 5 min		100	H2SO4 (96%), add H2O2(30%) 200ml				DI water rinse
2.00	**AlSi1% DEPOSITION AND PATTERNING-1**									
2.01	AlSi 1% Sputtering	Z4,Spider-600	75 s/ wafer			AlSi1%			0.5 µm	
2.02	Spin on S1805	Z1, RITE TRACK	40 s	1080					1.0 µm	with EBR (edge bead removal)
2.03	Softbake	Z1, RT	75 s		115					contact
2.04	Exposure	Z1, MA150	3 s				10 mW/cm^2	MET1	30 mW/cm^2	hard contact
2.05	Development	Z1, RT				MP 351				
2.06	Hardbake	Z1, RT	60 s		115					
2.07	AlSi 1% dry etching	Z2, STS	2 m 10 s/ wafer		RT	Cl2, BCl3	RF: 800 W Bias: 100 W			
2.08	S1805 Strip	Z2, WB remover	5 min + 5 min		70	Remover 1165				directly after dry etch!
2.09	Descum	Z5,Tepla	7 min			O2	500 W			PROG#05
3.00	**SiO2 DEPOSITION AND PATTERNING**									
3.01	SiO2 Sputtering	Z4, Spider 600	25 min/ wafer			SiO2			0.8 µm	
3.02	Dehydration	Z1, HMDS oven	25 min			HMDS				
3.03	Spin on S1818	Z1, RITE TRACK	25 s	4000					2 µm	NO EBR
3.04	Softbake	Z1, RT	120 s		115					
3.05	Exposure	Z1, MA150	8 s				10 mW/cm^2	CONT	80 mW/cm^2	
3.06	Development	Z1, RT				MP 351				
3.07	Hardbake	Z1, RT	90 s		115					
3.08	SiO2 dry etching	Z2, STS	4 m 30 s /wafer			CF4	RF: 1000W, Bias: 100 W			
3.09	S1818 Strip	Z2, WB remover				Remover 1165				
3.10	Descum	Z5,Tepla	7 min			O2	500 W			PROG#05

4.00	**AlSi1% DEPOSITION AND PATTERNING-2**									
4.01	O2 plasma	Z5,Tepla	7 min			O2	500 W			PROG#05 directly before sputtering
4.02	AlSi 1% Sputtering	Z4,Spider-600	75 s/ wafer			AlSi1%			0.5 µm	
4.03	Spin on S1805	Z1, RITE TRACK	40 s	1080			-	-	1.0 µm	with EBR
4.04	Softbake	Z1, RT	75 s		115					contact
4.05	Exposure	Z1, MA150	3 s				10 mW/cm^2	MET2	45 mW/cm^2	hard contact
4.06	Development	Z1, RT				MP 351				
4.07	Hardbake	Z1, RT	60 s		115					
4.08	AlSi 1% dry etching	Z2, STS	2 m 10 s/ wafer		RT	Cl2, BCl3	RF: 800 W Bias: 100 W			
4.09	S1805 Stripping	Z2, WB remover	5 min + 5 min		70	Remover 1165				directly after dry etch!
4.10	Descum	Z5,Tepla	7 min			O2	500 W			PROG#05
5.00	**SU-8 COATING AND PATTERNING**									
5.01	O2 plasma	Z5, Tepla	30 s			O2	350 W			PROG#37
5.02	Dehydration	Z1, Hot Plate	5 min		105					
5.03	Spin on SU-8 GM1040	Z1, RC8	40 s	3000					1.2 µm	wait 1 min for relaxation,
5.04	Soft Bake	Z1, Hot Plate	5min + 10 min		65, 90					Slow cooling
5.05	Exposure	Z6, MA6	6.5 s				10 mW/cm^2	ISOL	65 mW/cm^2	hard contact
5.06	Post Exposure Bake	Z1, Hot Plate	5min + 10 min		65, 90					Slow cooling
5.07	Development	Z1, WB_Solvent	30 s + 30 s			PGMEA				IPA rinse N2 dry
5.08	Hardbake	Z1, Hot Plate	1 h		130					Slow cooling

6.00	**SEED LAYER (Cr/Cu) EVAPORATION AND PATTERNING**									
6.01	Cr/Cu Evaporation	Z4, Alcatel EVA-600	~1 min ~ 7 min			Cr/Cu	0.3 kW, 1.82 kW		20nm/200nm	E-beam evaporation
6.02	Spin on S1818	Z1, RITE TRACK	25 s	4000					2 µm	NO EBR
6.03	Softbake	Z1, RT	120 s		115					
6.04	Exposure	Z1, MA150	8 s				10 mW/cm^2	SEED1	80 mW/cm^2	hard contact
6.05	Development	Z1, RT				MP 351				
6.06	Hardbake	Z1, RT	90 s		115					
6.07	Cu Etch	BM3.125	~50 s		RT	Natriumpersulfate 10g / 600 ml DI				DI water rinse
6.08	Cr Etch	Z5, WB Divers	~2 min		RT	KMNO4: 60 g/l, Na3PO4; 200 g/l			Cu selective	DI water rinse
6.09	S1818 Stripping	Z2, WB remover	5 min + 5 min		70	Remover 1165				DI water rinse
7.00	**MOLDING AND FeNi ELECTROPLATING-1**									
7.01	Dehydration	Z1, HMDS oven	25 min			HMDS				
7.02	Spin AZ9260	Z6, EVG150	100 s	2800					8 µm	with EBR
7.03	Soft Bake	Z6, EVG150	4 min		115					
7.04	Exposure	Z6, MA6	40 s				10 mW/cm^2	FENI-1	400 mW/cm^2	hard contact
7.05	Development	Z1, DV10	6 min			AZ 400K				
7.06	Surface Preparation	BM3.215	30 -60 s		RT	Dekacid® 200 ml, H2SO4 200 ml, DI 3.6 l				DI water rinse
7.07	FeNi Electroplating	BM3.215, Electroplating Tank	2 min		40	Given in CH III	14.5 mA/cm^2		4 µm	
7.08	AZ9260 Stripping	Z6, WB remover	5 min + 5 min		70	Remover 1165				DI water rinse

8.00	**MOLDING AND Cu ELECTROPLATING**									
8.01	Dehydration	Z1, HMDS oven	25 min			HMDS				
8.02	Spin AZ9260	Z6, EVG150	100 s	2800					8 µm	with EBR
8.03	Soft Bake	Z6, EVG150	4 min		115					
8.04	Exposure	Z6, MA6	40 s				10 mW/cm^2	COPR	400 mW/cm^2	hard contact
8.05	Development	Z1, DV10	6 min			AZ 400K				
8.06	Descum	Z5, Tepla	30 s				350 W			PROG#37
8.07	Surface Preparation	Z5, EP bench	15 s		RT	H2SO4 (4%)				DI water rinse
8.08	Cu Electroplating	Z5, WB EP	2 m 10 s		30 °C	* see table below	15 mA/cm^2		2 µm	
8.09	AZ9260 Strip	Z6, WB remover	5 min+ 5 min			Remover 1165				
9.00	**SEED LAYER PATTERNING**									
9.01	Spin AZ9260	Z6, EVG150	100 s	2800					8 µm	no EBR
9.02	Soft Bake	Z6, EVG150	4 min		115 °C					
9.03	Exposure	Z6, MA6	40 s				10 mW/cm^2	FENI-2	400 mW/cm^2	hard contact
9.04	Development	Z1, DV10	6 min			AZ 400K				
9.05	Descum	Z5, Tepla	30 s				350 W			PROG#37
9.06	Cu Etch	BM3.125	~50 s		RT	Natriumpersulfate 10g / 600 ml DI				DI water rinse
9.07	Cr Etch	Z5, WB Divers	~2 min		RT	KMNO4: 60 g/l, Na3PO4; 200 g/l			Cu selective	DI water rinse
10.00	**FeNi ELECTROPLATING-2**									
10.01	EBR	BM3.215, Spinner				Acetone				
10.02	Surface Preparation	BM3.215	30 -60 s		RT	Dekacid® 200 ml, H2SO4 200 ml, DI 3.6 l				DI water rinse
10.03	FeNi Electroplating	BM3.215, Electroplating Tank	2 min		40 °C	Given in CH III	14.5 mA/cm^2		4 µm	
10.04	AZ9260 Stripping	Z6, WB remover	5 min + 5 min		70 °C	Remover 1165				DI water rinse

11.00	**SEED LAYER ETCHING**									
11.01	Spin AZ9260	Z6, EVG150	100 s	2800					8 µm	no EBR
11.02	Soft Bake	Z6, EVG150	4 min		115 °C					
11.03	Exposure	Z6, MA6	40 s				10 mW/cm^2	SEED2	400 mW/cm^2	hard contact
11.04	Development	Z1, DV10	6 min			AZ 400K				
11.05	Descum	Z5, Tepla	30 s				350 W			PROG#37
11.06	Cu Etch	BM3.125	~50 s		RT	Natriumpersulfate 10g / 600 ml DI				DI water rinse
11.07	Cr Etch	Z5, WB Divers	~2 min		RT	KMNO4: 60 g/l, Na3PO4; 200 g/l			Cu selective	DI water rinse
11.08	AZ9260 Stripping	Z6, WB remover	5 min + 5 min		70 °C	Remover 1165				DI water rinse

Cu Electroplating Solution Composition

Chemicals	Concentration
$CuSO_4.5H_2O$	100 g/l
H_2SO_4	120 ml/l
NaCl	0.12 g/l
Copper Gleam Starter (CH)	5 ml/l
Copper Gleam 125 (CH)	5 ml/l

APPENDIX A–II

FABRICATION PROCESS FLOW FOR THE RING TYPE FLUXGATE MICRO SENSOR

Step No	Description	Equipment	Time	Speed (rpm)	Temp. (°C)	Source/ Composition/ Gases/Solvent	Power	Mask	Target	Remarks
1.00	**AlSi1% DEPOSITION AND PATTERNING-1**									
1.01	AlSi 1% Sputtering	Z4,Spider-600	75 s /wafer			AlSi1%			0.5 µm	
1.02	Spin on S1805	Z1, RITE TRACK	40 s	1080					1.0 µm	with EBR
1.03	Softbake	Z1, RT	75 s		115					contact
1.04	Exposure	Z1, MA150	3 s				10 mW/cm^2	MET1	30 mW/cm^2	hard contact
1.05	Development	Z1, RT				MP 351				
1.06	Hardbake	Z1, RT	60 s		115					
1.07	AlSi 1% dry etching	Z2, STS	~2 m 10s /wafer		RT	Cl2, BCl3	RF: 800 W, Bias: 100 W			
1.08	S1805 Stripping	Z2, WB remover	5 min + 5 min		70	Remover 1165				Directly after dry etch!
1.09	Descum	Z5,Tepla	7 min			O2	500 W			PROG#05
2.00	**SiO2 DEPOSITION AND PATTERNING**									
2.01	SiO2 Sputtering	Z4, Spider 600	25m /wafer			SiO2			0.8 µm	
2.02	Dehydration	Z1, HMDS oven	25 min			HMDS				
2.03	Spin on S1818	Z1, RITE TRACK	25 s	4000					2 µm	NO EBR
2.04	Softbake	Z1, RT	120 s		115					
2.05	Exposure	Z1, MA150	8 s				10 mW/cm^2	CONT	80 mW/cm^2	
2.06	Development	Z1, RT				MP 351				
2.07	Hardbake	Z1, RT	90 s		115					
2.08	SiO2 dry etching	Z2, STS	4 m 30 s /wafer			CF4	RF: 1000W, Bias: 100 W			
2.09	S1818 Stripping	Z2, WB remover				Remover 1165				
2.10	Descum	Z5,Tepla	7 min			O2	500 W			PROG#05

3.00	**AlSi1% DEPOSITION AND PATTERNING-2**									
3.01	Ar plasma	Z4,Spider-600	2 min							5 min wait after process
3.02	AlSi 1% Sputtering	Z4,Spider-600	75 s /wafer		-	AlSi1%			0.5 µm	
3.03	Spin on S1805	Z1, RITE TRACK	40 s	1080					1.0 µm	with EBR
3.04	Softbake	Z1, RT	75 s		115					contact
3.05	Exposure	Z1, MA150	3 s				10 mW/cm^2	MET1	30 mW/cm^2	hard contact
3.06	Development	Z1, RT				MP 351				
3.07	Hardbake	Z1, RT	60 s		115					
3.08	AlSi 1% dry etching	Z2, STS	~2 m 10s /wafer		RT	Cl2, BCl3	RF: 800 W, Bias: 100 W			
3.09	S1805 Stripping	Z2, WB remover	5 min + 5 min		70	Remover 1165				directly after dry etch!
3.10	Descum	Z5,Tepla	7 min			O2	500 W			PROG#05
4.00	**POLYIMIDE COATING-1**									
4.01	Descum	Z5,Tepla	7 min			O2	500 W			PROG#05
4.02	Adhesion Promoter VM 651	Z6, Wet Bench	30 s	3000		VM 651				wait 20s before, 1 min after coating
4.03	Polyimide Coating PI 2610	Z1, Savatec	40 s	3300		PI 2610				100 rpm/s ramp. Wait 1 min for relaxation.
4.04	Soft Bake	Z1, Hot Plate	3 min		150				2.5 µm after soft bake	Slow ramp & slow cooling, wafers in lateral position
4.05	Curing	Z2, Heraeus Oven	*see the plot below		*see the plot below				1.5 µm	Slow cooling

5.00	**AlSi1% DEPOSITION AND PATTERNING-3**									
5.01	O2 plasma	Z5,Tepla	30 s			O2	350 W			PROG # 37
5.02	AlSi 1% Sputtering	Z4,Spider-600	5 min /wafer		-	AlSi1%			2 µm	
5.03	Spin AZ92xx	Z1, RITE TRACK	45 s	2300					3 µm	with EBR
5.04	Soft Bake	Z1, RITE TRACK	2 min		115					
5.05	Exposure	Z6, MA6	14 s				10 mW/cm^2	MET-3	140 mW/cm^2	hard contact
5.06	Development	Z1, DV10	3 min							
5.07	AlSi 1% dry etching	Z2, STS	~8 m /wafer		RT		RF: 800 W, Bias: 100 W			
5.08	AZ92xx Strip	Z2, WB remover	5 min + 5 min		70	Remover 1165				directly after dry etch!
5.09	Descum	Z5,Tepla	30 s			O2	350 W			PROG#37
6.00	**POLYIMIDE COATING-2**									
6.01	Polyimide Coating PI 2610	Z1, Savatec	40 s	1300		PI 2610				100 rpm/s ramp, wait 1 min for relaxation,
6.02	Soft Bake	Z1, Hot Plate	3 min		150					Slow ramp & slow cooling, wafers in lateral position
6.03	Curing	Z2, Heraeus Oven	*see the plot below		*see the plot below				2.8 µm	Slow cooling
7.00	**SEED LAYER (Cr/Cu) EVAPORATION AND PATTERNING**									
7.01	Cr/Cu Evaporation	Z4, Alcatel EVA-600	~1 min, ~7 min			Cr/Cu	0.3 kW, 1.82 kW		20nm/200nm	E-beam evaporation

8.00	**MOLDING AND FeNi ELECTROPLATING**									
8.01	Dehydration	Z1, HMDS oven	25 min			HMDS				
8.02	Spin AZ9260	Z6, EVG150	100 s	2800					8 µm	with EBR
8.03	Soft Bake	Z6, EVG150	4 min		115					
8.04	Exposure	Z6, MA6	40 s				10 mW/cm^2	FENI	400 mW/cm^2	hard contact
8.05	Development	Z1, DV10	6 min			AZ 400K				
8.06	Surface Preparation	BM3.215	30 -60 s		RT	Dekacid® 200 ml, H2SO4 200 ml, DI 3.6 l				DI water rinse
8.07	FeNi Electroplating	BM3.215, Electroplating Tank	6 min		40	Given in CH III	14.5 mA/cm^2		2 µm	
8.08	AZ9260 Stripping	Z6, WB remover	5 min + 5 min		70	Remover 1165				DI water rinse
9.00	**SEED LAYER ETCHING**									
9.01	Cu Etch	BM3.125	~50 s		RT	Natriumpersulfate 10g / 600 ml DI				DI water rinse
9.02	Cr Etch	Z5, WB Divers	~2 min		RT	KMNO4 (60 g/l), Na3PO4 (200 g/l)			Cu selective	DI water rinse
10.00	**POLYIMIDE COATING-3**									
10.01	Polyimide Coating PI 2611	Z1, Savatec	40 s	3000		PI 2611				100 rpm/s ramp, wait 1 min for relaxation,
10.02	Soft Bake	Z1, Hot Plate	3 min		150					Slow ramp & slow cooling, wafers in lateral position
10.03	Curing	Z2, Heraeus Oven	*see the plot below		*see the plot below				3.5 µm	Slow cooling

11.00	**POLYIMIDE PATTERNING (3 LAYERS AT ONCE)**									
11.01	Spin AZ9260	Z6, EVG150	40 s	1800					10 µm	no EBR
11.02	Soft Bake	Z6, EVG150	6 min		115					
11.03	Exposure	Z6, MA6	45 s				10 mW/cm^2	ISOL	450 mW/cm^2	hard contact
11.04	Development	Z1, DV10	10 min			AZ 400K				
11.05	Polyimide dry etching	Z2, STS	~12 m /wafer		RT	O2	RF: 1000W, Bias: 150 W			
11.06	AZ9260 Stripping	Z6, WB remover	5 min + 5 min		70	Remover 1165				DI water rinse
12.00	**AlSi1% DEPOSITION AND PATTERNING-4**									
12.01	Ar plasma	Z4,Spider-600	2 min							5 min wait after process
12.02	AlSi 1% Sputtering	Z4,Spider-600	6 m 15 s /wafer		-	AlSi1%			2.5 µm	
12.03	Spin AZ92xx	Z1, RITE TRACK	100 s	2800					8 µm	with EBR
12.04	Soft Bake	Z6, EVG150	10 min		115					harder PR
12.05	Exposure	Z6, MA6	22 s				10 mW/cm^2	MET-4	220 mW/cm^2	hard contact
12.06	Development	Z1, DV10	6 min			AZ 400K				
12.07	AlSi 1% dry etching	Z2, STS	~8 m /wafer		RT	Cl2, BCl3	RF: 800W, Bias: 100 W			
12.08	AZ92xx Strip	Z2, WB remover	5 min + 5 min		70	Remover 1165				directly after dry etch!
12.09	Descum	Z5,Tepla	30 s			O2	350 W			PROG#37

Polyimide Curing Cycle

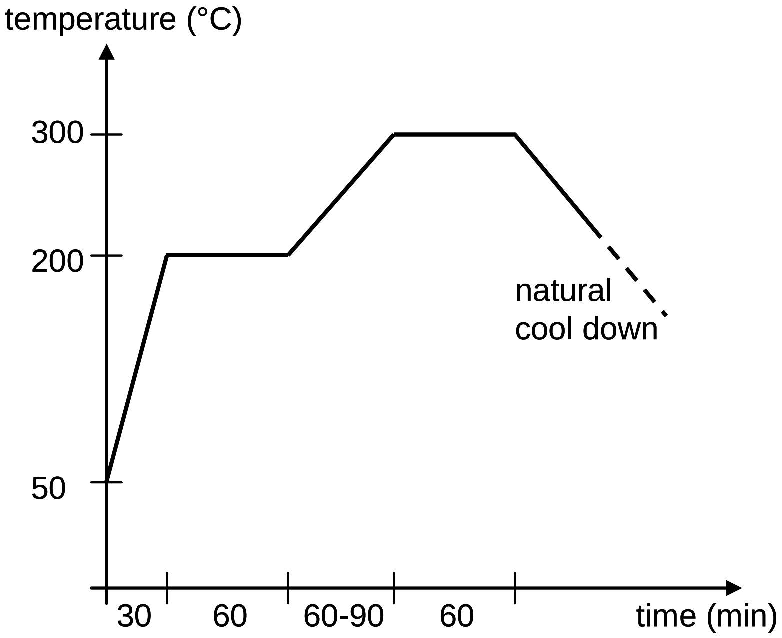

CIRRICULUM VITAE

Personal Information

Name: Özge Zorlu

Date of Birth: 20 June 1978

Place of Birth: Zonguldak, Turkey

Nationality: Turkey

Education

Dec 2003 – Feb 2008	PhD	Ecole Polytechnique Federale de Lausanne (EPFL), School of Engineering, Instutute of Microelectronis and Microsystems, Lausanne, Switzerland
Sep 2000 – Sep 2002	MSc	Middle East Technical University, Department of Electrical and Electronics Engineering, Ankara, Turkey (MSc Thesis: A Piezoresistive Pressure and Temperature Sensor Cluster)
Sep 1996 – Jun 2000	BSc	Middle East Technical University, Department of Electrical and Electronics Engineering, Ankara, Turkey

Professional Status

Dec 2003 – Feb 2008	Research Assistant – Ecole Polytechnique Federale de Lausanne (EPFL), School of Engineering, Instutute of Microelectronis and Microsystems, Lausanne, Switzerland
Sep 2000 – Nov 2003	Research and Teaching Assistant – Middle East Technical University, Department of Electrical and Electronics Engineering, Ankara, Turkey

List of Publications

Journal

[1] O. Zorlu, P. Kejik, R. S. Popovic, “An orthogonal fluxgate-type magnetic microsensor with electroplated Permalloy core,” Sensors and Actuators A: Physical, Volume 135, March 2007, pp. 43-49.

Conferences

[2] O. Zorlu, P. Kejik, R. S. Popovic, “Investigation of Giant-Magneto-Impedance (GMI) Effect and Magnetic Hysteresis in Microfabricated Permalloy/Copper Device,” Transducers’07, Lyon, France, 10-14th June 2007, pp: 2577-2580.

[3] O. Zorlu, P. Kejik, R. S. Popovic, “Fluxgate-Type Magnetic Microsensors For Wide Linear Measuring Range,” Sensors and Applications Symposium (SAS’07), San Diego CA, USA, 6-8th February 2007.

[4] O. Zorlu, P. Kejik, F. Vincent, R. S. Popovic, “An orthogonal fluxgate-type magnetic microsensor,” MEMS’06, Istanbul, Turkey, 22-26th January 2006, pp: 646-649.

[5] O. Zorlu, P. Kejik, F. Vincent, R. S. Popovic, “A novel planar magnetic sensor based on orthogonal fluxgate principle,” IEEE PRIME’05 Conf. Lausanne, Switzerland, July 2005 (Awarded by the "Gold Leaf" award, given to 10 papers out of 111)

Patent

[6] P. Kejik, O. Zorlu, “Orthogonal Fluxgate Magnetic Field Sensor,” EP 1,746,430, January 25, 2007.